THE EFFECT OF METALS ON THE GRAPHITIZATION OF THIN CARBON FILMS

A thesis submitted for the degree of

Doctor of Philosophy

in the

University of London

by

Mohan Chandra Borah, M.Sc.

Department of Chemical Engineering and
Chemical Technology,

Imperial College of Science and Technology,

London, S.W.7.

January, 1970.

ABSTRACT

A simple method for producing composite films of carbon and metal has been developed, and used for graphitisation studies in thin films. Several carbon/metal systems have been investigated, carbon/iron in detail. Films with iron concentration .6 to 22.2 wt. per cent were heated in vacuum and argon at temperatures ranging from 400-2000°C, and the resulting changes in microstructure studied, using electron microscopy and diffraction. On heating, a carbide of iron precipitated, which has been identified as cementite (Fe_3C); the growth of these particles has been studied as a function of time, temperature and iron concentration.

The growth kinetics have been analysed to give the diffusion coefficient of iron in evaporated carbon between 500 and 800°C. D_o was found to be $4.9 \times 10^{-12} cm^2/sec.$ and the activation energy U was calculated as 16.1 k.cal per mole.

At temperatures above 1000°C in vacuo the carbide particles disappeared, leaving a film composed of partially graphitic carbon, which was randomly oriented; this should be compared to the preferred orientation produced in pure carbon films on graphitisation. L_a and L_c measured from the breadths of prismatic and basal plane reflections were found to increase with iron concentration.

Pre-nucleation experiments in which cementite particles were developed in the films prior to a graphitisation treatment at 1200°C indicated that the final values of L_a and L_c were related to the size of the cementite precipitates.

Detailed studies indicate that graphitic carbon is formed at the cementite/carbon interface as a result of the cementite decomposition.

Ni, V, Pt and Cu were also studied. Ni and V both gave enhanced graphitisation by essentially the same mechanism described above. Pt precipitated predominantly as the metal, but some evidence was found for the existence of a carbide. Results for Cu were inconclusive due to its insufficient concentration in the films produced.

C O N T E N T S

	Page.
Abstract.	1
Chapter I.	12
1. Introduction.	12
1.1. Structure of graphite.	13
1.2. Defects in graphite.	16
1.3. Forms of graphite and Preparation.	17
1.3.1. Single crystal.	17
1.3.2. Polycrystalline graphite.	18
1.3.3. Pyrolytic graphite.	19
1.3.4. Carbon black.	21
1.3.5. Evaporated carbons.	22
Chapter II	23
2. Carbonisation and graphitisation.	23
2.1. Carbonisation.	23
2.2. Graphitisation.	26
2.2.1. Graphitising and non-graphitising carbons.	27
2.2.2. Ordering Parameters.	27
2.2.3. Analysis of Houska and Warren.	28
2.2.4. The definition of Maire and Méring.	29
2.2.5. Definition of Takahashi et. al.	31

		Page.
2.3.	Mechanisms of graphitisation.	32
2.3.1.	Franklin's model.	32
2.3.2.	Mizushima's model.	34
2.3.3.	Dislocation model.	35
2.4.	Kinetics of graphitisation	36
2.4.1.	Mizushima's analysis.	37
2.4.2.	Fischbach's analysis.	39
2.4.3.	Presland and White's analysis.	40
Chapter III		42
3.	Catalytic graphitisation.	42
3.1.	Graphitisation Catalysis by vacuum deposition on to heated metal foils.	45
3.2.	Graphitisation catalysis by pyrolysis of hydrocarbons over metals.	47
3.3.	Graphite from carbon-saturated metal melts.	49
3.4.	Fluidised bed method.	51
3.5.	Kinetic study of catalytic graphitisation.	51
3.6.	Effect of gas phase on graphitisation.	53
3.7.	Effect of stress on graphitisation.	54
Chapter IV		55
4.	Theory of precipitation.	55
4.1.	Laws of diffusion.	55
4.2.	Precipitation.	57
4.3.	Theory of growth of precipitates from solid solution.	58

Page

Chapter V		63
5.	Thin films.	63
5.1.	Introduction.	63
5.2.	Method of preparation of thin films.	63
5.2.1.	Vacuum evaporation.	64
5.2.1.1.	Evaporation of carbon.	65
5.2.2.	Preparation of alloy films.	66
5.3.	Sputtering.	66
5.4.	Chemical Vapour deposition.	67
5.5.	Tarnishing.	68
5.6.	Electrodeposition.	69
5.7.	Anodising.	69
5.8.	Growth and structure of vacuum deposited films.	69
5.8.1.	Condensation phenomenon.	69
5.8.2.	Nucleation and growth.	71
5.8.3.	Epitaxial growth.	72
5.8.4.	Structure and properties of thin films.	74
5.9.	Metastable alloy films.	76
5.9.1.	Transformation from amorphous to crystalline phases.	77
5.9.2.	Crystalline alloy films.	78

Page.

Chapter VI 81

6. Electron microscopy and diffraction. 81

6.1. Introduction. 81

6.2. Resolution of an electron microscope. 81

6.3. Design of an electron microscope. 82

6.4. Image formation (Bright field). 83

6.5. Image formation (Dark field). 85

6.6. Scanning electron microscopy. 86

6.7. Image contrast. 88

6.8. Moiré fringes. 89

6.9. Scattering and diffraction. 91

6.9.1. Scattering phenomena. 91

6.9.2. Electron diffraction. 91

6.9.3. Atomic scattering. 92

6.9.4. Kinematical theory of electron diffraction. 93

6.9.4.1. Scattering from a crystal. 93

6.9.4.2. Diffraction from a parallelipiped crystal. 98

6.10. Dynamical theory of electron diffraction. 101

Chapter VII 102

7. Diffraction analysis of carbonaceous materials. 102

7.1. Franklin's Analysis. 105

7.2. Analysis of Guentert and Cvikevich. 108

		Page.
Chapter VIII.		111
8.	Experimental procedure.	111
8.1.	Materials.	111
8.2.	Evaporation unit.	111
8.3.	Method of co-evaporation.	113
8.3.1.	Preparation of substrates.	113
8.4.	Measurement of film thickness.	115
8.4.1.	Estimation of film thickness during evaporation.	116
8.4.2.	Multiple beam interferometry.	117
8.5.	Determination of film composition.	117
8.5.1.	From direct calculation.	117
8.5.2.	Film composition by electron probe microanalysis.	120
8.5.2.1.	Theory of the electron probe microanalyser.	120
8.6.	Simultaneous evaporation.	122
8.7.	Preparation of carbon mounts.	123
8.8.	Mounting of specimens.	124
8.9.	Evaporation of carbon on to heated iron foil.	124
8.10.	Heat treatments.	125
8.10.1.	Temperature below 1000°C.	125
8.10.2.	Heat treatment at temperatures from 1000°C upwards.	126
8.10.3.	Heat treatment in argon atmosphere.	129
8.10.4.	Heat treatment in chlorine atmosphere.	130
8.10.5.	Disappearance of film.	130

		Page.
8.11.	Electron microscopy.	132
8.11.1.	Alignment of the instrument.	132
8.11.2.	Focusing and exposure.	132
8.11.3.	Photographic materials.	133
8.11.4.	Magnification.	133
8.11.5.	Anticontamination.	135
8.12.	Lensless diffraction.	135
8.13.	Selected area diffraction.	136
8.14.	Shadowing.	136
8.15.	Hot stage of the microscope.	137
8.16.	Dark field operation.	138
8.17.	Scanning electron microscopy.	138
8.18.	Determination of camera constant λL.	139
8.19.	Indexing of diffraction patterns.	140
8.20.	Microdensitometry.	140
8.21.	Measurement of La.	142
8.22.	Mean La values.	145
8.23.	Particle size measurements.	145
8.24.	Particle size analysis.	149
8.24.1.	Distribution laws.	152

Chapter IX

		Page
9.	Experimental results.	155
9.1.	Determination of specimen composition.	155
9.1.1.	Using parameters of the evaporant.	155
9.1.2.	Electron microprobe analysis.	156
9.2.	Composition V_S. frequency curve.	160
9.3.	Microstructure of as-deposited films.	160
9.4.	Microstructure of films heat treated below 1000°C.	161
9.5.	Cementite.	164
9.6.	Kinetics of precipitation.	164
9.6.1.	Particle size distribution.	165
9.6.2.	Influence of iron concentration.	171
9.6.3.	Influence of residence time.	171
9.6.4.	Effect of temperature.	174
9.6.5.	Number density with respect to residence time and temperature.	177
9.7.	Diffusion of iron through carbon.	187
9.7.1.	Calculation of D using Einstein's equation.	187
9.7.2.	Diffusion coefficient and activation energy from Wert's transformation equation.	194
9.7.2.1.	Calculation of density ρ_o of the as-deposited films.	198
9.7.2.2.	Calculation of fractional volume from direct measurements.	201
9.7.2.3.	Calculation of fv (fractional volume) of Fe_3C from surface area measurements.	202
9.7.2.4.	Calculation of fv by direct measurement after introducing a reducing factor.	204

Page

9.7.2.5. Diffusion coefficient. 211

9.8. Film thickness Vs. iron concentration. 213

9.9. Dark field microscopy of Fe_3C particles. 213

9.10. ffect of shadowing. 215

9.11. Faceting. 215

9.12. Kinetics of crystallisation. 220

Chapter X

10. Graphitised films. 222

10.1. Introduction. 222

10.2. Electron microscopy. 224

10.2.1. Bright field microscopy. 224

10.2.2. Dark field images. 225

10.2.3. Tilling experiment. 229

10.2.4. Scanning electron microscopy. 229

10.3. Measurement of L_a and L_c. 233

10.4. Effect of heat treatment temperature. 233

10.5. Effect of heat treatment time. 233

10.6. Effect of F_e concentration on L_a. 236

10.7. Effect of F_e concentration on L_c. 236

10.8. Prenucleation. 238

10.8.1. Constant pre-nucleation temperature and time but varying iron concentration. 240

10.8.2. Effect of pre-nucleation temperature and time. 240

10.9. Effect of heat treatment atmosphere. 240

10.10. Effect of chlorine atmosphere. 248

10.11. Anisotropic layer growth. 248

Page

Chapter XI

11. Effect of other metals. 253

11.1. Platinum/carbon system. 253

11.2. Nickel carbon system. 256

11.3. Vanadium/carbon system. 259

11.4. Copper/carbon system. 262

Chapter XII

12. Discussion. 265

12.1. Preparation of thin metal/carbon films by co-evaporation. 265

12.2. Phase transformation in metal/carbon films. 266

12.3. Coarsening of precipitates. 271

12.4. Diffusion of metal in carbon. 271

12.5. Decomposition of carbides. 274

12.6. Graphitisation catalysis. 276

12.7. Other metals. 280

12.7.1. Nickel. 280

12.7.2. Vanadium. 281

12.7.3. Platinum. 281

12.7.4. Copper. 282

12.8. Future developments. 282

References. 285

Acknowledgements 295

CHAPTER I

1. Introduction.

Graphite is one of the most widely used high temperature materials because of its unique combination of anisotropy and high thermal stability. It is used in a number of applications, especially in nuclear reactor and aerospace technology. Due to its extraordinary combination of properties it is of considerable interest to the materials scientist.

Graphite is generally produced commercially from carbonaceous starting materials by carbonisation and graphitisation. The structure and properties of commercial graphite are largely dependent on the methods of fabrication, and there are numerous papers on the subject of graphitisation of carbon by heat treatment at the very high temperatures necessary (3000°C). The conversion of amorphous carbon to graphite, which is the thermodynamically stable form of carbon at room temperature and pressure, necessitates the supply of large amounts of energy, the cost of which is considerable. It is therefore economically desirable to find a more favourable kinetic route from amorphous carbon to graphite involving lower temperatures, and the commonest technique for achieving this is the introduction of a so-called graphitisation catalyst. Considerable researches have already

been carried out since E. G. Acheson's time on the catalytic action of, for example, certain metals on the graphitisation of carbon, with a view to reducing the temperature of graphitisation. Most of the previous studies on this subject have been carried out using x-ray diffraction. The present work was undertaken to explore the catalytic action of a number of metals on the graphitisation of amorphous carbon, in the form of evaporated thin films.

These films were prepared by co-evaporation of carbon and metal; they were then heated in vacuum in the temperature range 400 - 2000°C and the resulting microstructural changes were investigated by electron microscopy and electron diffraction.

1.1. Structure of graphite.

Diamond and graphite are two crystalline forms of carbon. Bragg and Bragg[1] demonstrated clearly that in diamond each carbon atom is covalently bonded to four other carbon atoms arranged tetrahedrally, the C - C bond distance being 1.51Å. In graphite the crystal is composed of sheets of carbon atoms; the atoms forming each sheet are co-planar and lie at the corners of a hexagonal 'honeycomb' structure, the distance between any two neighbouring carbon atoms being 1.42Å. The distance between these layers is 3.354Å and they are held together

by comparatively weak van der Waal's type forces, so that the sheets can slide over one another, giving graphite its flaky character and lubricating properties. In the crystal the sheets are slightly staggered so that only alternate carbon atoms in any sheet are directly opposite carbon atoms in the neighbouring sheets. The most highly ordered form of graphite which occurs in natural single crystal is termed hexagonal graphite (Fig.1). A precise determination of the structure of a single crystal of graphite was made by Bernal[2] who observed that the lattice proposed by Hull[3] was correct. The rhombohedral unit cell he reported was 6.82Å high and 2.45Å on the side. A second modification of graphite has been found to exist and is referred to as rhombohedral graphite by Lipson and Stokes[4]. The only difference between the two lattices is in the relative arrangement of successive layers. The repeat unit in the hexagonal lattice consists of two layers and this arrangement is said to form an ABAB sequence, (Fig. 2A), whereas the rhombohedral unit cell contains three layers arranged in an ABCABC sequence, (Fig. 2B) with the c-axis repeat distance of 10.05Å. Rhombohedral graphite is found in small quantities in natural graphites and is detected by additional lines in the diffraction photographs. The percentage of rhombohedral graphite can be increased considerably by cold working. Conversely, on heating to

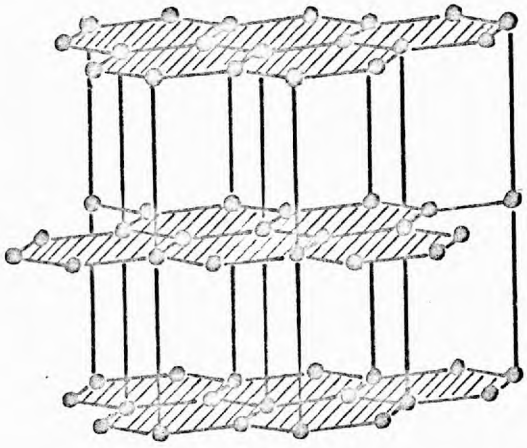


FIG.1. THE STRUCTURE OF GRAPHITE

HEXAGONAL RHOMBOHEDRAL

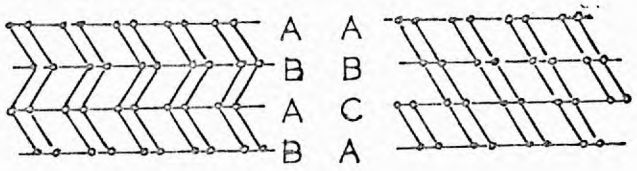


FIG. 2A. FIG. 2B.

very high temperature the rhombohedral lattice reverts to hexagonal. Recent work[5] has revealed that rhombohedral graphite does not exist as a separate structure but is formed by the passage of dislocations in the hexagonal form which cause the stacking sequence to change from ABAB to ABCABC.

1.2. Defects in graphite

The graphite structure described above refers only to perfect crystals. In practice all crystals suffer from various kinds of defect, plane, line and point. The planar deviations from perfection involve (1) stacking disorder (2) rotation between the successive sheets. The following are the simple stacking faults in graphite.[6]

(a) ababacaca or ababcbcbc. This type of fault contains one triplet of layers in the rhombohedral arrangement.

(b) ababcacac or abacbcbcb. This is produced when one crystal part is shifted with respect to another part and contains two triplets of layers in the rhombohedral form.

(c) ababcabab or abacbabab. This is generated when a single sheet c is inserted in the normal sequence of abab.

(d) ababcabab. This kind of fault has two over-lapping triplets of rhombohedral arrangement.

Extensive studies concerning the structures of the different stacking faults and dislocations have been made by Amelinckx and his co-workers[6,7,8], and will not be discussed here. Fuzita and Izui[9] pointed out four

different kinds of dislocations in the graphite lattice; both basal and non-basal dislocations may occur. Basal dislocations are characterised by a Burger's vector parallel to the basal planes and non-basal dislocations can be characterised by a Burger's vector c [0001] . Hashimoto and Uyeda[10] were the first to point out that dislocations in crystals can be detected through their effect on moiré patterns, and Dawson and Follett[11] studied the dislocations in synthetic graphite using these moiré patterns. The basal plane dislocations can be identified readily using electron microscopy whereas non-basal dislocations are difficult to detect. Thomas[12] used optical microscopy for the study of the non-basal dislocation and the pioneers[13-15] in this field subsequently developed various theories and techniques for their observation and interpretation. For a review of the various kinds of dislocation associated with graphite the reader is referred to reference 6.

1.3. Forms of Graphite and preparation.

1.3.1 Single crystal.

Carbon exists in a wide variety of structural forms, ranging from glassy non-crystalline carbon to almost perfect single crystals of diamond and graphite. Graphite is found as a mineral in Ceylon, Madagascar, Siberia, Ticonderoga (New York) and elsewhere. Single crystals are

usually found embedded in calcite or pyroxene which can be dissolved away to leave the graphite. Traces of metallic impurities must be removed by treatment with hydrochloric acid followed by hydrofluoric acid, resulting in graphite of low ash content.[16] 'Kish' graphite which occurs in the manufacture of cast iron can be obtained by dissolving away the iron and the ash content is about 2% after purification.[17]

Large perfect single crystals of graphite occur very rarely in nature, and attempts to produce single crystals have become an important line of research in carbon science to-day. Tsuzuku[18] produced very small crystals by heating carbon black to 2500°C in a small graphite crucible. Blackman and Ubbelohde[19] found that by heating pyrographite under pressure they obtained specimens which gave the x-ray diffraction patterns of a single crystal. Foster and his co-workers [20] were able to produce single crystals of graphite by decomposing aluminium carbide at 2500°C. Austerman[21] et.al produced large and relatively perfect single crystals of graphite by precipitation from carbon-saturated molten iron and nickel. Most recently Presland and Walker[22] reported a method of producing single crystal graphite by pyrolysing acetylene over platinum and nickel foil at a temperature of about 1000°C.

1.3.2. Polycrystalline graphite.

A large number of industrial carbons possess only

small regions of highly graphitic material distributed in a less crystalline matrix. Thus these carbons contain a whole range of structures varying from graphitic order to near complete disorder. Industrially anthracite or coke particles are bonded with pitch and extruded into bars followed by heat-treatment at temperatures up to 3000°C in the absence of air. This results in so-called poly-crystalline graphite, consisting of small crystallites which have very little preferred orientation one to another.

1.3.3 Pyrolytic graphite

This can be obtained by the deposition of the thermal decomposition products of hydrocarbons (e.g. methane, propane, benzene, acetylene etc.) on to a hot substrate [23]. There is a preferred orientation of the crystallites and the most probable c-axis direction is at right angles to the deposition surface, but no ordering of the crystallites in the a-axis direction normally takes place. Graphite prepared by this method at a temperature of 2150°C has a directional spread of crystallite c-axes of about 10-15° and the alignment of the c-axes can be improved by heating the material at 3100°C in a resistance furnace[24]. To produce graphite with the smallest c-axis spread, pyrolytic carbon is annealed at about 3000°C under an externally applied stress of around 400 atmospheres[25] normal to the plane of deposition. The mechanism of

pyrolytic deposition is not well understood. The kinetics of deposition of the pyrolytic carbons have been studied by Diefendorf[26], Oxley[27] et.al and Hirt and Palmer[28]. Recent studies have revealed that the structures of these carbons vary widely depending on the deposition conditions.

Carbons deposited in fluidised beds have become of considerable technological importance nowadays. The important carbon structures that are deposited in fluidised beds have been divided by Bokros et.al.[29-31] into three groups according to their microstructures, namely (a)laminar (b) isotropic and (c) granular. The laminar carbons have a high degree of preferred orientation of the layer planes parallel to the deposition plane, the isotropic carbons have random structures and the granular carbons are dense with very little orientation and are more crystalline than the others deposited at the same temperatures.

Another form of artificial graphite is the whisker, whose properties have been described by Bacon[32]. Whiskers are formed in a carbon arc at 3600°C when operated under 92 at ms of argon and may have diameters of up to five microns. Meyer [33] reported formation of good whiskers when pyrolytic graphite was deposited from acetylene at 1.33 mm of Hg. pressure at 2000°C.

1.3.4 Carbon black

On passing a hydrocarbon gas or vapour through an enclosure heated to a high temperature a sooty deposit is formed. Sooty carbons also result from the incomplete combustion of hydrocarbons. The carbon deposits from both these processes are called carbon blacks. It posed a major problem as to whether carbon black consisted of finely divided graphite crystals or another form of carbon with a lower degree of order until Warren[34,35] put forward his widely accepted model of their structure. Carbon black has been described[34] as "a simple and definite example of an intermediate form of matter which is different from both crystalline and amorphous states". The term 'turbostratic' has been suggested for this kind of solid. The carbon blacks are composed of graphite-like layers arranged roughly parallel and equidistant in stacks of several layers, but with each layer having a completely random orientation about the layer normal. The layer separation in carbon blacks is larger than in graphite. The sizes of the layers and heights of the stacks characterise the structure of a particular black. The crystallite size of most of the blacks is in the range of 11-15Å along the c-axis and 15-20Å in the basal plane.

1.3.5. Evaporated carbons

Bradley[36] developed a method for evaporating carbon on to a substrate in a vacuum. Generally such deposits are very poorly crystalline[37,38,39] and heat treatment at 2800 - 3000°C is required to convert the material to graphite. Recently Presland and White[40] reported the structure of evaporated carbon films heat treated in the range of 1000 - 2200°C and their results will be discussed in more detail in a later chapter. Becker[41] developed a method for producing carbon films at a very slow rate using electron bombardment method. He observed marked differences between the structures of the resulting films produced by the usual Bradley method and by the electron bombardment method, and found that properties and structure of evaporated carbon films are dependent on the material used for the carbon rods, on the pressure during evaporation, on the nature of the substrate and on the rate of evaporation. (cf. Presland and White).

CHAPTER II

2. Carbonisation and graphitisation

2.1. Carbonisation

Carbonisation is the process by which carbons are produced from various carbonaceous materials by heating them under different conditions. The transformations, which are very complex, take place in several stages during heat treatment. The first step, in which the thermal decomposition of the organic molecules and the condensation of the aromatic rings proceed simultaneously, resulting in the formation of crystallites, can be called the process of carbonisation, which continues up to 1800°C.

The mechanism of carbonisation was pictured by Hoffman[42] as follows:- during the initial stages of heating highly condensed aromatic molecules are formed and they arrange themselves in a graphite-like layered structure. As the temperature rises graphite nuclei are formed surrounded by chemically bound complex hydrocarbon rings and chains. As coking proceeds they decompose, some of the carbon atoms being lost in the form of volatile compounds and the remainder attaching themselves to the edges of the hexagon planes, thus causing the lateral growth of the graphite crystallites.

Blayden et.al[43] made a quantitative study of crystallite growth in the temperature range 400-1300°C during carbonisation of cellulose and Northumberland coal. They observed that the a-dimension of the crystallites showed a continuous growth with carbonisation temperature whilst the c-dimension remained practically constant. The interatomic distance of the carbon atoms in the layer planes was 1.37Å as against 1.415Å in the case of macro-crystalline graphite, indicating a more powerful bonding of the carbon atoms in microcrystalline graphite. They extended their investigation[44] to include one American and two Welsh anthracites, lignin, and an Irish peat, and used carbonisation temperatures up to 2200°C. Here in the case of anthracites they observed a decrease in c-dimension as the carbonisation temperature was increased from 400 - 900°C which was interpreted as due to disruption of the crystallites, whereas the peat coke crystallites showed a very rapid growth in the c-direction between 700 and 1000°C which was believed to be a catalytic effect.

Carbons prepared by the carbonisation of polymers possess physical characteristics imposed upon them by virtue of their structure and also by the conditions of carbonisation[45,46]. The extent to which these carbons graphitise on further heat treatment at temperatures above 2000°C depends very largely on the properties of the carbon

prepared at 700 - 800°C.[47,48] Kipling[47] investigated the relationship between melting during the carbonisation process and the ability of the resultant carbons to graphitise at higher temperatures. He made the point that if a graphitising carbon is to be formed, fusion of the polymer must take place so that polycyclic aromatic structures formed at lower temperatures readily orientate to form graphite.

Carbons produced by the low temperature charring of organic compounds exhibit wide variations in their graphitisability depending upon the structure of the organic compounds. Kinney and his co-workers[49,50] reported that charring of anthracene produced carbon of high graphitisability, whereas phenathrene, an isomer of anthracene, yielded a carbon of poor graphitisability. Kinney concluded that phenathrene, which has a molecule with an angular shape, cannot condense into sheets of aromatic structure except by the orientation of the molecules in a manner which does not correlate with the preferred chemical behaviour of the molecule. Since the chemical behaviour probably governs a sufficient number of the condensation reactions to strongly influence the structure of the char formed, a non-graphitising carbon results. Anthracene which is in relative abundance in coal tar is of considerable importance to graphite manufacturers whose raw materials consist

primarily of petroleum coke and coal tar pitch.

Considerable interest however, has been aroused recently in the mechanism of the carbonisation of organic solids. In a recent note, Thomas et al[51] suggested that carbonisation is effected by structural irregularities such as dislocations and even point defects. Well defined large sucrose single crystals produced from concentrated aqueous solutions and given a heat treatment in vacuum at temperatures from 120°C to 140°C revealed well defined decomposition 'volcanoes' on the <100> faces. The density of these volcanoes was approximately $10^5 cm^{-2}$, and they were arranged in crystallographic directions along the surface. Hence it was concluded that dislocations play an important part in the carbonisation process.

2.2. Graphitisation.

Graphitisation is the process of production of artificial graphite from carbon, with or without additives. There are several parameters which can be varied in order to alter the resultant structure. The most effective of these is the temperature of heat treatment. Both temperature and duration of heating play a part in increasing the crystallite size and decreasing the disorder. This gradual development, which finally leads to large regions having three-dimensional order, is referred to as graphitisation.

2.2.1 Graphitising and non-graphitising carbons.

Not all carbons can be graphitised. There are some carbons which retain a high degree of non-crystallinity even at high temperatures. Franklin [48] was able to classify a number of carbons, obtained by pyrolysing organic starting materials, into graphitising and non-graphitising carbons. Examples of the former are pitch and petroleum cokes and the pyrolysed residue from the polymer polyvinyl chloride. These on heating to 2000°C can produce ordered crystallites several hundred of angstroms across and there is relatively little disordered carbon in the matrix. On the other hand materials such as charcoal and the carbons from polyvinylidene chloride and polyfurfuryl alcohol do not form large crystallites even at 3000°C. Franklin showed that these two types of carbon can be distinguished even at 1000°C by measuring their crystallite size.

2.2.2. Ordering parameters.

The five well-known parameters to describe the degree of ordering in carbons are L_a, L_c, d, p and t. For a given carbon, L_a and L_c are the average overall dimensions of the crystallites measured parallel and perpendicular to their layer planes, and these dimensions are deduced from the widths of the appropriate diffraction lines.

The parameter 'd' which is the interlayer spacing in carbons varies from a value of 3.44Å for turbostratic carbons to a value of 3.35Å for graphite. Franklin[52] assumed that the observed value of interlayer spacing for any carbon was made up of differing proportions of these two discrete values 3.35Å and 3.44Å. She suggested that the observed interlayer spacing was related to a disorder parameter p by the following equation,

$$d = 3.44 - .086\ (1 - p^2) \quad \ldots\ldots\ldots\ldots\ldots\ldots (1)$$

The parameter p is the proportion of mutually disoriented layer pairs; when p = 0, d = 3.354Å and there is no disorder, while when p = 1, d = 3.44Å and there is complete disorder. The disorder parameter is often used to characterise carbons and is usually calculated by using Bacon's[53] modifcation of Franklin's equation,

$$d = 3.44 - .086\ (1 - p) - .064p\ (1-p) \quad \ldots\ldots (2)$$

2.2.3. Analysis of Houska and Warren.

Houska and Warren[54] defined a parameter p_1, the probability that a pair of neighbouring layer planes has the graphite orientation. Before the onset of graphitisation the layer planes of a parallel layer group have random orientation about the layer normal with a spacing a_3'. In the early stages of graphitisation some of the pairs of neighbouring layer planes assume the graphite relation, the spacing being $a_3 = 3.354$Å. Nearest neighbour pairs of

layers take the ordered graphite relation independently producing both A-B-A and A-B-C sequences. This ordering produces modulations in the two-dimensional (hk) reflections from which p_1 can be obtained. In terms of $a_3 = 3.354\text{Å}$ and $a'_3 = a_3(1 + z_1)$, where z_1 is the distortion in a_3 produced by the presence of distorted layer planes, these authors showed the average interlayer spacing to be equal to

$$d_{002} = P_1 a_3 + (1 - P_1)\, a'_3 \quad \ldots\ldots\ldots\ldots\ldots\ldots\ldots (3)$$

Using one set of experimentally determined values of d_{002} and P_1 they found a'_3 to be 3.44Å which is in good agreement with the value of Franklin for the spacing of disordered neighbouring layer planes. Putting $a_3 = 3.354\text{Å}$ and $a'_3 = 3.44\text{Å}$, the above equation can be reduced to,

$$d_{002} = 3.440 - .086\, P_1 \quad ; \ldots\ldots\ldots\ldots\ldots\ldots (4)$$

The value of P_1 can either be derived from the modulations of (hk) reflections or from the average interlayer spacing using equation (4).

2.2.4 <u>The definition of Maire and Méring</u>.

Maire and Méring[55,56] simply defined the degree of graphitisation as the coefficient 'g' measuring the fraction of carbon layers modified by the graphitisation process and having a spacing of 3.354Å. This coefficient can be deduced using the relation

$$d_{002} = a_3 g + (1 - g)\, a'_3$$

or,

$$d_{002} = 3.440 - .086g \quad \ldots\ldots\ldots\ldots\ldots\ldots (5)$$

From an x-ray study of the polyvinyl chloride char they concluded that in a partially graphitised sample the layers of both kinds, namely graphitised layers and non-graphitised layers, are stacked at random and nearest neighbour layers order independently. Thus they replaced the idea of the graphitis tion of the elementary layers. In addition they suggested a relation between the probability P_1 defined by Houska and Warren and the coefficient 'g' which was,

$$P_1 = g^2 \quad \ldots\ldots\ldots\ldots\ldots\ldots (6)$$

If P_r is the probability that (n + 1) adjacent layers are ordered the hypothesis of two types of layers leads to the generalisation of the above equation in the form,

$$P_n = g^{n+1} \quad \ldots\ldots\ldots\ldots\ldots\ldots (7)$$

P_n denotes the probability that a given packet of (n +1) layers is completely ordered. Experimentally it was found that $P_n = g^{2n}$, which is equivalent to,

$$P_n = (P_1)^n$$

Maire and Méring suggested that it was not the state of the layer in the packet but the state of its surface which controls its ability to order with respect to its neighbour, but that there is no relation between the states of the two faces of the same layer.

2.2.5 Definition of Takahashi et al.

Takahashi et al[57] showed that, regardless of the type of carbon used, the product of $(1 - P_1)$ and L_a, the crystallite dimension along the a-axis, is a constant for L_a values greater than 110Å.

Hence, $$(1 - P_1) \times L_a = 110$$

or $$P_1 = 1 - \frac{110}{L_a} \quad \ldots\ldots\ldots\ldots\ldots\ldots (8)$$

Also it has been claimed that d_{002} can be expressed as a single linear function of the reciprocal of the L_a dimension,

$$d_{002} = 3.354 + \frac{9.5}{L_a} \quad \ldots\ldots\ldots\ldots\ldots\ldots (9)$$

This shows that the interlayer spacing can serve as a good measure of crystallite growth in the graphitisation process.

Other authors also attempted to relate crystallinity and stacking order, notably Maire and Méring,[58] and their plot of L_a vs. P_1 exhibited similarity to that of Takahashi et al. Their plot of L_c vs P_1 however, indicated that the stacking height saturates and has a limiting value of approximately 220Å even when the stacking order exceeds 50%.

More recently Ruland [59] has attempted to establish a more general relation for disorder in graphitic carbons, and to show how the parameters based on this relation can describe the transition from non-graphitic carbons to graphite. The following relationship was deduced,

$$d_{002} = 3.354 + .425\ \Delta^2_{a,b}$$

where $\Delta_{a,b}$ is the relative lateral displacement of the adjacent layers a,b.

2.3 Mechanisms of graphitisation

The process by which graphitisation occurs is complex and is not well understood. Until recently there has been considerable lack of information on this subject. Although several theories of graphitisation have been proposed a real understanding of the graphitisation process in terms of empirical relationships between the average interlayer spacing and other parameters has not yet been reached.

2.3.1 Franklin's model.

Franklin investigated the structure of carbons of different origin treated at different temperatures between 1000 and 3000°C, and showed that the graphitising and non-graphitising carbons formed two distinct and well-defined classes. The graphitising carbons included a pitch coke, a petroleum coke, cokes prepared from coking coals and chars obtained by pyrolysis of polyvinyl chloride. These carbons were heated to temperatures of up to 1720°C only, a temperature sufficient to produce a layer diameter of about 70Å and parallel layer groups containing about 30 layers. At higher temperatures than this, further increases in layer diameter and the height of parallel layer groups led

to graphitisation. The non-graphitising carbons were polyvinylidene chloride (saran), sugar charcoal and Northumberland coal. Franklin observed the difference between the two classes of carbon even in the early stages of the carbonisation process. The graphitising carbons, at 1.000°C, had approximately four layers per parallel group (M) and for non-graphitising carbons produced under the same conditions the value of M was between 2 and 2.5. At higher temperatures, the layer diameter increased rapidly with a rapid increase in M in the case of graphitising carbons, while in the non-graphitising carbons there appeared to be little change in layer diameter with practically no change in M.

Franklin[48] has proposed that all carbons can be described as graphitising or non-graphitising carbons according to their behaviour towards graphitisation. For soft carbons below 1300°C growth occurs by incorporation of a disorganised phase, above 1300°C at the expense of other crystallites. In both cases it is hard to see why the growth stops when a definite size is reached. In a detailed discussion of the problem she came to the conclusion that growth occurs by displacement of whole layer planes. Thus as the size of the planes increases higher temperatures are required to provide sufficient energy to displace them and thus to continue the process of crystallite

growth. She discarded the idea of growth by the movement of isolated atoms or small groups of atoms from one crystallite to another since this would involve the breaking of strong c-c bonds, which would require a higher energy of activation than is consis ent with the observation of growth at temperatures as low as 1000°C.

The graphitisation process for hard carbons seems to be more complicated than for soft ones. Franklin found that although the bulk of a hard carbon resists graphitisation up to quite high temperatures, small amounts (~ 2%) of other phases are present which graphitise as easily as soft carbons. This she ascribed to the existence of sufficiently large thermal stresses in hard carbons as to lead to local crystallisation under high pressure.

2.3.2. Mizushima's model

Mizushima[60] proposed that the movement of whole layer planes as large as a few hundred angstroms is not possible and the increase of the layer diameter must thus be caused mainly by the atomic movement of the boundaries between the neighbouring layers. It is also improbable that a layer plane of such a large diameter could rotate around its c-axis to establish orientation with the neighbouring layers. He believed that three dimensional ordering took place by the movement of boundaries made up of arrays of dislocations. From an energy consideration he showed that the driving force for the two-dimensional growth of the layer planes is

a function of the layer diameters. The change in the peripheral energy of a layer plane which is associated with either the escape of, or the attachment of, an atom at the edge was given by,

$\delta E = \pm 85$ K cal/ϕ Å . Where ϕ is the layer diameter.

When an atom escapes from a layer of diameter ϕ_1 and becomes attached to another layer of diameter ϕ_2, the energy change in the whole system,

$$\Delta E = 85 \left(\frac{1}{\phi_2} - \frac{1}{\phi_1}\right) \quad \ldots\ldots\ldots\ldots\ldots (10)$$

If $\phi_2 > \phi_1$, there will be an energy released from the system which will act as the driving force. This two dimensional crystallite growth takes place irrespective of the relative orientation in the parallel layer group. Three dimensional growth takes place when the layer diameter becomes larger than a certain critical value, when the energy release for two dimensional growth becomes equal to that required for ordering.

2.3.3. Dislocation model.

Turnbull and Williamson[61] studied graphitisation of evaporated carbon films heat treated at high temperatures, and proposed that crystal growth in graphite occurs by the climb of edge dislocations which comprise tilt boundaries.

Screw dislocations in twist boundaries provide the driving force for the climb thus eliminating both boundaries by a single process. The authors believed that this dislocation mechanism was independent of the original material once graphitisation had begun.

2.4. Kinetics of graphitisation.

In order to understand in detail the mechanism of graphitisation, information on the kinetics of the process is essential. Kinetic studies by Fair and Collins[62] on a conventional composite pitch coke carbon indicated that the rate of graphitisation decreased rapidly with increasing heat treatment time and the degree of graphitisation appeared to approach a limiting value at any given heat treatment temperature. However, in general a zero rate of change was never attained. From the experimental data it was demonstrated that the variation in layer plane orientation with time and temperature could be expressed quite satisfactorily with rate expressions based on an activation energy which increases rapidly as the three dimensional crystal order approaches completion. They observed a maximum rate of change of the layer plane orientation and the layer diameter at around 2350°C for most graphitisable carbons and carbon blacks. Since the average layer plane diameter and interlayer spacings of different carbons at this temperature are different they concluded that the structural modifications taking place do not depend upon

any critical plane diameter. Rather they must be intrinsic modifications of the structure associated with definite activation energies with the same values in different types of carbon.

2.4.1 Mizushima's analysis.

Mizushima[63] investigated the rate of graphitisation of carbon by making measurements of the electrical and thermal conductivity and the crystallite dimensions. He found that the electrical and thermal conductivity changes took place linearly with the logarithm of the heat treatment time and obeyed an expression of the form,

$$\sigma = \sigma_o + c \log (t_o + t)/t_o \quad \ldots\ldots(11)$$

where σ is electrical conductivity at time t, σ_o is the initial value which depends on the history of the specimen, c and t_o are constants ($t \gg t_o$) and can be determined from the σ Vs log t plots.

From (11),

$$\frac{d\sigma}{dt} = C(t + t_o)^{-1} \quad \ldots\ldots\ldots\ldots(12)$$

Putting (11) in (12) one can write,

$$\frac{d\sigma}{dt} = \frac{c}{t_o} \exp \left[- \frac{\sigma - \sigma_o}{c} \right] \ldots\ldots(13)$$

Since σ was found to change linearly with L_a, $\sigma - \sigma_o$ can be replaced by $p (L_a - L_{ao})$, where p is a constant. Hence

$$\frac{dL_a}{dt} = \left(\frac{c}{t_o}\right) \exp \left[- (L_a - L_{ao}) / \frac{c}{p} \right] \ldots\ldots (14)$$

The rate of increase of L_a with time at a given temperature T was expressed by the relation,

$$\frac{dL_a}{dt} = f(L_a) \exp \left[- \frac{E(L_a)}{RT} \right] \ldots\ldots\ldots\ldots (15)$$

where $f(L_a)$ is an unknown function and $E(L_a)$ is the activation energy for crystallite growth. Mizushima calculated the activation energy by comparing the final rate of change of conductivity at a temperature T_1 with the initial rate at the next higher temperature T_2 for the same specimen heated successively at T_1 and T_2. He postulated the following equation similar to the one already mentioned,

$$\frac{d\epsilon}{dt} = g(\epsilon) \exp \left[- \frac{E(\epsilon)}{RT} \right] \ldots\ldots\ldots (16)$$

From which follows,

$$\left(\frac{d\epsilon}{dt}\right)_{T_1 \text{ final}} \cdot \left(\frac{d\epsilon}{dt}\right)_{T_2 \text{ final}} = \exp \left[- \left(\frac{1}{T_1} - \frac{1}{T_2}\right) \frac{E(\epsilon)}{R} \right] \ldots\ldots\ldots (17)$$

because $g(\epsilon)$ is common to both. The same procedure was applied to the thermal conductivity. He calculated the activation energy between 900°C to 2500°C and it was found that it rose from 75 to 210 Kcal per mole in the temperature

range studied. From the measurement of the interlayer spacing and of the crystallite size dimensions he also observed that the activation energies clustered around two values, one of about 100 Kcal, and the other around 200 Kcal per mole.

On the basis of these results Mizushima concluded that the graphitisation of carbons proceeds by two distinct groups of processes. The first one, associated with an activation energy centred around 100 Kcal, includes such atomic processes as disappearance of dislocations formed during carbonisation, the removal of interlayer clusters and vacancies of different sizes. These processes decrease the interlayer spacing, straighten up the layer planes and bring order in each plane. The second process, with an activation energy around 200 Kcal, begins above 2200°C and is associated with crystallite growth, mainly in the a-direction, by the movement of boundaries between adjacent layer planes.

2.4.2. Fischbach's analysis.

A recent investigation by Fischbach [64,65] of the kinetics of graphitisation of pyrolytic carbons has shown that in these materials graphitisation occurs in two stages, which could be described by a sequence of two simple first order rate processes. He observed that quantities like diamagnetic susceptibility, anisotropy ratio χ/χ_{11}, preferred orientation and layer plane diameter L_a, all

increase slowly during the first stage and rapidly during the second stage. He calculated the activation energy corresponding to the first stage of graphitisation as 260 Kcal per mole, but he was unable to calculate the energy of activation for the second tage for want of sufficient data. Later investigation of a petroleum coke carbon gave a value of the activation energy 250 Kcal per mole which was in excellent agreement with the one obtained for pyrolytic carbons. This suggested that the graphitisation process is the same in the two types of carbon and that the activation energy is constant. The different kinetic behaviour in different carbons was attributed to the detailed micro-structure of the materials.

2.4.3. Presland and White's analysis.

Recently Presland and White [66,67] and [40] studied the graphitisation of evaporated carbon films using electron microscopy and electron diffraction. The as-deposited film, which was quite amorphous, was heat treated in vacuo in the temperature range 1000 - 2400°C, followed by characterisation by electron microscopy and diffraction; the material was found to be graphitising. They showed that even at low heat treatment temperatures there existed two stages in the process of graphitisation and deduced the activation energy corresponding to the first process as approximately 2 ev (46 Kcal/mole). They showed that there was a parabolic

relationship between L_a and the heat treatment time represented by,

$$L_a - L_{ao} = (K_1 t)^{\frac{1}{2}} \quad \ldots\ldots\ldots\ldots\ldots(18)$$

where $L_a - L_{ao}$ is the increase in crystallite dimension during heat treatment time at a particular temperature. The values of $K_1^{\frac{1}{2}}$ and L_{ao} were obtained from the L_a vs $t^{\frac{1}{2}}$ plots. K_1 was assumed to be of the form,

$$K_1 = K_o \exp\left(-\frac{U_1}{kT}\right) \quad \ldots\ldots\ldots\ldots(19)$$

where U_1 is the activation energy of the process. The plot of $\log_e K_1$ against $\frac{1}{T}$ was a straight line, the gradient of which gave U_1. From the extremely small value of the activation energy (2ev) it was suggested that this stage involves growth of crystallites by means of the attachment of atoms from the adjacent disorganised material where the atoms are free to link up with the ordered regions without the necessity of breaking σ bonds.

Since their activation energy values during the early stage of graphitisation fell close to that of Mizushima's value of 40 Kcal per mole for the breaking of the single covalent bond in graphite they suggested an alternative in which the growth of larger crystallites takes place by accretion of atoms liberated from smaller neighbouring crystallites by the breaking of single covalent bonds.

CHAPTER III

3. Catalytic graphitisation.

As has been pointed out earlier, catalysis of graphitisation of carbon is of much fundamental and practical interest at the present time. Considerable research has been carried out since Acheson's[68] time but a proper understanding of the mechanism of graphitisation catalysis has not yet been achieved. At the end of the nineteenth century Acheson referred in a series of patents to the catalytic action of certain metals on the graphitisation of carbon. He heated carbonaceous materials in the presence of these metals (in solid or vapour form) in an electric furnace to a very high temperature. He proposed that the metal first combines with carbon forming the carbide which further decomposes into graphite and the metal. At high temperatures the volatilizable materials are vaporised and permeate the charge, facilitating graphitisation. No mention was made, however, of the range of temperatures to which the charge in the furnace was heated.

Akamatu and Sato[69] showed that the carbon produced by catalytic decomposition of carbon monoxide by iron at the comparatively low temperature of 500°C is not amorphous carbon but graphite. In the early stages of formation the deposit was established to be cementite, which then underwent

further decomposition to graphite. They suggested that the reaction takes place according to the scheme,

$$3\,Fe + 2\,CO \rightarrow Fe_3C + CO_2$$

$$Fe_3C \rightarrow 3Fe + C$$

The catalytic acti n of iron was hindered by the existence of oxygen. The catalytic decomposition of carbon monoxide never takes place if iron is oxidised before cementite is formed.

Yamada[70] studied the catalytic graphitisation of thermal black using silicon, iron, cobalt, nickel etc. as catalyst. He observed that the different metals behaved differently in the graphitisation process and in this connection he was able to classify the metals into two groups, one consisting of metals like silicon which formed graphite crystals by formation and decomposition of carbide and the other consisting of metals like iron which acted upon the carbon, dissolved it and segregated it as graphite. The formation of silicon carbide began just above the eutectic point, at 1500°C; it was stable up to 2000°C and at about 2200°C it decomposed forming graphite crystals. With iron, however, graphite formation was barely recognizable at 1200°C (which is higher than the eutectic point of iron and carbon (1150°C))and iron was considered to act by segregation, in the form of graphite, of carbon which had been dissolved in iron. He observed

similar effects with nickel and cobalt. The most extensive study has been made by Ishikawa et al [71,72] who investigated the catalytic action of as many as thirty-one kinds of metallic elements chosen from each group of the periodic table to establish significant relations between the catalytic action on graphitisation and the physical and chemical properties of each of the various metallic elements. They found that many metals gave little or no effect but that iron, titanium and vanadium had a marked effect. They proposed that the carbon obtained from the carbide is not in the form of graphite but is a highly graphitising carbon. They further obtained evidence that the graphitisability is influenced by the ash composition and proposed a more elaborate scheme for catalysed graphitisation taking this point into consideration.

Gillot and Lux[73] studied the catalysis of graphitisation of a furfuryl-alcohol-coke by titanium and vanadium. Mixtures of powders of furfuryl-alcohol-coke (which is non-graphitising) and titanium or vanadium carbide were pressed into pellets and heat treated for 20 hours at temperatures ranging from 1800°C to 2800°C. During heat treatments small carbide particles entered the grains of coke and migrated in them leaving behind a trail of relatively well crystallised graphite. With titanium the migration of the carbide began at 2200°C and with vanadium at 1800°C. A treatment

at higher temperatures did not modify the crystalline parameters of the phases that were formed at lower temperature by the catalysis. This process was concluded to be a catalysis of graphitisation through dissolution of the carbon in a carbide and subsequent precipitation.

3.1. Graphitisation catalysis by vacuum deposition on to heated metal foils.

Irving and Walker[74] reported on the interaction of evaporated carbon with metal substrates heated during deposition. They evaporated carbon in vacuo at a pressure of 5×10^{-5} torr on to foil substrates of Pt, Mo, W, Ti, Ta and Hf which were heated at 1000°C for 30 minutes prior to evaporation. After evaporation the foils were allowed to cool to room temperature before being exposed to air. The films were removed from their substrates using the appropriate solvents. From this study they reported that at 1000°C evaporated carbon reacts rapidly with Ta, Ti and W foils forming a mixed carbide/carbon film. Over platinum and molybdenum no carbide was detected. The carbon films showed differences in crystallinity over the different metal substrates. The resultant film on tungsten consisted of partially graphitised carbon as well as WC (identified by the selected area diffraction patterns) which showed moderately sharp lines resulting from carbon and arcs arising from WC. With titanium they observed spectacular carbide formation, some of the

crystals observed being 4μ in length. The film formed on tantalum was unlike that on any of the other metals. Some areas of the film gave spotty diffraction patterns of single crystal graphite while some areas gave diffraction patterns identical to TaC. They suggested that enhanced graphitisation takes place by one of two mechanisms. In one the metal acts as a solvent for carbon, and the solubility increases with increasing temperature. In the presence of a temperature gradient carbon atoms continually enter the metal at the higher temperature and leave the metal at lower temperature. The atoms leaving the metal have high mobility and a good probability of participating in the growth of highly crystalline graphite. In the second mechanism the interaction of carbon with the metals forms the carbide. At some temperature the carbide decomposes to the metal and carbon which is highly crystalline. With W, Ti, and Ta massive deposits of carbides were formed at 1000°C in about one minute which shows the high reactivity of vapour species of carbon with the metals. They interpreted the absence of carbides with Pt and Mo as that their presence could not be detected because of the fact that the warm HNO_3 used to dissolve the substrates might attack the carbides. However, the occurrence of platinum carbide is not expected from a thermodynamic point of view.

3.2. Graphitisation catalysis by pyrolysis of hydrocarbons over metals.

Karu and Beer[75] obtained crystalline graphite films by pyrolysis of methane over heated nickel foil in the temperature range 900 - 1100°C. The nickel, which was pre-annealed in vacuo, acted as a catalyst for the decomposition of methane and also as a substrate for the growth of graphite, presumably on the etched surface formed during the pre-heating.

Presland and Walker[22] produced single crystal graphite by pyrolysis of acetylene over foils of platinum and nickel heated to 1000°C. From a study by optical and electron microscopy they showed that nucleation of graphite took place preferentially at substrate grain boundaries and kink sites. In the case of nickel surface steps also influenced growth and the graphite film prepared by complete coverage of the substrate appeared to be under compressive stress. They reported three requirements for single crystal formation i.e. low rate of nucleation, low rate of growth and high mobility. In their experiments the mobility was kept constant by keeping the substrate temperature at a fixed value, the carbon deposition rate slowly increased with time, and some time after the beginning of pyrolysis the combination of deposition rate and mobility was such as to favour formation of crystalline graphite. The heterogeneous nucleation at favoured sites

of the substrate was believed to be due to (a) the local change in topography at the intersection of a grain boundary with the surface, (b) the diffusion of carbon atoms or point defects through a favourable route such as a grain boundary or (c) the effect of localised impurity concentrations resulting from segregation to the boundary.

The growth of graphite on platinum and nickel took place by the lateral extension of the nuclei and in nickel this growth was strongly influenced by the step and terrace structure of the substrate.

The authors put forward three possible mechanisms of graphitisation during pyrolysis of acetylene; they were described as 'chemical', 'thin film' and 'metallurgical'.
(a) Chemical model:- The formation of graphite occurs through free radical polymerisation followed by cyclization to polybenzenoid radicals. Platinum and nickel are efficient dehydrogenation catalysts and this is an important factor for the formation of highly crystalline graphite. The production of crystalline graphite is only possible with highly mobile species with a long life time.
(b) Thin film model:- This suggests that the growth of graphite crystals is like the growth of thin metal films by vacuum evaporation. After dehydrogenation of acetylene the mobile carbon atoms give rise to nucleation and growth of islands resulting in the formation of graphite crystals.

(c) Metallurgical model:- Both nickel and platinum dissolve a considerable amount of carbon (Ni dissolves 1.1 at.% at 1000°C and Pt dissolves 4 at.% at 1734°C) which is precipitated as graphite during cooling.

Recently Robertson [76] produced graphite by pyrolysing methane over transition metal foils such as iron, cobalt and nickel at relatively low temperatures. The electron micrographs and the electron diffraction patterns of the deposited material revealed high crystallinity. The occurrence of moiré patterns in the micrographs and the hexagonal spot patterns obtained by electron diffraction both point to the presence of single crystal graphite. However, no possible mechanism was suggested.

3.3. Graphite from carbon saturated metal melts.

Recently Austerman et al[21] have obtained graphite single crystals by precipitation from carbon-saturated melts of iron and nickel. The commonest and most rapidly growing crystals found in their study were graphite platelets of about 30 mm across and 1 mm thick. Less common were thick tabular crystals with maximum dimensions of a few millimeters. Under certain circumstances columnar crystals of 2 mm length or less were also formed.

The mechanism of growth of platelets put forward by these authors is as follows. The basal plane bonds between the carbon atoms are strong, which is conducive to

permanent attachment of carbon atoms to the crystal edges, whereas the bonds between the planes are of weak van der Waal's type. Whenever a new layer is nucleated, rapid lateral growth of the layer to the edge of the crystal would be expected, producing broad crystals with small thickening. The mechanism suggested for columnar crystals was somewhat different. During initial crystallization a series of small platelet crystals are formed whose basal planes are roughly parallel to the plane of the surface of the melt. The melt surface is depressed locally by the intruding crystal, because of the high interfacial energy between melt and graphite, thus giving intimate contact between the tip of the crystal and the melt. During cooling the melt contracts and the melt surface recedes; eventually contact between the melt and the crystal tip is broken. Thus it was as if these columnar crystals had been pulled from the melt.

Noda et al[77] also produced single crystal graphite films as big as 30 mm. across and .06 mm. thick from a carbon saturated iron melt. These films possessed a lustrous surface with many cracks along $\langle 10\bar{1}0 \rangle$ and many hexagonal growth steps on the surface which was in direct contact with the iron melt during the formation of the film. From the observed growth patterns it was suggested that the growth of the crystal films from the melt was

caused by a two dimensional nucleation mechanism.

3.4. Fluidised bed method

It has been shown by Schwartz and Bokros[78] that graphitisation of carbons deposited in fluidised beds can be catalysed by titanium. A controlled amount of titanium was introduced into the fluidising furnace by passing a metered portion of the helium diluent through a gas-liquid contactor filled with $TiCl_4$. The concentration of $TiCl_4$ carried into the furnace was calculated from the weight loss of the $TiCl_4$ and the total gas flow rate. Catalysis occurred when carbon co-deposited with Ti at 1200°C was annealed at 2200°C for four hours; the carbon deposited at $>$ 2000°C was graphitised during deposition, when the deposition rate was low, and higher deposition rates required annealing at 2200°C for four hours to produce graphite. The mechanism was assumed to involve a thermodynamic equilibrium between carbon, titanium carbide and titanium, in which a conversion from carbon to graphite took place, the driving force being supplied by the free energy of the transformation from carbon to the stable graphite phase.

3.5. Kinetic study of catalytic graphitisation.

Recently Yokokawa et al [79] have made a kinetic study of catalytic graphitisation of hard carbon using cupric oxide as catalyst. The degree of graphitisation (X%) was calculated using the expression,

$$X\% = \frac{2 \times G \times 100}{100 - Cu\%}$$

From a preliminary experiment using graphitised pitch, in which the normalised G was obtained, the relative diffraction intensity $\frac{I \text{ carbon}}{I \text{ LiF}}$ was plotted against the measured amount of carbon present; Cu% was the concentration of copper in the heat treated carbon. They plotted log (100-x) against residence time at each temperature for three different carbonised resins, IRC - 50 (amberlite), DVBP (divinyl benzene polymer) and FFR (furfural-furan resin), and observed that in every case graphitisation proceeded according to a first order rate equation. In order to calculate the activation energy for these carbons the logarithm of the specific rate constant K' was plotted against the reciprocal of heat treatment temperature. The specific rate constant $K' = K.[Cu]$, where K was a catalytic coefficient with dimension of $min^{-1}g^{-1}$. The copper concentration in carbon was assumed to be constant during graphitisation since the loss of carbon or copper is negligible between 1475°C and 1525°C. The energy of activation of the process was 100, 110 and 150 Kcal per mole for IRC - 50, DVBP and for FFR carbons respectively. In the case of hard carbons the resistance to graphitisation was explained on the basis that the condensed aromatic clusters are linked to each other in a random way by

thermally stable carbon-carbon bonds, and their mechanism for the catalytic action of copper was that copper cleaves the cross-linking carbon-carbon bonds. The differences in the activation energies were suggested as being due to structural differences between the carbons.

3.6. Effect of gas phase on graphitisation.

Noda and his co-workers[80,81] have recently investigated the effect of the ambient gas phase on the graphitisation of carbon. A petroleum coke and a carbon black were heat treated at various temperatures in air, nitrogen, argon and carbon dioxide. The experiments revealed that oxygen in the ambient gas phase accelerates the graphitisation of carbon and carbon dioxide has a similar but lesser effect, while no noticeable effect was detected in the case of nitrogen and argon. They suggested that the chemical reaction of gasss such as oxygen and carbon dioxide with carbon might remove the non-graphitising carbon phase by preferential oxidation.[82] Alternatively, these atmospheres might accelerate the movement of the crystallite boundaries along the carbon hexagon planes by removing obstacles for crystallite coalescence. More recently Pearce and Heintz[83] suggested that the mechanism whereby an oxygen bearing atmosphere enhances graphitisation is due to the dynamic chemical equilibrium between the solid and the gas phase. During oxidation of graphitised and partially graphitised material the most disorganised

carbon atoms are preferentially reacted. In this case the oxidation process represented by the forward reaction of $2C + O_2 \rightleftharpoons 2CO$ might act as an unblocking mechanism and remove barriers which oppose the reorientation of other atoms, thus reducing the activation energy for the graphitisation process.

3.7. Effect of stress on graphitisation.

Another significant factor in reducing the energy barrier to the graphitisation process concerns the effect of applied stresses. Bragg et al[84] have shown that the reorientation of carbon atoms into an ordered lattice is favoured by applied external stresses, which appear to provide the energy required for individual reorientation. Noda and Kato[85] have published dramatic evidence of the marked effect of pressure on the graphitisation of some commercial and laboratory cokes. However, in this connection the possible effects of other catalysts in inducing areas of local stress should not be ruled out.

CHAPTER IV.

4. Theory of Precipitation

4.1. Laws of Diffusion

The thermally activated transport of atoms through matter is known as diffusion. Fick proposed that diffusive flow of an atomic species is proportional to the concentration gradient in the same way as heat flow is proportional to the temperature gradient. For unindirectional flow in the x - direction, Fick's first law may be expressed as,

$$J_x = -D_x \frac{\partial c}{\partial x} \quad \text{.....(20)}$$

where c is the concentration of the species at the point x in gram atoms or number of atoms per unit volume, J_x is the flux, i.e. the number of gram atoms or atoms flowing through unit area in unit time in the x-direction (J_x has units of length^{-2} time^{-1}). The negative sign indicates that diffusion occurs from high to low concentration. This law can be applied experimentally only if a steady state exists in which the concentration at every point is constant i.e. $\frac{\partial c}{\partial t} = 0$ for all values of x. The non-stationary flow equation can be derived from (20) above by

considering the rate of increase of the number of atoms $(\frac{\partial c}{\partial t})$ in a unit volume of specimen. This is equal to the difference between the flux coming in and going out of the volume under consideration. If the specimen is of unit cross-sectional area then unit volume may be defined by two planes separated by a distance of unity. Then the flux across one plane is J_x and across the other is $(J_x + \frac{\partial J}{\partial x})$ the difference being $-\frac{\partial J_x}{\partial x}$

Hence, $$\frac{\partial C_x}{\partial t} = -\frac{\partial J_x}{\partial x} = \frac{\partial}{\partial x}\left(D_x \frac{\partial c}{\partial x}\right) \quad \ldots\ldots(21)$$

which is Fick's second law of diffusion. When D is independent of concentration the above equation becomes,

$$\frac{\partial C_x}{\partial t} = D_x \frac{\partial^2 C}{\partial x^2} \quad \ldots\ldots\ldots\ldots\ldots\ldots(22)$$

The diffusion coefficient D generally conforms closely to an Arrhenius type relation given by,

$$D = D_o e^{-\frac{U}{kT}} \quad \ldots\ldots\ldots\ldots\ldots\ldots(23)$$

where D_o is the so-called frequency factor and U the activation energy. This energy of activation is the isothermal work done in moving an atom from an equilibrium position to the top of the adjacent potential energy barrier. A local dilation of the lattice has to be induced by thermal fluctuations to create voids in the solvent lattice sufficient to permit the passage of the solute atoms.

The work done is largely dependent on the relative size of the solute and solvent atoms and the elastic constants of the solvent. For further information about the subject reference (86) may be consulted.

4.2. Precipitation.

The study of precipitation has attracted considerable experimental interest and many authors have developed theories to deal with the situations encountered. Works of Hardy and Heal[87], Turnbull[88] and also of Christian[89] are excellent reviews of both theoretical and experimental work on precipitation.

It is useful to distinguish between two broad types of diffusional reactions in multicomponent systems. In the first, known as discontinuous precipitation, the structural and compositional changes occur in regions adjacent to the advancing interface. The parent phase remains unchanged until swept over by the interface and the transition is complete in regions over which the interface has passed. After a steady state has been obtained the rate of growth is constant until two regions of product impinge, when the rate decreases abruptly to zero. Eutectoid formation is an example of this class. In the second type, called continuous precipitation, atoms are transported to the growing nuclei by diffusion over relatively large distances in the parent phase. The mean composition of the parent phase changes continuously towards

its equilibrium value. The structural change if any is localised at the interface. The rate of growth depends upon the relative rates of the interface reaction and diffusion and will only be constant if the former is very much slower than the latter. Precipitation from many supersaturated solid solutions involves continuous precipitation.

4.3. Theory of growth of precipitates from solid solution.

The theory of Zener and Wert[90,91] for the growth of a collection of small spherical particles from a uniform solution deserves particular mention at this point. They studied the formation of precipitates from solid solutions of carbon and nitrogen in α-iron by means of the internal friction peak associated with the stress-induced interstitial diffusion of the solute atoms. If the rate of growth is governed by volume diffusion in the supersaturated α-phase, the linear dimension of a precipitate crystal is given by Zener's equation

$$S = \alpha_\lambda (Dt)^{\frac{1}{2}} \quad \ldots\ldots\ldots\ldots\ldots\ldots (24)$$

where D is the atomic diffusion coefficient, α_λ is the growth coefficient and is a function of the pertinent concentrations. The suffix λ refers to the number of dimensions. Experimental tests of the assumption that the growth velocity depends on the coefficient of lattice diffusion have been undertaken for some reactions; here

we quote the work of Wert[92] for the precipitation of carbide and nitride phases from solution in α-iron. Approximate verification of this assumption is possible by examining the rate of growth of individual particles by means of an electron or optical microscope, since to an order of magnitude the above equation may be written as,

$$s \sim (Dt)^{\frac{1}{2}}$$

for most reactions. Turnbull[93] estimated D from this relation using published results on the precipitation of silicon, $CuAl_2$ and $AgAl_2$ from binary alloys of aluminium with silicon, copper and silver respectively. The results agreed with the experimentally determined lattice diffusion coefficients to within rather large limits of accuracy.

Wert's studies of precipitation of carbides and nitrides from dilute α-iron solutions were made by measurement of the internal friction peak, whose height is proportional to the amount of solute remaining in the solution after a certain period of time. The results were analysed by using an equation of the same form as that developed by Johnson and Mehl[94] to characterise crystal growth when particles of a second phase grow in a matrix without mutual interference. The rate of transformation may be written as,

$$\frac{dw(t)}{dt} = f(t) \qquad \text{.....(25)}$$

where W(t) is the fraction of transformed material and f(t) is some function of time. Because of mutual interference this rate will be lessened and the decrease will be proportional to the fraction already transformed. Hence the above equation may be written as,

$$\frac{dW(t)}{dt} = [\ 1 - W(t)\ ]\quad f(t) \quad \text{.....(26)}$$

solving this equation gives,

$$W(t) = 1 - \exp\left[\ -\int_0^t f(t)dt\ \right]$$

The explicit form of this equation used was,

$$\frac{\Delta c(t)}{c_o} = 1 - \exp\ [\ -(\frac{t}{\tau})^n] \quad \text{.....(27)}$$

where $\Delta c(t)$ is the amount of transformed material at time t, c_o is the initial concentration of the solute atom, τ is a time constant dependent on c_o and temperature and n is some number independent of T and c_o. The above equation was written in the form,

$$\log \ln (\frac{c_o}{c(t)}) = n\log t - n\log \tau \quad \text{.....(28)}$$

where c(t) is the concentration in solution at a time t and $c_o = c(t) + \Delta c(t)$.

The data obtained for the precipitation of Fe_3C at various temperatures was plotted according to equation (28). From the slopes of the lines and their intercepts

on the $\ln(\frac{c_o}{c(t)})$ axis the values of n and τ were calculated respectively. The values of n varied from 1.2 to 1.7 with a mean of 1.45 which could correspond to spherical growth with all nuclei present originally. Wert stated that before impingement begins, the lowest possible value of n is 1 5 so that the overall transformation law leads to the conclusion that the nucleation rate during transformation is zero. Wert considered only the average value of n but later work[95,96] has shown that the variation of n with temperature and with carbon content is a real effect and that n could have values less than 1.5.

Wert obtained a value of 17.5 ± 1.7 Kcal. per mole for the activation energy for diffusion of carbon in the case of precipitation of Fe_3C. In a later survey of the results of measurements of the diffusion coefficients using elastic after-effect and internal friction methods below 123°C and the precipitation method at 150°C and 200°C, Wert[97] concluded that the activation energy for volume diffusion is 20.1 Kcal. per mole. The precipitation results were considered to be fairly consistent with this activation energy as is required by the growth theories. In a careful study Doremus[98] has observed that the activation energy for precipitation as measured by the thermal cycling method is appreciably lower than the activation energy given by the relaxation methods. He

noticed no variation of activation energy with temperature of reaction, initial concentration of carbon and mechanical deformation up to 4% strain, and obtained a value of 17.1 ± 0.5 Kcal. per mole.

So far it has been tacitly assumed that the precipitate particles were spherical. It was for long thought that the time dependence of non-spherical particles would be quite different. For example Zener and Wert[92,99] suggested that whilst the radius of a cylindrical precipitate is proportional to $t^{\frac{1}{2}}$ the length should be proportional to t and thus the volume to t^2. Similarly it was proposed that the radius of a disc is proportional to t and the thickness to $t^{\frac{1}{2}}$ giving the volume proportional to $t^{5/2}$. Ham[100,101], however, showed that the concentration conditions at the edges of cylinders and discs do not remain constant during diffusion controlled growth. By approximating cylinders and discs to prolate and oblate spheroids respectively he was able to show that provided the shape remains constant during growth all dimensions are proportional to $t^{\frac{1}{2}}$ and the volume to $t^{3/2}$. When the rate of growth varies with direction due to some surface process, the shape of the particle as defined by the eccentricity of the spheroid changes. For a disc of constant thickness growing radially only, the radius is linearly related to time and the volume to t^2. The length and volume of a cylinder of constant radius is proportional to time t.

CHAPTER V

5. Thin films

5.1. Introduction

The study of the structure of thin solid films has been of continuing interest, especially since the discovery of the electron diffraction technique in 1927, and the development of high resolution electron microscopy has provided a means by which the nucleation, growth and structure of thin films can be understood and correlated with their properties. The basic requirement for transmission electron microscopy is that the specimen must be thin and have a clean surface, so that it is particularly suited to the examination of thin films. The transparency of the specimen depends upon the energy of the electrons and the atomic number of the material. Thus, for uranium the specimen thickness should be < 500 Å, while for light elements such as aluminium it may be $\sim$ one micron.

5.2. Methods of preparation of thin films

The techniques for producing continuous solid films $< 1\,\mu$ in thickness may be divided into two main classes:

(a) by mechanical, chemical or electrochemical thinning of the bulk material

(b) by depositing thin films by vacuum evaporation, electrodeposition etc.

The former are of no interest in the context of this thesis, but the latter methods will now be discussed briefly.

5.2.1. Vacuum evaporation

Vacuum evaporated thin films are nowadays widely used in industry and research. Deposition is commonly carried out at a pressure of about 10^{-4} torr or less. The material to be evaporated is heated to a temperature such that its vapour pressure exceeds that of the residual gas pressure. Atoms vaporised from the source travel in straight lines and deposit as thin films on any surface in their path, provided the pressure within the system is such that the mean free path of the vaporised atoms is large compared with the distance between the source and the deposition plane.

Various types of source are possible depending upon the nature of the evaporant. The following are the most widely used forms of source; they can be divided into two groups.

(i) Filament

(ii) Boat

Filaments or baskets, usually made of refractory materials, can be used to evaporate a wide range of metals. They may be V-shaped, straight helices or conical baskets, and are usually made from tungsten wire. The boats are constructed from foils of molybdenum or tantalum bent into

the form of a trough or boat. This type is not suitable for those metals which readily wet the surface of the boat, because on melting the metal flows over the heater and considerably lowers the resistivity, leading to burning out.

Materials which alloy readily with the heater material can be evaporated successfully from a crucible of alumina or beryllia heated by an embedded filament. Further discussion of the various methods will be found in Holland[108].

5.2.1.1. Evaporation of carbon

The evaporation of carbon was a problem until Bradley[36] developed a method for carbon evaporation which consisted in passing a high current through two pointed carbon rods in a vacuum chamber. The two carbon rods are held in contact by gravity or a spring while the current flows. Heat produced at the junction of the two rods is sufficient to cause rapid evaporation. This kind of evaporation is termed resistive evaporation as opposed to arc evaporation, in which the two rods are briefly separated so as to strike an arc between them; the carbon films so produced are amorphous and have wide applications especially in electron microscopy. Alternatively carbon films can be produced at a very slow rate by electron bombardment of a carbon rod. Becker[41] produced carbon films by this method and claimed that they were more

crystalline than those produced by arc evaporation.

5.2.2. Preparation of alloy films

Alloy films can be deposited by the vacuum evaporation technique, although it is always difficult to produce homogeneous films of predictable composition when the components have widely differing vapour pressures. Harris and Siegel[109] described a technique in which the powdered alloy was fed slowly onto a heated molybdenum boat causing instantaneous evaporation. Another method is to use multiple sources for the pure components of the alloy. The sources are operated simultaneously and by pre-calibrating them it is possible to control the composition of the deposited film.

Alloy films can also be prepared by successive evaporation followed by homogenisation at suitable temperatures. Compound films of metals and non-metals can be prepared by first making the metal film followed by heat treatment in a suitable atmosphere. Pitch[110] used this method to prepare iron/carbon and iron/nitrogen films. Nagakusa[111,112] in his study of the formation and decomposition of different metallic carbides also prepared thin films of iron and carbon by this method.

5.3. Sputtering

When an electrical discharge is passed between electrodes at a low gas pressure the cathode will eject surface atoms due to bombardment by the ionised gas

molecules. These ejected atoms can then be condensed on a substrate as in vacuum evaporation. This cathode disintegration is believed to be due either to local heating and thermal evaporation, the heat being supplied by the energy of the impinging ions, or to the emission of atoms on ion impact in a manner similar to that observed in secondary electron emission. The method has an advantage over the evaporation method in that there is no chance of container alloying; it is also a useful technique for the deposition of alloy films.

5.4. Chemical Vapour deposition

This is a very simple and widely used method for deposition of thin films. Deposition of a material is obtained on a surface in the preparation chamber which contains vapour in equilibrium with its solid or liquid phase.

Films can be deposited according to the following three mechanisms.

(a) Disproportionation

If a gas AB which is in equilibrium at high temperature is allowed to pass into low temperature zone, then disproportionation takes place and a deposit of A will be obtained. The reaction can be put down as,

$$A + AB_2 \rightleftharpoons 2AB$$

(b) Reduction or oxidation

This can be accomplished using a halide of the metal which has a high vapour pressure. Moreover it is easier to remove the by-products. A typical oxidation reaction can be written as,

$$ACl_2 + H_2O \rightarrow AO + 2HCl$$

and on reduction

$$ACl_2 + H_2 \rightarrow A + 2HCl$$

where A stands for a metal.

(c) Decomposition

This is a very simple method to grow thin deposits either by photolysis or by pyrolysis. The reaction can be represented as,

$$AB \rightarrow A + B$$

It is possible to obtain unusual growth features such as whiskers, and perfect crystals with interesting mechanical properties.

5.5. Tarnishing

This method produces compound films of which the substrate is a component. The substrate is generally exposed to the appropriate atmosphere for the deposition. For example when silver is exposed to hydrogen sulphide a composite film of silver sulphide results. Similarly when metals are exposed to oxygen films of metal oxides are obtained.

5.6. Electrodeposition

The deposition of thin films by this method is quite old, and is governed by the two well known laws of electrolysis. This involves deposition of one metal on another and since it is difficult to detach the film from the metal substrate, the method is not widely used. Several investigators [113,114] made thin films of nickel by electrodeposition on to copper and the films were detached by dissolution of the copper in suitable complexing solvents.

5.7. Anodising

This is a method by which oxide films can be produced. The process of growth depends on the diffusion of metal ions from the anode to the oxygen source such as water or fused sodium nitrite, depositing an oxide on the outer surface. This migration is possible at room temperature only by the application of very high fields of about 10^7 volts/cm. in order to lower the high thermal activation barrier. The materials which can be successfully anodised are the metals aluminium, tantalum, niobium, zirconium and titanium, and also silicon. For a further account of the subject reference (115) may be consulted.

5.8. Growth and structure of vacuum deposited films

5.8.1. Condensation phenomenon

R.W.Wood[116,117] first investigated the phenomenon of condensation which occurs when a stream of metallic vapour is allowed to impinge on a surface of glass or other

material. He observed that when the vapour density was below a certain value for a given substrate temperature condensation did not take place. In other words there is always a critical substrate temperature for a given vapour stream density above which no deposition is formed. Langmuir[118] confirmed this idea and showed that there is a relationship between the critical substrate temperature and the vapour intensity, the former increasing with the latter. He showed that the incident vapour atoms move on the surface on which they impinge for a finite time before evaporating.

Frankel[119] developed Langmuir's reevaporation theory; he assumed that the average life time of an atom on a substrate surface was sufficiently long so that another atom could collide with it and an atom pair would be formed; the life time of the resultant dimer would be longer than that of the single atom, (i.e. the energy required to reevaporate the pair would be considerably increased). Benjamin et al[120] calculated the energy of condensation of the vapour for different materials.

Levenstein[121] found that the aggregates condensed on the substrate for slow evaporation rate were larger in size than those condensed rapidly. He explained this behaviour by expanding Frenkel's concept of surface mobility as follows: (a) the number of atoms in motion on the substrate is proportional to the number of atoms

arriving at the surface per unit time (b) atoms move over the surface until they suffer a collision with other atoms and thereby lose their mobility. He showed that the mean mobility time for antimony is 2×10^{-5} sec. Meyer[122] showed that the surface mobility also depends upon the forces between the substrate and deposited atoms. Campbell[123] observed variations in mobility in the case of gold by a factor of ten when evaporated on to different substrates.

The degree to which an atom is bound to a substrate can be measured by determining the heat of evaporation from the substrate. Values of the heat of evaporation of metals from glass and other metal substrates have been reported by Cockcroft[124] and Eastermann[125].

5.8.2. Nucleation and growth

The rate of deposition and the temperature of the substrate play an important role in the growth of thin films. It has been shown by Levenstein that higher deposition rates resulted in a larger number of nucleation centres leading to the formation of a continuous film. A slow rate of deposition on the other hand resulted in island formation. Pashley[126] also observed this phenomenon and concluded that for the system the initial stages of growth involved the formation of three dimensional nuclei even when the average thickness of the deposit was less than one atomic diameter. Newman and Pashley[127] also observed the

sudden appearance of nuclei when they deposited copper films on to single crystal substrates of silver.

More recently Bassett[128] observed directly in the electron microscope the growth of silver deposited on to molybdenum disulphide cleavage faces. Nuclei approximately 100Å diameter were observed followed by their lateral growth. Pashley examined in detail the growth of gold films on molybdenum disulphide at 400°C during the initial stage of deposition. The adjacent nuclei were observed to join together in a liquid like manner in less than .1 second. The nuclei initially possessed well defined crystallographic shapes, but became rounded during coalescence, whereupon the composite structures took up crystallographic shapes again. It has been concluded that the mechanism responsible for this liquid-like coalescence is surface diffusion. For a detailed discussion readers may be referred to Pashley[129].

5.8.3. Epitaxial growth

The nucleation and growth of a film is affected by the nature of the substrate surface. The one surface feature which is well established as a nucleation site is the surface step. Bassett[130] first obtained a clear decoration effect of gold nuclei at monomolecular steps (height 2.83 Å) on rock salt cleavage surfaces. Epitaxy, which is the phenomenon of the formation of overgrowth crystals oriented with respect to the substrate, has been

extensively reviewed by Pashley [129,131] and will be mentioned here briefly. Orientation of the deposit film is mainly determined by the orientation of the crystal face of the substrate and to a lesser extent by conditions of deposition. A slow rate of deposition favours the occurrence of orientation while a fast rate favours the formation of a continuous coherent film and hence a compromise is necessary for coherent oriented films. In a few instances changing the temperature of the substrate at which deposition is carried out may change the orientation of the overgrowth film. There exist many differences in experimental detail reported by various authors for production of well-oriented films. An experimental situation which yielded an oriented film on one occasion may produce an only partially oriented film on another. Surface contamination of the substrate seems a likely cause of the variation in behaviour and great attention has been paid to the orientation of films in U.H.V. systems where contamination of the substrate can be made quite negligible. The mechanism of growth of such films is not well understood; however the observations show that the deposits grow continuously from small nuclei to full coherence when the thickness has reached a critical value. A theoretical treatment concerning the nucleation and growth of deposited films appears in reference 132.

5.8.4. Structure and properties of thin films

The fact that the structure and properties of a thin film deviate from those of the bulk material may be due to three reasons: (a) the small thickness (b) large surface to volume ratio (c) high possible disorder.

The small thickness leads to phenomena such as the increase in electrical resistance as film thickness diminishes and numerous other mechanical, electrical magnetic and optical effects which provide considerable interest for the materials scientist. The large surface to volume ratio influences such phenomena as adsorption, diffusion and chemical reaction at the film surfaces. Films of high structural disorder such as condensed metals and semiconductors can differ in their properties quite considerably from bulk samples. Note that the first two reasons would apply to thin sections, e.g. cleaved from a bulk crystal, whereas the third only applies to 'built up' thin films and is a function of the method and conditions of deposition. Thus we can list three kinds of growth in evaporated films, namely two dimensional, three dimensional and three dimensional epitaxial growth. The classic example of the first type of growth is the growth of evaporated carbon films where the carbon atoms freeze at the point of impingement preventing the growth of nuclei. The grain size is extremely small and a quantitative estimate is not feasible. In the case of metallic films produced by

evaporation a large number of discrete three dimensional nuclei are formed in the earliest stage of growth. For gold evaporated on rock salt at 300°C Pashley[133] reported about 10^{11} nuclei per sq. cm. with a distance of about 20Å across each nucleus. The nuclei were ordinarily distributed at random but were occasionally observed at preferred sites. The preferential nucleation and growth of gold film on cleavage steps of rock salt single crystals is an example of the third type of growth mentioned above. Continued deposition leads to an increase in size of the nuclei until they grow to the point when they touch each other, leading to the phenomenon of coalescence, and at this point rapid change in geometry and orientation occur. Evaporated thin films are usually associated with various kinds of defects such as point defects, dislocations and stacking faults, and the perfection can be improved by annealing treatments either on the substrate or after separating from the substrate. Pashley found that the annealing of gold films was accompanied by the rearrangement of some of the dislocations into low angle grain boundaries. Many other dislocations are eliminated by mutual annihilation. The number of dislocation lines extending through unit area of gold films could be easily reduced from 10^{10} per sq.cm. to less than 5×10^{8} per sq.cm. by this process.

5.9. Metastable alloy films

When an alloy film is prepared by the simultaneous evaporation of the components on to a very cold substrate the atoms arriving successively on the substrate form a random and homogeneous mixture. This technique can be used to produce metastable alloy films. Kneller[134,135] produced metastable Co-Cu solid solutions in the concentration range between 12% and 95% of Cu and also Fe-Cu with copper concentrations up to 80% by simultaneous vapour deposition on to cold substrates. In these binary systems no thermodynamically stable solid solutions exist at any temperature in this concentration range, and the co-evaporation technique allowed the study of phases not found in the bulk alloy.

Recently Mader[136,137] described the results of a systematic study of the occurrence of metastable phases in binary alloy systems and their dependence on alloy composition, thermal stability and other properties. The resulting structures were either crystalline solid solutions of concentrations higher than the solubility limit or amorphous solutions. The reasons for the existence of the amorphous structures were the difference in the atomic radii of the components and the low substrate temperature. The amorphous structures usually transformed to crystalline phases at a temperature around $.3T_m$ where T_m is the average melting point of the components of the

alloy. For example films of Cu + 50% Ag were amorphous when deposited at 80°K and transformed to single phase f.c.c. structure at 360°K. Another example of an amorphous structure was the Cu + Mg alloy system which had the largest size factor (ratio of $r_{Cu}/r_{Mg} = 1.25$) so far reported by Mader. Co-evaporated films in the whole range of compositions including Cu + 33% Mg and Cu + 66% Mg formed amorphous structures. This was because the arriving atoms 'froze' at the point of impingement and were therefore unable to migrate even as far as the repeat distance within the unit cell of the appropriate crystalline phase. These examples show that amorphous structures occur at high alloy concentrations and exhibit metastability. In order to transform these into a crystalline structure, they require substantial thermal activation.

5.9.1. Transformation from amorphous to crystalline phases

When an amorphous alloy film is heated its structure changes into a crystalline one at a temperature of crystallisation T_x. The ratio of the temperature of crystallisation T_x to the average melting point T_m of the components of the alloy centres around a value of .3 as observed by Mader. For example for Cu-Ag, $T_x/T_m = .28$, for Cu-Mg it is .35 etc. T_x/T_m is higher for the amorphous Cu-Mg alloys presumably because they have a higher size

ratic. This increased metastability accounts for the fact that they can be obtained even by deposition at room temperature. It was observed that the transformation from amorphous to crystalline structure is a microscopically homogeneous process. However exceptions to this behaviour were observed in the Au-Mg and Cu-Mg systems.

Recently Mader[138] summarized the results of his study of films of several binary systems, shown in Table I. This shows the temperature of crystallisation, the grain size and the structure of several binary systems during the annealing stage.

5.9.2. Crystalline alloy films

F.c.c. and h.c.p. crystalline metastable phases were observed as intermediate phases by the crystallisation of amorphous structures. Mader[137] observed the epitaxial growth of a metastable alloy by depositing Co- 65% Cu on to the cleavage face of MoS_2 at room temperature. He observed complete epitaxy of the metastable alloy such that a (111) plane of the solid solution was parallel to the basal plane of MoS_2 and close packed directions of both the structures coincided. Another example of the crystalline metastable structure is from the Cu-Mg alloy system. From the densitometer tracing of an electron diffraction pattern of Cu + 15% Mg deposited at 80°K it was shown that the lines of a single f.c.c. structure were clearly resolved and the (220) and (311) lines showed

the same intensity which is to be expected for a randomly oriented polycrystalline f.c.c. structure.

Mader interpreted his results on evaporated alloy films with the help of the following model. If spheres of two different sizes are mixed randomly in any proportion and deposited on to a tilted tray the following situations will be observed.

(i) Spheres of one size will form close packed crystalline arrays with large grain size.

(ii) Mixtures in any proportion of two types of sphere with a small size difference will also form crystalline arrays with smaller grain size.

(iii) When the size difference is large crystalline arrays are only obtained up to a certain limiting fraction.

(iv) Mixtures of a proportion beyond that fraction cannot form crystalline arrays even of small grain size; they will form an amorphous structure.

If the spheres are subjected to vibration they will tend to attain a stable configuration with the help of small displacements, and in order to produce substantial changes in the amorphous structure a considerable thermal activation is necessary.

TABLE I

Alloy	Temperature of crystallisation (^{o}K)	Grain size Å and structure after annealing stage
Au + 50% Mg	230 R M	200, B_2 (Au Mg)
Au + 75% Mg	320 M	Inhomogeneous, hex. $AuMg_3$
Cu + 35% to 65% Ag	370 R M	50, f.c.c.
Co + 25% to 60% Au	430 R M	50, f.c.c.
Co + 17% to 50% Ag	180 R M	30, f.c.c. + traces of h.c.p. (Co)
Fe + 20% to 35% Au	150 R M	10,000, b.c.c.
Fe + 40% to 60% Au	200 R M	Larger than 10,000 f.c.c.
Cu + 50% Mg	370 M	100, C15 (Cu_2Mg)
Fe + 50% to 80% Gd	480 R	

R observed by resistivity annealing stage.

M observed microscopically.

CHAPTER VI

6. Electron microscopy and diffraction.

6.1. Introduction.

The electron microscope is one of the most important new instruments of the present time because of the truly extraordinary way it has widened our ability to see directly into the fine structure of matter. The impossibility of forming a correct optical image of an object smaller than about half the wavelength of the observing light has shown that in order to see things smaller than about .2μ, one must use some kind of illumination having a very short wavelength. Fast moving electrons (de Broglie) are associated with short wavelengths but they cannot be focussed to form an image in the same way as glass lenses focus light. However, properly shaped electric and magnetic fields can focus these moving charges, and the electron microscope takes advantage of this fact.

6.2. Resolution of an electron microscope.

The main advantage of an electron microscope is its high resolution. However, the resolution is limited by diffraction and the spherical aberration of the objective lens. The diffraction limited resolution d is expressed by the equation $d = \frac{\lambda}{\alpha}$ .....(29)
and the limit set by the spherical aberration is of the

form,

$$\delta_s = C_s \alpha^3 \quad \ldots\ldots\ldots\ldots\ldots\ldots (30)$$

where C_s is a constant and is of dimension length. Since the magnitudes of these resolution limits are oppositely affected by variations in α, the semiangular aperture, a compromise usually adopted is to treat them as error functions in order to obtain the overall resolution,

$$\delta_T = \sqrt{d^2 + \delta_s^2} \quad \ldots\ldots\ldots\ldots (31)$$

From this an optimum value of α can be deduced by differentiating and equating to zero giving,

$$\alpha_{opt} = \left(\frac{\lambda}{V^3 C_s}\right)^{\frac{1}{4}} \quad \ldots\ldots\ldots\ldots (32)$$

and

$$\delta_{opt} = 1.14 \, (C_s \lambda^3)^{\frac{1}{4}} \quad \ldots\ldots\ldots\ldots (33)$$

Hence there is a critical aperture for a particular accelerating voltage V which would make the resolution a maximum. Modern electron microscopes can give a resolution $\sim 4\text{Å}$ when they are properly aligned.

6.3 Design of an electron microscope

A transmission type electron microscope has components that fulfill the same functions as those of an optical microscope. It has an electron gun that acts as a source of illumination, lenses which function as condenser, objective and projector/eye piece, a specimen holder situated between condenser and objective and a photographic

plate or film for photographic reproduction. Since electrons are invisible to the eye, however, a fluorescent screen is necessary for visual observation, since electrons are strongly scattered when passing through matter, it is necessary for any electron optical system to be under a high vacuum. In the electron microscope the column is connected to a vacuum system of diffusion and rotary pumps to ensure that a pressure of less than 10^{-5} mm. of Hg is always maintained during operation.

6.4. Image formation (Bright field).

To form an image three lenses (objective, intermediate and projector) are used. Their geometrical arrangement is shown in fig. 3. The electrons emitted by the source which is generally a heated tungsten filament are converged by the condenser lenses to a focus at the specimen (placed between the condenser and the objective lens); this then scatters them in the form of one or more Bragg diffracted beams at very small angles (1 to 2°) to the incident beam, which are then focussed by the objective to form the first stage image. The focusing action of electron lenses is most simply understood in terms of optical analogies. A beam of light is deviated and focussed by a glass lens as a consequence of the change in velocity it suffers when passing between media of two different refractive indices. In an electron lens whether electromagnetic or electrostatic, electrons experience similar changes of velocity and

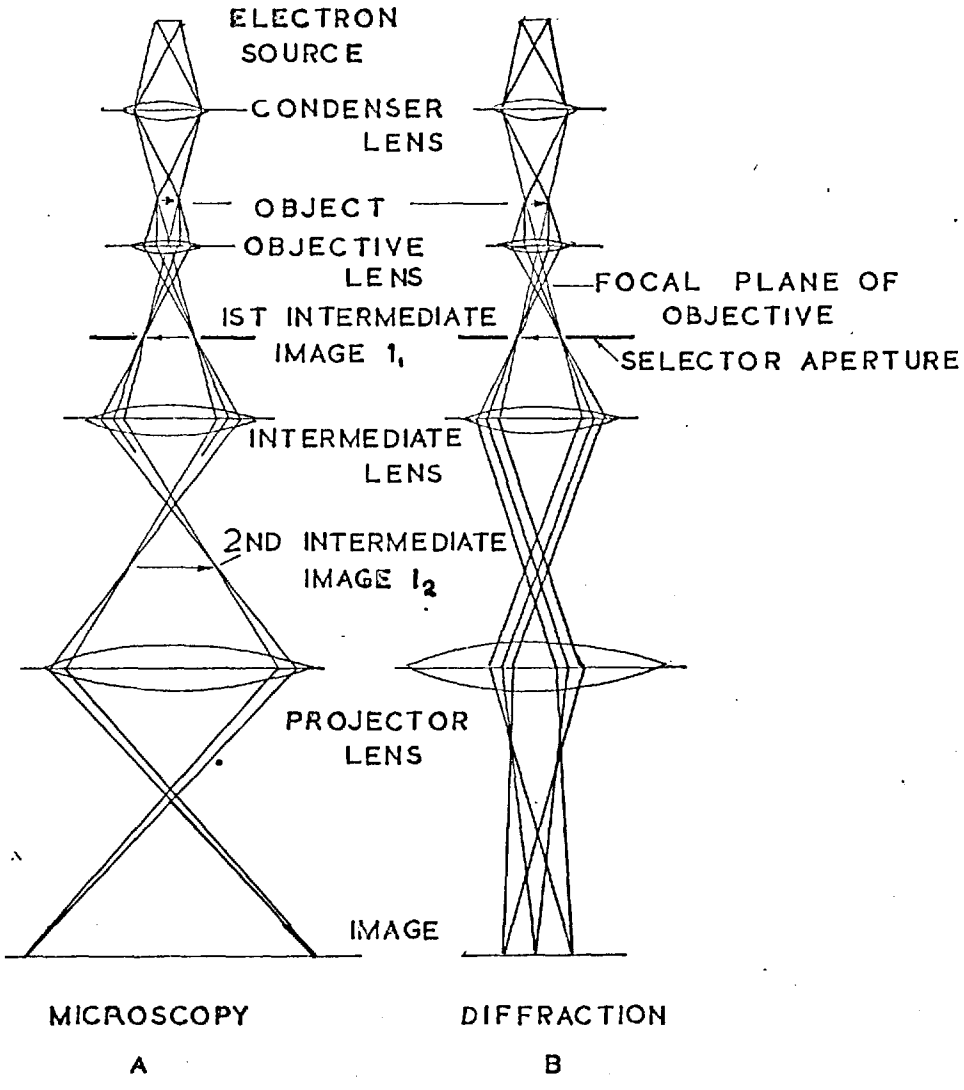


FIG 3: RAY PATHS IN THE ELECTRON MICROSCOPE
A UNDER MICROSCOPY CONDITIONS AND
B DIFFRATION CONDITIONS

direction. An aperture is placed in the focal plane of the objective lens which prevents scattered electrons from taking part in the image formation. The image thus formed by the direct beam alone is called the bright field image. Second and third stage images are produced by the intermediate and projector lenses respectively, and these two lenses are responsible for most of the magnification of the microscope. It is, however, not the aim here to give a detailed account of the principles and design of the electron microscope, and the interested reader may be referred to several authoritative texts[139-142] and review articles dealing with the special field of electron optics and with the design of the instrument.

6.5. Image formation (Dark field).

In electron microscopy it is also possible to form images by focusing the scattered electrons only to the exclusion of the direct beam. This can be achieved in two ways. The objective aperture can be displaced so that the image is formed not by the incident electron beam but by an appropriate diffracted beam. The dark field image will then reveal which region of the specimen is contributing to the diffracted beam and provides useful information as to the nature of the particular region. This is the simple dark field technique. The contrast will usually be reversed by changing from bright to dark field

illumination. Fig. 4 illustrates the arrangements for (a) bright field and (b) dark field illumination. Alternatively, the dark field image may be obtained by tilting the electron gun through 2 to 3° (corresponding to twice the appropriate Bragg angle) to exclude the direct beam and to allow a Bragg reflection to pass through the centered objective aperture. The dark field image is mainly controlled by a single diffracted beam and hence is of a much higher contrast than the bright field image.

6.6. Scanning electron microscopy.

The scanning electron microscope also consists of an electron gun, a system of lenses and a recording system. Electrons accelerated to the working energy in the electron gun are allowed to scan over a solid surface, a reasonable proportion of these electrons are scattered back from the surface and may be used to form an image. The advantage of the method lies in its ability to be used directly on bulk specimens without the use of intermediate replicas and also its ability to examine specimens at different glancing angles. This instrument has proved extremely valuable in examining widely varying types of material. Although structures may be examined with resolutions better than even five angstroms by transmission electron microscopy, until quite recently the examination of surface topography was limited to the resolution and depth of focus by a factor of at least 300 times and the scanning microscopy bridges

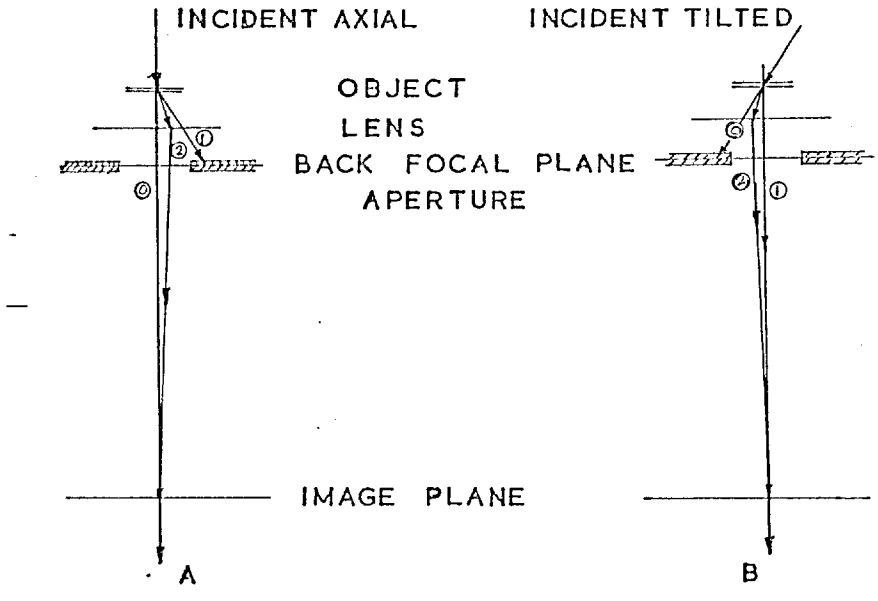


FIG 4: DIAGRAM ILLUSTRATING DIFFRACTION CONTRAST IN
A BRIGHT FIELD
B DARK FIELD

the gap between optical and transmission electron microscopy. The magnification of the instrument can be changed readily from X20 to about X 50,000. The micrographs obtained show a realistic three dimensional image which can easily be interpreted and the effect can be enhanced by taking stereo-pairs, obtained by rotating the specimen through a few degrees. For further details concerning the design and use of the scanning electron microscope the work of Thornton[143] may be consulted.

6.7. Image contrast.

We can detect differences in the structure of a specimen only when there is variation in intensity between different areas of the specimen in the image plane. We can say contrast is high when observable intensity variations are great. Image contrast is a function of the interaction of the beam with the specimen structure and also of the properties and adjustments of the optical system.

When electrons are incident on the specimen some of them are transmitted while others are scattered at various angles. The transmitted electrons are focussed by the objective lens at its back focal plane and each point in the back focal plane of the objective lens corresponds to a particular direction of scattering from the specimen. The most useful method of interpreting electron images is to assume that all electrons except those in the zero order beam are allowed to fall outside the objective aperture,

situated at the back focal plane of the objective lens. Thus this aperture permits only those electrons travelling in a particular direction (zero order beam) to contribute to the image. Contrast in crystalline specimens thus depends on diffraction: areas diffracting strongly away from the aperture will appear dark whereas areas transmitting a beam through the aperture will appear bright.

Contrast arises as a result of differential scattering, therefore the atomic number contrast is due to the fact that the interaction of electrons is dependent on the atomic number of the species comprising the specimen, so that the higher the atomic number the greater is the scattering effect.

If again the object is composed of only one kind of material, brightness variations in the image are due to thickness variations in the object; this is the situation usually observed in the electron microscopy of thin replicas of the surface contours of a solid. The contrast so produced is termed thickness contrast.

Contrast may also be increased as a result of certain instrumental factors such as (i) reducing the objective aperture (ii) increasing the scattering cross sections by lowering the beam potential.

6.8. Moiré fringes.

When two crystals are superimposed, periodic intensity

variations occur in the image. These periodic images are called moiré patterns. Generally clays and layer minerals give rise to this phenomenon. Two basic types of moiré patterns are known. If two structures with spacings d_1 and d_2 are superimposed parallel then the moiré periodicity D will be given by,

$$D = \frac{d_1 d_2}{d_1 - d_2} \qquad \text{.....(34)}$$

The periodicity D may be sufficiently large to resolve in the electron microscope even though d_1 and d_2 may be below the resolution limit. This type of pattern is known as the parallel moiré pattern.

If the two structures have identical spacings d but are twisted with respect to each other through a small angle α, then the moiré periodicity D can be written as,

$$D = \frac{d}{\alpha} \qquad \text{.....(35)}$$

The moiré magnification is then defined as,

$$M = \frac{D}{d}$$

It becomes possible to observe lattice imperfections in crystals whose spacings are considerably below the resolution limit of the microscope. Bollman[144] has used rotational moires in the layer structure of graphite to detect radiation damage. The intensity distribution in the moiré patterns has been discussed in detail by Hashimoto[145]

using the dynamical theory of electron diffraction.

6.9. Scattering and diffraction.

6.9.1. Scattering phenomena.

Because of the negative charge associated with an electron, a beam of electrons passing through matter will suffer deflections owing to the fields of force exerted by the electronic fields within the atom. The effect of the positively charged nucleus is to produce a scattering of electrons with a change in direction only i.e. with no loss in velocity. These electrons are then said to be elastically or coherently scattered. When the electron beam interacts with the atomic electrons inside the specimen however, the scattered electrons also suffer changes in velocity and they are then said to be inelastically scattered.

6.9.2. Electron diffraction.

The subject of electron diffraction by crystalline and amorphous materials is a vast one and is described in several text books, e.g. Thomson and Cochrane[146], Pinsker[147] and Hirsch[104] et.al. In view of this abundant literature on the subject only a brief outline will be given here.

The fact that electrons can be diffracted by a periodic arrangement of scattering centres was first predicted by de Broglie in 1924 and was demonstrated

experimentally by Davisson and Germer[148] in 1927. The stream of particles behaves like a wave motion and so must have a wavelength associated with it. The theory of wave mechanics shows that,

$$\lambda = \frac{h}{mv} \qquad \ldots\ldots\ldots\ldots\ldots\ldots(36)$$

The K.E. of the electrons is,

$$\tfrac{1}{2} mv^2 = eV \qquad \ldots\ldots\ldots\ldots\ldots\ldots(37)$$

where e is the charge and V is the accelerating voltage. From (36) and (37) one can write,

$$\lambda = \sqrt{\frac{150}{V}} \qquad \ldots\ldots\ldots\ldots\ldots\ldots(38)$$

when λ is in angstroms and V is in volts. The wavelength needs relativistic correction at higher values of V due to the variations in electron mass m with its velocity v.

6.9.3. Atomic scattering.

When a beam of electrons strikes an atom scattering of the beam takes place in two ways i.e. nuclear scattering and electron scattering. The former is due to the attraction of the beam by the positively charged nucleus and the other is due to the repulsion of the beam by the cloud of electrons. The atomic scattering amplitude $f(\theta)$ can be

written as,

$$f(\theta) = \frac{m_o c^2}{2h^2} \left(\frac{\lambda}{\sin\theta}\right)^2 (Z-fx) \quad \ldots\ldots\ldots(39)$$

where, $\frac{m_o c^2}{2h^2} = 2.38 \times 10^{-10}$.

The scattering amplitude decreases rapidly as the scattering angle increases and increases with the atomic number as shown in fig. 5.

6.9.4. Kinematical theory of electron diffraction.

The kinematical theory of diffraction provides a simple method for obtaining the intensities of electrons scattered into Bragg reflections. The following assumptions are involved in the kinematical theory e.g. (a) the incident beam is not exactly in the Bragg condition for reflection so that the diffracted intensity is small compared to the intensity of the direct beam. (b) a two beam approximation is used, i.e. it is assumed that only one diffracted beam (plus the direct beam) is excited in the crystal, (c) the crystal is thin so that there is negligible rescattering or absorption.

6.9.4.1. Scattering from a crystal.

Consider n number of scattering points at distances $\underline{r}_n$ from the origin. The scattering amplitude for these n atoms can be written as,

$$\Phi_g = \sum_n fn\,(\theta)\, e^{-2\pi i \underline{K}'.\underline{r}n} \quad \ldots\ldots\ldots(40)$$

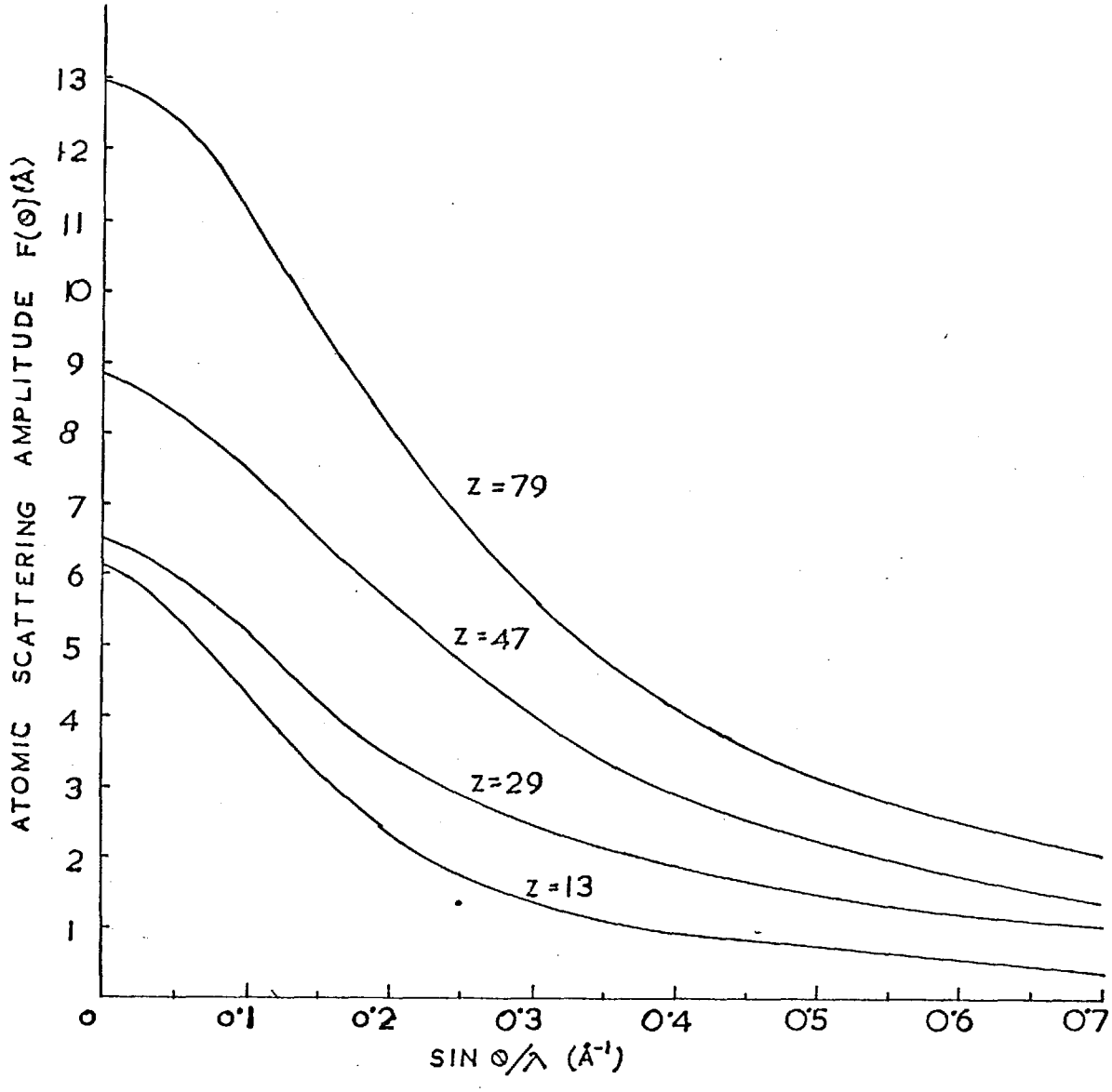


FIG 5: ATOMIC SCATTERING AMPLITUDES AS A FUNCTION OF SIN θ/λ FOR AL (Z = 13) CU (Z = 29) AG (Z = 47) AND AU (Z = 79)

where $\underline{K}' = \underline{\kappa}' - \underline{\kappa}$, where κ' and κ are wave vectors for the scattered and incident waves. Also $|K'| = \frac{2\sin\theta}{\lambda}$, In crystals the atoms are regularly arranged, so we can write for the vector distance $\underline{r}_n$ of the cell n in terms of the unit cell translations a, b, and c,

$$\underline{r}_n = n_1\underline{a} + n_2\underline{b} + n_3\underline{c}$$

n_1, n_2 and n_3 are integers. Now it is convenient to express $\underline{K}'$ as a vector in reciprocal space. In terms of reciprocal lattice co-ordinates $\underline{a}^*$, $\underline{b}^*$ and $\underline{c}^*$, K' can be written as,

$$\underline{K}' = \xi\,\underline{a}^* + \eta\,\underline{b}^* + \zeta\,\underline{c}^*$$

where ξ, η and ζ may take any value.
Substituting for $\underline{K}'$ and $\underline{r}_n$ in (40) we can write,

$$\Phi_g = \sum_n f_n(\theta)\, e^{-2\pi i(n_1\xi + n_2\eta + n_3\zeta)}$$

For this to be a maximum we must have

$n_1\xi + n_2\eta + n_3\zeta$ as an integer. The n_i are integers, so we must have

$\xi = h$, $\eta = k$, $\zeta = l$, where h, k and l are integers and we obtain the Laue conditions,

$$\underline{K}'\underline{a} = h\,, \quad \underline{K}'\underline{b} = k \quad \text{and} \quad \underline{K}'\underline{c} = l \quad \ldots\ldots(41)$$

But a reciprocal lattice vector can be written as,

$$\underline{g}_{hkl} = h\underline{a}^* + k\underline{b}^* + l\underline{c}^*$$

which is normal to the crystal plane with spacing d_{hkl} and

is of length $|\underline{g}_{hkl}| = \frac{1}{d_{hkl}}$

Hence, $\underline{K}' = \underline{g}$, from which we can get the Bragg relation,

$$2d \sin\theta = \lambda \quad \text{.....(42)}$$

when d is the interplanar spacing, λ is the wavelength and θ is the Bragg angle.

This diffraction condition can be represented by a simple equivalent geometrical construction. Consider a point O as origin (Fig.6.) and a vector O'O opposite in direction to that of the incident beam and of length equal to $\frac{1}{\lambda}$. Now with O' as centre a sphere of radius $\frac{1}{\lambda}$ is drawn; where this sphere (called the Ewald sphere) intersects a reciprocal lattice point such as G there will be a diffracted Beam O'G. The point O' will lie on a plane which is the perpendicular bisector of the reciprocal lattice vector g. The electron wavelength at 100Kv is .037Å giving an Ewald sphere of radius 27^{-1}Å . This is so large that the sphere may be approximated by a plane, so that the observed electron diffraction pattern may be considered as a plane section of the reciprocal lattice.

When an electron beam strikes a crystal a reflected pencil leaves the crystal at an angle 2θ to the incident

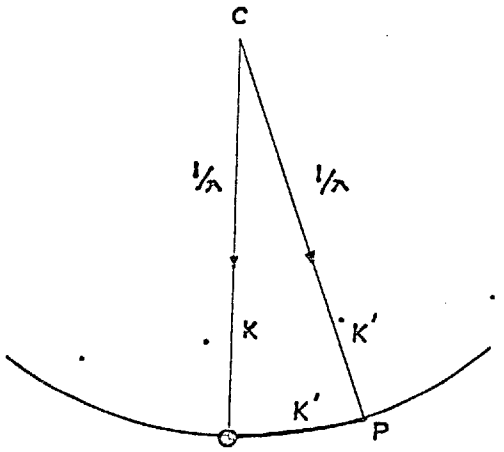


FIG 6. REFLECTING SPHERE CONSTRUCTION.

beam and appears as a spot on the screen. If the specimen is composed of a large number of small crystals randomly oriented then the many reflections occurring will form hollow cones which intersect the photographic plate or film to give rise to diffraction rings. If R is the radius of a diffraction ring then the interplanar spacing d can be calculated using the relation,

$$R = \frac{\lambda L}{d} \qquad \ldots\ldots\ldots\ldots\ldots\ldots (43)$$

when L is the distance of the specimen from the plate or screen as shown in figure 7. In electron microscopes the value of L cannot be accurately measured and hence the constant λL is determined by calibration. The distances in the diffraction patterns are reciprocal to the distances in the scattering object. Equation (43) is used to relate the diffraction pattern to the real crystal.

The amplitude of a Bragg reflection is dependent on the structure of the unit cell, since it is proportional to the structure factor which is a function of the arrangement of atoms within the unit cell.

3.9.4.2. Diffraction from a Parallelipiped crystal.

Strong reflection occurs if $\underline{K}' = \underline{g}$. But when $\underline{K}' = \underline{g} + \underline{s}$ then the amplitude of scattering will be,

$$\Phi_g = \sum_n F_g \, e^{-2\pi i(\underline{g} + \underline{s})\,\underline{r}_n}$$

$$= \sum_n F_g \, e^{-2\pi i\, \underline{s}\,\underline{r}_n} \qquad \text{since the product } \underline{g}\underline{r}_n \text{ is an integer,}$$

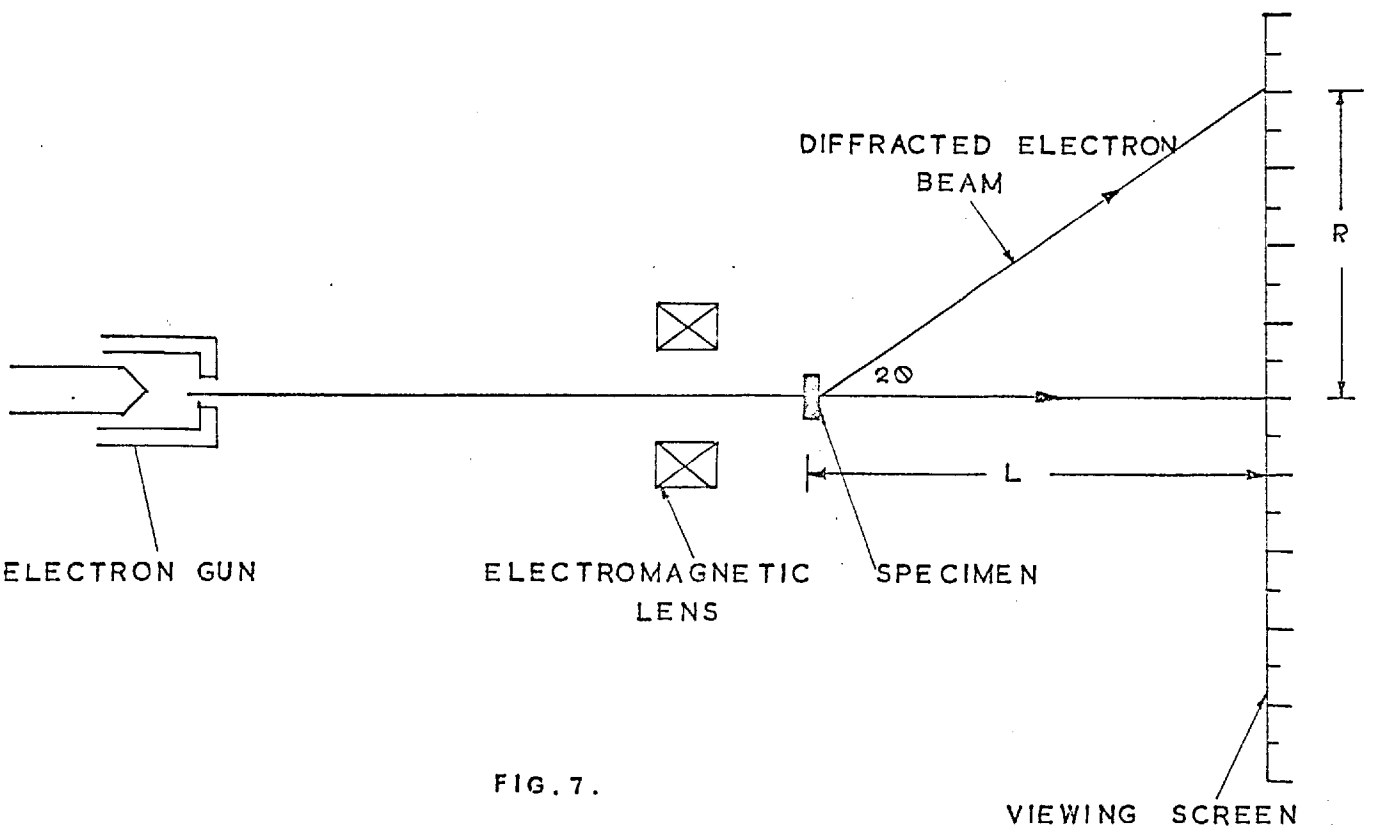

DIFFRACTED ELECTRON BEAM
R
2Θ
L
ELECTRON GUN
ELECTROMAGNETIC LENS
SPECIMEN
VIEWING SCREEN

FIG. 7.

Here $\underline{s}$ is the deviation parameter, F_g is the structure factor for reflection $\underline{g}$. $\underline{s}$ is small and the summation can be approximated by an integral,

$$\Phi_g = \frac{F_g}{V_c} \int_{\text{crystal}} e^{-2\pi i \underline{s}\cdot\tau} \, d\tau \qquad \text{where } \tau \text{ is an element of volume}$$

$$= \frac{F_g}{V_c} \int_0^A \int_0^B \int_0^C e^{-2\pi i(u_x+v_y+w_z)} \, dx\,dy\,dz \, .$$

Where V_c is the volume of the unit cell, A, B and C are the edges of the crystal along x, y and z directions respectively. The above integral can be evaluated as,

$$\Phi_g = \frac{F_g}{V_c} \cdot \frac{\sin \pi Au}{\pi u} \cdot \frac{\sin \pi Bu}{\pi v} \cdot \frac{\sin \pi Cw}{\pi w} \quad \ldots \quad (44)$$

u, v and w are the components of $\underline{s}$ along x, y and z directions. The intensity distribution is given by $\Phi_g \Phi^*_g$. The central maximum has a half peak width $\sim \frac{1}{A}$ so that the width of the peak at half intensity is a measure of the dimensions of the scattering lattice. For a plate-like crystal the intensity is in the form of a spike normal to the plate and for a spherical crystal the distribution is spherically symmetrical. In transmission electron microscopy the crystal is usually in the form of a thin plate normal to the beam and the intensity distribution around each reciprocal lattice point is in the form of

a spike normal to the crystal plate.

6.10. Dynamical theory of electron diffraction.

The transmission and scattering of electrons by crystals is a complicated process which is properly dealt with by the dynamical theory of electron diffraction. The kinematical theory of electron diffraction breaks down when the scattered amptitude Φ_g is greater than the incident amplitude Φ_o , and as a result the scattering equation has to be modified. This can be achieved by the so-called dynamical theory of electron diffraction which takes into account the interactions between diffracted and undiffracted waves as well as the effects of multiple scattering. The detailed analysis and the mathematics involved in the dynamical theory of electron diffraction can be obtained in Hirsch et.al.[104]

CHAPTER VII

7. Diffraction analysis of carbonaceous materials

Warren[34] developed the theory of random layer lattices which paved the way for the authentic study of carbon. A random layer lattice is defined as a stack of parallel and equidistant identical layers, stacking being random in translation parallel to the layers and random in rotation about the normal to the layers. Biscoe and Warren[149] suggested the word 'turbostratic' to describe the crystallographic nature of the crystallites in carbon black, consisting of carbon atoms arranged in honeycomb-like flat layers of random layer lattice character.

Diffraction patterns of carbonaceous materials contain two or three broad diffuse peaks having roughly the same positions as the strongest peaks of graphite. Biscoe and Warren showed that the x-ray patterns of a number of carbon blacks consist of crystalline reflections (bol) and two dimensional lattice reflections, hk. Warren deduced the following expression for the intensity of the hk reflections

$$I_{hk} = F^2 \frac{\mathrm{Sin}^2(\pi/\lambda)(S-So).N_1a_1 \; \mathrm{Sin}^2(\pi/\lambda)(S-So)N_2a_2}{\mathrm{Sin}(\pi/\lambda)(S-So).a_1 \; \mathrm{Sin}\,(\pi/\lambda)\,(S-So).\; a_2} \quad \ldots(45)$$

where N_1a_1 and N_2a_2 are the dimensions of the layer, F is the structure factor, S, S_o the unit vectors that define the direction of the primary and the diffracted beams, and λ the wavelength of radiation. Restricting attention to one particular reflection (hk) the usual approximation can be made i.e.

$$\frac{\sin^2 Nx}{\sin^2 x} \longrightarrow N^2 \exp\left[- \frac{N^2}{\pi} x^2 \right]$$

Equation (45) was written as,

$$I_{hk} =$$

$$F^2 N_1^2 N_2^2 \exp. \quad - \frac{\pi}{\lambda^2} \left[\left\{ (\Delta s . N_1 a_1)^2 + (\Delta s N_2 a_2)^2 \right\} \right] \ldots (46)$$

where $\Delta s = s - s_o$.

The distribution of intensity in a two dimensional reflection is then given by the following two equations:

$$P'_{2\theta} = \frac{KmF^2 (1 + \cos^2 2\theta)}{4 \sin\theta \ (\sin^2\theta - \sin^2\theta_o)^{\frac{1}{2}}} \ldots\ldots\ldots (47)$$

and for small values of a,

$$P'_{2\theta} = \frac{KmF^2 (1 + \cos^2 2\theta)}{2(\sin\theta)^{\frac{1}{2}}} \left[\frac{La}{\pi^{\frac{1}{2}} \lambda} \right]^{\frac{1}{2}} F(a) \ldots . (48)$$

$P'_{2\theta}$ is the power per unit length of the diffraction circle of radius R.

where,

$$a = \frac{2\pi^{\frac{1}{2}} La}{\lambda} (\sin\theta - \sin\theta_o) \ldots\ldots\ldots (49)$$

θ is the half scattering angle and F is the structure

factor K is a constant equal to,

$$K = \frac{I_o e^4}{M^2 c^4} \frac{N_1 N_2 M \lambda^2}{4\pi R A_a} \quad \ldots\ldots\ldots\ldots\ldots (50)$$

M = number of layers in the sample.

A_a = area defined by a_1, a_2

M = multiplicity of hk reflection

La = diameter of the layer.

F(a) is a function of variable a given by the expression (49) and tabulated in reference (34). The distribution of intensity in a two dimensional reflection can be obtained for small values of $\sin\theta - \sin\theta_o$ using the equation (48) and equation (47) should be used for larger values.

Warren's relation leads to a simple relation for La, since as Warren states for peaks which are not too diffuse, the variations in intensity over the range of angles included between the half maximum intensity values can be considered as due solely to variations in F(a). From a plot of F(a) it was found that the half maximum intensity breadth corresponds to a change in 'a' of amount

$\Delta a = 3.26$. From equation (49)

$$3.26 = \frac{2\sqrt{\pi} L}{\lambda} \Delta \sin\theta \quad \ldots\ldots\ldots (51)$$

from which L can be calculated,

$$L = \frac{1.84\lambda}{\beta \cos\theta} \quad \ldots\ldots\ldots\ldots\ldots (52)$$

Warren pointed out that equation (52) is identical with the Scherrer equation for size determination except that the coefficient 1.84 is about twice the value given in the Scherrer calculation for cubic crystallites.

Since the maximum of L occured at a = .55 Warren was able to write,

$$.55 = \frac{2\pi^{\frac{1}{2}} L}{\lambda} \quad (\sin \theta_m - \sin \theta_o) \quad \ldots\ldots(53)$$

where $\sin \theta_m$ is the position of the maximum. Thus the peak for the two dimensional diffraction is shifted away from the exact Bragg angle towards higher angles by an amount,

$$\Delta \sin \theta = \frac{.16\lambda}{L}$$

7.1. Franklin's analysis.

Franklin wrote Warren's equation as,

$$I = K \frac{mF^2}{2\sqrt{2}\ n\ A_a} \left[\frac{L}{\sqrt{\pi}}\right]^{\frac{1}{2}} S^{-3/2} F(a) \quad \ldots\ldots\ldots(54)$$

where $S = \frac{2 \sin \theta}{\lambda}$, n is the number of atoms per unit cell and $F(a) = \int_o^{\infty} \exp\left[-(x^2 - a^2)\right] dx$.

where, $a = \pi^{\frac{1}{2}} L (s - s_o)$

For large values of a,

$$F(a) = \left(\frac{\pi}{4a}\right)^{\frac{1}{2}}$$

Hence, $F(a) = \pi^{\frac{1}{4}}/2(L)^{\frac{1}{2}} (s - s_o)^{\frac{1}{2}}$

substitution of the above in equation (54) yields the

intensity in a form free of L,

$$I = K \frac{m F^2}{4\pi n A_a} \quad s^{-1} (s^2 - s_o^2)^{-\frac{1}{2}} \quad \text{.....(55)}$$

Franklin pointed out that the approximations involved in the derivation of equation (52) lead to values of L which are too large in cases of small layers which give very broad rings. A better approximation was tried by Franklin but that also proved unsatisfactory as it depended on accurate measurement of the position of maximum intensity. It was concluded that the only satisfactory way of using Warren's equation in the case of small layers is to compare experimentally determined half widths with the half widths found from plots of the intensity profile calculated from equation (54). By this method Franklin found a value of 16 ± 1 Å for the layer size in a film formed by pyrolysis of Polyvinyledene chloride at 1000°C.

Besides yielding information of crystallite size, comparison of experimental results with theoretical values allows estimation concerning the relative amounts of crystalline and non-crystalline material.[48] In equations (54) and (55) it was observed that the intensity of the (10) band is greater than the theoretical intensity whereas that of the (11) band is only 65% of the theoretical. The anomalously high intensity of the (10) band generally occurring in carbon is believed to be due to the non-spherical character of the carbon atoms.

Following Warren several workers notably Wilson,[151] Brindley and Méring[152] and Warren and Bodenstein[153] have considered the profiles of the diffraction bands from random layers. Approximating functions of the type $\frac{\sin^2 Nx}{\sin^2 Nx}$ the layer dimension L was expressed in terms of the breadth at half maximum intensity by the relation (52). Warren and Bodenstein showed that if disc-like layers were considered instead of the parallelograms considered earlier by Warren, the Gaussian approximation could be eliminated, and they arrived at an expression for L, the average layer dimension,

$$L = \frac{1.77\lambda}{\beta \frac{1}{2}\cos\theta} \quad \ldots\ldots\ldots\ldots\ldots(56)$$

The numerical constant differs by only 4% from that of equation (52). The two treatments refer only to average layer dimensions for differently shaped layers.

Because of the fact that the (004) reflection occurs at the high angle side of the (10) reflection which affects the sizes of the crystallites from half peak breadths, Warren and Bodenstein suggested the following expression for the determination of the layer dimension,

$$L = \frac{.94\lambda}{\beta \frac{2}{3}\cos\theta} \quad \ldots\ldots\ldots\ldots(57)$$

Equation (57) will give large values of L compared to (56) because the larger layers will contribute to the upper part

of the peak, and the effect of the (004) reflection on (10) can thus be minimised.

For larger sized layers ($L_a > 50\text{Å}$) these equations give a satisfactory representation but for samples in which the layers are very small it is necessary to develop the diffraction pattern from the general Debye scattering equation. The problem has been treated in this way by Diamond[154,155] and Warren and Bodenstein[35]. Diamond evaluated the powder pattern for the case of a single layer by using the Debye scattering equation,

$$I_s = \sum_m \sum_n fn\ fn \frac{\sin 2\pi S r_{mn}}{2\pi S r_{mn}} \quad \ldots\ldots(58)$$

r_{mn} is the distance between atoms m and n. For a sample containing single layers the values tabulated by Diamond give a rigorous representation of the (hk) peaks.

7.2. Analysis of Guentert and Cvikevich

The expressions derived by Warren as well as those of Wilson and Brindley and Mering and also the data calculated by Diamond are strictly applicable only to those materials in which the layers are randomly oriented. Guentert and Cvikevich[156] investigated the effect of preferred orientations on the shape of (hk) reflections in the diffraction patterns of pyrolytic graphite, where the layers align themselves preferentially parallel to the deposition plane. They introduced a correction term which reduces the (hk) peak shapes to those corresponding to

random layers. The corrected peak may then be analysed in the usual way using Warren's theory. Measuring the intensity of the (002) reflection as a function of the inclination angle δ they found the preferred orientation of the layers in samples of pyrolytic graphite could be described by a factor of the form $\cos^m \delta$. Assuming this orientation factor they derived an expression,

$$\frac{I \text{ random}}{I \text{ preferred orientation}} = Cm \left[\frac{\sin \theta}{\sin \theta_{hk}} \right]^m \quad \ldots\ldots(60)$$

The expression was checked for a sample having m = 8 by comparing the diffraction profiles from a flat specimen with its basal planes parallel to the deposition plane with the profile given by the same material in the form of a finely ground powder. It was confirmed that the peak from the specimen with preferred orientation of the layers could be made to fit that from the powder sample by use of the correction factor indicated by equation (60). It should be noted that this correction factor only applies to materials which satisfy an orientation factor of the form $\cos^m \delta$. The corrected (hk) reflections can then be subjected to Warren's analysis for random layers in order to calculate the structural parameters.

A study of evaporated carbon by electron diffraction is due to Kakinoki et.al.[157] who analysed the diffraction

profiles by the methods commonly used for analysis of diffraction from gases and vapours. These methods are based on the Debye[154] formula (equation 58) which can be used in two ways. A model may be assumed for the structure of the specimen under examination and a theoretical curve calculated and compared with the experimental curve. Alternatively the Fourier inversion of the formula may be applied to the experimental data to obtain the radial atomic distribution function. They suggested that two different bond distances existed in the carbon film, corresponding to the nearest neighbour distances in diamond (1.51Å) and graphite (1.42Å) the ratio of the numbers of bonds of the two types being 1.1. They concluded that the film consisted of graphite-like and diamond-like regions ~10Å in size, the proportion of the diamond-like regions being somewhat larger than the former.

CHAPTER VIII

8. Experimental procedure.

The various kinds of apparatus and experimental techniques with their applications used in the present study are described in this chapter.

8.1. Materials.

Carbon rods (grade RW-0) of diameter 6.14 mm made by Ringsdorff and supplied by Mining and Chemical Products, London, and iron wires of diameter .025 cm. supplied by the Johnson and Matthey Co. Ltd. London were used for the preparation of the composite iron carbon films. The purity of the spectroscopic carbon rods was as follows:

Impurities in PPM:

B	<	0, 01	Mg	<	0, 05
Ca	<	0, 2	Si	<	0, 3
Cu	<	0, 08	Ti	<	0, 5
Fe	<	0, 2	V	<	0, 2 .

8.2. Evaporation Unit.

Evaporation was carried out in a Balzers Micro BA3 Unit (Fig.8.) filled with carbon evaporation accessories. The present experiments were carried out in a pressure of about 5×10^{-5} torr. The vacuum chamber was a glass cylinder of 8 cm. internal diameter and 25 cm. long connected vertically or horizontally to the pumping unit

FIG 8



by a side tube. The chamber was evacuated by a Balzers high vacuum pumping unit, which used a two stage rotary vane pump for roughing, and for backing an air cooled diffusion pump.

8.3. Method of co-evaporation.

The R.W.O. carbon rods were turned down to 2.3 mm. diameter in the lathe to make spigots of length about 2 cm. The spigots were then coiled with iron wire as closely as possible as shown in figure 9. The carbon electrodes were then fitted in to the quick release flange of the evaporation unit, which was then connected to one end of the vacuum chamber and the necessary electric connections made. The two electrodes were then brought together and separated, thus striking an arc. Evaporation was carried out on to substrates of glass or freshly cleared mica about .8cm^2 area, placed at the centre of silicon discs, 1.8 cms in diameter. The substrates were mounted vertically below the source at a distance of about 10 cms. from the latter.

8.3.1. Preparation of substrates.

Electron microscopy demands absolute cleanliness, and freshly cleaned mica is an ideal substrate from this point of view. When glass substrates were used the cleaning process employed was the action of nitric acid and isopropyl alcohol, followed by swilling with distilled water. After cleaning, a drop of detergent (Teepol) was polished into

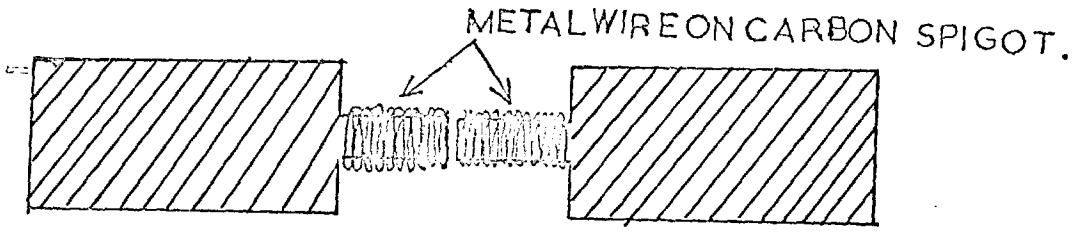


FIG. 9.

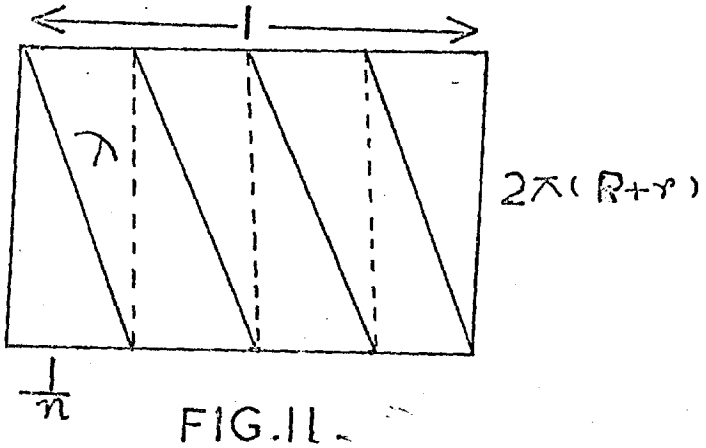


FIG. 11.

the glass surface; this acted as a hydrophilic stripping layer. The use of glass as a substrate was preferred to mica, due to the difficulty in stripping off the film from mica, and eventually glass was used in all cases.

8.4. Measurement of film thickness

In thin film tecnnology the film thickness is an important parameter, and there are several methods for measuring it. For detailed discussions references 159 and 160 may be consulted.

The thickness of a deposited film can be determined from a knowledge of the mass and density of the evaporant provided the evaporation is carried out from a point source. If it is assumed that evaporation takes place from a point source on a surface of a sphere of radius r, a uniform thickness of deposit t can be calculated using the relation, $t = \frac{m}{4\pi r^2 \rho}$ where r is the distance of the plane receiver from the source, m and ρ are the mass and density of the evaporant. This simple method proved unsuccessful in the present case because the mass of evaporant used could not be ascertained accurately.

By measuring the deposition rate with rate meters precise values of film thickness can be obtained by simply multiplying rate and deposition time provided the rate was constant. A knowledge of the deposition rate is desirable as film structure and properties are more or less affected

by the rate. The simultaneous measurement of thickness and rate is possible with the modern rate monitoring devices.

Alternatively the thickness of a film can also be determined with the help of the specially constructed micro-balances capable of measuring very small masses. This method necessitates a knowledge of the density of the deposited film which in fact not the same as that of the bulk material. A suitable technique is therefore necessary to determine the density of the film to make use of this simple method of measuring film thickness.

3.4.1. Estiration of film thickness during evaporation.

The film thickness was estimated by the change of colour produced on a gold film by carbon. A thin film of gold deposited on aluminium was mounted beside the substrate and when the gold film appeared deep blue, the evaporation was stopped. The thickness of such a film has been shown to be about 240Å. The variation of colour produced by carbon has been tabulated below:[158]

Colour	Thickness of carbon films
Orange	~150 Å
Indigo red	~200 Å
Deep blue	~240 Å
Blue green	~350 Å
Green-silver	~430 Å

8.4.2. Multiple beam interferometry.

A direct and more accurate method was used for determining the film thickness. After a film has been deposited its thickness can be measured most accurately by multiple beam interferometry as described by Tolansky[161]. A typical arrangement for multiple beam interferometry is shown in figure 10. The film whose thickness is to be measured is deposited in such a way as to form steps on the substrate and the whole of the substrate and film is covered with a thin layer of evaporated silver or aluminium. The metal simply replicates the step in the film, and also has a high reflection coefficient for light. The metal surface containing a step the height of the film thickness is arranged against an optical flat so that interference occurs between them. The interference fringes are spaced by half a wavelength of the monochromatic light used and the step height can be measured as a fraction of the half wavelength. If λ is the wavelength and h is the step height then the thickness will be given by $\frac{\lambda}{2}$ x h in Å units.

8.5. Determination of film Composition.

8.5.1. From direct calculation.

After deposition attempts were made to estimate the composition of the films using the following simple consideration.

'VARIAN' MULTIPLE BEAM INTERFEROMETER

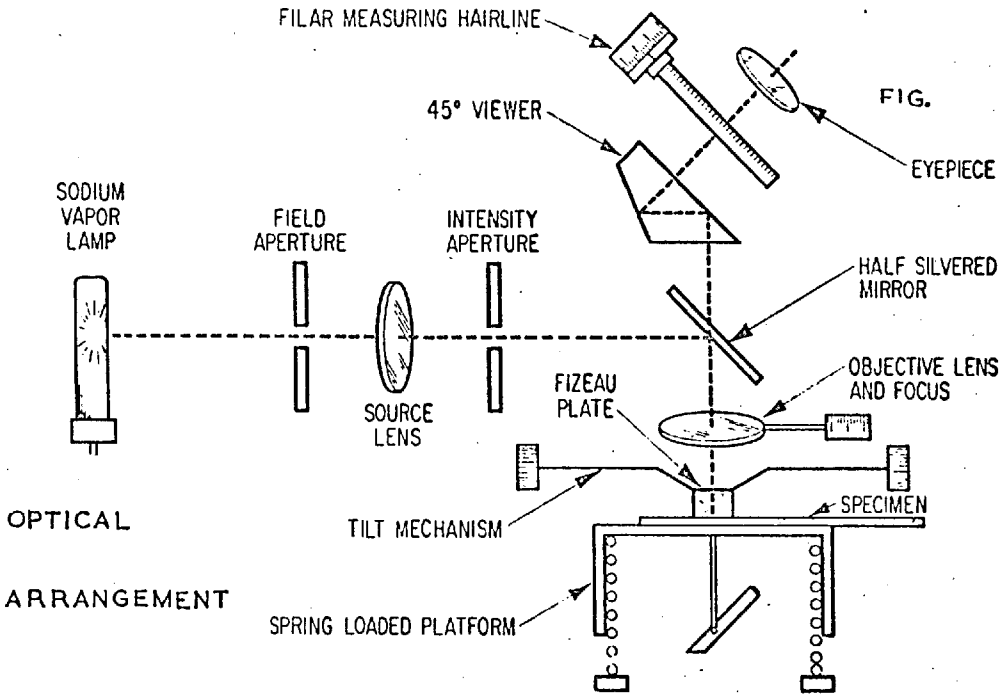
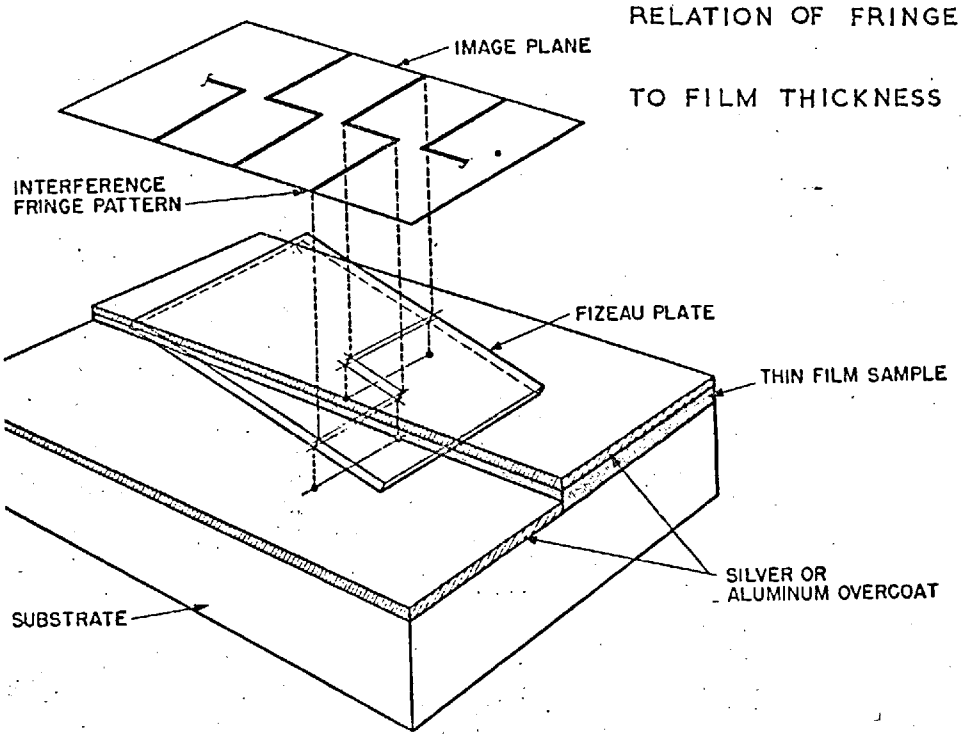


FIG.

OPTICAL

ARRANGEMENT



RELATION OF FRINGE STEPS

TO FILM THICKNESS STEP

FIG.10

Let R and r be the radii of the carbon spigot and iron wire (Fig. 11) respectively and n be the number of turns of wire per unit length of the spigot.

The length of the iron wire per turn on the spigot will be,

$$\lambda = \sqrt{4\pi^2(R + r)^2 + \frac{1}{n^2}}$$

If L is the length of the spigot, then total length of wire in L will be,

$$nL\lambda = nL\sqrt{4\pi^2(R + r)^2 + \frac{1}{n^2}}$$

$$\therefore \text{ Volume of wire } = \pi r^2 nL\sqrt{4\pi^2 (R + r)^2 + \frac{1}{n^2}}$$

And volume of spigot $= \pi R^2 L$.

Hence,

$$\frac{\text{volume of Metal}}{\text{volume of carbon}} = \frac{r^2}{R^2}\sqrt{4\pi^2 n^2 (R+r)^2+1}$$

It has maximum when $2nr = 1$ and an effective minimum when $n = 1$.

This procedure to determine the composition of the film proved unsatisfactory, because it was not possible to estimate the amount of iron evaporated. This was because some of the iron melted and dropped down as globules instead of being evaporated, due to the big difference in melting points of the two materials. Hence the film composition was determined using an electron probe microanalyser, as described in the next section.

8.5.2. Film composition by Electron Probe microanalysis.

The silicon discs were submitted for microanalysis to estimate the relative amounts of iron and carbon in the films. The reason for using silicon as a substrate for deposition of the films for microanalysis was that it could be obtained with very high (semiconductor) purity, and in particular was absolutely free from iron, an important requisite for the present purpose. Glass, mica and even aluminium showed the presence of iron in the electron probe microanalyser.

8.5.2.1. Theory of the Electron Probe microanalyser.

The microanalyser uses a scanning electron beam to generate characteristic x-rays in the specimen. These are then passed through an x-ray spectrometer and a counter so that the intensity of the characteristic lines can be measured. By the use of calibration specimens and after making correction for the background intensity, quantitative estimates of the specimen composition can be obtained. The basic construction of the probe is shown in figure 12. A beam of electrons generated from the gun strikes the specimen; some of the electrons reaching the specimen are reflected and the remainder penetrate the specimen. The latter excite the atoms in the specimen which causes emission of the characteristic x-radiation of each element present. The wavelength of the characteristic x-radiation is

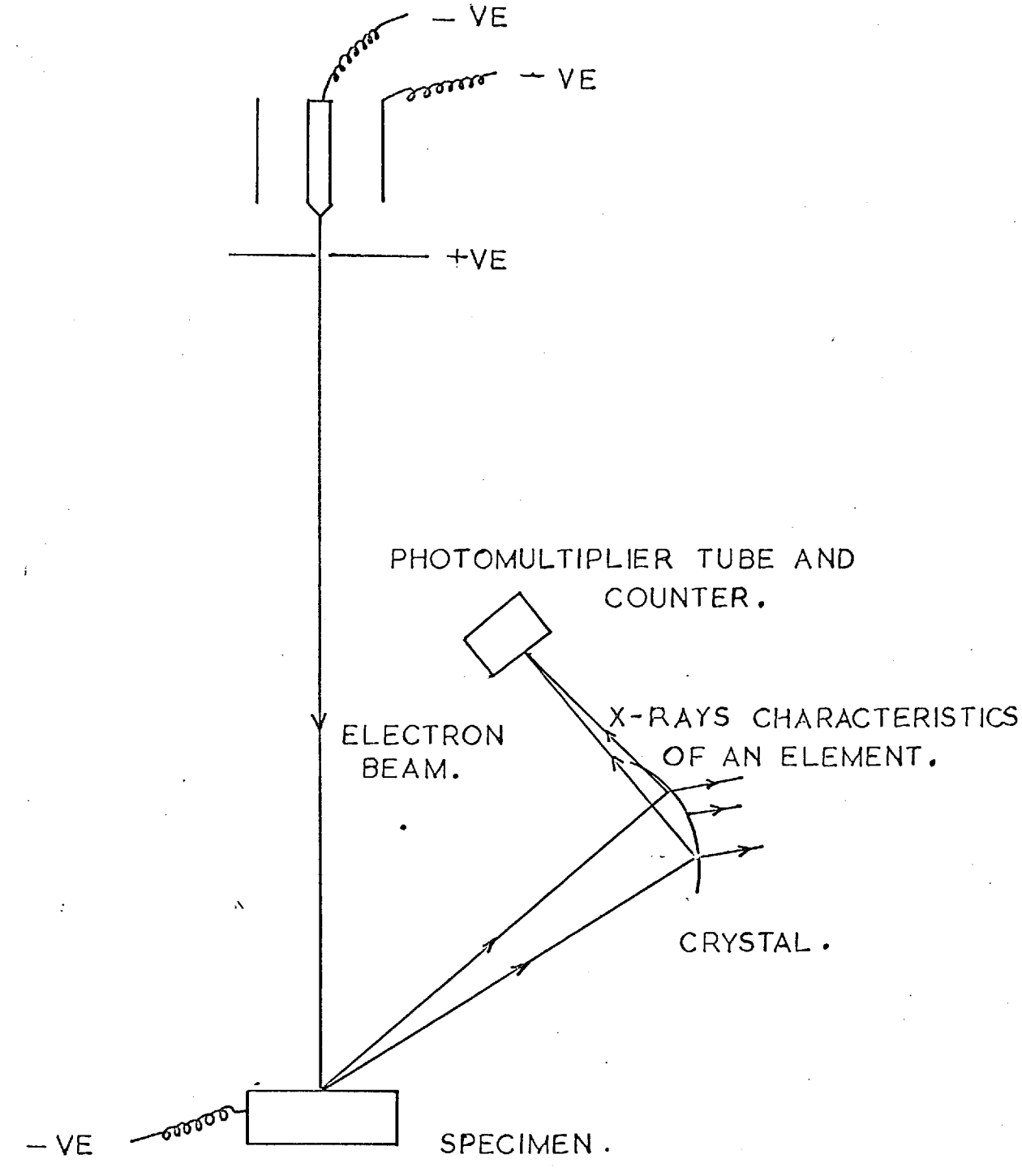


FIG. 12.

BASIC CONSTRUCTION OF THE ELECTRON PROBE MICROANALYSER.

dependent on the atomic number of the element. The wavelength λ of the radiation is related to the atomic weight W of the element according to the relation,

$$\log \frac{\lambda}{\rho} = K \log W.$$

Where K is a constant and ρ is the density of the element. For a given beam intensity, the intensity of the x-radiation emitted from the specimen is dependent on the weight percentage present of the particular element.

The x-rays emitted from the surface at a certain angle strike an optical crystal. When the crystal is at a certain angle to the x-ray beam the characteristic x-rays of a particular wavelength will be reflected. The intensity of these reflected rays is measured by photomultiplier tubes and pulse counters. The surface of the crystal is curved to focus the beam into the photomultiplier tube and counter. When the crystal is moved to a different angle it must remain at the same angle to the specimen as the intensity of the emitted x-rays is dependent on the angle of take-off from the surface i.e. $I_\theta = I_o \cos \theta$, which dictates the geometric relationship between the specimen, crystal and the analyser. For further discussion on Electron Probe microanalysis the references 162, 163 may be consulted.

8.6. Simultaneous evaporation.

Composite films of carbon and iron have also been prepared by evaporation from two different sources. The

vacuum chamber of the Balzer unit was used in a horizontal position, the carbon source was fitted at one end, iron was evaporated from a V shaped tungsten filament at the other. The substrates were placed in the middle of the chamber resting on a block of metal. Both the sources were operated simultaneously so that atoms of both species arrived at the substrates at the same time. A rough estimate of the amount of material deposited was obtained by weighing the carbon electrodes and the filament with the wire before and after the evaporation. But the material is not generally radiated with spherical symmetry and hence an estimate obtained from this measurement is inaccurate. The electron microprobe analysis of the films prepared by this method showed that the films were inhomogeneous and hence the co-evaporation method was preferred for all subsequent film preparation.

8.7. Preparation of carbon mounts.

In a graphitisation study of thin carbon films by electron microscopy and diffraction metal grids cannot be used due to contamination of the film at high temperatures. Grids made of the same material as that of the film were therefore used. The preparation of the carbon grids is as follows: The R.W.O. carbon rods of 6.14 mm. diameter were turned down to 2.3 mm. in the lathe using a special cutting tool. Then from the rod of 2.3 mm. diameter, carbon discs of thickness about .020" were cut using a parting tool in

the lathe. These discs after polishing with emery paper were drilled with six or seven holes of about .005" diameter. Finally they were ultrasonically cleaned with water and then with acetone to remove grease.

8.8. Mounting of specimens.

After evaporation each film was scored into many squares with a tweezer and then the glass slide with the scored film was lowered into distilled water at a slight angle so that the film was stripped off and floated freely on the surface of the water. Each square was then scooped up on to carbon mounts. These were then preserved in a vacuum dessicator for characterisation by electron microscopy and diffraction after heat treatment. It has been observed that when the iron concentration in the film is high the film tends to fold when placed into the water and thus become wasted.

8.9. Evaporation of Carbon on to heated iron foil.

Carbon was also deposited on to heated iron foil of thickness .005" placed at a distance of about 10cms. from the evaporation source. (3x1)cm. iron foil was clamped in a flange of the evaporation unit and connected to one end of the vacuum chamber above the carbon source. Prior to evaporation the foil was degassed at a higher temperature by passing a current through it for a considerable time and then the temperature was kept constant at 600°C. The temperature was measured by a thermocouple connected across

the foil. There was a temperature gradient across the foil, the hottest region being at its centre. After evaporation it was observed that there was no carbon deposited in the central region which was perhaps due to re-evaporation or direct solution of carbon into iron. The foil was allowed to cool down to the room temperature before it was taken out of the vacuum chamber. The foil was cut to pieces and then dissolved in dilute nitric acid and the carbon film obtained after dissolution of the metal was washed with water and mounted on the carbon grids.

3.10. Heat treatments.

Three furnaces were used to permit heat treatments to be carried out under vacuum and inert atmosphere. Arrangements were also made to facilitate heat treatment of the film under chlorine atmosphere.

8.10.1. Temperature below 1000°C

For temperature below 1000°C a resistance wound silica tube furnace as shown in figure 13 was used. The length of the tube was 40 cm. and its diameter 2.3 cm. and it could be fitted to a vacuum system via a port in the vacuum chamber in which a pressure of less than 5×10^{-5} torr could be attained. The specimen to be heated was supported at the centre of the tube on a glass spoon. When the pressure in the system was about 5×10^{-5} torr the temperature of the furnace was raised to the desired value, maintained by a controller. This was an Ether model 15-98, which could provide 3 kw, and control over the temperature

range 0-1200°C using chromel/alumel thermocouples with cold junction compensation. The controller was capable of giving an accuracy of ± 5°C at 1000°C which was regarded as sufficient for the purpose. The chromel/alumel thermocouples used by the controller were situated inside the furnaces in close proximity to the specimen. After heat treatment the furnace was allowed to cool to room temperature before it was let down to air to avoid oxidation of the specimen.

8.10.2. Heat treatment at temperatures from 1000°C upwards.

For heat treatment of specimens at temperatures 1000°C onwards a vacuum furnace[164] was used which is shown in figure 14. It consisted essentially of a hollow tube, the length and diameter of which were about 1 cm. and .53 cm. respectively cut from a block of pyrolytic graphite so that the direction of high electrical resistance (the c-axis direction) lay along the tube axis. The tube, with a resistance of about 3-4 ohms, was heated by passing high current (~ 100 amps) from a transformer which provided a maximum power output of one kilowatt. The specimen to be heated was placed on a graphite electrode which was fitted in turn into a groove in a copper plate. The graphite furnace tube rested vertically on the lower electrode surrounding the specimen. The top end of the tube was connected to another graphite electrode which was again

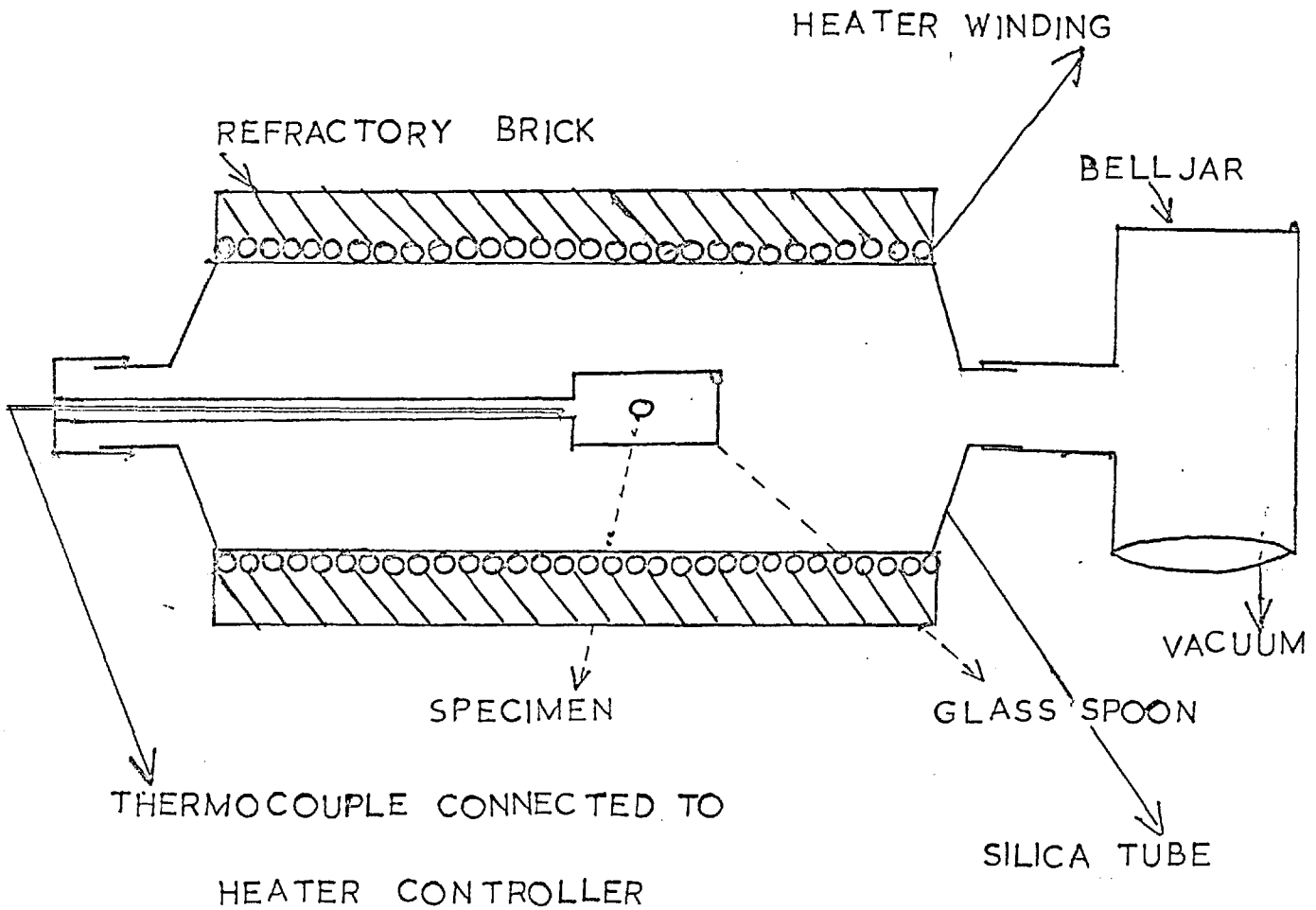

HEATER WINDING
REFRACTORY BRICK
BELL JAR
VACUUM
SPECIMEN
GLASS SPOON
THERMOCOUPLE CONNECTED TO
HEATER CONTROLLER
SILICA TUBE

FIG. 13.



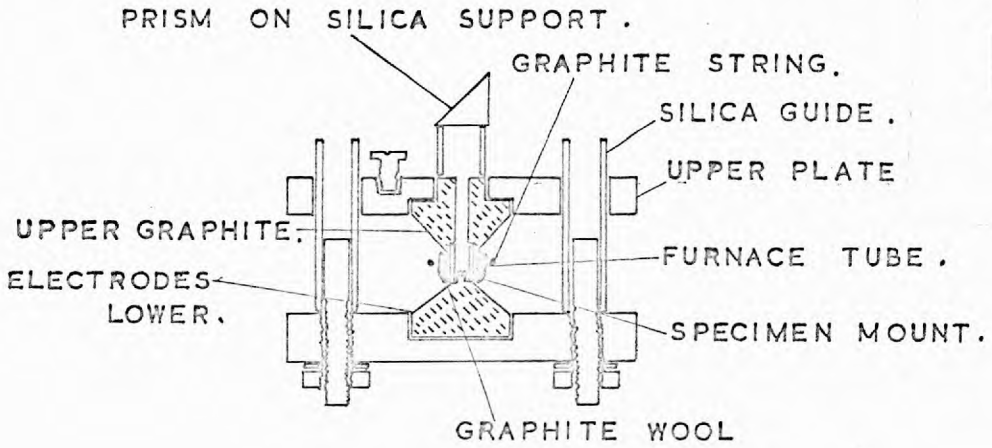


FIG.14 SECTION OF VACUUM FURNACE.

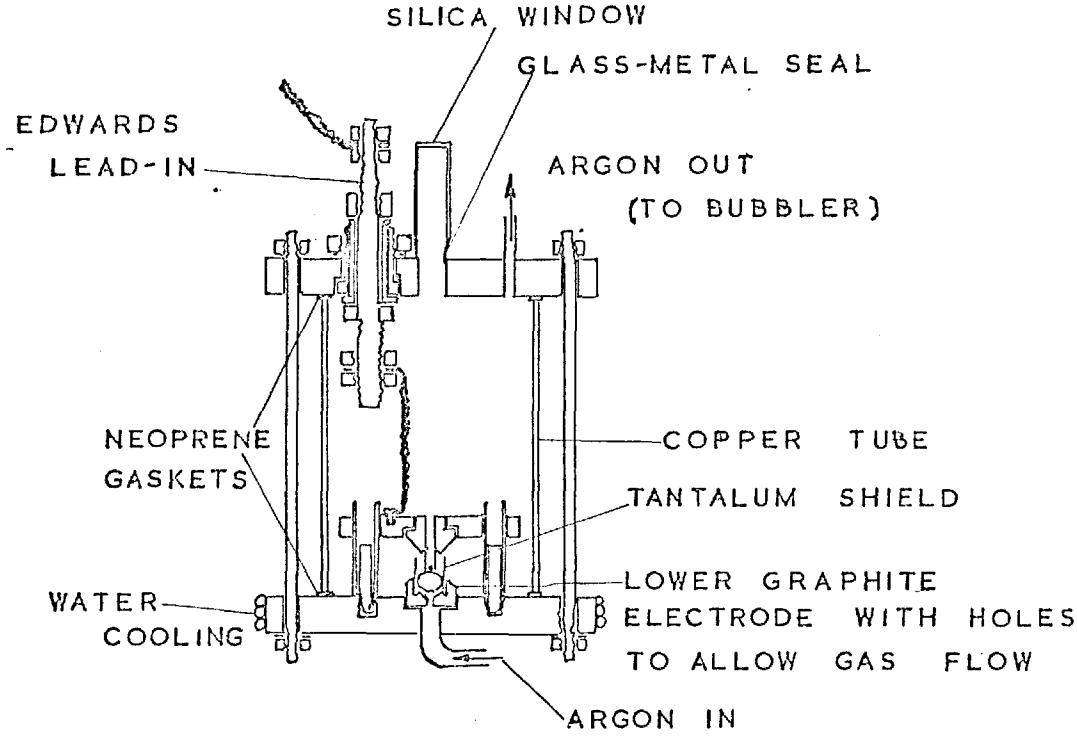
fitted into the groove of an upper copper plate. The electrical contacts at various points were thus made via graphite electrodes and copper surfaces and maintained by gravity and were quite reliable. The heat lost by radiation was minimised by putting a cylindrical shell of thin tantalum foil around the graphite tube in a groove cut in the lower graphite electrode for the purpose. The whole furnace was supported in a bell jar vacuum system.

The system was allowed to pump down until a pressure of 5×10^{-5} torr was reached before commencing heat treatment, and for temperatures above 1200°C the system was pumped overnight. Temperature measurement was carried out with a disappearing filament micro-Pyrometer which gave a magnified image (approx. 18x) of the specimen surface as viewed through a hole in the upper graphite electrode through a prism mounted about the furnace. The specimen and furnace satisfied black body conditions and consequently no corrections were required to convert brightness temperatures, for which the pyrometer was calibrated, to true temperatures. The accuracy of this method of measurement was checked by measuring the temperature of a specimen at 1000°C using the Ether controller and was found to be in fairly good agreement (±10°C). There appeared to be temperature differences at different parts

of the specimen the magnitude of which was sometimes ± 20°C. This was believed to be due to the poor contact of the film to the mount. One of the difficulties encountered was that at temperatures above 1800°C the graphite tube began to sublime in the vacuum; the carbon vapour so formed condensed, thereby thickening the specimen and making it unusable. This effect appeared pronounced when the residence time was above four or five minutes, depending on the temperature at which the furnace was operating.

8.10.3. Heat treatment in argon atmosphere.

Specimens were heated in argon atmosphere in a furnace similar to that of the vacuum furnace but with some modifications in the lower electrode to provide the gas flow, the design being shown in figure 15. Argon from a cylinder, after passing through silica gel, molecular sieve and finally through heated copper to remove oxygen, was admitted through the bottom of the furnace and left at the top, passing through a bubbler to air. The furnace was enclosed in a copper cylinder. The copper plate at the bottom was provided with water cooling for heat treatment at higher temperature. The argon was usually flushed for at least an hour before commencing any heat treatment. The specimen temperature was measured directly



SECTION OF ARGON FURNACE

FIG.15

with an optical Pyrometer as before. Care was necessary, as when argon was passed at high pressure the film broke and sometimes even the whole mount with the film was blown away from its position. After heat treatment the argon was allowed to flow continuously until the furnace attained room temperature. Here also at higher temperature ($\sim$ 2000°C) the same trouble of thickening of the film by evaporation of carbon from the furnace was observed.

8.10.4. Heat treatment in chlorine atmosphere.

Attemrts were made to heat specimens in a chlorine atmosphere to remove the iron from the film after pre-treatment to form the carbide. As before the specimen was placed at the centre of the low temperature tube furnace and chlorine from a cylinder was passed through the tube for sometime before commencing heat treatment. The escaping chlorine was allowed to dissolve in sodium hydroxide solution kept in a trough, and a bell jar connected to one end of the furnace was clamped and inverted over the trough containing the solution as shown in the figure 16. It was found that the effect of chlorine was to cause the film to decompose even at temperatures as low as 300°C. The method for the control and measurement of temperature was the same as before.

8.10.5. Disappearance of the film.

One difficulty encountered during heat treatment was the disappearance of the film. The films were found to have

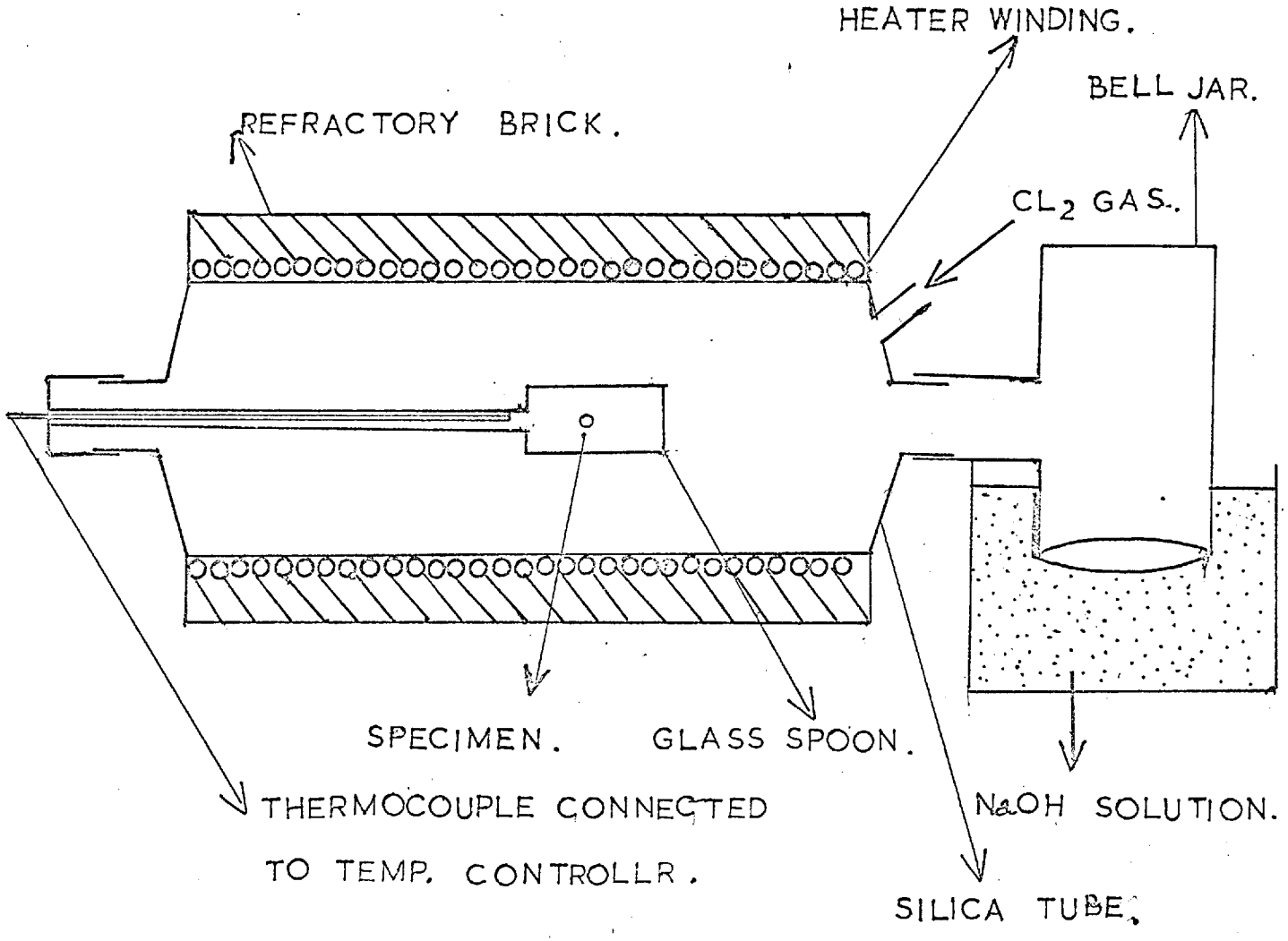

HEATER WINDING.
BELL JAR.
REFRACTORY BRICK.
CL_2 GAS.
SPECIMEN.
GLASS SPOON.
THERMOCOUPLE CONNECTED
TO TEMP. CONTROLLR.
NaOH SOLUTION.
SILICA TUBE.

FIG. 16.

poor adhesion to the mounts which deteriorated during heat treatment.

8.11. Electron microscopy.

The instrument used was a Siemens Elmiskop I which is a three stage microscope with objective, intermediate and projector lenses with double condenser illumination system. The maximum resolution obtainable using this microscope was ~15Å and it provided a very wide range of magnifications ranging from 1000 x to 160,000 x. Also diffraction patterns could be obtained without interfering with the position of the specimen or with the vacuum. The microscope was usually operated at 80 kv for most of the time.

8.11.1. Alignment of the instrument.

In order to produce electron micrographs of high quality it is essential to align the different components of the microscope as accurately as possible. The full procedure of alignment is necessary only when the column of the microscope is disturbed and in practice the alignment of the illuminating system, namely the condenser and the gun, was required most frequently.

8.11.2. Focusing and exposure.

Fresnel fringes were employed to establish best focus. It is well known that Fresnel fringes are produced by the interference of the direct beam with that scattered by the edge of an object; the first Fresnel fringe appears bright

when underfocused and dark when overfocused; the best focus is obtained when it just disappears. These fringes can be observed at higher magnifications and a low power telescope was used for focusing the image. The exposure time was ascertained by the visual estimation of the screen brightness and usually two to three plates were exposed for each area and the best selected.

8.11.3. Photographic materials.

Ilford special lantern contrasty plates were used and were developed and fixed using P-Q Universal Developer and Hypam fixer. The plates were usually developed for 6-8 minutes and then fixed for about 5-6 minutes before washing for about half an hour in running water.

8.11.4. Magnification.

The Elmiskop I is provided with a projector with four variable pole piece apertures to facilitate a wide range of magnifications up to a maximum of x160,000. In order to produce a particular magnification the required pole piece aperture was imaged so as to fit exactly with a circle inscribed on the viewing screen by adjusting the strength of the current through the projector lens. Internal calibra- for magnification of the microscope was carried out using a diffraction grating replica with 32,700 lines per inch and is shown in figure 17. In the present study the magnification generally used was 40,000x.



FIG 17 16,000

8.11.5. Anticontamination.

The deposition of amorphous material upon the specimen during examination in the electron microscope has been studied extensively,[165,166] since Watson[167] demonstrated this effect while studying the formation of films by electron and ion bombardment. These deposits are insidious and a prevalent source of error in electron microscopy. The instrument used was fitted with a decontaminator cooled with liquid nitrogen to reduce the rate of contamination of the specimen. With this arrangement the surroundings of the specimen could be cooled to about - 150°C.

8.12. Lensless diffraction.

The availability of a very wide bore pole piece in the final magnification stage of the Elmiskop I enabled it to be used as a simple electron diffraction camera. For this operation the specimen was mounted in the normal position and all lenses except the condensers switched off. The excitation of the second condenser lens was adjusted so as to obtain the sharpest possible transmission diffraction pattern. In the present study the crystallite dimensions were measured using diffraction line breadths obtained from this lensless diffraction method. One advantage of this method over the selected area diffraction method is that λL remains constant throughout. The diffraction patterns were always taken using the smallest condenser aperture and minimum filament current.

8.13. Selected area diffraction.

This is a very powerful technique which makes it possible to select a small region of interest of the specimen and to obtain its diffraction pattern with the aid of the imaging lenses. This enables one to correlate between the features observed on the micrograph and the crystallography of the particular area of the specimen. The area of interest can be defined by means of an aperture A at the normal image plane of the objective. In the absence of spherical aberration of the objective it is equivalent to an area $\frac{A}{M}$ at the specimen where M is the magnification of the lens. The objective lense operating at the normal strength forms a diffraction pattern at its back focal plane from a small area of the specimen. By reducing the strength of the intermediate lens it is possible to coincide its object plane with the back focal plane of the objective; this can be judged by making the central spot as small and round as possible. Thus the transmission diffraction pattern of the area can be observed and imaged on the viewing screen.

8.14. Shadowing.

Some heat treated specimens were placed in the Balzers coating unit and a few angstroms thickness of 40% palladium/gold was deposited at an angle, (30° and 45°). Deposition was carried out by wrapping a piece of 40% palladium/gold wire of .010 inch diameter around a

V-shaped filament of tungsten wire which was then electrically heated in a vacuum of about 1 x 10^{-4} torr to evaporate the shadowing material. A shadow free of metal was on the lee-side of any features projecting above the general level of the film and the front side collected a correspondingly greater amount of metal. Owing to the high scattering power of the heavier metals for electrons, the features were shown with great clarity in the image. The micrograph of a shadow cast specimen is usually printed or projected as a negative, the shadows (free of the shadowing material) then appearing dark and the regions covered with the shadowing materials light. The image appears as if illuminated obliquely i.e. as if the shadowing atoms were a beam of illumination. Knowing the angle of deposition the height of the specimen details can be estimated from the length of the shadows they cast.

8.15. Hot stage of the microscope.

The Jem-7 electron microscope is provided with a heating stage, the maximum specimen temperature being 1000°C. This was used to observe changes in the structure of the specimens during heating e.g. the nucleation, growth and decay of the particles of Fe_3C. The hot stage consisted essentially of a specimen heating device, a tilting stage to facilitate good contrast of the features during the inevitable slight buckling of the specimen during heating,

and the associated power supply for heating the specimen electrically. This enabled a continuous observation of the changes in microstructure of the specimen, but unfortunately sever specimen drift hindered the recording of events during heating.

8.16. Dark field operation.

It is a very powerful technique in electron microscopy of thin films and the simplest mode of dark field operation is to select the desired diffracted beam by displacement of the objective aperture and then operate the microscope in the normal manner. With adequate controls on the intermediate lens current this can be a speedy and efficient operation but the main limitation arises from the spherical aberration of the objective lens, since the diffracted beams are automatically inclined to the objective axis, which affects the resolution of the dark field image. This difficulty can be largely overcome by tilting the illuminating system until the desired diffracted beam passes accurately along the objective axis. The JEM-7 microscope has provision for tilting the illuminating beam through a large angle, using an electromagnetic system which shortens the alignment procedure, thus minimising specimen contamination.

8.17. Scanning electron microscopy.

A few heat treated specimens with different iron

concentrations were observed in the scanning electron microscope to determine the shape and size of the microstructural features in three dimensions. The scanning microscope was operated at 20 and 50 kv and with different magnifications up to 55,000 x. The specimens appeared to be magnetic and since the focussing of the image was carried out by electromagnetic methods, the focus was affected by the magnetism of the specimen giving slightly poor quality pictures.

8.18. Determination of camera constant λL.

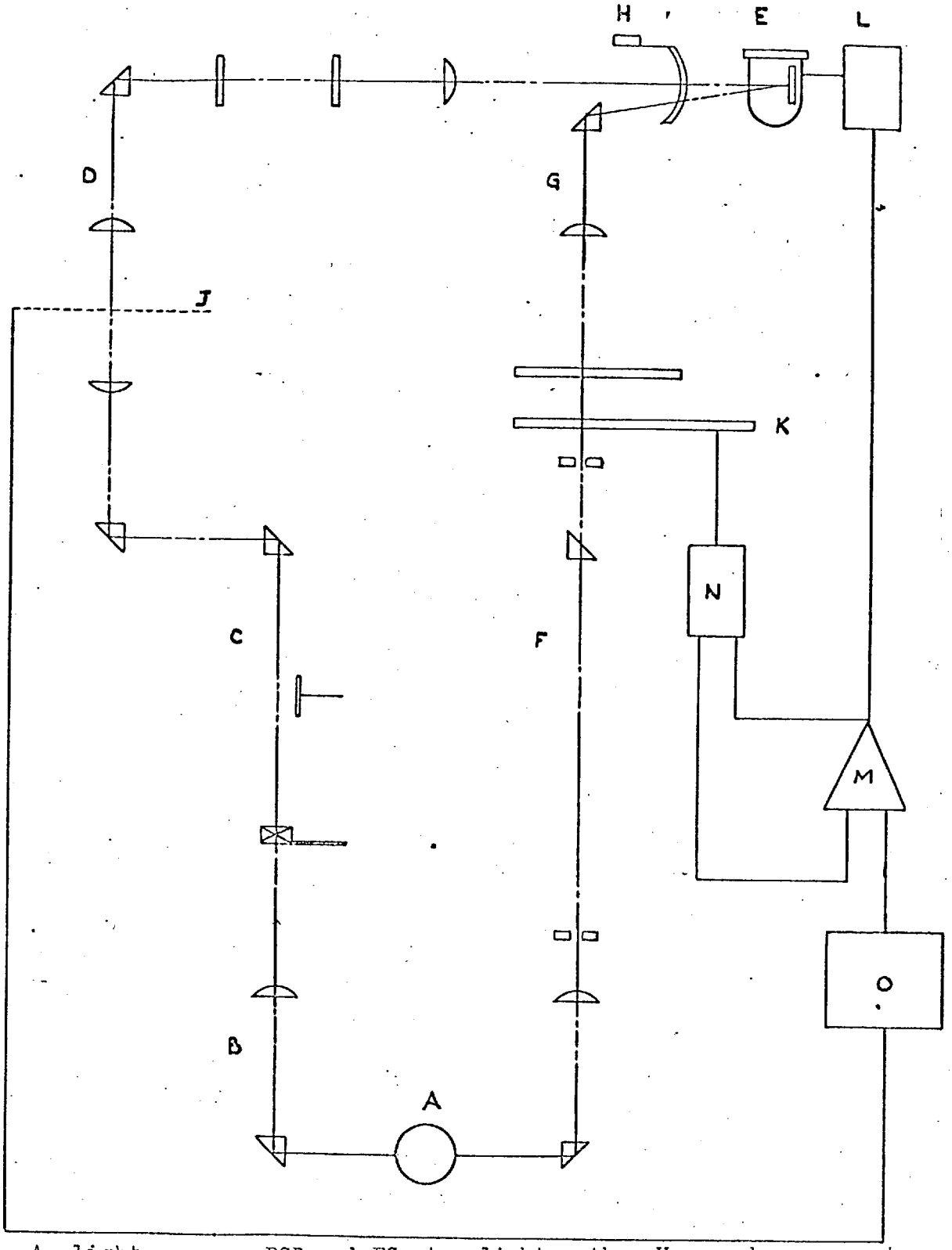
For this purpose a gold film was prepared by vacuum evaporation and then an electron diffraction pattern obtained in the electron microscope whose λL value was to be determined. From the electron diffraction pattern the diameter of the (200) ring was measured and this was substituted in equation (43) to calculate d which is the spacing of the plane under consideration. For gold d_{002} is 2.039 Å. The value of λL obtained from these data was 2.378 and this value has been used where necessary. Since the diffraction rings are not perfectly circular, the diameter D will vary from point to point. As a result there will be a series of values for λL corresponding to the different D values. The value of λL cited above corresponds to the highest value of the ring diameter, since it was assumed that the largest ring would provide the most accurate value.

8.19. Indexing of diffraction patterns.

The diffraction patterns of the heat treated specimens were indexed by measuring the ring diameters followed by calculation of the interplanar spacings using equation (43) corresponding to each value of ring diameters and comparing the observed interplanar spacings with the known A.S.T.M. data. Another way of identifying the patterns is to take the ring radii of the diffraction pattern and plot them on a logarithmic scale and compared with the known data plotted on the same scale from the A.S.T.M. index [177].

8.20. Microdensitometry.

The intensities of the diffraction lines were measured using a Joyce Loebel microphotometer, shown diagrammatically in figure 18. The plates with the diffraction patterns (negatives) were traced in a direction parallel to the length of the plate and from the tracing the line breadths of different reflections e.g.(00ℓ), (10) and (11) reflections were measured. The instrument was always operated under the same conditions of setting viz. constant slit size, bed speed and magnification. The instrument has several magnification stages up to a maximum of fifty. A magnification of five was generally chosen to work with and the magnification was tested and found to be in exact agreement with the given magnification



A- light source, BCD and FG- two light paths, H- synchronous motor, J- specimen plane, K- optical wedge, E- photomultiplier, L- constant gain device, M- amplifier, N- servomotor.

FIG.18.

SCHEMATIC DIAGRAM OF OPTICAL AND SERVO SYSTEMS.

of the microphotometer. However, there was no arrangement for rotating the plate during tracing which would minimise the variations due to the granular nature of the emulsion. Some plates were traced in several directions by rotating the plate azimuthally in steps of 20°, using a specially constructed holder, to investigate the anisotropic character of the specimen. The methods of measurements of the line breadths of each reflection are stated below.

8.21. Measurement of La.

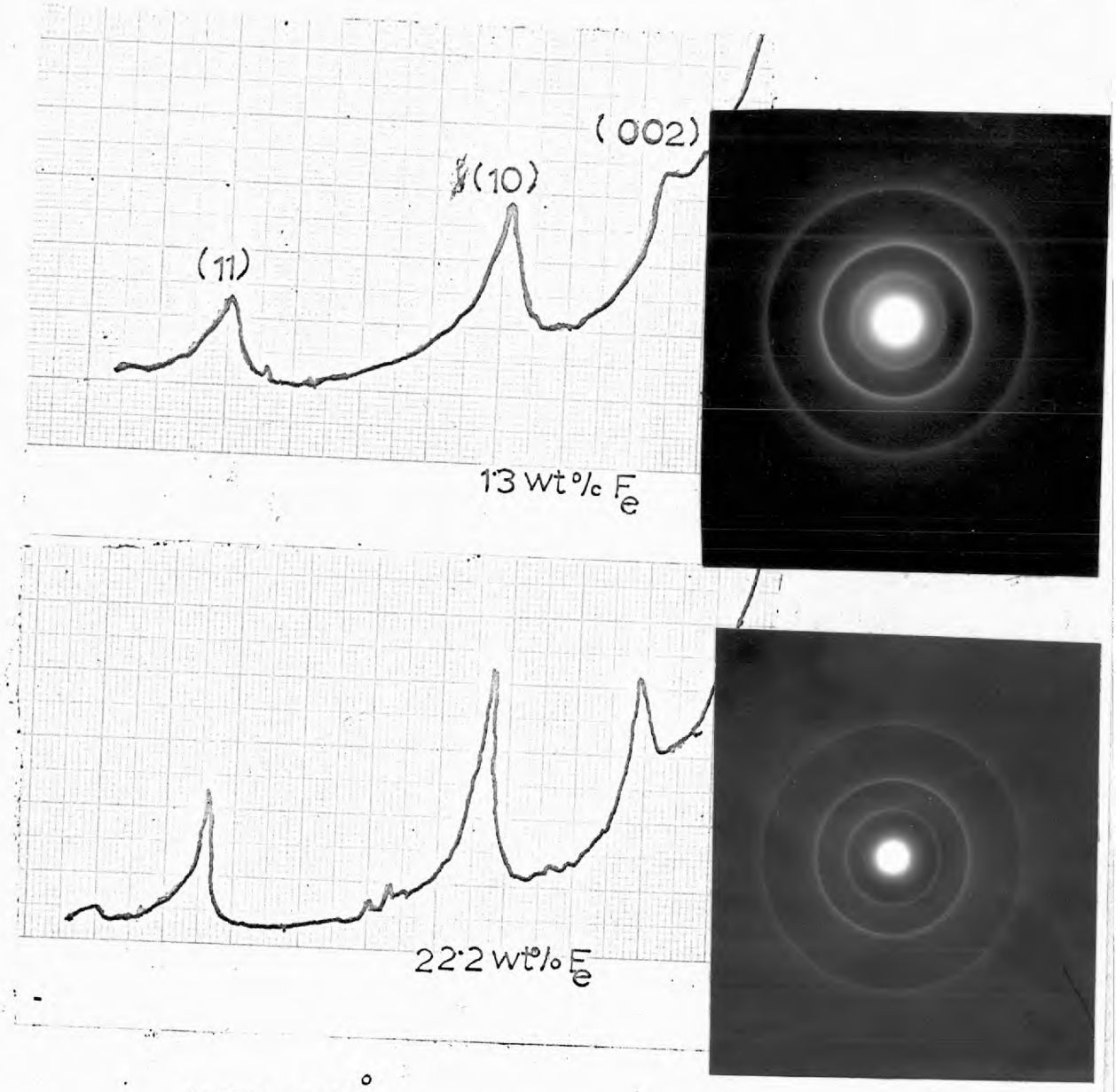
The layer diameter La in the graphitised films was measured using equation (56) discussed in Chapter VII which necessitates a knowledge of the breadth of the diffracted line. For a quantitative treatment it is first necessary to define breadth. A line on a diffraction photograph shows maximum intensity at the centre and fades away on either side; a simple definition of breadth is the angular width between the points at which the intensity falls to some fraction of its maximum value. Layer diameter was therefore calculated using equation (57) given earlier. Here $B_{\frac{2}{3}}$ is the angular breadth of the reflection at $\frac{2}{3}$ of the peak height. This fraction is useful in reducing the effect of the (004) reflection which occurs on the high angle side of the (10) line producing an extra broadening, as stated in Chapter VII.

Microphotometer traces of the electron diffraction patterns were obtained by traversing each plate across the

illuminated slit in a direction parallel to the length of the plate. Some plates were also traced along different diameters to investigate the angular dependence of diffraction profile and hence to study anisotropic layer growth in the specimens. Examples of the microphotometer traces are shown in figure 19 along with the corresponding diffraction patterns.

The development and treatment of the plate for microphotometry was quite important. After fixing and thorough washing, great care was observed in drying as a single speck of dust on the emulsion or a scratch was found to vitiate line breadth measurement.

The background of each microphotometer tracing was estimated by constructing a smooth line with a 'Flexicurve' tangent to the observed intensity profile at points quite distant from the peaks. The line so constructed was taken as the reference line from which the peak height was measured. Line breadths at the desired fraction of the peak height were required, and these fractions were measured along the vertical from the background to the centre of the peak. Lines were then drawn through these positions parallel to the background, which intercepted the reflection profile in two places; the horizontal distance between the two intercepts was taken as the line breadth at the particular peak height. In the present study line breadths at $\frac{1}{2}$ and $\frac{2}{3}$ peak heights were measured from the (10) and (11) reflections



H.T.T. 1200°C

FIG.19

for calculation of La values, and at $\frac{1}{2}$ peak height from (002) reflections for calculation of Lc values, using appropriate equations.

8.22. Mean La values.

The La value is the mean of four results obtained from the breadths of the two dimensional (10) and (11) diffraction rings at $\frac{1}{2}$ and $\frac{2}{3}$ peak heights. The accuracy indicated in each La value thus obtained is the square root of the variance of the four results.

8.23. Particle size measurements.

Recently a completely novel principle has been introduced for the rapid measurement of particle size. The instrument, called the Quantimet (Q.T.M.), is illustrated in figure 20, and a simplified block diagram is shown in figure 21. In brief the principle is as follows: An epidiascope or microscope projects an image on to the screen of a television camera. The electrical output from this camera passes into a closed circuit television monitor which provides a large display image. The electrical output also passes into a detector unit which can be set to distinguish the required features to be measured from the unwanted ones. The output from the detector consists of pulses from the detected freatures which are then fed into the monitor and into the computer which can be set to measure any of the following five functions: the total



FIG. 20

'QUANTIMET' IMAGE ANALYSING COMPUTER

SIMPLIFIED DIAGRAM

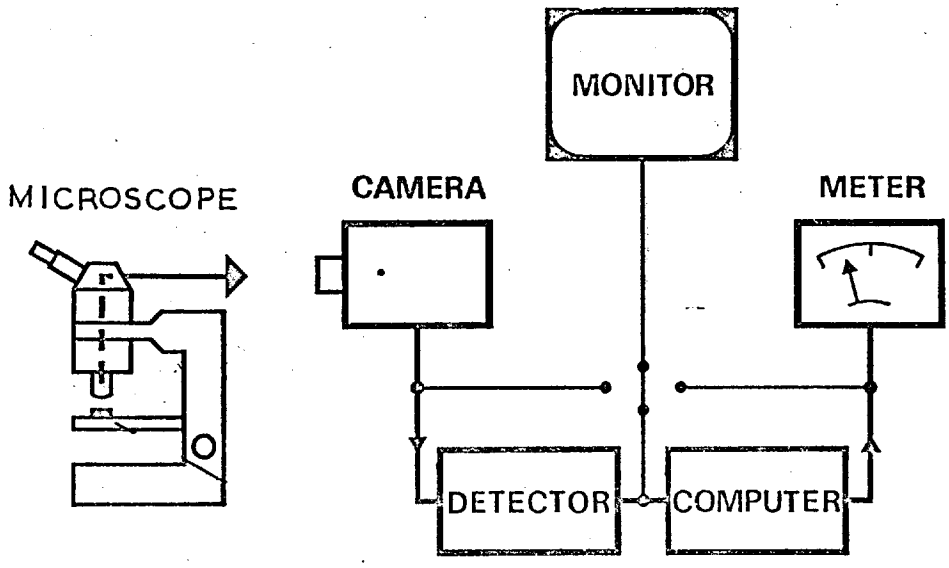


FIG. 21

particle projected area, the total particle number, the total particle length, the particle size distribution and the total particle chord size distribution. All these measurements are read out on the meter on the front of the instrument. The features which have been detected are automatically marked on the screen so that the operator has an instantaneous visual check on the correct setting and operation of the instrument. For a detailed account references 168 and 169 may be consulted.

The quantement could not be operated to measure the size of the carbide particles directly from the plates taken in the electron microscope. They were therefore photographed on to 35 mm. films using a photoreduction method, with a reduction factor of about 10x. From the films the percentage of projected area covered by the particles was measured in the Quantiment for at least ten different fields of view from which the mean was estimated. From this measurement other parameters such as mean particle size, volume fraction etc. were derived using appropriate relations. This instrument was found to work fairly well with photographs having very high contrast. The micrographs of carbide particles in our present investigation did not have the requisite black and white contrast and this hindered the successful operation of the instrument. Due to this poor contrast inherent in the specimen the matrix

surrounding the carbide particles produced an overlapping effect thus giving inconsistent results.

The instrument can also measure the number of particles in the field of view, provided these are spherical. In the present investigation the carbide particles were not all spherical and each non-spherical particle was registered in the meter more than once, as shown in figure 22.

Hence it was preferred to measure the size of the particles using a microviewer which could provide a magnification of 10x of the field of view. This visual method of measurement although tedious and time consuming was at least reliable. The number of particles was obtained from actual counting from the plate or the print.

8.24. Particle size analysis.

It is appropriate to say something about particle size distribution at this stage. The size of a particle is the dimension which best describes its state of subdivision (extension). For a spherical homogeneous particle its diameter is used as its size, for a cuboid the length along one edge, and so on. It is well known that the sizes of small particles of a particulate system are not usually uniform and that there will be a distribution of particle sizes rather than a single size. It is therefore necessary to deal with the distribution aspect

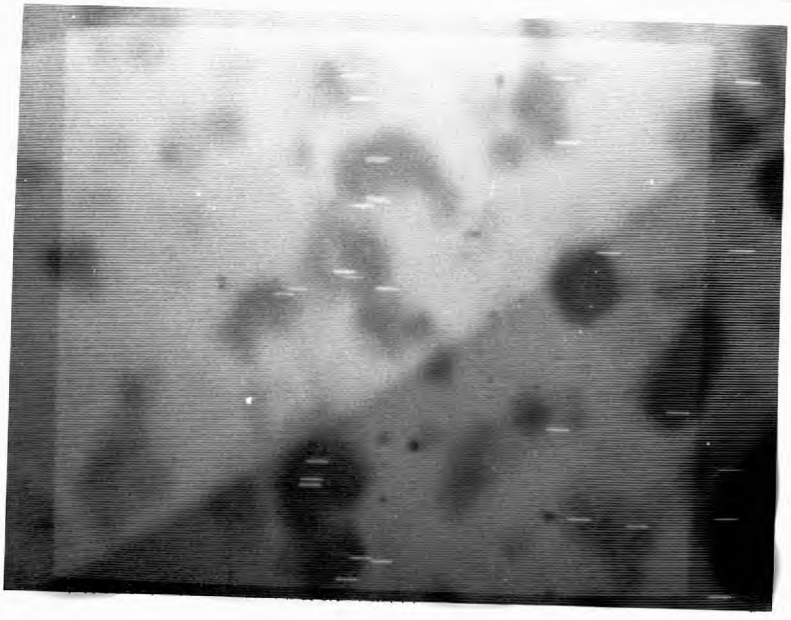


FIG. 22

of the problem. The significance of the distribution is more easily grasped when the data is presented pictorially, the simplest form of which is the histogram. A histogram is a plot in which the number of particles with diameters within any given range is plotted as if they all have the diameter of the middle of the range.

There are three ways to represent a histogram. In the first a rectangle is constructed over each class interval, the height of which is proportional to the number of particles in that interval. Another way is to construct rectangles where areas are proportional to the number of particles in the intervals. The third way of representing the dependence of frequency on particle size is in the form of a straight line relationship. Here the information can be plotted as a cumulative distribution on a probability grid, where the abscissa is particle radius r, and the ordinate is the percentage of the total number which is smaller or larger than r. The cumulative values are plotted against the class interval limits and not against the class interval centres as in the case of the frequency curve. A straight line relationship indicates that the distribution is governed by the so-called normal law. Although the cumulative curve often conceals details, the median size and the percentage of the number of particles between any two sizes can be obtained directly.

8.24.1. The distribution Laws.

The distributions found experimentally are generally described by one of two laws: (a) Gaussian distribution or the normal law (b) The log normal distribution or skewed distribution.

The mathematical representation of the normal distribution is,

$$y = \frac{1}{\sigma\sqrt{2\pi}} \exp\left[- \frac{(x - \bar{x})^2}{2\sigma^2} \right] \quad \text{.....(61)}$$

where y represents probability density, x the diameter of the particle, $\bar{x}$ the arithmetic mean and σ the standard deviation defined as,

$$\sigma^2 = \frac{\Sigma (x-\bar{x})^2}{N-1}$$

where N is the number of measurements made.

(b) Log-normal distribution.

More often the distribution curve is skewed and is then found to conform to the log-normal distribution fairly well. If the logarithm of particle size is plotted on the abscissa instead of the actual size, a symmetrical curve of the same form as the normal graph is often obtained. The equation representing the Log-normal distribution is given by,

$$y = \frac{1}{\log \sigma_g \sqrt{2\pi}} \exp\left[- \frac{(\log x - \log x_g)^2}{2 \log^2 \sigma_g} \right] \quad \text{.... (62)}$$

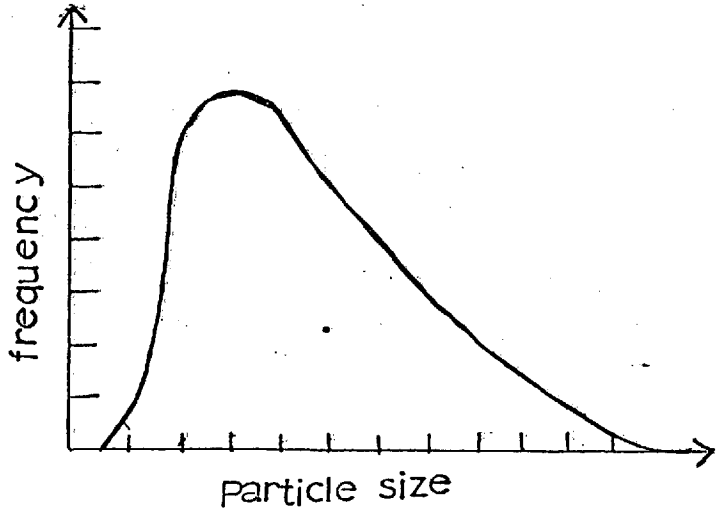


FIG. 23

where x_g is the geometric mean and σ_g the geometric standard deviation which is the standard deviation of the distribution of ratios around the geometric mean and whose logarithm is the standard deviation of $\log x$.

It is necessary to point out that the so-called Gaussian or normal distribution of particle sizes rarely if ever occurs. Actual distributions are almost always skewed[170] (Fig. 23) i.e. the tendency to deviate is greater on one side usually to the right of the mean than on the other.

Particle size analysis has been the subject of a considerable amount of research; there is no room in this account for a full description and the interested reader is referred to the comprehensive and excellent book by Herdan (1953).[171]

CHAPTER IX

9. Experimental Results.

9.1. Determination of specimen composition.

9.1.1. Using Parameters of the evaporant.

In the first place attempts were made to estimate the specimen composition using evaporant parameters such as length diameter, etc. and an example is given below.

Length of the spigots evaporated = .75 cm. = L

Diameter of the spigot = .23 cm. = D

Diameter of iron wire = .025 cm. = d

Length of the wire = 21.58 cms. = $\frac{L}{d} \pi D$.

Number of turns = 18

volume of iron = $\pi . r^2 nL\sqrt{4\pi^2(R + r)^2 + \frac{1}{n^2}}$

$= 3.14 \times .0125^2 \times 18 \times .75\sqrt{4 \times 3.14^2(.115 + .0125)^2 + \frac{1}{324}}$

$= .0053$ c.c.

volume of carbon $= \pi R^2 L = 3.14 \times .115^2 \times .75$

$= .0311$ c.c.

$\therefore \quad f = \frac{\text{volume of metal}}{\text{volume of carbon}} = \frac{.0053}{.0311} = .17$ (approx)

There were some drawbacks in employing this method for estimation.

(1) It was difficult to measure actual length of the carbon spigot evaporated because of uneven erosion of material at the ends during evaporation.

(ii) The difference of vapour pressures between the two evaporants is very large and hence at the temperature produced during arc evaporation some of the iron instead of evaporating melted and dropped as globules of which no account could be taken in the above calculations.

(iii) All the vapours of the evaporants do not condense on the substrate; some are condensed on the walls of the bell jar in the evaporating unit.

9.1.2. Electron microprobe analysis.

The simple method described in the previous section did not give satisfactory results and hence electron probe micro analysis was used for the determination of film composition. The specimen was scanned in several directions in the microprobe and a number of points counts taken from which the mean count was estimated for composition analysis. The counts corresponding to 100 % Fe and 100 % C were obtained from spectroscopically pure iron and carbon specimens. After making corrections for the background signal a quantitative estimate of the specimen composition was obtained using the relation,

$$\frac{C - Bg_C}{C_{100} - Bg_C} \times \frac{F_{100} - Bg_{Fe}}{Fe - Bg_{Fe}} = \frac{Wt\ \%\ C}{Wt\ \%\ Fe} \quad .....(63)$$

where C and Fe represent counts for carbon and iron in the specimen whose composition is to be estimated, C_{100} and Fe_{100} are the counts from spectroscopically pure carbon and iron,

and Bg is the background signal. An illustration of the data from which composition was calculated using equation (63) is shown in table 2.

Table 2.

	Carbon (counts)	Iron. (counts)
	1046	1216
	1106	1239
	1079	1340
	1075	1244
Average.	1076	1259
Background	302) 327) 314	347) 399) 373
Standard	17853	676441
Background	300	1204.

Putting these values in the above equation the concentration of iron in the specimen was estimated to be 2.9 wt. percent.

The weight percent of the metal can be expressed in terms of atom percent as follows:

Here the weight percent of carbon is 97.1 and weight percent of iron is 2.9.

Hence,

$$\frac{97.1}{2.9} = \frac{\text{Number of carbon atoms} \times 12}{\text{Number of iron atoms} \times 55.8}$$

or

$$\frac{\text{Number of carbon atoms}}{\text{Number of iron atoms}} = \frac{97.1 \times 55.8}{2.9 \times 12} = 155.7$$

let number of iron atoms = n

and then the number of carbon atoms = 100 - n

Hence,

$$\frac{100 - n}{n} = 155.7$$

or $n = .63$

so the composition of the above specimen (in terms of atom percent) is .63 atom percent of iron and 99.37 atom percent of carbon.

Point counts across the specimen showed the homogeneity of the composition, and the microanalyser line scan tracing in figure 24 is an illustration of this fact. The top line represents iron and the bottom represents carbon. Within instrumental errors the height of the peaks on both graphs appear to be fairly constant. ($\pm$ 5%)

As mentioned earlier two substrates were used for deposition, silicon for microanalysis and glass for microscopy and diffraction; the latter was always placed at the centre of the silicon disc. Since the same specimen could not be used for both purposes some doubt arose over the reliability of the procedure and on one occasion therefore, the composition determined from the silicon disc was compared with that on the glass by subjecting both the

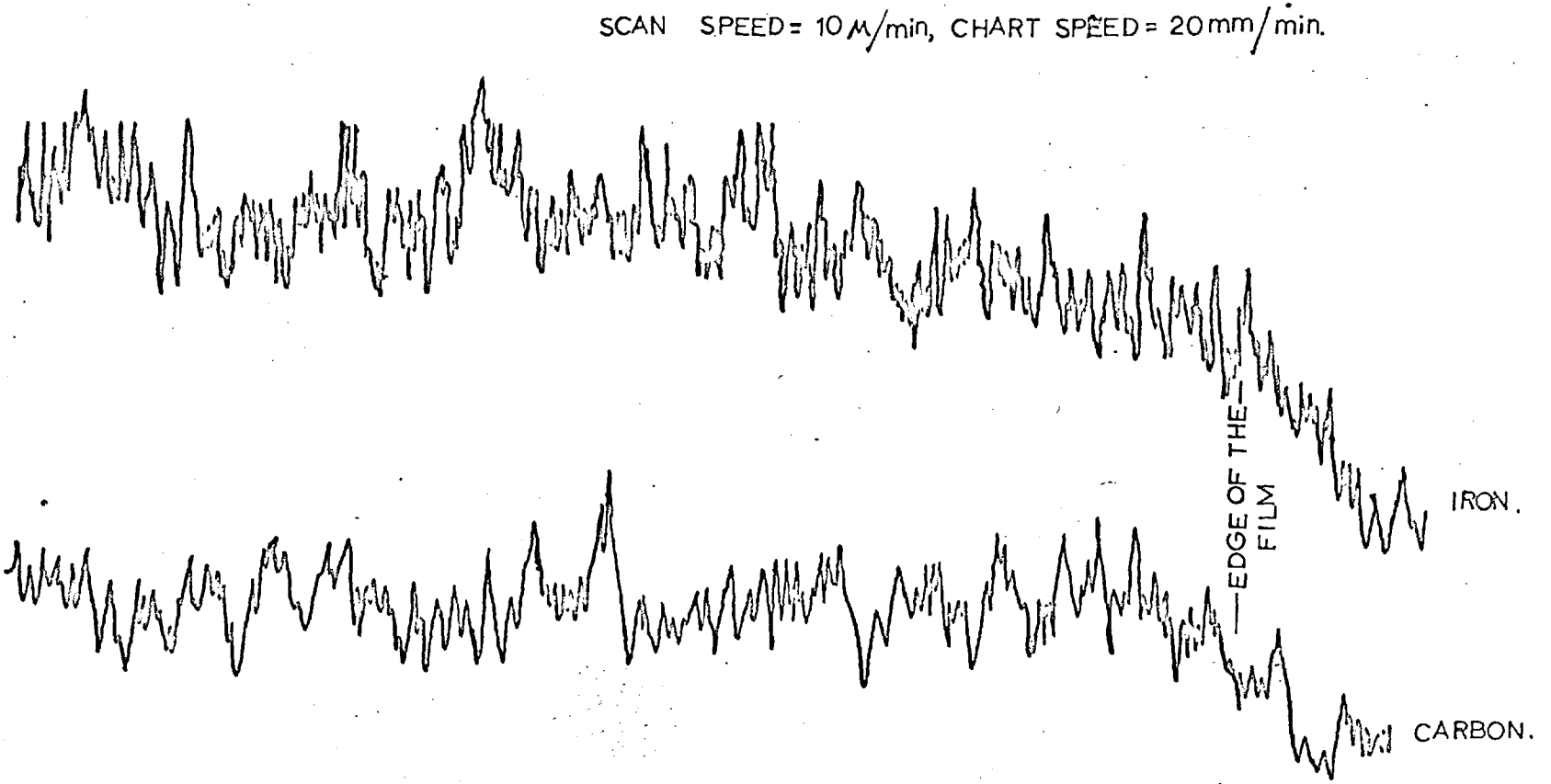

SCAN SPEED = 10 μ/min, CHART SPEED = 20 mm/min.
EDGE OF THE FILM
IRON.
CARBON.

FIG. 24

substrates from one evaporation to microanalysis; a good agreement was found between the two compositions. However, a slight increase of iron content in the ease of glass was attributed to the fact that glass contains traces of iron. and this was the main reason why glass as a substrate for microanalysis was replaced by silicon discs absolutely free from iron.

9.2. Composition Vs. frequency curve.

It was not possible to prepare a composite film with a desired iron concentration. The histogram of figure 25 shows a plot of iron concentration Vs. frequency and this reveals that the probability of producing films with high iron concentration is low. The most probable iron concentration lay within the range 0-2 wt%, (0-.43 at %). The highest iron concentration obtained was 22.2 wt.percent; (5.8 at %) it is not included in figure 25.

9.3. Micro structure of as-deposited films.

The structure of the as-deposited film appeared to be identical to that of amosphous carbon. Figure 26 is an electron diffraction pattern from an as-deposited film with iron concentration of 5.1 wt. percent (1.1 at %) and this shows the typical broad halos representative of amorphous carbon. The presence of iron could not be detected in the diffraction patterns obtained from as-deposited films. Fig. 27 is an electron micrograph of

an as-deposited film, showing little contrast in the electron image and showing no features which could be interpreted as due to agglomeration of iron.

9.4. Microstructure of films heat-treated below 1000°C.

When the as-deposited amorphous films which showed a diffraction pattern with broad diffraction halos were heated in vacuo the structure of the films changed as a result of heat treatment. The broad diffraction halos gradually split in several rings which subsequently sharpen and develop into a crystalline diffraction pattern as shown in fig. 28A. In the microscope image we could recognise crystalline particles and the material seemed to consist of these particles as shown in fig. 28B. The interplanar spacings calculated from an electron diffraction pattern of a specimen with 4 wt. percent iron (.88 at %) and heat treated at 550°C in vacuo for 2 hours were identified as Cementite (Fe_3C). Table 3 gives the observed values of the electron diffraction pattern. The corresponding d-spacings for Fe_3C from A.S.T.M. index have also been given for comparison. The intensities of the diffraction lines have also been indicated in the table.

The interplanar spacings for Fe_3C are available in the A.S.T.M. index file only up to a value of 1.58Å. In the present work weak diffraction lines were often found with interplanar spacings below 1.58Å; these sometimes corresponded

GRAPH SHOWING THE PROBABILITY OF OCCURRENCE OF A PARTICULAR COMPOSITION RANGE.

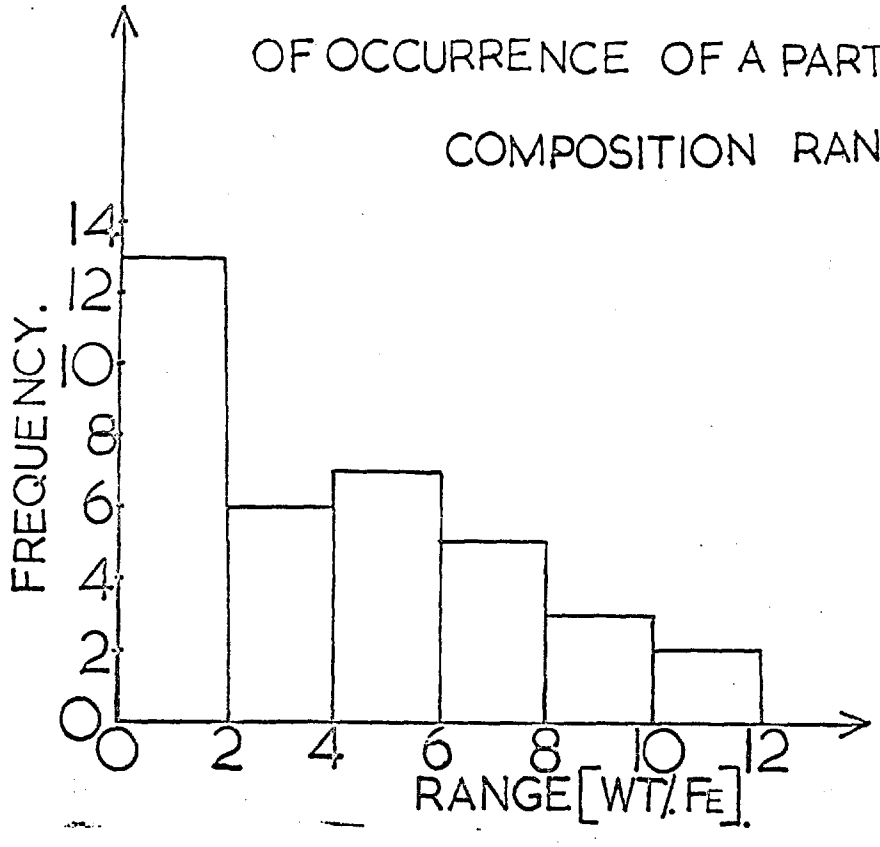


FIG. 25

Table 3

EXPERIMENTAL				Fe_3C A.S.T.M.		
P.N.	DIA.	dÅ	INT.	dÅ	INT.	hkl
1	1.40	3.39	M			
2	2.0	2.37	M	2.38	65	112 & 021
3	2.10	2.26	M	2.26	25	200
4	2.30	2.06	S	2.06	70	210
5	2.35	2.02	S	2.02	60	022
6	2.40	1.98	M	1.96	55	211
7	2.55	1.86	M	1.87	30	113
8	2.85	1.66	W	1.68	15	004, 023
9	2.95	1.58	W	1.58	20	130
10	3.35	1.42	W			
11	3.90	1.21	S			
12	4.10	1.16	W			

S = Strong.

M = Medium.

W = Weak.

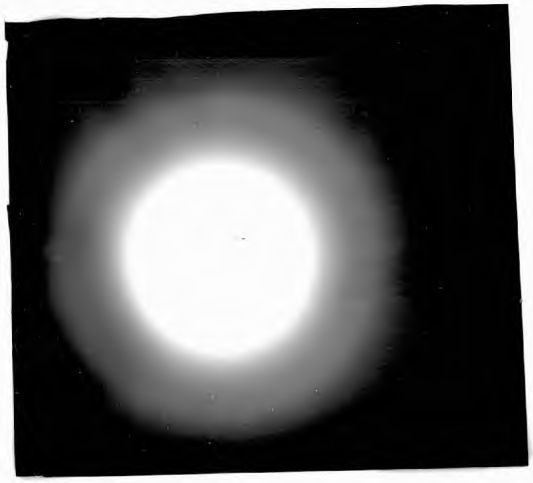


FIG. 26



FIG 27 X40,000

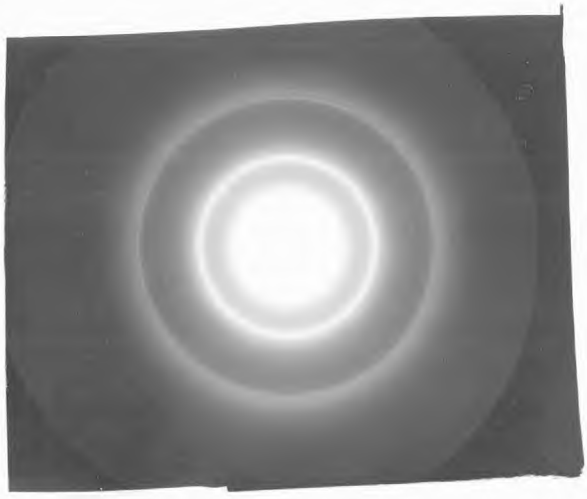


FIG 28 A

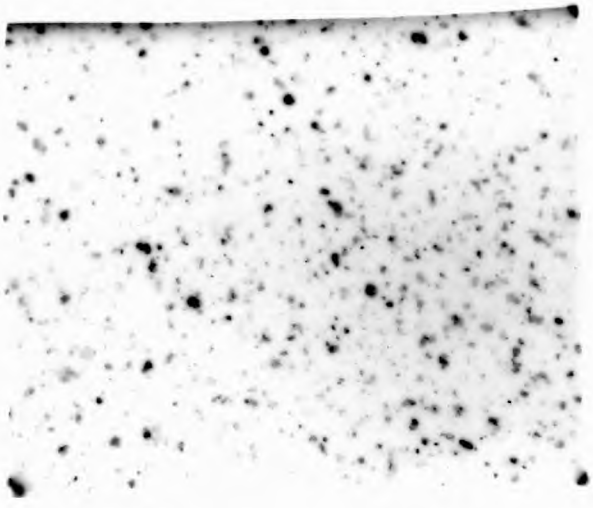


FIG 28 B X40,000

to one or two of the Fe_2C lines, which were available, but they could well have been due to Fe_3C. In addition, two diffraction lines were invariably observed with interplanar spacings of 3.39 and 1.21Å; these were believed to correspond to the 0002 and $11\bar{2}0$ reflections of graphite.

9.5. Cementite.

Cementite (Fe_3C) is always the prevalent carbide in plain carbon and low-alloy steels. In the iron-carbon system, iron-graphite is the strictly equilibrium phase while cementite is a metastable phase. The structure of Fe_3C has originally been determined by Westgren and Phragmen[172] and Hendricks[173] and has been redetermined by Lipson and Petch.[174] Its unit cell is orthornombic and contains four molecules (16 atoms). The cell dimensions are[174],

$a = 4.5144Å$, $b = 5.0787Å$, $c = 6.7297Å$.

Hume-Rothery, Raynor and Little[175] slightly modified these values while Petch[176] further discussed the structure and affirmed that its composition does not deviate from Fe_3C.

9.6. Kinetics of precipitation.

The rate of precipitation of Fe_3C depends on a number of factors. Among these are temperature, residence time of heat treatment and degree of supersaturation. The electron microscope provides an exact and direct visual method of studying the formation, growth and decomposition of precipitates and their size, shape, size distribution and

degree of dispersion.

9.6.1. Particle size distribution.

It will be convenient to deal first with the distribution aspect of the problem. One of the clearest ways in which to represent the distribution of sizes is by means of a histogram. Fig.29 represents a histogram showing the distribution of Fe_3C particles from a specimen with iron content 1.9 wt. percent (.41 at %) and heat treated in vacuo at 600°C for 3 hours. The diameters of the particles were measured visually from a print of a micrograph, the overall magnification of the print being 200,000 X. The diameters of 564 particles in the micrograph were measured and found to range from 50 to 600Å. Table 4 refers to the histogram of figure 29 in which the number of particles with diameters within any given range is plotted as if they all had the diameter of the middle of the range. For example the 10 particles with diameters lying between 25 and 50Å are regarded as having the diameter 37.5Å and so on.

The distribution curve (Fig.29) constructed from the above experimental data did not conform to the Gaussian distribution. Since the curve was skewed, it was thought that it might conform to the 'Log-normal' distribution. The data was therefore replotted, the cumulative frequency being plotted against the logarithm of the particle diameter, using probability paper. Fig. 30 shows that a straight line resulted, indicating a Log-normal distribution.

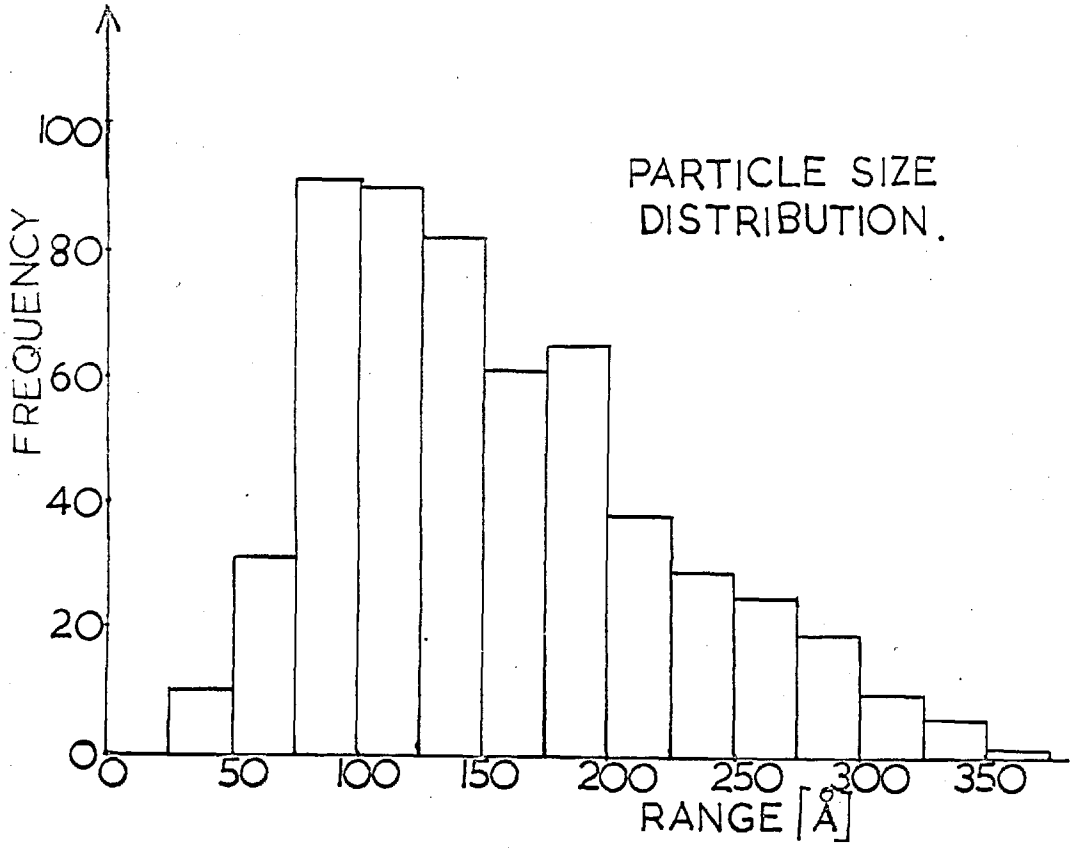

PARTICLE SIZE
DISTRIBUTION.
FREQUENCY
100
80
60
40
20
0
0
50
100
150
200
250
300
350
RANGE [Å]

FIG. 29

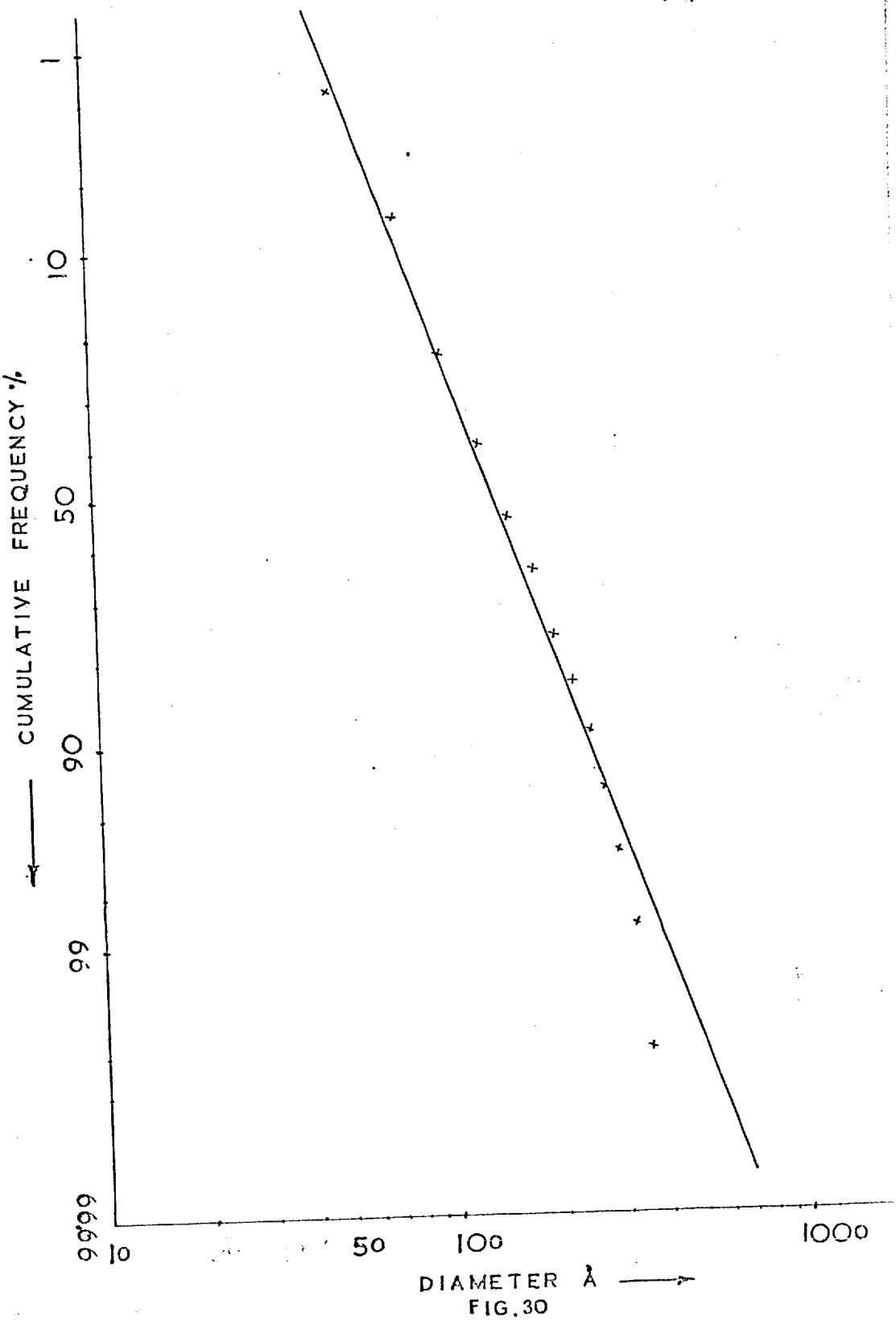

CUMULATIVE FREQUENCY %
1
10
50
90
99
99.9
10
50
100
1000
DIAMETER Å

FIG.30

Table 4.

Frequency distribution of particle size

Particle size (Å)	25	50	75	100	125	150	175	200	225	250
Number of Particles	0	10	31	91	90	82	61	65	38	29

Particles size (Å)	275	300	325	350	375	400	425	450	475
Number of Particles	25	19	10	6	1	0	3	1	0

Particle size (Å)	500	525	550	575	600	Total.
	1	0	0	0	1	564.

Fig. 31 illustrates another distribution curve obtained from the same specimen in the same manner as in fig.29 but with heat treatment at 800°C for 5 hours. The distribution curves constructed from the experimental data will deviate more or less widely from the ideal form, partly because the number of particles in the sample is limited and partly because the postulated distribution law is not obeyed perfectly. Fig. 32 shows the straight line plot obtained on probability graph paper from the data in fig.31. The tailing-off of the curve at high values of the particle diameter is due to misclassification in the size analysis, which may be expected at the ends of the size spectrum.

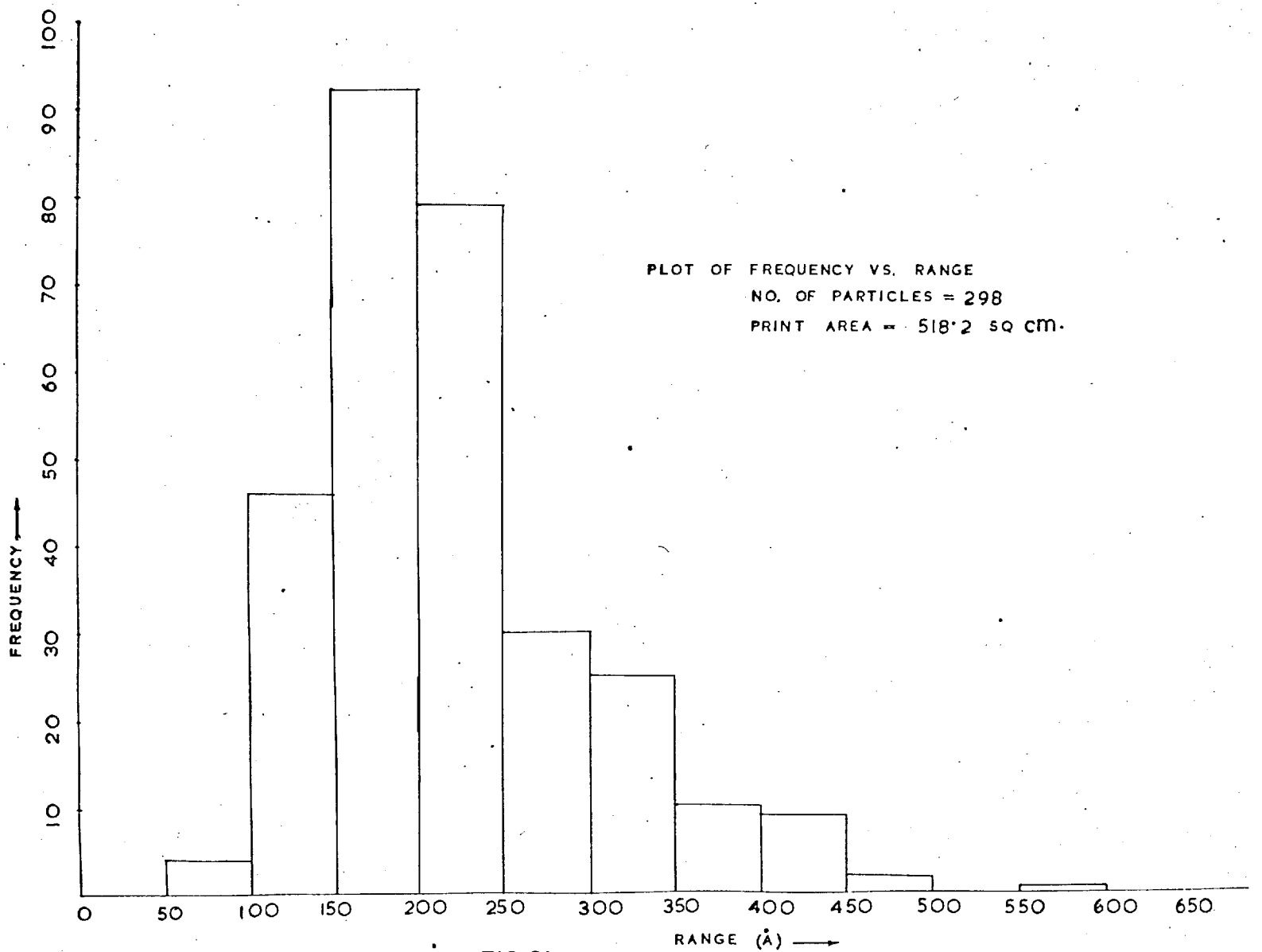

PLOT OF FREQUENCY VS. RANGE
NO. OF PARTICLES = 298
PRINT AREA = 518·2 SQ CM.
FREQUENCY
10
20
30
40
50
60
70
80
90
100
0
50
100
150
200
250
300
350
400
450
500
550
600
650
RANGE (Å)

FIG. 31

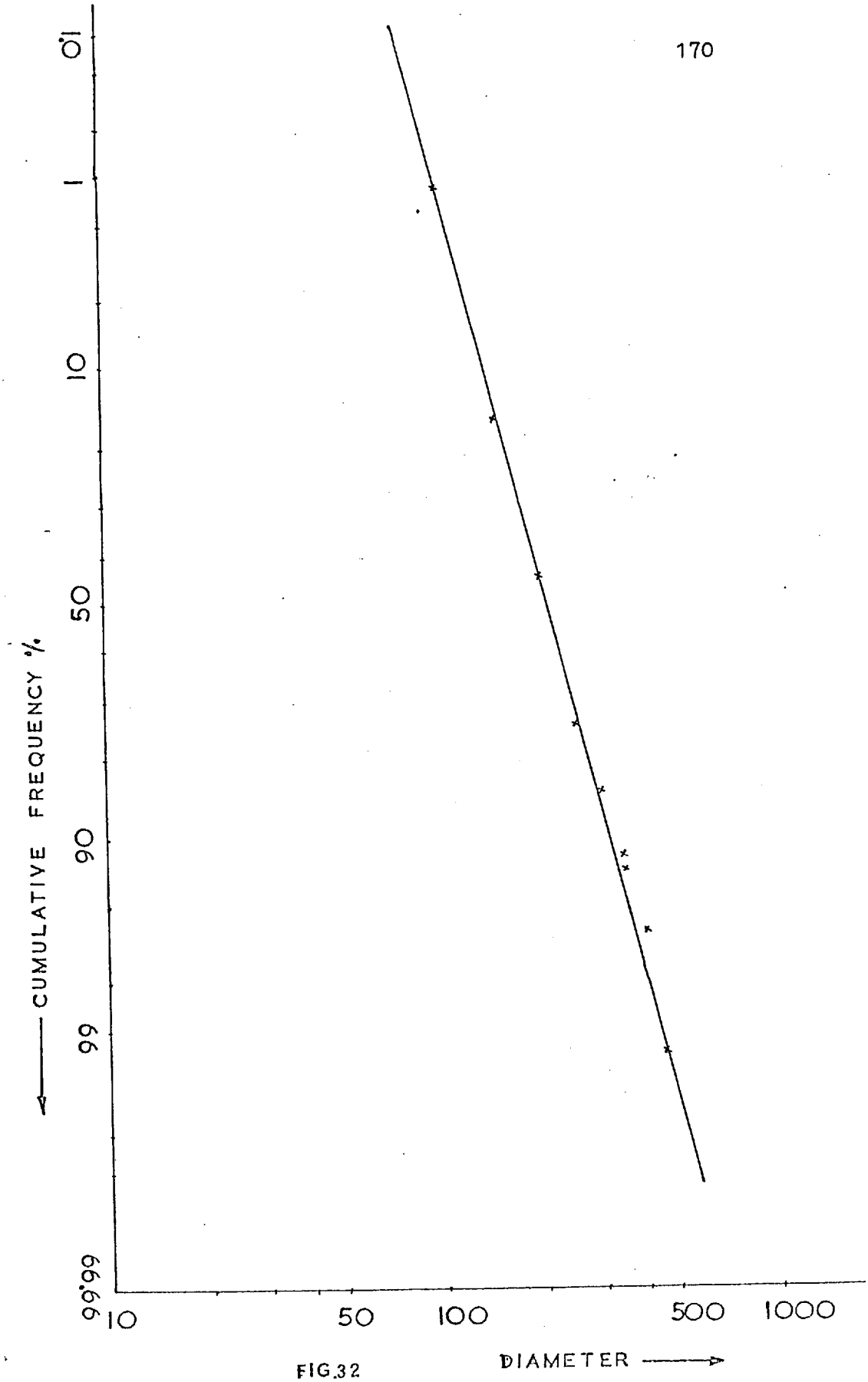

0·1
1
10
50
90
99
99·99
CUMULATIVE FREQUENCY %
10
50
100
500
1000
DIAMETER

FIG.32

9.6.2. Influence of iron concentration.

The carbide particles grow in size with increasing iron concentration at a fixed temperature and time. Fig.33 represents a plot of particle diameter D (in Å) vs. wt% of iron. Specimens with differing iron concentrations were prepared and heat treated in vacuum at 600°C for 2 hours. Electron diffraction patterns and electron micrographs were then taken from each specimen. The electron diffraction patterns gave diffraction rings identical to Fe_3C. From the electron micrographs the diameters of the particles were measured using a magnifying viewer with graticule. In each case an area from each micrograph was chosen at random for measurement and the mean diameter representative of the area was plotted in Fig.33 against iron concentration. A few representative electron micrographs are given in Figure 34.

9.6.3. Influence of residence time.

The carbide particles were observed to grow with increasing time at constant temperature until a maximum size was reached. Thus Figure 35 corresponds to specimens with iron content of 7.8 wt. percent (1.7 at %) heat treated in vacuo at 600°C. Later further investigations were made with specimens with lower iron concentrations 1.9 wt.percent (.41 at %) and at different heat treatment temperatures from 500°C to 900°C; the results are given in figure 36 which is seen to follow the same trend. It was observed that above

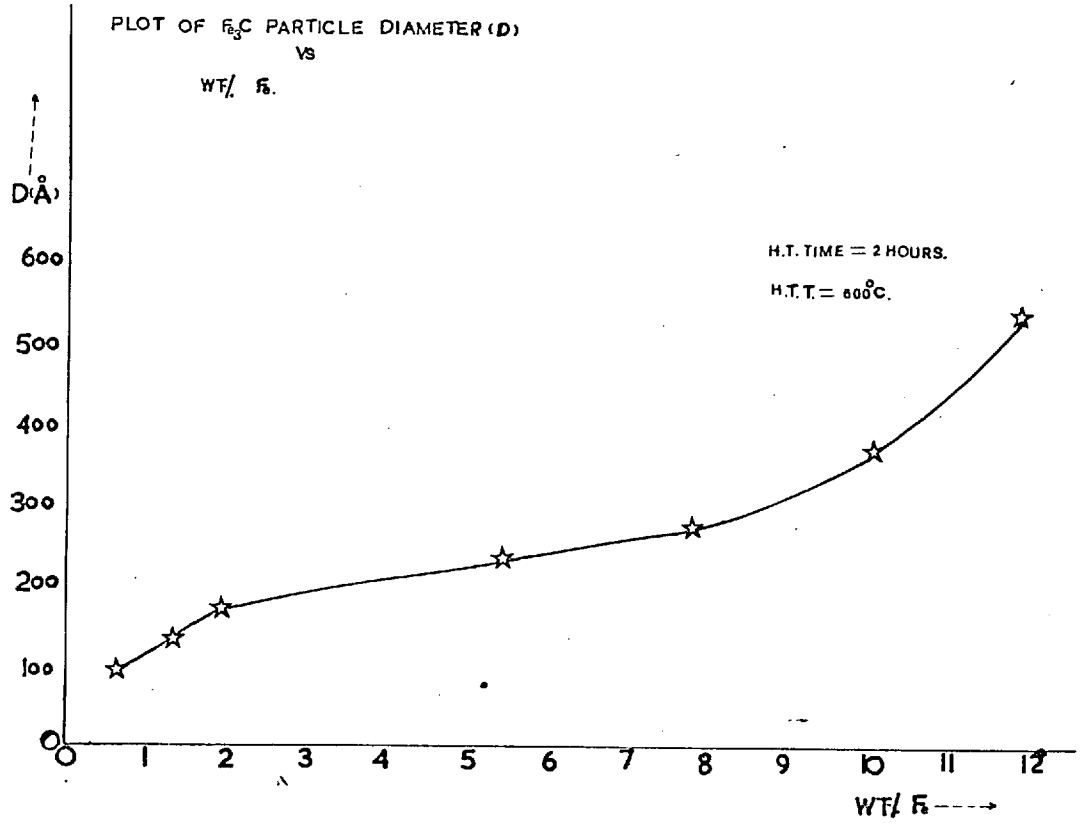
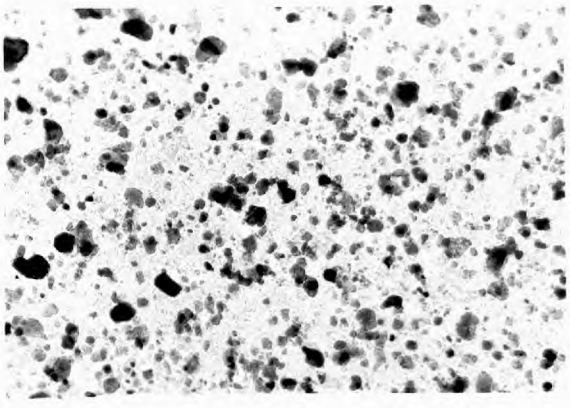

PLOT OF Fe_3C PARTICLE DIAMETER (D)
VS
WT/ Fe.
D(Å)
600
500
400
300
200
100
0
H.T. TIME = 2 HOURS.
H.T.T. = 600°C.
0
1
2
3
4
5
6
7
8
9
10
11
12
WT/ Fe

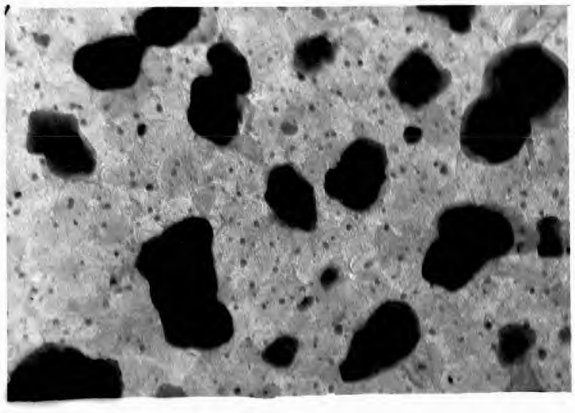
FIG. 33



·6 wt% Fe



7·8 wt% Fe



22·2 wt% Fe

FIG. 34 X40,000

850°C the carbide particles began to decrease in size and at 900°C all particles were found to disappear completely, leaving behind only carbon (as determined by electron diffraction). The temperature of decomposition was found however to rise for increasing iron concentrations. Fig.37 and Fig. 38 show representative micrographs corresponding to each plot above.

9.6.4. Effect of temperature.

The carbides grew with increasing temperature for a fixed heat treatment time until a maximum size was reached. At temperatures higher than this they disappeared. Plots in figs.39 and 40 represent the variation of particle size with temperature for iron concentrations of 1.9 and 11.9 wt. percent respectively. It was observed that the film with the lower iron concentration produced its highest particle size at 800°C (for a particular residence time) whereas for the film with the higher iron concentration this occured at 900°C (for the same heat treatment time). All the carbide particles in the case of the specimen with 11.9 wt. percent of iron disappeared in two hours at 1000°C whereas some particles were still present when heat treated for only 30 minutes at this temperature. (see Fig.41). For the specimen with 1.9 wt. percent of iron a temperature of 900°C was sufficient to cause complete decomposition of the particles within 30 minutes. Fig. 42 gives an electron diffraction pattern and a micrograph from a specimen heated

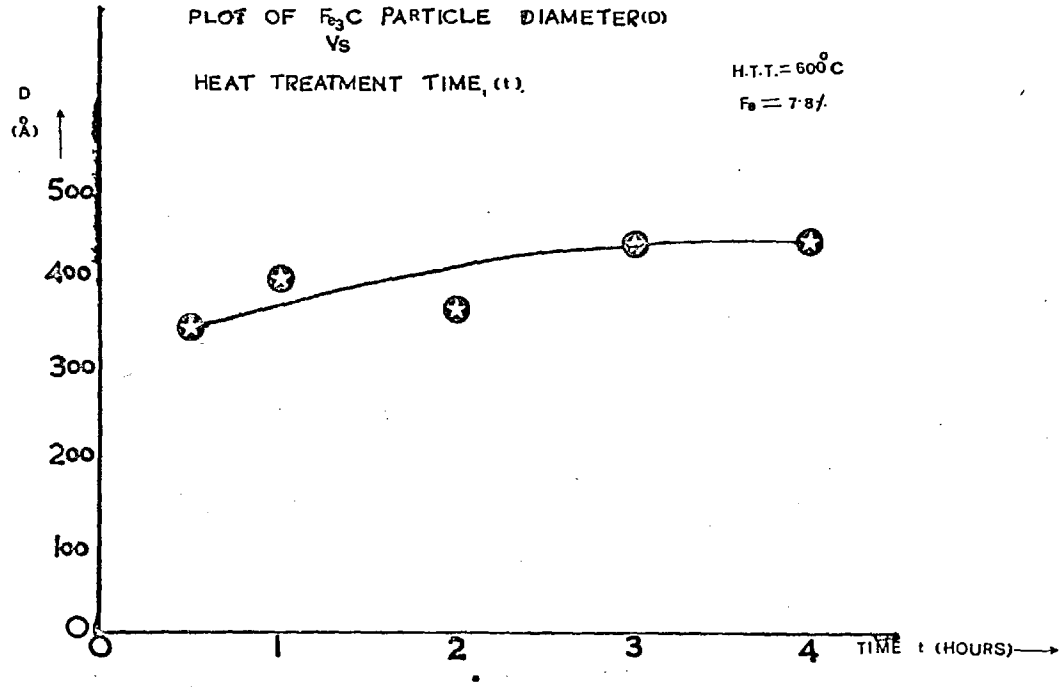

PLOT OF Fe_3C PARTICLE DIAMETER(D)
Vs
HEAT TREATMENT TIME, (t).
H.T.T.= 600°C
Fe = 7·8%
D
(Å)
500
400
300
200
100
0
0
1
2
3
4
TIME t (HOURS)

FIG .35

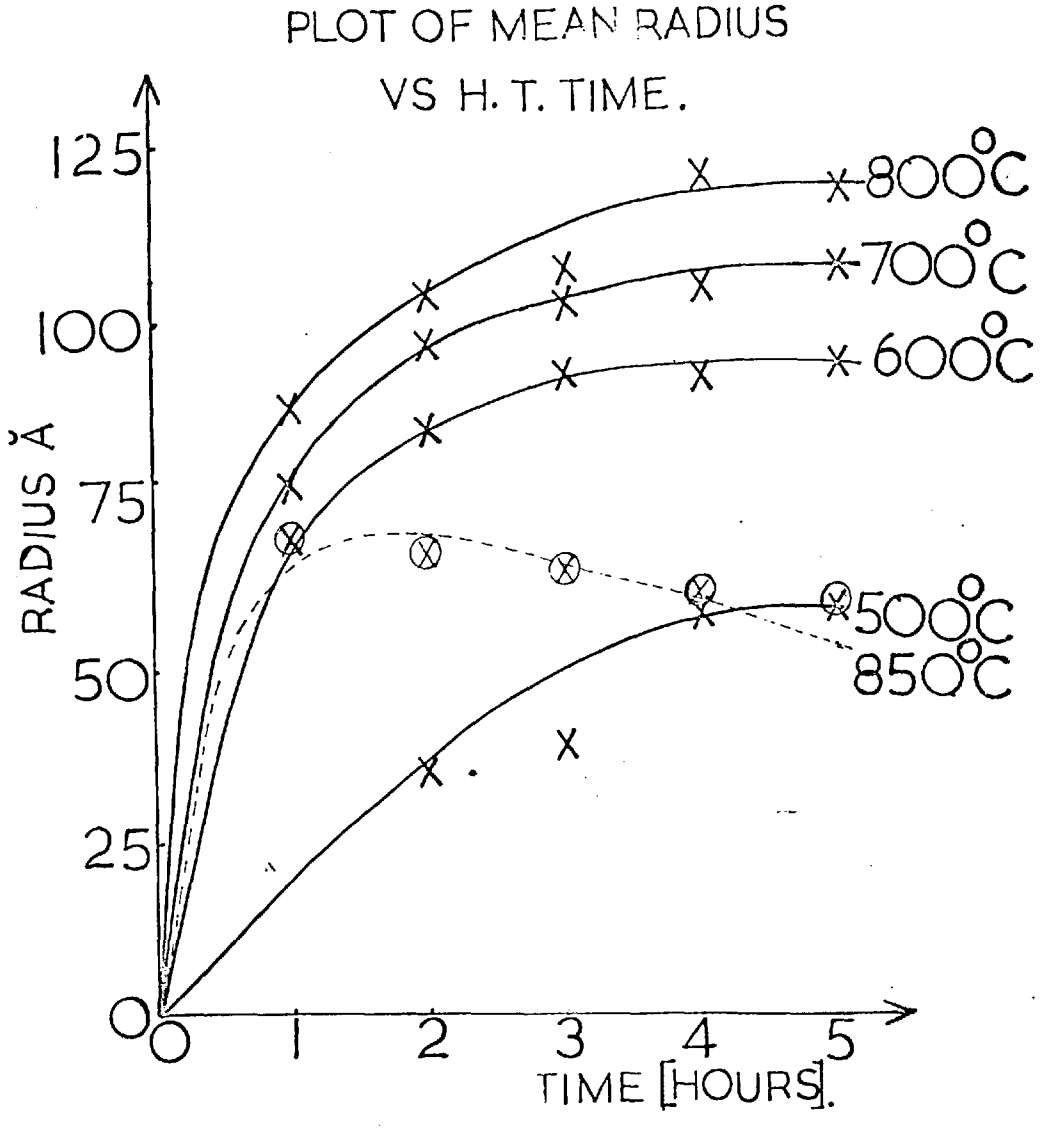

PLOT OF MEAN RADIUS
VS H. T. TIME.
125
100
75
50
25
0
RADIUS Å
0
1
2
3
4
5
TIME [HOURS].
800°C
700°C
600°C
500°C
850°C

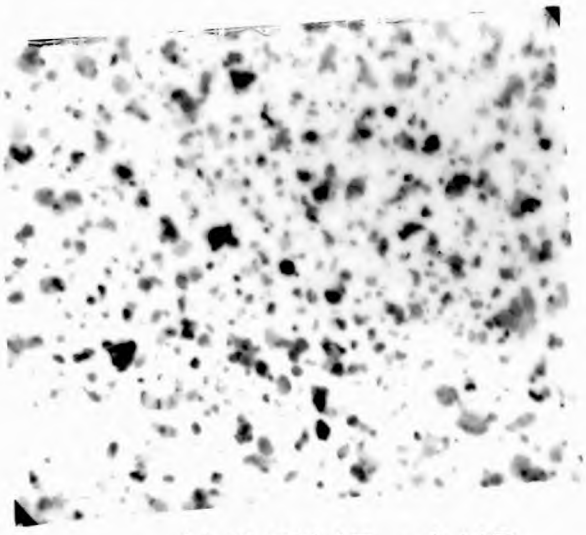
FIG. 36

for 30 minutes at 900°C; the former corresponds to graphitic carbon only, while the latter shows that the precipitate has completely disappeared.

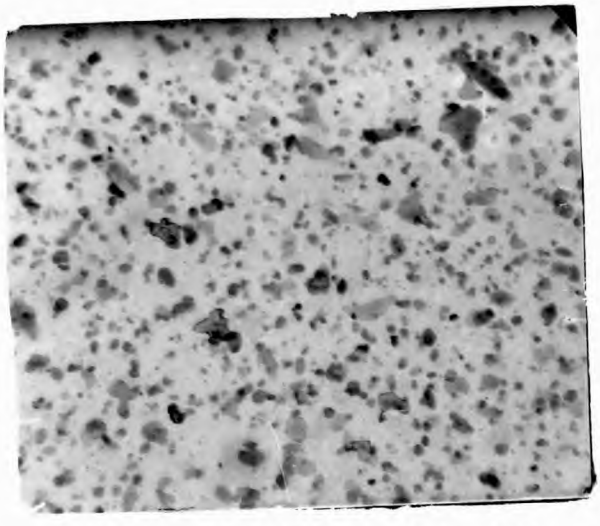
The higher is the concentration of iron in the film, the lower is the temperature needed to produce the carbide. Specimens with very low iron content did not show carbide precipitation at 400°C. Thus a specimen with 11.9 wt. per cent of iron (2.8 at %) heat treated at 400°C for two hours gave an electron diffraction pattern (Fig.43A) of Fe_3C while the electron diffraction pattern (Fig.43B) from a specimen with .6 wt% iron (.13 at %) subjected to the same conditions of temperature and time, shows the broad halos characteristic of amorphous carbon. The micrograph in Fig.43C, corresponding to the specimen of fig.43A indicates however that the particle boundaries have not yet been developed fully to facilitate their measurements.

9.6.5. Number density per unit area with respect to residence time and temperature.

A plot of number density vs. heat treatment time at different temperatures is shown in fig. 44. The curve reveals that initially the number density rises rapidly and then gradually decreases with time until a levelling off occurs; this behaviour is typical of nucleation followed by coarsening. The next plot of number density vs. heat treatment temperature for a treatment time of 5 hours, shows

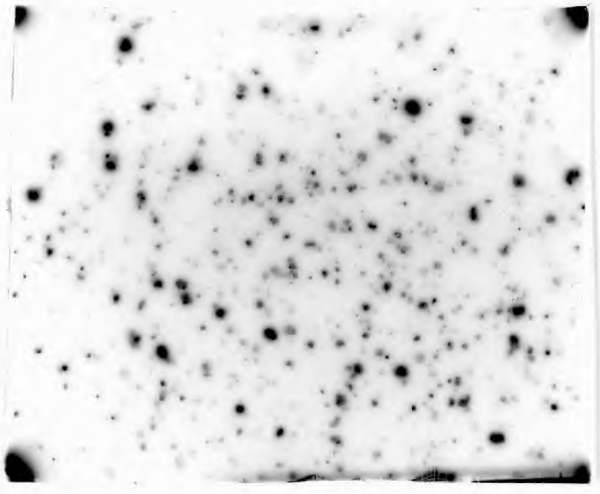


H. T. TIME = 1 HR.

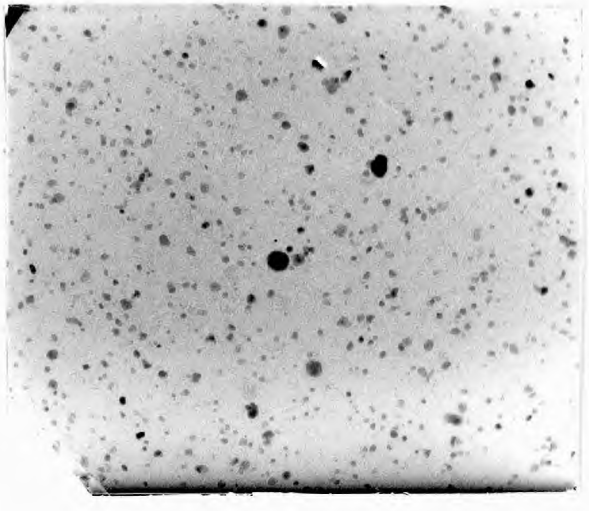


H. T. TIME = 4 HRS.

FIG. 37. X40,000



H. T. Time 2 hours



H. T. Time 5 hours

Fig. 38. H. T. T. 800° C

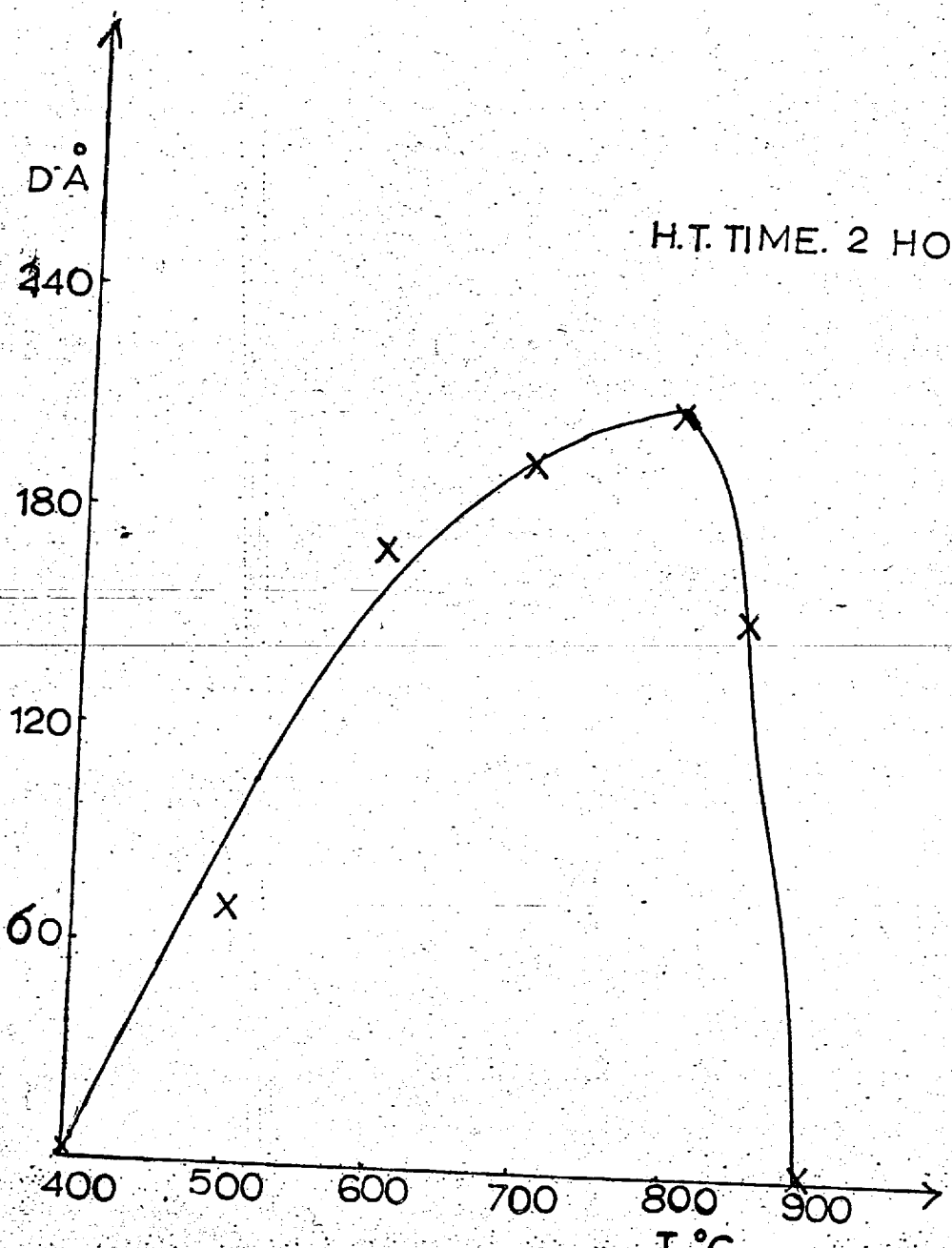


FIG. 39.

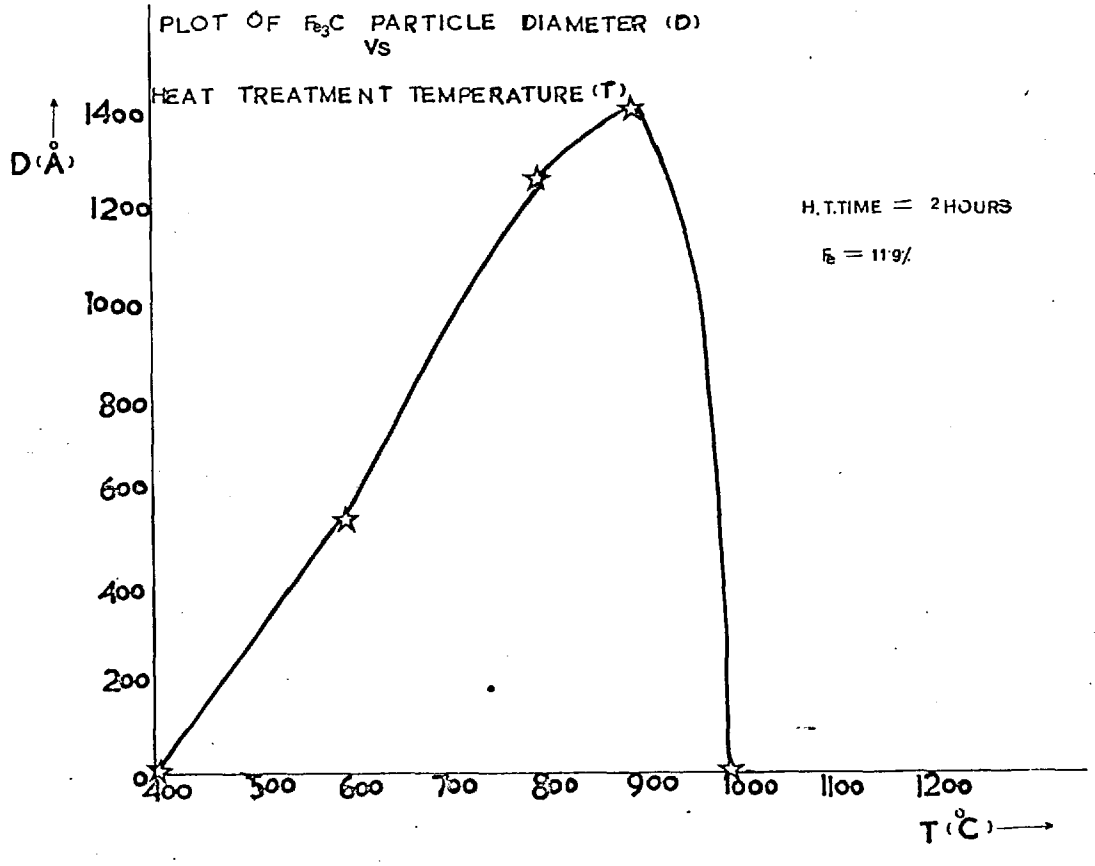

PLOT OF Fe_3C PARTICLE DIAMETER (D)
Vs
HEAT TREATMENT TEMPERATURE (T)
D (Å)
1400
1200
1000
800
600
400
200
0
400
500
600
700
800
900
1000
1100
1200
T (°C)
H.T.TIME = 2 HOURS
Fe = 11·9%

FIG.40



FIG. 41 X 80,000



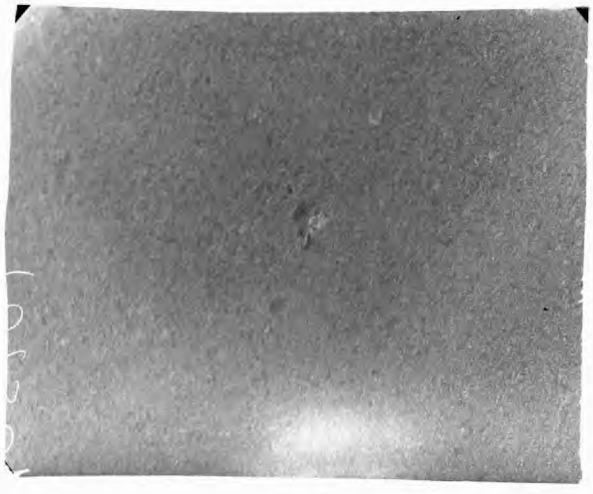
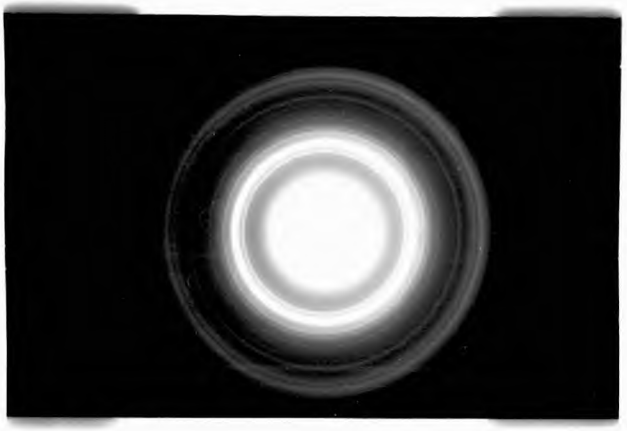
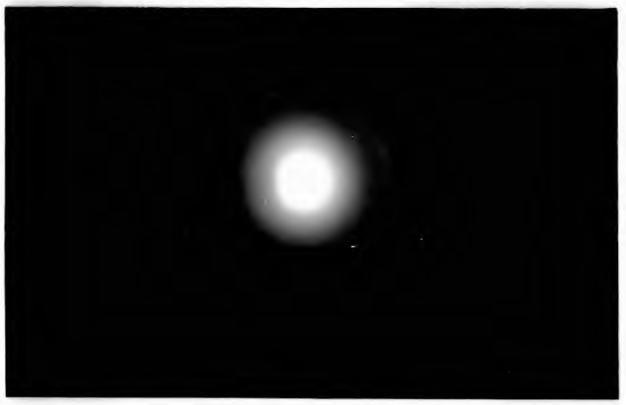


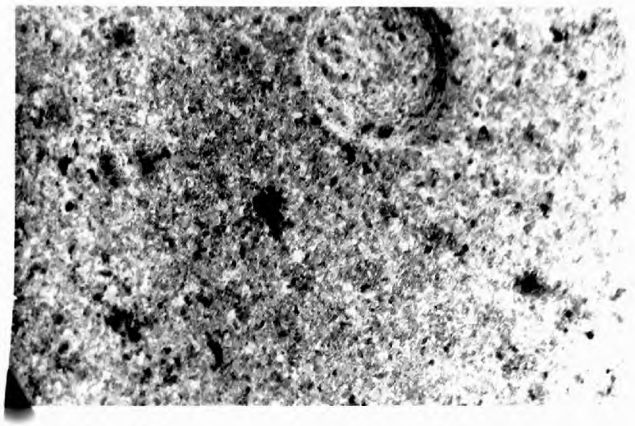
FIG. 42 X40,000



A



B



C

FIG. 43 X 40,000

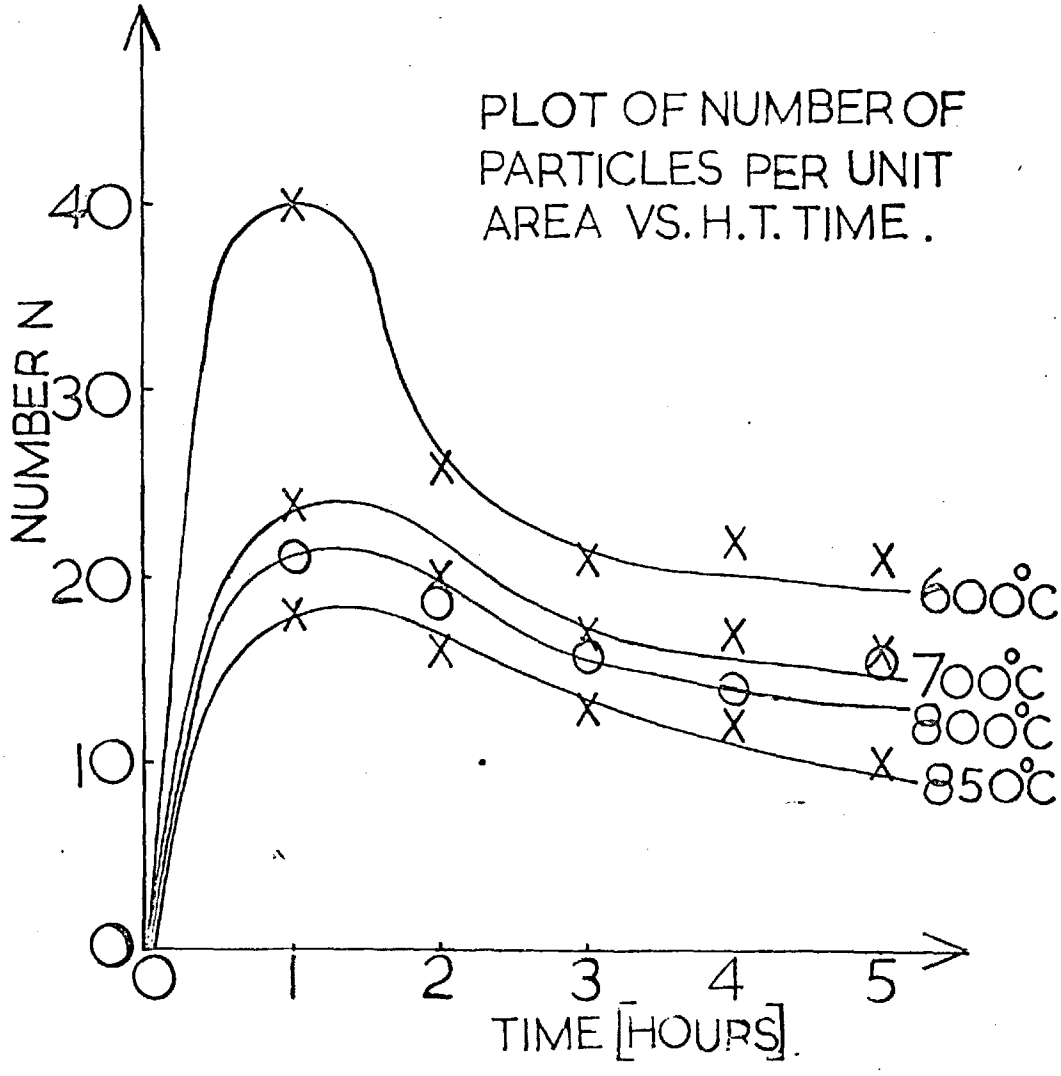

PLOT OF NUMBER OF PARTICLES PER UNIT AREA VS. H.T. TIME.
NUMBER N
40
30
20
10
0
0
1
2
3
4
5
TIME [HOURS].
600°C
700°C
800°C
850°C

FIG.44

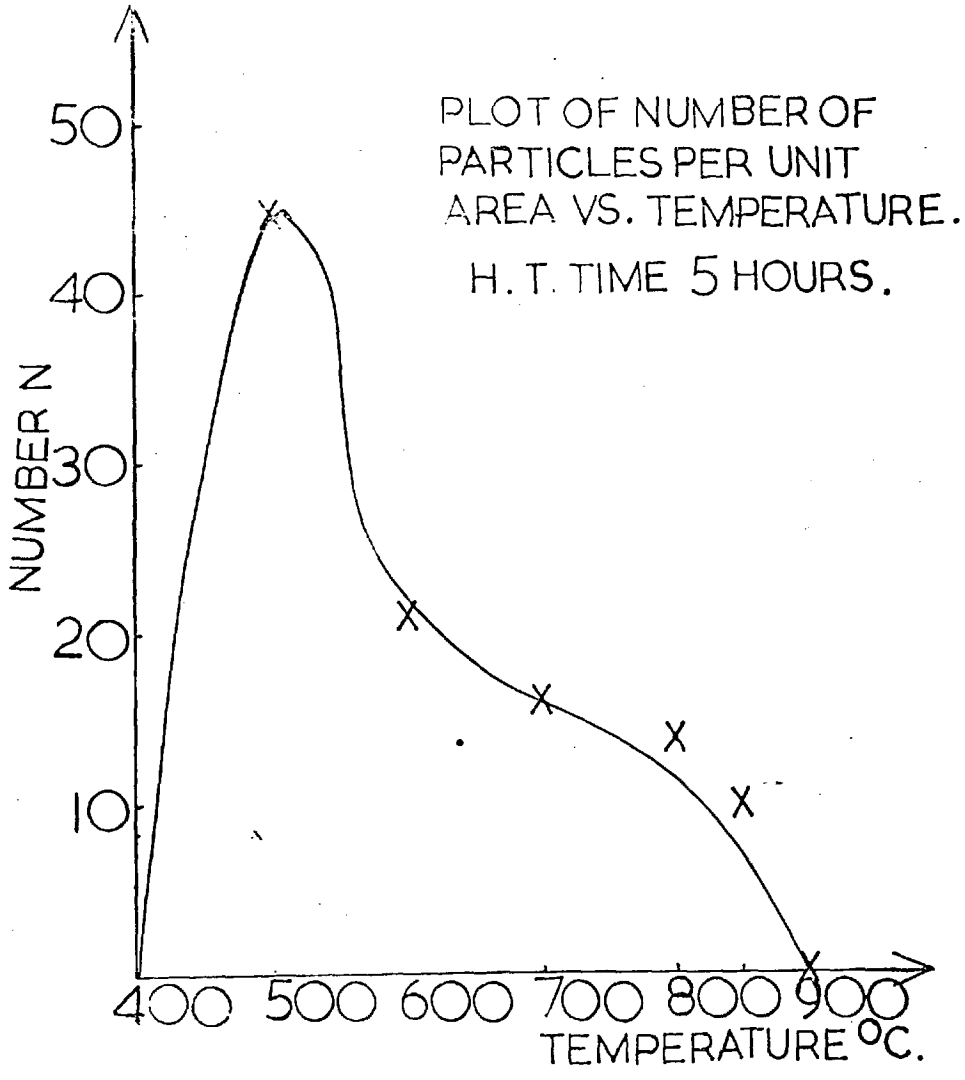

PLOT OF NUMBER OF
PARTICLES PER UNIT
AREA VS. TEMPERATURE.
H. T. TIME 5 HOURS.
NUMBER N
50
40
30
20
10
400
500
600
700
800
900
TEMPERATURE °C.

FIG. 44A

that the number of particles decreased rapidly with increasing temperature and became zero at the decomposition temperature (Fig.44 A).

9.7. Diffusion of iron through carbon.

At this stage attention was turned to a study of the diffusion of iron through carbon since it was felt that data was available which would permit an approximate calculation of the diffusion coefficient and possibly the activation energy for diffusion; neither of these quantities could be found in the literature.

9.7.1. Calculation of D using Einstein's equation.

If the assumption is made that diffusion in a thin film takes place mainly in the plane of the film, Einstein's equation can be used to obtain an approximate value of the diffusion coefficient D. Einstein's equation states that for an atom starting from the origin at a time t = 0 and moving in a plane by a random walk process the mean square distance $\overline{x^2}$ reached after time t is given by,

$$\overline{x^2} = Dt \qquad \text{.....(64)}$$

where D is a constant known as the diffusion coefficient. If in fig. 45, A and B represent two cementite particles separated by a distance 2s, then we can assume that all the iron in solution to the left of the imaginary line PP' diffuses to A while all to

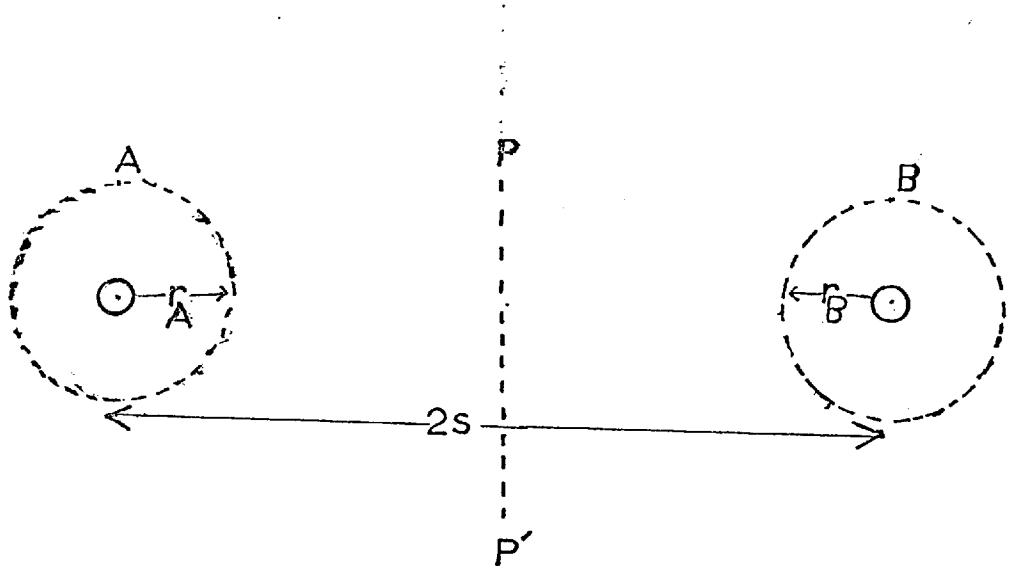


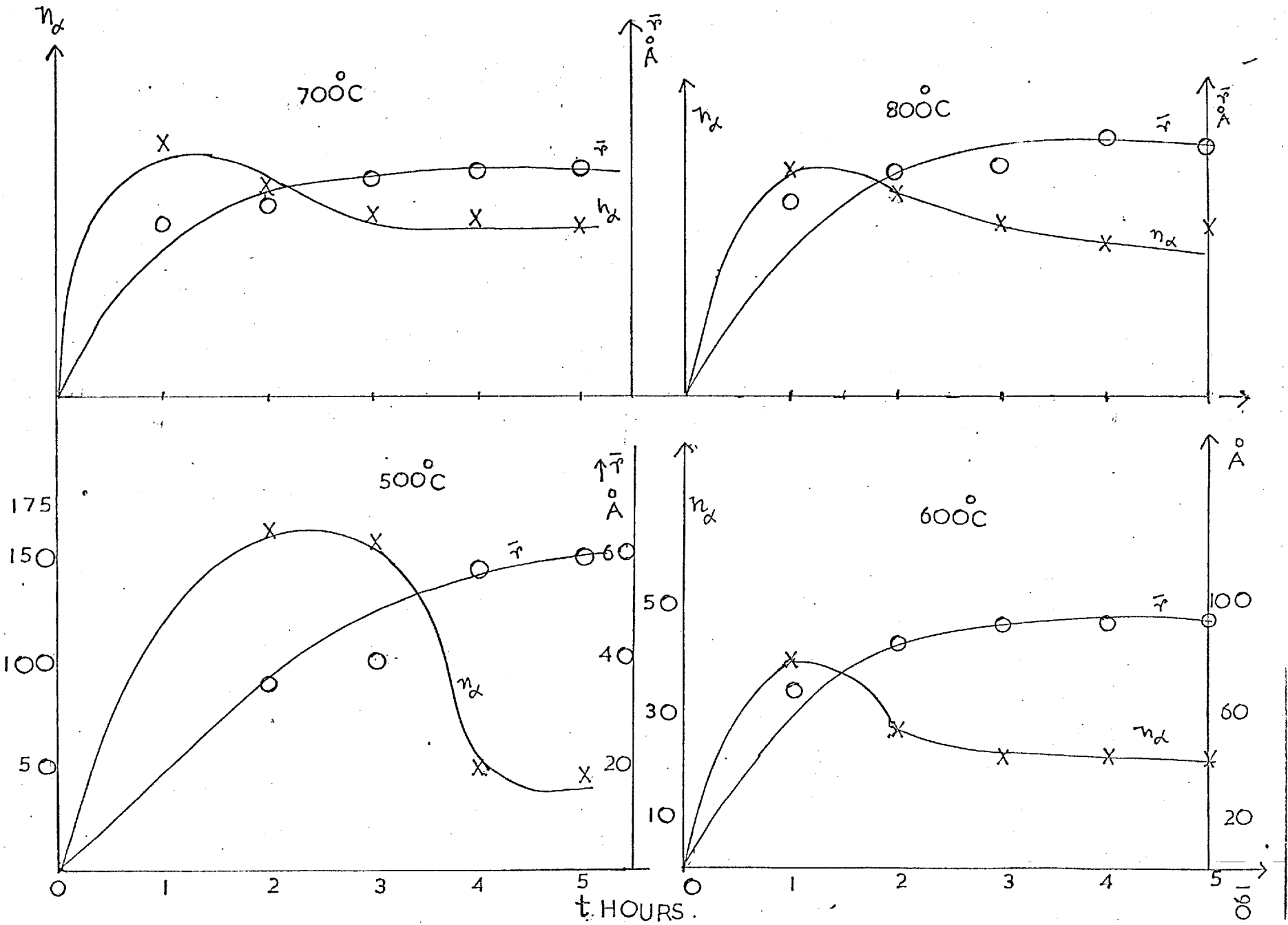
FIG. 45

the right diffuses to B. If the figure represents the final sizes of A and B when all the iron has been precipitated from solution then we can say that an iron atom at O must traverse the distance between O and the surface of the particle A in time t by a random walk process. This distance is $s - r_A$, where r_A is the radius of A. Putting this value into equation (64) and replacing r_A by the mean particles radius $\bar{r}$ we have that,

$$(s - \bar{r})^2 \sim Dt.$$

The application of this equation is made more difficult by the fact that the mean radius $\bar{r}$ is continually being changed by coarsening of the precipitates, i.e. by the fact that the smallest particles lose iron by diffusion to the largest. This effect is shown in fig.46 which demonstrates that the number of particles per unit area n_α initially increases with time to a maximum and then decreases, finally showing a tendency to level off. The dotted line indicates the expected behaviour of n_α if coarsening did not occur.(FIG.48)

In order to apply Einstein's equation therefore, a value of s was taken corresponding to the peak value of n_α using the fact that $2s \simeq \sqrt{\frac{1}{n_\alpha}}$. The appropriate time was taken to be that at which n_α reached its peak and the corresponding value of $\bar{r}$ was read off from the equivalent plots of $\bar{r}$ vs. t.


η_α
$\bar{r}$ Å
700°C
800°C
500°C
600°C
175
150
100
50
60
40
20
30
10
0 1 2 3 4 5
t. HOURS.

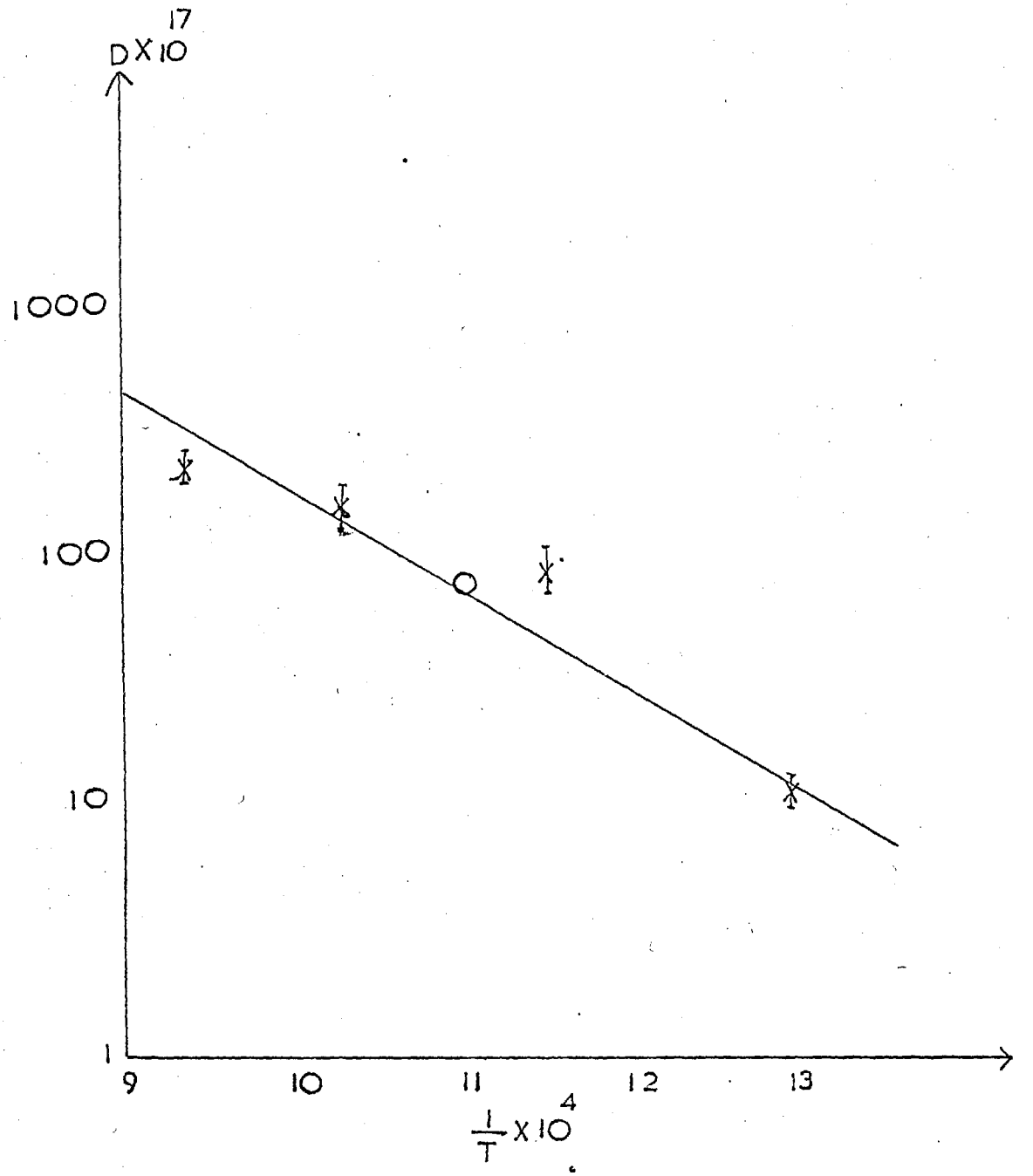


FIG. 47 B.

In this way the diffusion coefficient D was calculated at 500°C, 600°C, 700°C and 800°C and the data are presented in Table 5.

Table 5

Temperature °C	n_α = Number / area of image	s cm.	$\bar{r}$ cm.	t hour	D cm^2/sec.
500	160	9.0×10^{-7}	3.5×10^{-7}	2	4.2×10^{-17}
600	40	19.0×10^{-7}	6.9×10^{-7}	1	40×10^{-17}
700	24	25.0×10^{-7}	7.6×10^{-7}	1	84×10^{-17}
800	21	27.0×10^{-7}	8.7×10^{-7}	1	93×10^{-17}

since D is a function of temperature through the Boltzmann relation we can write,

$$D = Do\, e^{-\frac{U}{KT}}$$

Fig. 47A shows an Arrhenius plot of $\log_{10} D$ vs $\frac{1}{T}$. It can be seen that the points lie on a smooth curve which is not a straight line but which turns over towards the $\frac{1}{T}$ axis at higher temperatures. Before concluding that the diffusion process in the range of temperature between 500-800°C is not governed by a single activation energy however, it was thought desirable to try to make some allowance for the errors involved.

Considering the n_α vs. t plots it is reasonable to expect that the peak of the plot should move towards the origin for increasing temperatures. On examination of these

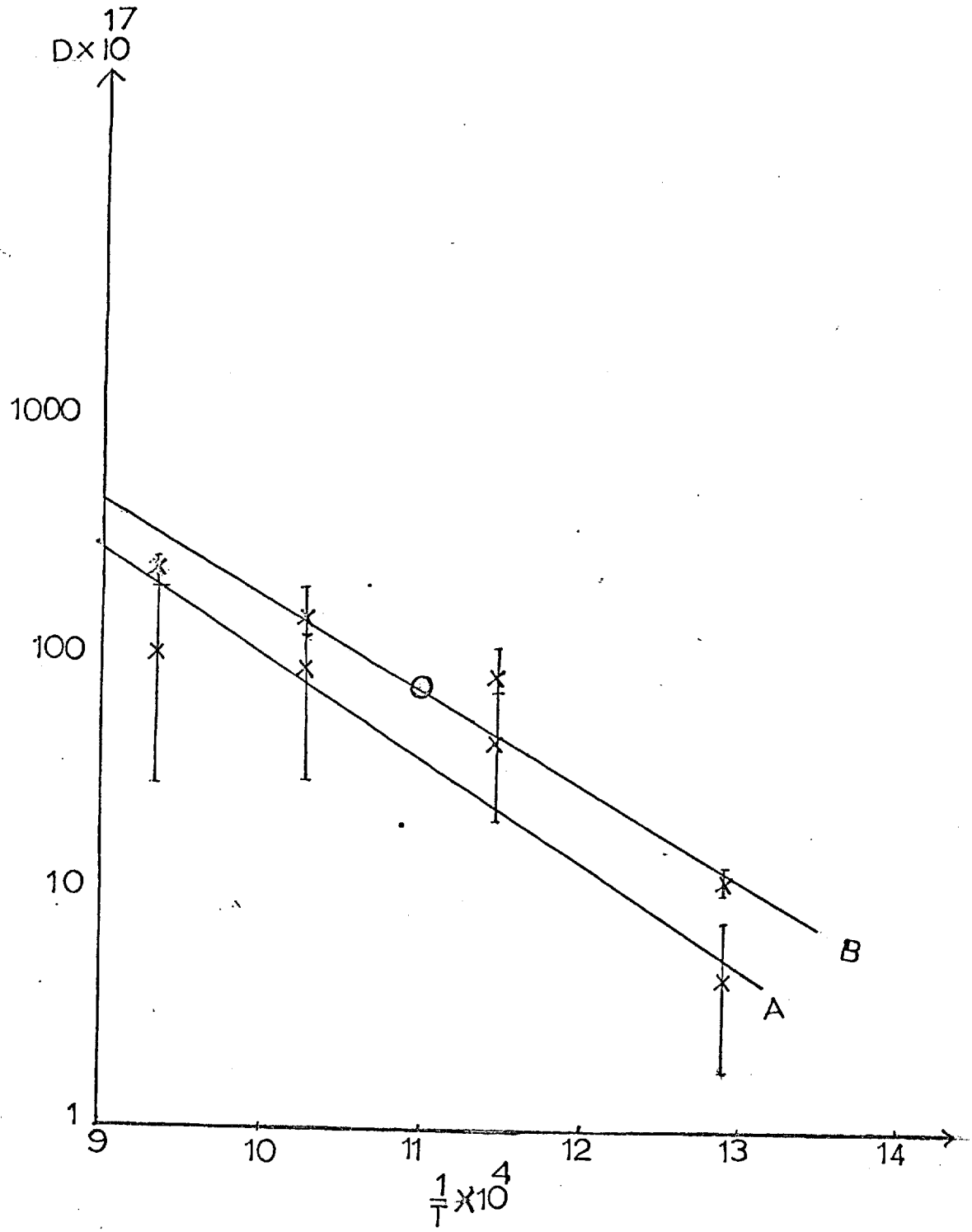


FIG.47

plots however, it is clear that the heating times used were too widely spaced to permit an accurate assessment of the time corresponding to maximum n_{α}, especially at higher temperatures. In order to make allowance for this the following procedure was adopted. Since the heating times used were increased in units of one hour it was (somewhat arbitrarily) assumed that t_{max} lay within a half hour on either side of the apparent value of t_{max}. At the same time upper limits to the equivalent value of n_{α} were obtained by joining the apparent peak to the neighbouring experimental value on either side as shown in the figure (48). Corresponding values of $\bar{r}$ were also obtained from the figure. When these extreme values of n_{α}, t and $\bar{r}$ were put into equation (64), upper and lower limits could be assigned to the calculated values of D at each temperature, and fig. (47A) shows the magnitude of these limits. When this was done the best straight line through the best values of D also lay within the extreme values as shown in the figure.

The activation energy calculated from the Arrhenius plot was found to be equal to .85ev or 19.5 k.cal per mole.

9.7.2. Diffusion coefficient and activation energy from Werts[92] transformation equation.

An attempt was made to fit the experimental data to a transformation equation used by Wert to study the

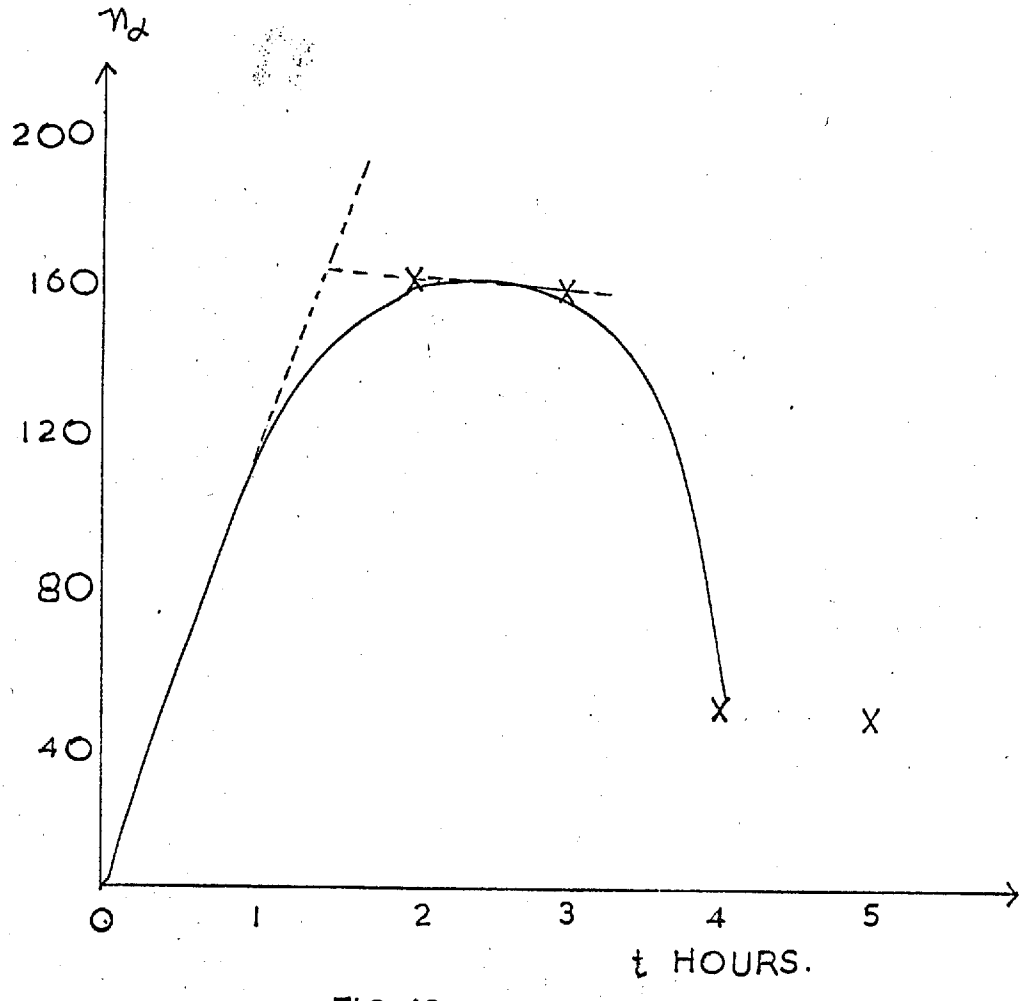


FIG.48.

formation of carbide and nitride precipitates from solid solutions of carbon and nitrogen in α-iron. The form of the equation employed by Wert was,

$$\frac{\Delta c(t)}{C_o} = 1 - \exp\left[- \left(\frac{t}{\tau}\right)^{n} \right] \quad \ldots\ldots\ldots\ldots (65)$$

where $\Delta c(t)$ is described by Wert as the amount of transformed material in time t, C_o is the initial concentration of solute atoms, τ is a time constant depending on C_o and temperature and n is some number independent of T and C_o.

Suppose, at time t that 'a_1' iron atoms (per unit volume of film) have transformed into Fe_3C.

Let there be γ atoms of Fe per unit volume of Fe_3C.

Then, if volume of precipitate particles is v this will contain γv atoms of iron = a_1 (Provided that we are still considering unit volume of film.

i.e. volume fraction of precipitate, $f_v = v$

Hence, $a_1 = \gamma f_v$

Thus, $\Delta c(t) = a_1 = \gamma f_v$.

The unit cell of Fe_3C contains 12 atoms of iron and has a volume abc where a, b and c are the cell dimensions. Hence,

$$\gamma = \frac{12}{abc}$$

Now, C_o = initial concentration of Fe atoms

= number of iron atoms per unit volume of film.

$$= \frac{\text{mass of iron per unit volume}}{\text{mass of one iron atom.}}$$

$$= \frac{w_o \rho_o}{A_{Fe} M_H} ,$$

where, w = Wt. fraction of iron

ρ_o = density of as-deposited film.

A_{Fe} = Atomic wt. of iron.

and M_H = Mass of a hydrogen atom.

Hence $$c_o = \frac{W_o \rho_o}{100\, A_{Fe} M_H} \quad \ldots\ldots\ldots (66)$$

where W = weight percentage of iron in film.

So we can write the L.H.S. of equation (65) as follows:

$$\frac{\Delta c(t)}{Co} = \frac{12fv.}{abc} \frac{100\, M_{Fe}}{W_{Fe}\ o\rho_o} = \frac{12fv}{abc} \frac{100\, A_{Fe}\, M_H}{W_{Fe}\ o\rho}$$

$$= \frac{12\, A_{Fe}\, M_H}{abc} \cdot \frac{100}{W_{Fe}\ o\rho_o} \cdot fv.$$

$$= \frac{\rho_t}{\rho} \frac{1}{w_{Fe}} fv. \quad \ldots\ldots\ldots (67)$$

where, ρ_t = density of transformed iron = $\frac{12\, A_{Fe} M_H}{abc}$

gms/cm^3 .

ρ_o = density of as-deposited film in gms/cm^3.

w_{Fe} = Weight fraction of iron in film = $\frac{W_{Fe}}{100}$

where W_{Fe} is weight percentage of iron in film.

fv = volume fraction of precipitates.

when transformation is complete,

$$\frac{\Delta c(t)}{C_o} = 1$$

i.e. $$f_{v\,max} = \frac{\rho_o}{\rho_t} w_{Fe} \quad \text{.....(67A)}$$

9.7.2.1. Calculation of density ρ_o of the as-deposited film.

The density of the as-deposited composite film can be calculated from the expressions developed and shown below. Consider n_c atoms of carbon with atomic volume σ_c and mass M_c and n_{Fe} atoms of iron with atomic volume σ_{Fe} and Mass M_{Fe}

Adding, $n_c + n_{Fe} = N$ .....(68) (total no. of atoms).

$n_c M_c + n_{Fe} M_{Fe} = M$ .....(69) (total mass)

$n_c \sigma_c + n_{Fe} \sigma_{Fe} = V$ .....(70) (total volume, assuming no change of volume on mixing)

Final density $\rho_o = \frac{M}{V}$ .....(71)

We know that,

$$\frac{n_{Fe} M_{Fe}}{n_{Fe} M_{Fe} + n_c M_c} = w \quad \text{.....(72)}$$

Also we know that the density of amorphous carbon is ρ_c i.e. unit volume of amorphous carbon contains $\frac{\rho_c}{M_c}$ atoms = n_c (say).

$\therefore \quad n'_c \sigma_c = 1$

$$\therefore \quad \sigma_c = \frac{1}{n'_c} = \frac{M_c}{\rho_c} \qquad \ldots\ldots\ldots\ldots(73)$$

Similarly, $$\sigma_{Fe} = \frac{M_{Fe}}{\rho_{Fe}} \qquad \ldots\ldots\ldots(74)$$

Hence from (70)

$$\frac{n_c M_c}{\rho_c} + \frac{n_{Fe} M_{Fe}}{\rho_{Fe}} = V \qquad \ldots\ldots\ldots\ldots(75)$$

From (72)

$$w = \frac{1}{1 + \frac{n_c M_c}{n_{Fe} M_{Fe}}} = \frac{1}{1 + \nu/u} \qquad \ldots\ldots(76)$$

where, $\nu = \frac{n_c}{n_{Fe}}$, $u = \frac{M_c}{M_{Fe}}$

Writing (75) as

$$\frac{n_{Fe} M_{Fe}}{\rho_{Fe}} \left(1 + \frac{n_c M_c}{\rho_c} \cdot \frac{\rho_{Fe}}{n_{Fe} M_{Fe}} \right) = V$$

i.e. $$\frac{n_{Fe} M_{Fe}}{\rho_{Fe}} \left(1 + \nu u \frac{\rho_{Fe}}{\rho_c} \right) = V \qquad \ldots\ldots\ldots(77)$$

Also from (69)

$$n_{Fe} M_{Fe} \left(1 + \frac{n_c M_c}{n_{Fe} M_{Fe}} \right) = M$$

i.e. $$n_{Fe} M_{Fe} \left(1 + \nu/u \right) = M \qquad \ldots\ldots\ldots(78)$$

Substituting for $n_{Fe}M_{Fe}$ in (77) we get,

$$\frac{M}{1+\delta\mu}\cdot\frac{1}{\rho_{Fe}}\cdot\left(1+\delta\mu\frac{\rho_{Fe}}{\rho_c}\right)=V$$

or $$\frac{M}{V}\cdot\frac{1}{1+\delta\mu}\cdot\frac{1}{\rho_{Fe}}\left(1+\delta\mu\frac{\rho_{Fe}}{\rho_c}\right)=1$$

Hence, $$\rho_o=\frac{\rho_{Fe}\ (1+\delta\mu)}{1+\delta\mu\frac{\rho_{Fe}}{\rho_c}}$$

But from (76) $$1+\delta\mu=\frac{1}{w}$$

and $$\delta\mu=\frac{1}{w}-1$$

Hence,

$$\rho_o=\frac{\rho_{Fe}\ \frac{1}{w}}{1+\frac{\rho_{Fe}}{\rho_c}\left(\frac{1}{w}-1\right)}$$

or, $$1+\frac{\rho_{Fe}}{\rho_c}\left(\frac{1}{w}-1\right)=\frac{\rho_{Fe}}{\rho_c}\cdot\left(\frac{1}{w}\right)$$

$$\therefore\quad w+\frac{\rho_{Fe}}{\rho_c}(1-w)=\frac{\rho_{Fe}}{\rho_o}$$

$$\therefore\quad w+\frac{\rho_{Fe}}{\rho_c}-\frac{\rho_{Fe}}{\rho_c}\cdot w=\frac{\rho_{Fe}}{\rho_o}$$

$$\therefore\ \frac{\rho_{Fe}}{\rho_c}+w\left(1-\frac{\rho_{Fe}}{\rho_c}\right)=\frac{\rho_{Fe}}{\rho_o}$$

$$\text{or } \rho \frac{1}{\rho_c} + w\left(\frac{1}{\rho_{Fe}} - \frac{1}{\rho_c}\right) = \frac{1}{\rho_o} \quad \ldots\ldots\ldots(79)$$

$$\text{or } \Phi_c + w\left(\Phi_{Fe} - \Phi_c\right) = \Phi_o \quad \ldots\ldots\ldots(80)$$

where the Φ's are specific volumes (i.e. $\frac{1}{\rho}$) and w is the fractional weight of iron in the film ($= \frac{wt\%}{100}$).

Hence from equation (79) above the density of the composite film can be obtained by substituting the known values of the densities of carbon and iron. Putting $\rho_c = 2.4^{153}$ and $\rho_{Fe} = 7.8$ gms. per c.c., the value of ρ_o was found to be equal to 2.5 gms/c.c. for a film of composition 1.9 wt.% Fe.

9.7.2.2. Calculation of fractional volume from direct measurements.

The measurement of fractional volume fv, for precipitate particles in a thin film introduces considerable difficulty, since only the projected image is available. Initially, this was dealt with by supposing the particles to be spherical. The fractional volume was then calculated from the following simple considerations.

Let average particle radius = $\bar{r}$.

Film thickness = h

Number per unit projected area = n_α

Number per unit volume = n_v

Then volume fraction $f_v = n_v \frac{4}{3} \pi \bar{r}^3$.

The number in area A is An_α and the volume is Ah so that

the number per unit volume $= \frac{n_\alpha A}{Ah} = \frac{n_\alpha}{h} = n_v$.

Hence, volume fraction, $f_v = \frac{n_\alpha}{h} \cdot \frac{4}{3} \pi \bar{r}^3$ .....(81)

Now after making proper allowance for the magnification of the image and replacing $\bar{r}$ by $\frac{\bar{d}}{2}$ equation (81) can be written as,

$$fv = \frac{5\pi}{12} \cdot \frac{n_\alpha \bar{d}^3}{h} \quad \text{.....(82)}$$

where n_α is number/cm^2

$\bar{r}$ in mm. $= \bar{r} \times 10^{-1}$cm $= \bar{r} \times 10^{-1}/M$ cms.

where M is the magnification factor of the print of the plate from which $\bar{d} = 2\bar{r}$ is measured and h is thickness in angstroms.

9.7.2.3. Calculation of fv (fractional volume) of Fe_3C from surface area measurements.

The 'Quantimet' described in the experimental section provides a measurement of the total projected area of the particles. The instrument gives directly the percentage area covered by the particles (A_p in equation (84)) observations were made for at least ten different areas of the micrograph and the mean of these was taken as the projected area of the Fe_3C precipitate particles. From this the value

of fv can be obtained, using an expression developed below:

Let number of particles per unit volume of the film = n_v

volume of the film = 1 x 1 x h, where h is thickness.

Number in this volume = $n_v l^2 h$.

$\therefore$ number per unit area in image = $n_v h = n_\alpha$ (say) ...(83)

Let mean radius of the particles = $\bar{r}$

$\therefore$ Total projected area/ per unit area $= n_\alpha \pi \bar{r}^2 = \alpha_P$ .....(84)

But total surface area per unit volume = $n_v 4\pi \bar{r}^2$

$= \alpha_s$ .....(85)

Hence, $\alpha_s = 4\pi \frac{n_\alpha}{h} \cdot \bar{r}^2$ from (83)

and,

$$\bar{r}^2 = \frac{\alpha_P}{\pi n_\alpha}$$

$$\therefore \alpha_s = 4\pi \frac{n_\alpha}{h} \cdot \frac{\alpha_P}{\pi n_\alpha} = \frac{4\alpha_P}{h} \quad \text{.....(86)}$$

But, fv $= \frac{V_P}{V}$ = fractional volume of Fe_3C precipitate

$$= n_v \cdot \frac{4}{3} \pi \bar{r}^3$$

$$= \frac{n_\alpha}{h} \cdot \frac{4}{3} \pi \left[\frac{\alpha_P}{\pi n_\alpha} \right]^{3/2}$$

$$= \frac{4}{3h} \pi^{-\frac{1}{2}} n_\alpha^{-\frac{1}{2}} \alpha_P^{3/2}$$

$$= \frac{4}{3h} \left\{ \frac{\alpha_P}{\pi n_\alpha} \right\}^{\frac{3}{2}} \quad \text{.....(87)}$$

Employing equation (87) fv can be calculated. The quantity

n_A in the above equation was obtained by actual counting of the particles in a micrograph. The 'Quantimet' was also employed for this purpose, but it provided erratic results because the particles were not perfectly spherical (this is an essential requisite of the 'Quantimet' for correct operation). The film thickness h was estimated during film fabrication by the method of colour variation described earlier.

The mean radii of the particles calculated from projected area measurements were compared with those measured by the direct method; they are shown in figure 49. The radii obtained from the projected area measurements were found to be less than those from direct measurements. This inconsistency is believed to be due to the lack of sufficiently high contrast in the images of the precipitate particles. The carbide particles in the micrographs showed varying optical densities, some being light and some very dark. It is possible that the Quantimet did not take into consideration the area covered by the lighter particles, thus accounting for the reduced averaged particle size obtained by this method.

9.7.2.4. Calculation of f_v by direct measurement after introducing a reducing factor.

Using equation (82) f_v values were calculated for specimens with iron concentration of 1.9 wt. percent (.41 at %)

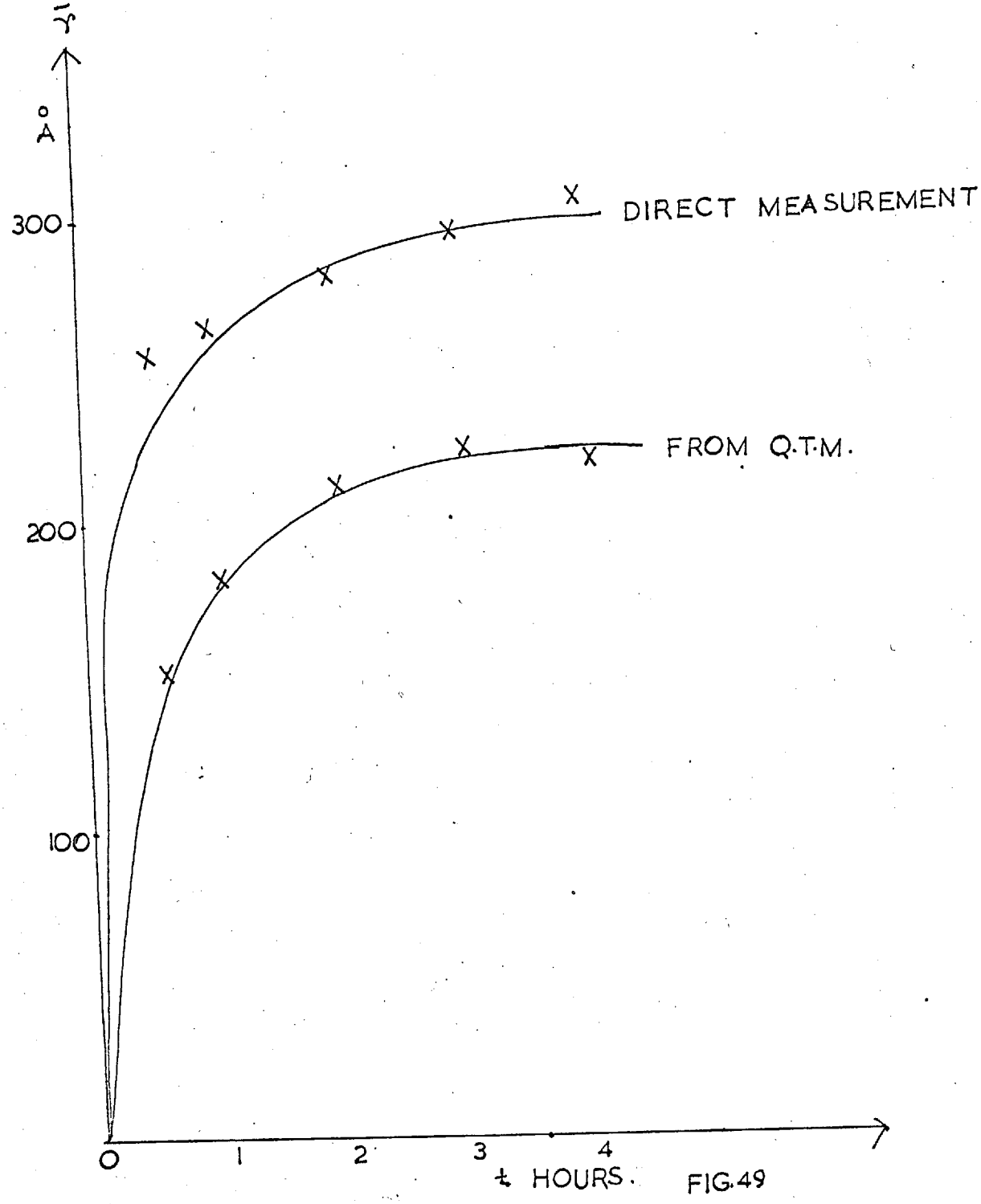


FIG.49

at different temperatures and residence times and the results are plotted in fig. 50. It was found that the fv values in almost every case were higher than the maximum possible value that fv could attain at any temperature and residence time for this iron concentration. This maximum value ($^{f}v_{max}$) can be calculated using eqn. (67A) for any iron concentration. This discrepancy may have been due to any of the following reasons: 1. The particles were not spherical 2. The initial iron content was higher than that estimated 3. The precipitates may not have been Fe_3C 4. Estimation of incorrect values for n , $\bar{d}$, or h. The iron concentration in the film was checked and found the same. The electron diffraction evidence showed that the precipitates are Fe_3C. n and $\bar{d}$ which are measured visually from the micrograph are quite reliable and h, the film thickness was measured accurately using multiple beam interferometry. The last three reasons cannot therefore be responsible and the first one, dealing with particles shape, was believed to be the dominant cause for the discrepancy.

The micro/ sccpe gives precise information concerning the dimensions of each particle in the plane of the film. It is possible, however, that the precipitates are not equi-axed, but consist of flat discs. The problem was therefore approached by considering the particles to be oblate spheroids of eccentricity e, assumed constant during growth

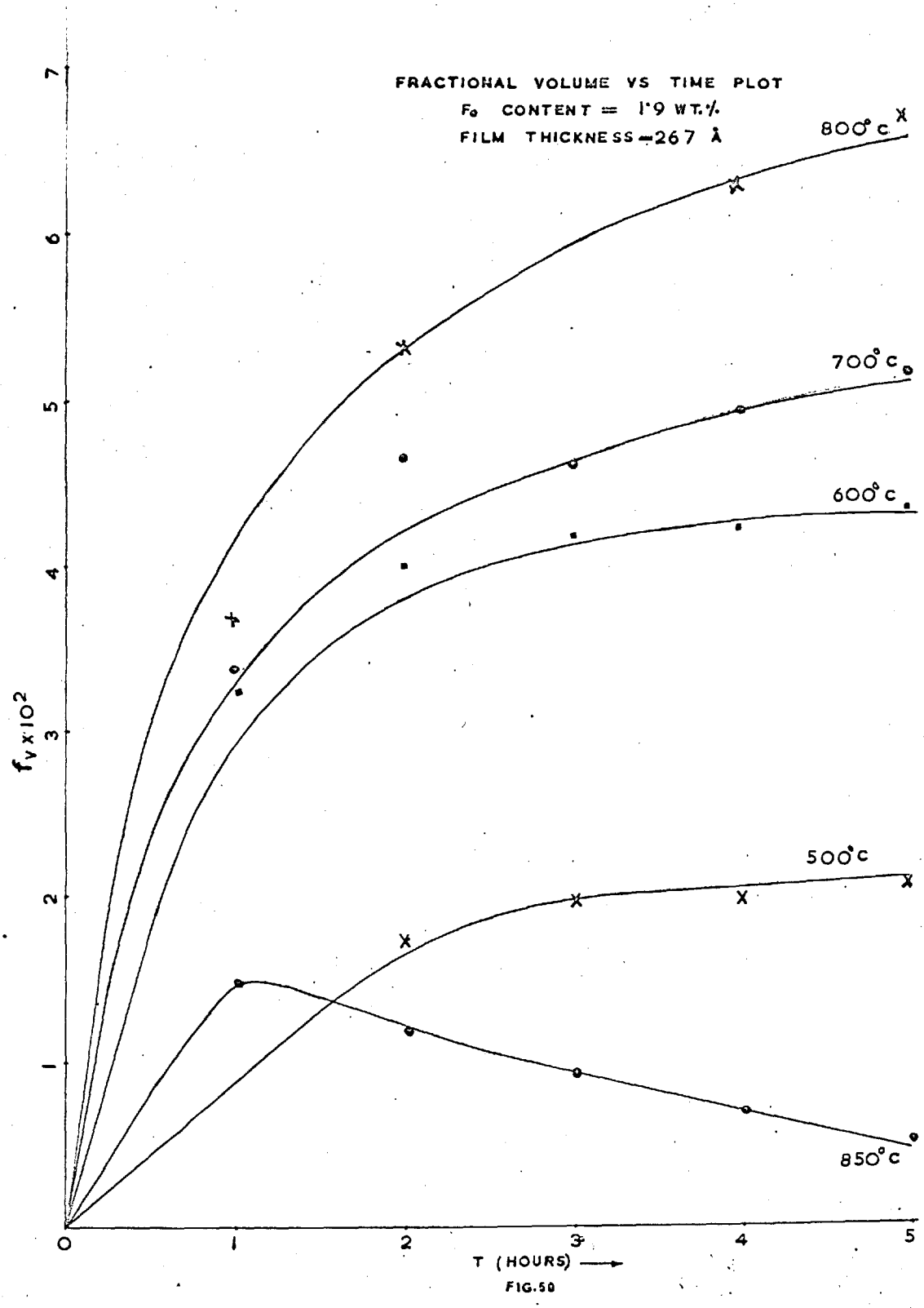

FRACTIONAL VOLUME VS TIME PLOT
Fo CONTENT = 1·9 WT.%
FILM THICKNESS = 267 Å
800°C
700°C
600°C
500°C
850°C
$f_V \times 10^2$
T (HOURS) ⟶
0
1
2
3
4
5
1
2
3
4
5
6
7

FIG.50

(ref 101). The volume of the spheroid will then be,

$$\frac{4}{3}\pi \bar{r}^3 (1 - e^2)^{\frac{1}{2}}$$

The volume fraction f_{Ve} is written as,

$$f_{Ve} = \frac{4}{3}\pi \bar{r}^3 \frac{n_i}{h}(1 - e^2)^{\frac{1}{2}}$$

$$= f_{Vs} \quad (1-e^2)^{\frac{1}{2}}$$

where f_{Vs} denotes volume fraction for spherical particles. The value of the expression $(1-e^2)^{\frac{1}{2}}$ is determined from the following considerations,

The Maximum value of f_{Ve} will be $= \frac{\rho_{ow}}{\rho_t}$

Hence,

$$f_{v_{max}(e)} = \frac{w}{\rho_t} = \frac{4}{3}\pi r^{-3} \frac{n_i}{h} (1-e^2)^{\frac{1}{2}}$$

$$\text{or} \quad (1-e^2)^{\frac{1}{2}} = \frac{\rho_{ow}/\rho_t}{fv_s} \qquad \ldots\ldots\ldots(88)$$

fv_s is a maximum at 800°C for five hours residence time in the present experiment. Its value was determined to be equal to 7.67×10^{-2} by calculating $fv_s = \frac{4\pi}{3h} \Sigma n_i r_i^3$, using the particle size distribution for this specimen, and $(1-e^2)^{\frac{1}{2}}$ was then estimated using the equation (88). The fv_s values shown in fig. 50 were then multiplied by the reducing factor $(1-e^2)^{\frac{1}{2}}$. Putting these reduced fv values

in equation (67), the values of $\frac{\Delta c(t)}{Co}$ were then calculated for each temperature and heat treatment time

Now consider equation (65),

$$\frac{\Delta c(t)}{Co} = 1 - \exp\left[-\left(\frac{t}{\tau}\right)^n \right]$$

$$\exp\left[- \left(\frac{t}{\tau}\right)^n \right] = 1 - \frac{\Delta c(t)}{Co}$$

$$\text{or} \quad - \left(\frac{t}{\tau}\right)^n = \log_e\left(1 - \frac{\Delta c(t)}{Co} \right)$$

$$\text{or} \quad \left(\frac{t}{\tau}\right)^n = \log_e \left(\frac{1}{1 - \frac{\Delta c(t)}{Co}} \right) \quad \text{.....(89)}$$

The values of $\log_e \left(\frac{1}{1 - \frac{\Delta c(t)}{Co}}\right)$ are then calculated for each temperature and time and then plotted according to equation (89), i.e. $\log_e\left(\frac{1}{1 - \frac{\Delta c(t)}{Co}}\right)$ vs log t and the results are shown in fig. 51. The value of n obtained by averaging the slopes of these four curves was $n = 1.1 \pm .109$. Therefore the value of n will be taken to be approximately unity in all subsequent considerations.

Putting n = 1 in equation (89) the relaxation time τ can be obtained. τ values corresponding to five residence times at each heat treatment temperature have been calculated from the above equation and a mean value corresponding to each temperature attained (Table 6).

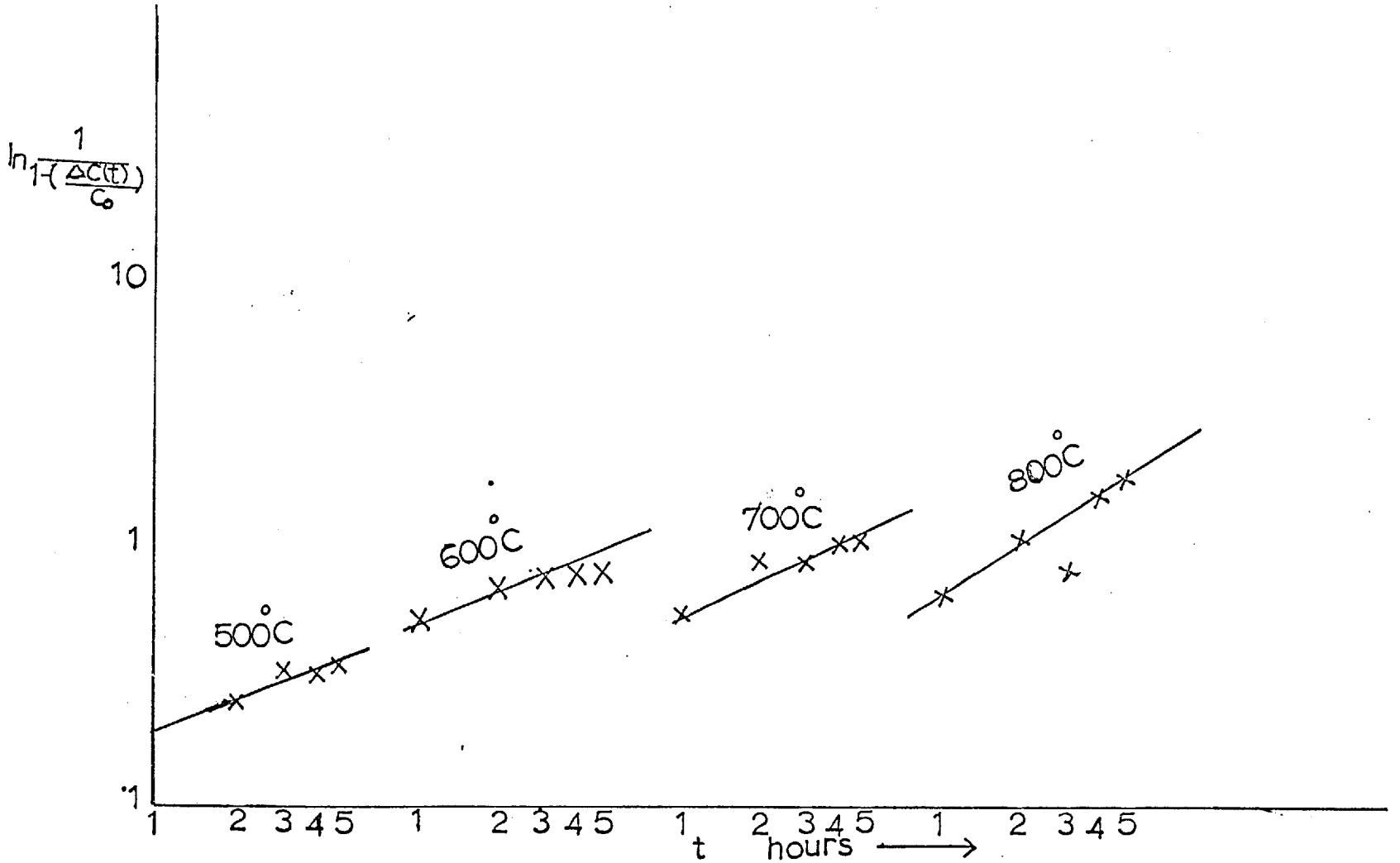

$\ln \frac{1}{1-\left(\frac{\Delta C(t)}{C_0}\right)}$
10
1
·1
500°C
600°C
700°C
800°C
1 2 3 4 5 1 2 3 4 5 1 2 3 4 5 1 2 3 4 5
t hours ⟶

FIG.51

9.7.2.5 Diffusion coefficient.

Knowing the relaxation time τ and the interparticle distance r_e at a particular temperature, the diffusion coefficient D can be evaluated from the following equation,[178]

$$\tau = \frac{r_e^2}{2D} \left(\frac{C_P}{C_o}\right)^{\frac{1}{3}} \quad \text{.....(90)}$$

C_P and C_o are concentrations of iron in the precipitate and the film respectively. C_o is known from our experiment, and C_P can be calculated as follows:

We know that the unit cell of Fe_3C contains 12 iron atoms and 4 carbon atoms. Hence the total mass in unit cell of Fe_3C will be

$$12 \times 55.8 + 4 \times 12 = 717.6$$

$$\therefore \quad \% \text{ Fe } (^w/_w) \text{ in pure } Fe_3C = \frac{12 \times 55.8 \times 100}{717.6}$$

$$= 93.3 \%$$

The interparticle distance r_e can be determined from the relation,

$$r_e = \frac{1}{2}\sqrt{\frac{A}{n}}$$, where A is the area of a micrograph and n is total number of particles in it. The r_e values increase with the increase in heat treatment temperature. At each temperature five r_e values are obtained corresponding to five heat treatment time and the mean was determined to employ in the calculations for D. The D values so calculated at different temperatures have

been shown in Table 6 below.

Table 6

Temperature °C	r_e values Å	τ values (Hours)	$(\frac{C_P}{C_o})^{\frac{1}{3}}$	D in cm^2/sec.
500	148	10.5±1.4		10.6×10^{-17}
600	251	4.1± .8	3.67	78.3×10^{-17}
700	297	3.3± .6		136.2×10^{-17}
800	320	2.5± .3		208.7×10^{-17}

Fig. 47B shows an Arrhenius plot of $\log_{10} D_{vs} \cdot \frac{1}{T}$. As before it can be seen that the points lie on a smooth curve which turns over towards the $\frac{1}{T}$ axis at higher temperatures. The upper and lower limits have been assigned to the calculated values of D at each temperature and figure 47B shows the magnitude of these limits. The upper and lower limits were calculated using the smallest and the highest τ values as shown in the table 6.

The Arrhenius plot in fig.47B also gave a similar value for the activation energy as that calculated from Einstein's equation (16.1 K. cal.).

9.8. Film thickness Vs. iron concentration.

The film thickness 'h' was usually estimated from the colour variation chart given in chapter 8. Since the quantity 'h' occurred in the denominator of the expression for fv it was contemplated that the higher values of fv might be due to inaccurate 'h' values so estimated. It was therefore decided to measure the film thickness accurately using multiple beam interferometry. Although errors were found, they were too small to account for the high fv_s values; it was, however, observed that the film thickness was systematically higher than the estimated value for specimens with higher iron concentrations. Fig. 52 is a plot of iron concentration vs film thickness (measured by multiple beam interferometry) for several specimens of nominal constant thickness as determined by the colour method. It is interesting to note that the relationship is a linear one.

9.9. Dark field microscopy of Fe_3C particles.

The microstructures of the carbide particles were also observed in the dark field conditions using parts of the 002 ring both for simple and tilted conditions. Fig. 53A is the dark field micrograph of a specimen with 22.2 wt % iron heated in vacuo at 1000°C for 15 mins. The bright field micrograph is shown in figure 53B. The bright features around each carbide particles of the dark field image may be

PLOT OF FILM THICKNESS VS COMPOSITION

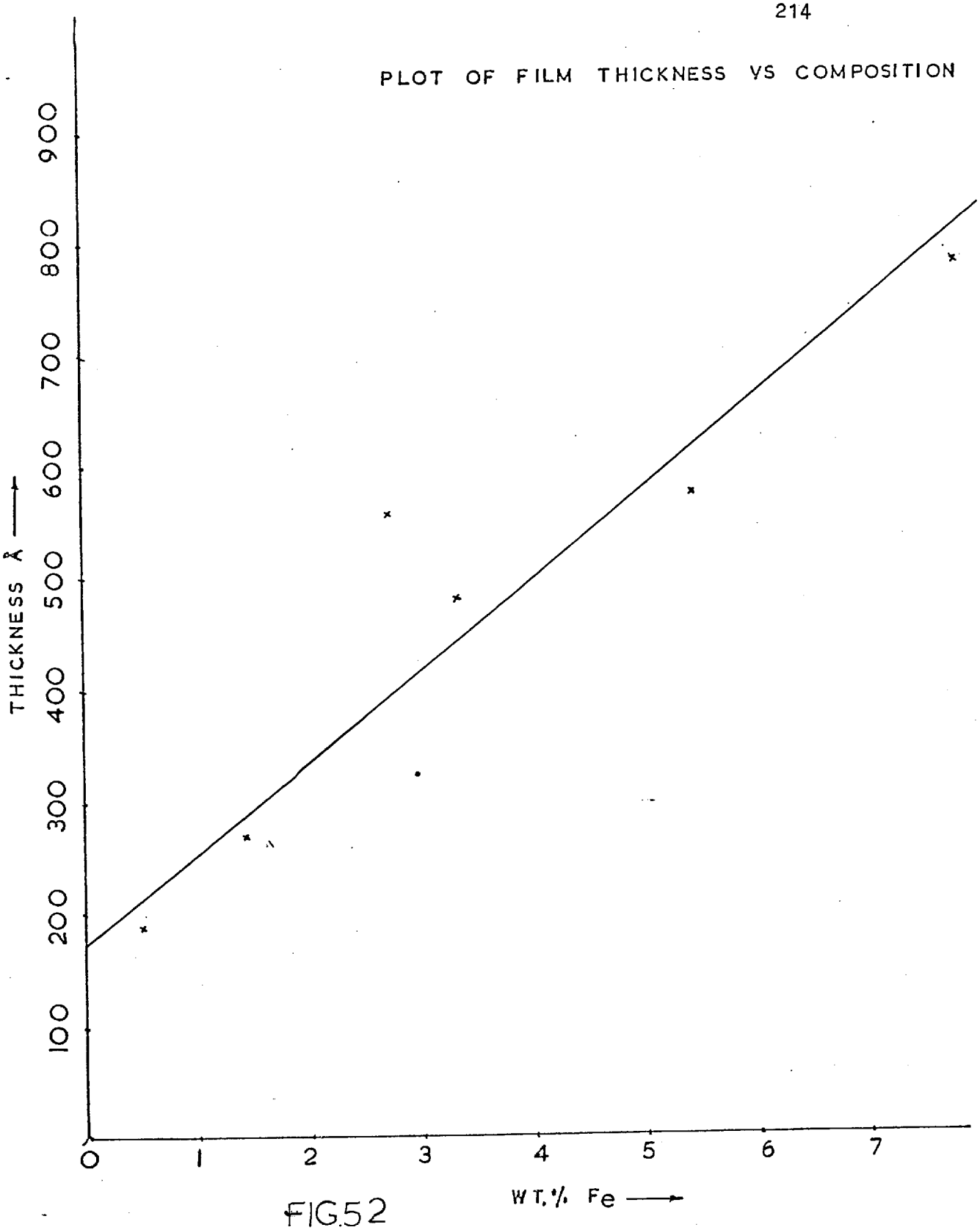


FIG.52

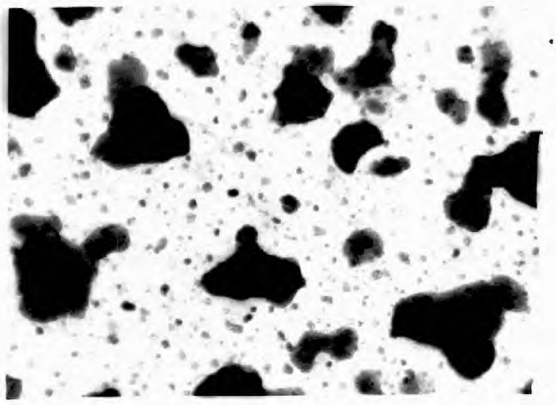
interpreted as due to the basal planes produced at the edge of the particles.

9.10. Effect of shadowing.

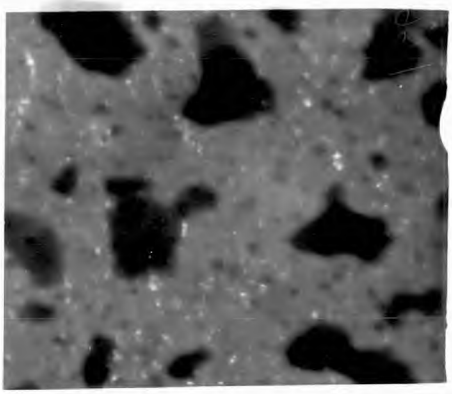
Specimens (22.2 wt.%Fe) after heat treatment at 1000°C to develop the carbide particles were shadowed with gold/palladium at different angles between 30° and 45° to reveal the extent to which particles projected above the film surface. No observable shadows appeared in the image (except in S) as is evident from the micrograph shown in Fig. 54. It was therefore decided to observe the particles in the scanning electron microscope. Fig. 55A is a scanning electron micrograph of a specimen with 22.2 wt.% iron heated at 1000°C in vacuo and reveals that the particles are not perfectly spherical. Fig. 55B is another micrograph at 1000°C with lower iron content which showed almost spherical particles which was always the case observed just before their decomposition.

9.11. Faceting.

Faceted particles were observed during heat treatment. Fig. 56 is an example showing well developed facets in the particles. The selected area diffraction pattern corresponding to this micrograph was spotty, indicating the large crystal size of the particles.



B



A

FIG 53 X40,000

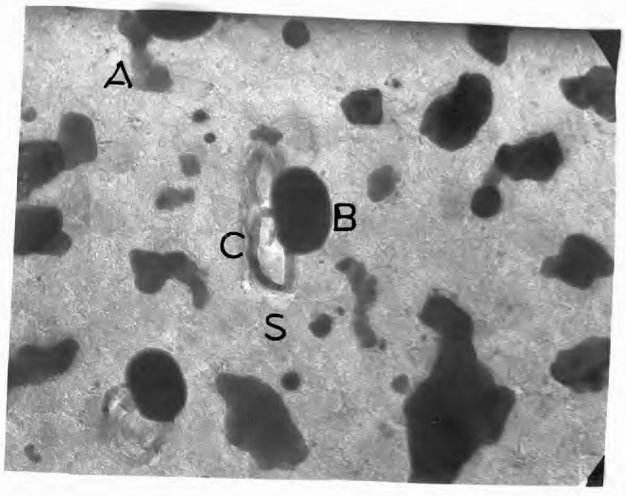


FIG. 54 X40,000

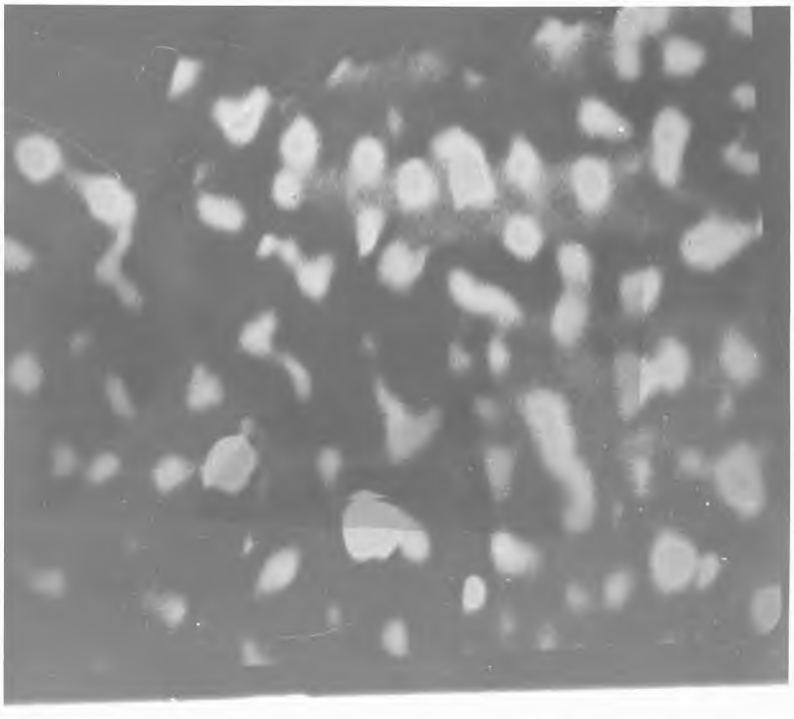


FIG. 55A X38,500

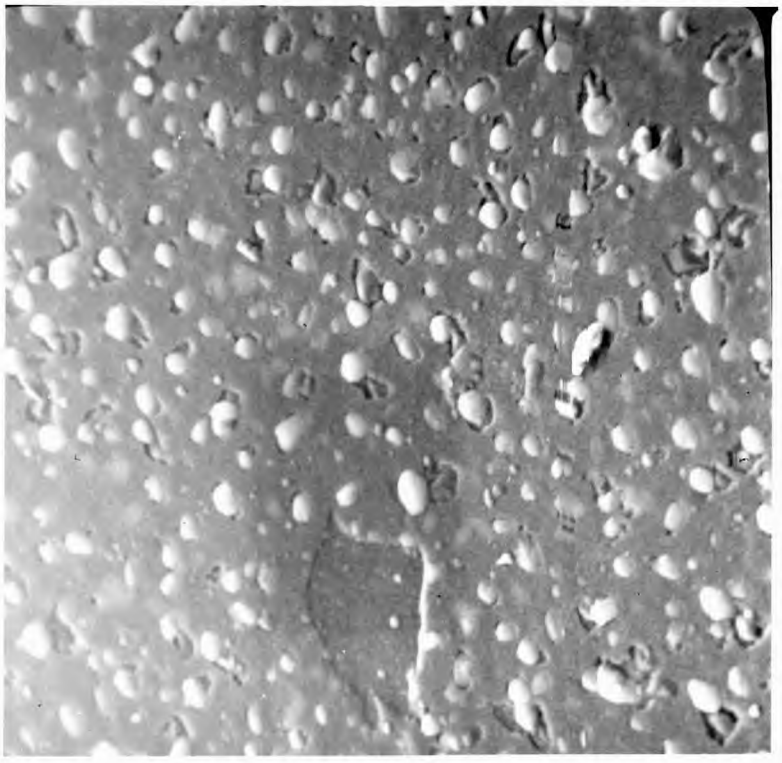
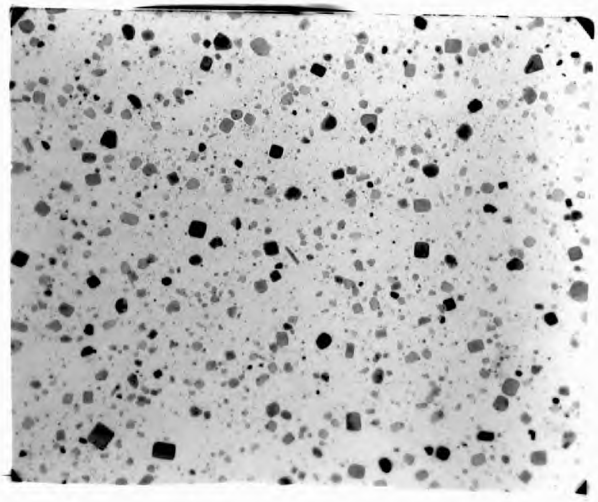
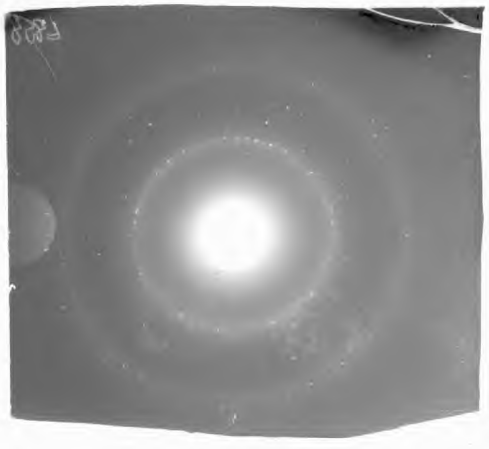


FIG. 55 B, X14,000



A

X 40,000



B

FIG. 56

9.12. Kinetics of crystallization.

Foregoing results show that although the as-deposited films are amorphous, long range order begins to develop at above 400°C. Crystallization in amorphous thin alloy films has been extensively studied by Mader[136-138]. He defined a reduced temperature of crystallization $\frac{Tx}{Tm}$ of amorphous alloy structures, where Tx is the transition temperature from the amorphous to the crystalline phase and Tm is the average melting point of the alloy under consideration. He showed that the ratio $\frac{Tx}{Tm}$ centered around a value of .3.

Now applying this relationship to our carbon/iron system, we can estimate the temperature of crystallization. Unfortunately carbon does not melt and so it is not possible to substitute the melting point. An upper limit to Tx can be obtained however, by inserting the sublimation point which is 3652°C.

Now $\frac{Tx}{Tm} = .3$ (90A) $Tm = \left(\frac{3925 + 1808}{2}\right)^{\circ}$ K. = 2866°K.

M.P. of iron = 1535°C.

$\therefore$ Tx = (.3 x 2866)°K = 859.8°K = 586.8°C.

The temperature of crystallization calculated this way gives the upper limit. The observed crystallization temperature was about 500°C in the composition range so far studied.

Mader also studied the decomposition of his crystalline alloy films and concluded that the decomposition temperature

Te was also related to the average melting point in the following way,

$$\frac{Te}{Tm} = .4$$

using the above relation it was found that the observed decomposition temperature was higher than the calculated value which was 873°C using the sublimation point for carbon. The observed decomposition temperature was 900°C or more depending on the iron concentration of the specimen. This discrepancy might be due to the scatter of values for $\frac{Te}{Tm}$ (ranging from .36 to .45) in Mader's systems. Moreover, as has already been said, the crystallization and decomposition temperatures are observed to be dependent on the alloy composition. Thus the higher the concentration of iron, the lower is the crystallization temperature and the higher is the decomposition temperature.

CHAPTER X

10. Graphitised films.

10.1. Introduction.

When films were heated above 1000°C in vacuo, decomposition of the carbide took place and the carbide particles disappeared. The subsequent diffraction patterns consisted of the three dimensional (002) reflection and the two dimensional (10) and (11) reflections characteristic of carbon. All traces of iron had disappeared (Fig.57). This was believed to be due to the fact that the films were heated in a vacuum better than 10^{-4} torr. The vapour pressure of iron at 1094°C is $\sim 10^{-5}$ torr. It therefore seems probable that iron liberated by decomposing Fe_3C diffused to the film surface and there vaporised.

The most striking features of these diffraction patterns was the appearance of the (002) reflection which was shown by Presland and White to be absent in carbon films heated without iron.[40,66,67] The presence of (002) reflections in the present study permitted the estimation of Lc values in the graphitised films. La values were measured from the breadths of the (10) and (11) rings as described in Chapter VIII.

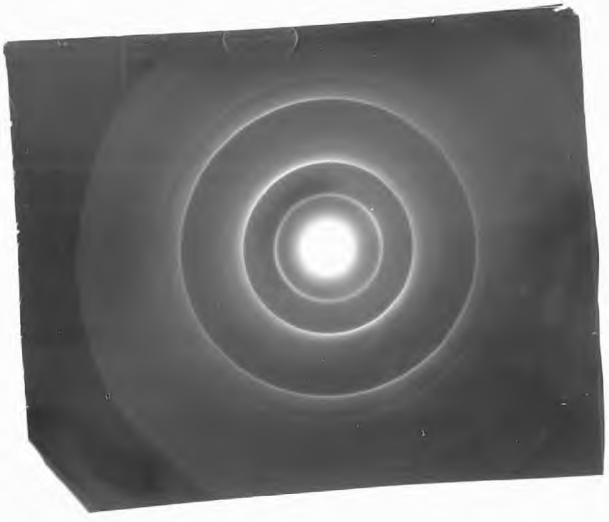


FIG 57

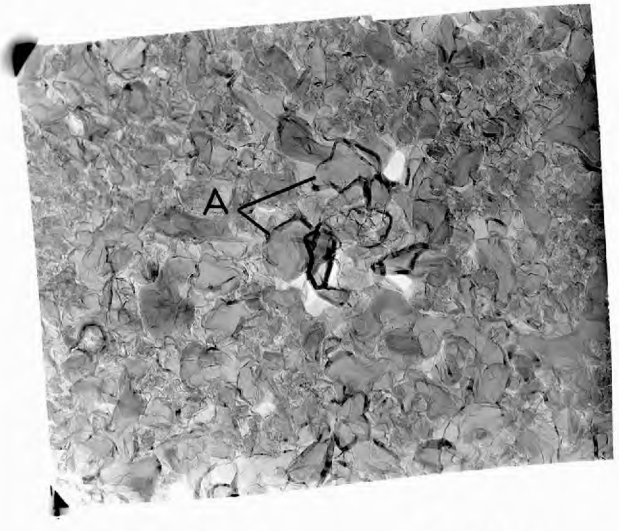


FIG 58 X40,000

10.2. Electron microscopy.

In general, films heat treated at temperatures above the decomposition temperature of cementite showed very interesting features both in bright and dark field conditions. It should be pointed out that the microstructures observed in the present study are quite different from those of pure carbon films.[66] Some of the more interesting details in the electron image are discussed below.

10.2.1. Bright field microscopy.

A typical microstructure found in the bright field image of most specimens, particularly those with higher iron content, is shown in figure 58. This micrograph corresponds to a specimen containing 11.9 wt.% of iron heat treated in the vacuum furnace for 30 minutes. The micrograph appears to show a two phase structure produced as a result of heat treatment. The crumpled structures are believed to occur as a result of the diffusion of metal atoms to the adjacent cementite particles produced at the early stages of heat treatment, thus leaving behind a porous structure in the remaining matrix. Features such as shown at A in Fig. 58, having well-defined boundaries and sizes of the order of 2000 Å are the structures produced in the remaining material after the decomposition of the carbides formed during diffusion. At higher temperatures much of the crumpled structures shown in fig. 58 is replaced by the

microstructures similar to those in fig. 59 which was obtained from a specimen with 22.2 wt % of iron heat treated at 2000°C in vacuo for five minutes. At higher temperatures much of the finer details are also found to disappear.

10.2.2. Dark field images.

Dark field microscopy using part of the basal plane reflections was found to reveal groups of parallel bright fringes (Fig.60). These were shown by Presland and White[60] to correspond to rotation moiré patterns resulting from two or more crystallites situated side by side. The basal planes of these crystallites lie parallel to the direction of the electron beam, but the crystallites are tilted slightly relative to one another about an axis parallel to the beam. (Fig.61).

From the method of formation it is clear that the traces of the reflecting basal planes lie perpendicular to the long dimension of the fringes. In addition, the mere presence of such contrast features proves the existence of local regions of highly graphitic carbon. Fig.62 shows the same region as Fig.60. in bright field.

Another interesting example is that shown in bright field in fig.63. This was obtained from a specimen with the highest iron content (22.2. wt. per cent) which was pre-heated at 1000°C followed by heat treatment at 1200°C for 30 minutes in the vacuum furnace. The micrograph reveals clearly that the graphitised carbon film replicates the

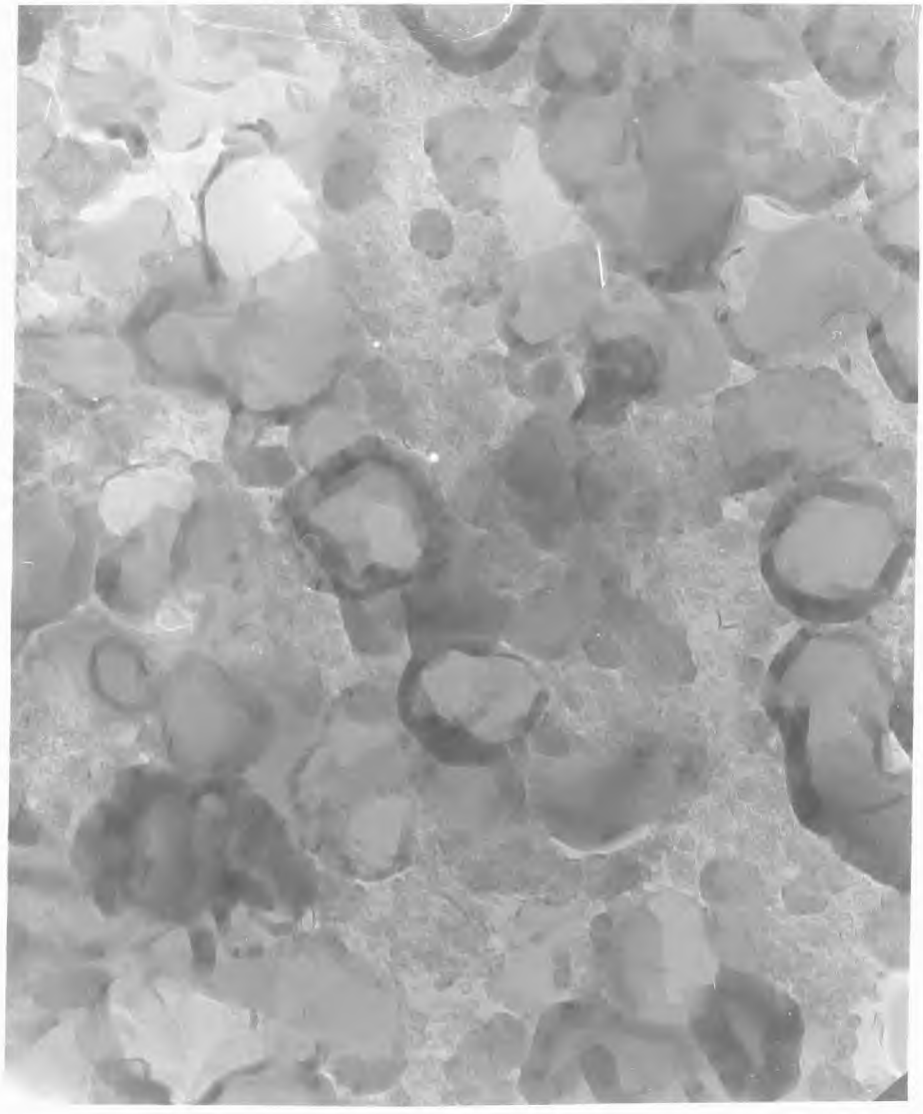


FIG. 5 9 X 80,000

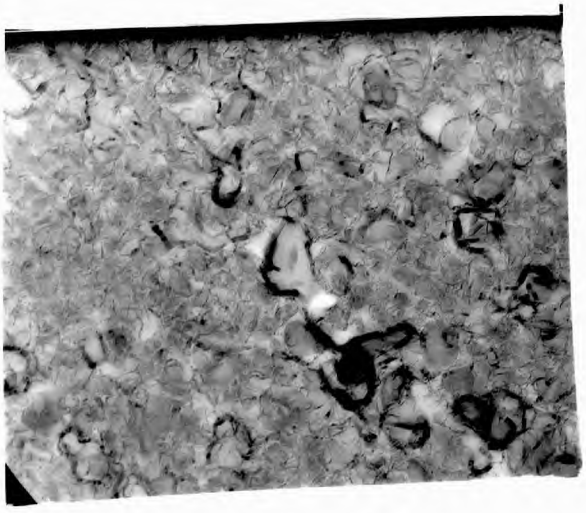


FIG. 62 BRIGHT FIELD X40,000



FIG. 60 DARK FIELD X40 000

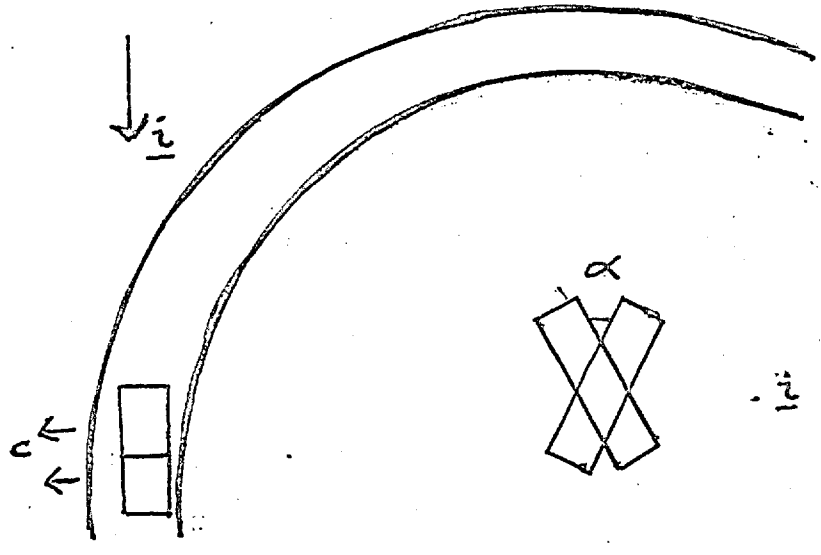


FIG. 61

PRODUCTION OF MOIRÉ FRINGES.

big carbide particles produced during preheating, which subsequently decomposed during heating at 1200°C. Note again the appearance of a two-phase structure. The dark field micrograph from the corresponding area of fig. 63 is shown in fig.64 and exhibits the moiré patterns already mentioned.

10.2.3. Tilting experiments.

The tilting of a specimen having the microstructures shown in fig.58 was performed using a Valdré tilting stage producing a range of 22°. The features described above were found to be present throughout the tilting operation showing that they are typical of the whole specimen, that they are localised, and that they are not merely contrast effects. Fig.65 represents micrographs from the same field of view before and after tilting; showing the same structures in the two different orientations.

10.2.4. Scanning electron microscopy.

Scanning electron microscopy was also performed on specimens exhibiting the crumpled structures shown in the transmission electron micrograph shown in Fig.58. The scanning electron micrograph obtained from specimens containing these structures is shown in figure 66. showing the bumps which are believed to be produced by the undulating microstructures of the specimen. The diameters of the semicircular white bands roughly correspond to the diameters obtained from the structures produced by such films in



FIG.63 brigt field. X40,000

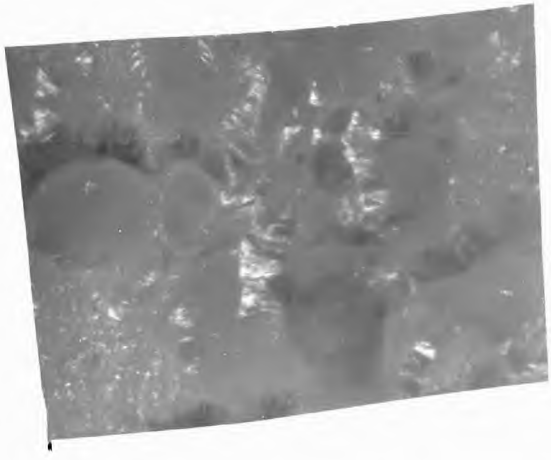


FIG.64 dark field. X40,000

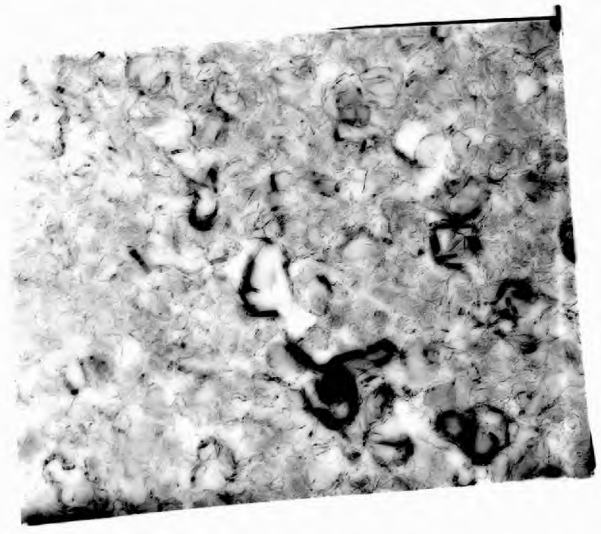
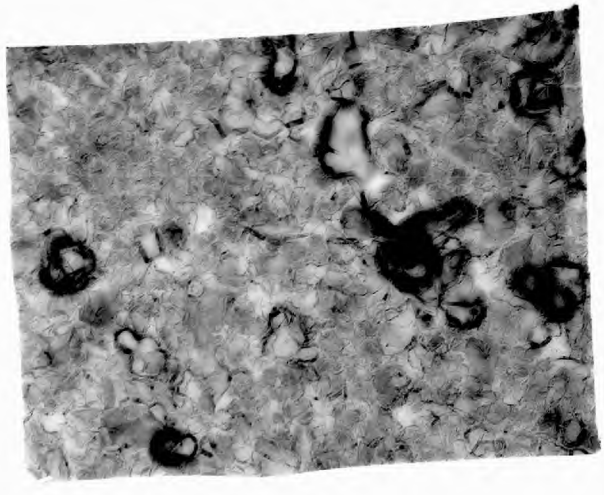


FIG. 65 NORMAL



AFTER TILTING

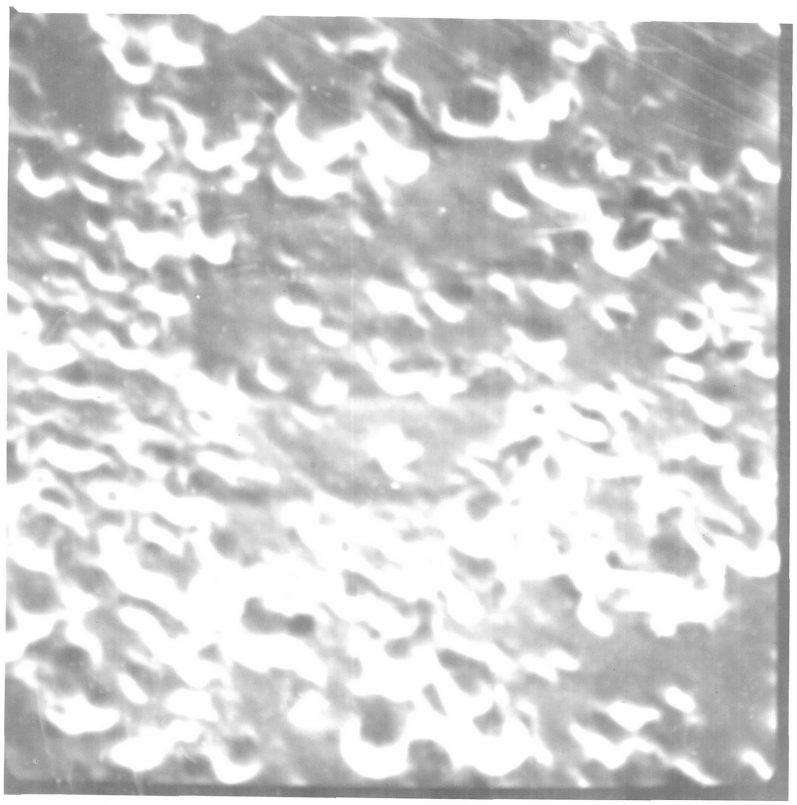


FIG 66 X23,500

transmission electron microscopy.

10.3. Measurement of La and Lc.

The electron diffraction patterns obtained from each specimen after removal of iron by heating above 1000°C gave (002), (10) and (11) reflections only. Even selected area diffraction patterns did not exhibit any spottiness, indicating that even the largest graphitic regions did not exceed a few hundred angstroms in size. Thus contrary to appearances regions such as A in fig. 58 do not consist of large graphite crystallites.

From the line breadths of each diffraction ring the values of Lc and La were measured, the procedure for which has been described in the experimental section.

10.4. Effect of heat treatment temperature.

Specimens with the same iron content (.9 wt.%) were heated for a constant time (5 minutes) at temperatures ranging from 1000°C to 1800°C and the results are shown in figure 67 which shows that La remains unchanged for a certain range of temperatures after which it begins to increase. Heat treatments at much higher temperatures was hampered by the thickening effect of the film due to evaporation of the furnace material.[40]

10.5. Effect of heat treatment time.

Films with varying iron concentrations were heat treated at 1200°C for times ranging from 3 minutes to 30

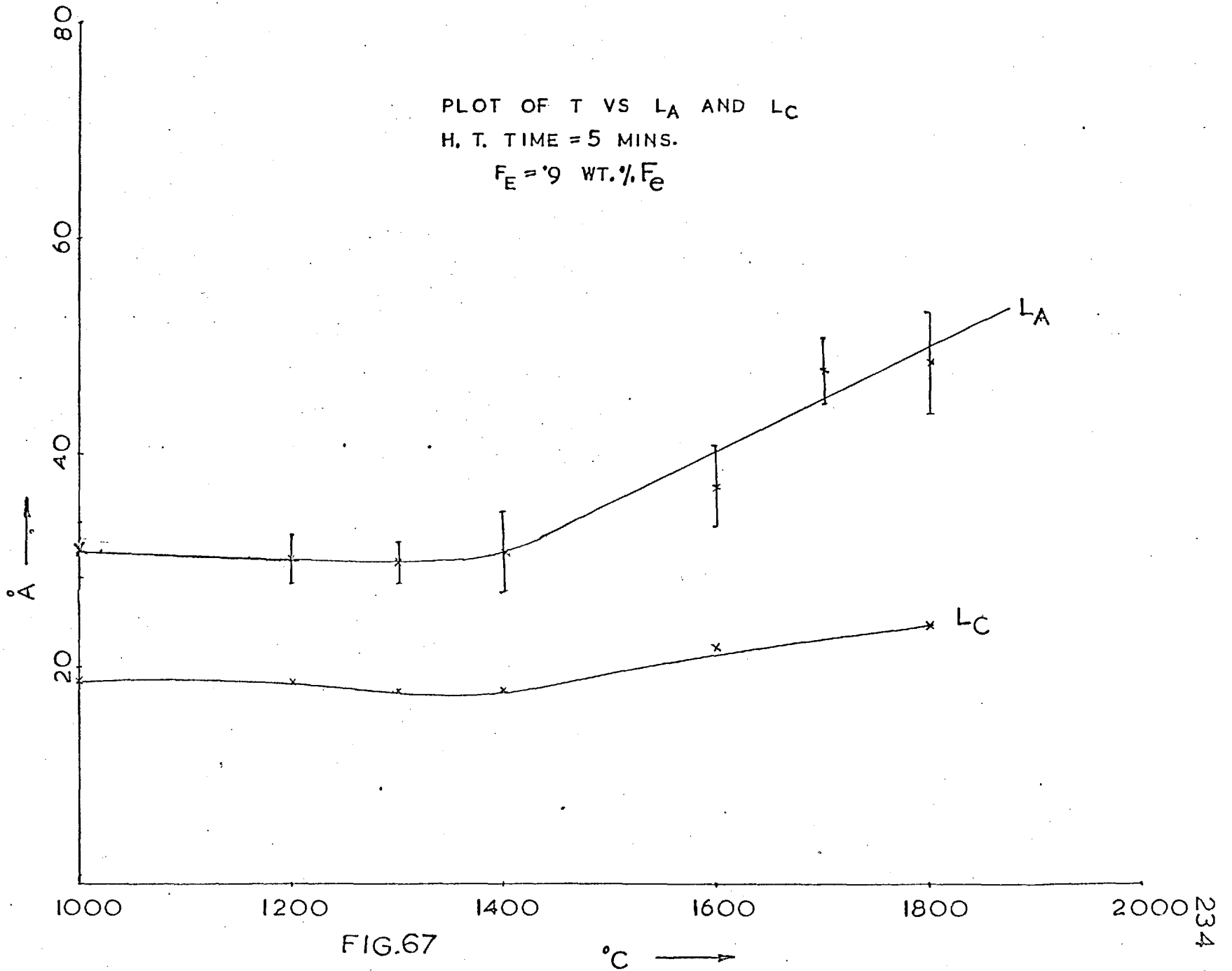
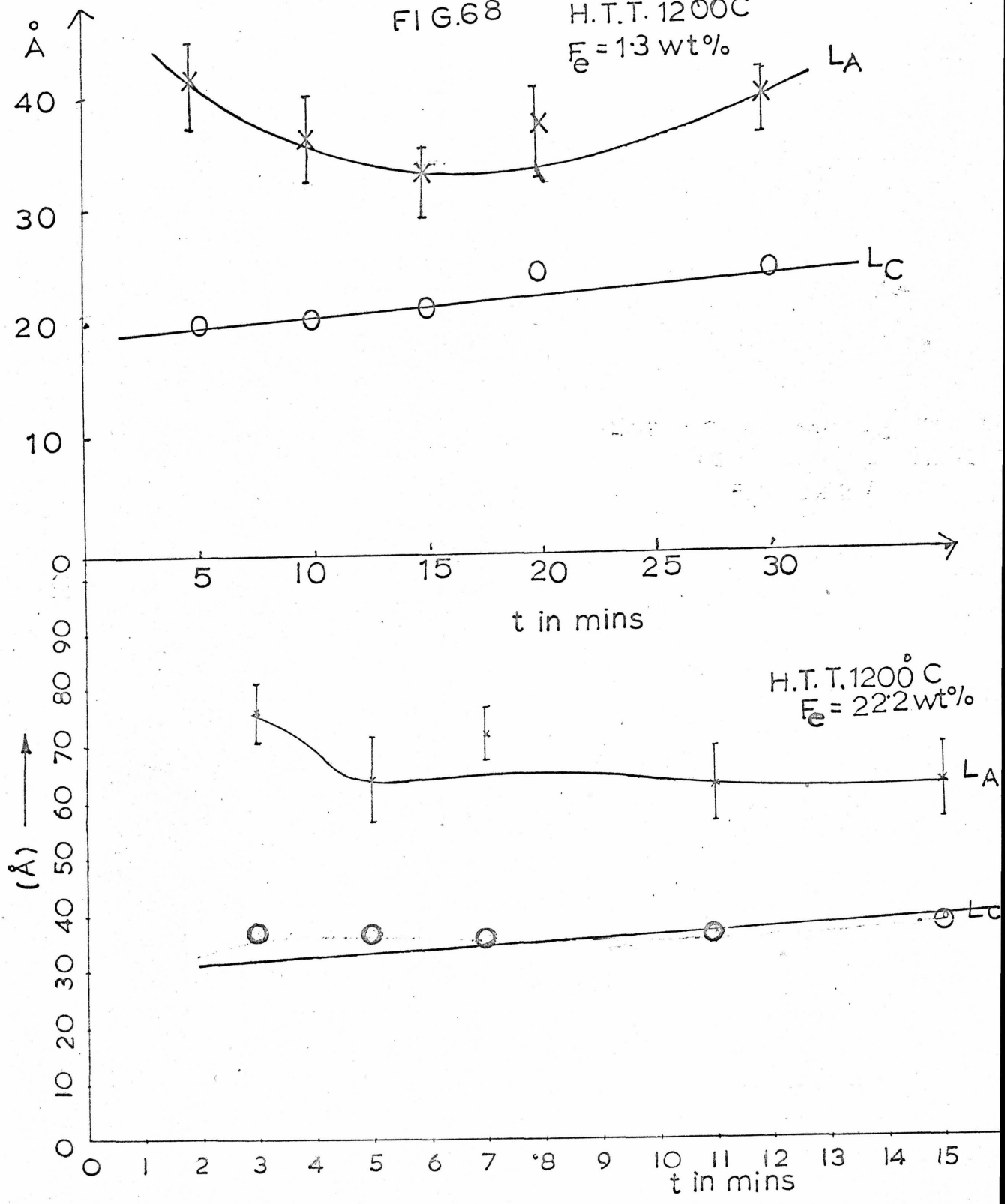

PLOT OF T VS L_A AND L_C
H. T. TIME = 5 MINS.
F_E = '9 WT.% Fe
80
60
40
20
Å
L_A
L_C
1000
1200
1400
1600
1800
2000
°C

FIG.67

FIG.68


H.T.T. 1200°C
Fe = 1·3 wt%
Å
40
30
20
10
0
L_A
L_C
5
10
15
20
25
30
t in mins
H.T.T. 1200° C
Fe = 22·2 wt%
(Å)
0
10
20
30
40
50
60
70
80
90
L_A
L_C
0
1
2
3
4
5
6
7
8
9
10
11
12
13
14
15
t in mins

minutes. Fig. 68 represents a plot of La and Lc vs. heat treatment time for two groups of specimen with iron concentrations of 1.3 wt.%. and 22.2 wt.%. Both of the curves for La show a tendency to fall at first, followed by a levelling off or even a slight rise. Lc shows a continuous but very slight rise. It is noteworthy, however, that increasing the Fe concentration leads to a marked increase in both La and Lc, and this effect was investigated further.

10.6. Effect of Fe concentration on La

Specimens with increasing iron concentration were prepared and heated in vacuo at 1200°C for 30 minutes. La values from each specimen were calculated from the (10) and (11) reflections, using equations (52) and (57). Using the average La value, Δ La was then calculated using the relation,

$$\Delta La = La - La_o$$

La_o is the value of the layer size given by a pure carbon film at this temperature and heating time and was taken from the recent work of Presland and White.[66] The results obtained from specimens with varying iron content have been represented in Figure 69. This shows a steady increase in La with increasing iron concentration.

10.7. Effect of Fe concentration on Lc

The Lc values measured from specimens with varying

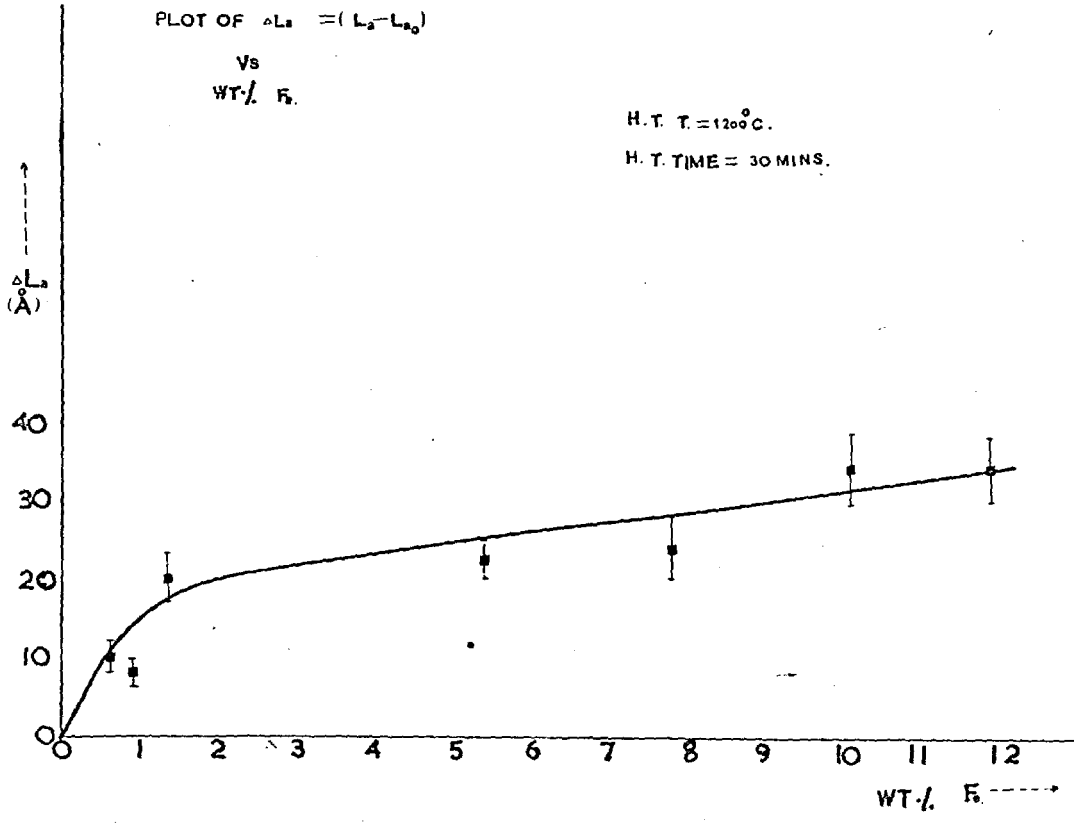

PLOT OF ΔLa = (La − La0)
Vs
WT·/. Fe.
H.T. T. = 1200°C.
H. T. TIME = 30 MINS.
ΔLa (Å)
40
30
20
10
0
0
1
2
3
4
5
6
7
8
9
10
11
12
WT·/. Fe

FIG. 69

amounts of iron heat treated at 1200°C for 30 minutes were used to calculate ΔLc, using the expression

$$\Delta Lc = Lc - Lc_o .$$

Here Lc_o should denote the value of Lc in the absence of iron. Since Lc cannot be measured in a pure carbon film due to the absence of three dimensional (002) reflections, a specimen with the smallest quantity of iron was used to estimate the value for Lc_o and hence in the present discussion Lc_o refers to the value of Lc from a specimen containing .6 wt % of iron. Fig.70 shows a plot of Δ Lc vs. concentration.

10.8. Effect of Prenucleation.

It can be seen that increasing the iron content increased the value of both La and Lc. This should be compared with the effect of iron concentration on t. D, the diameter of the cementite particles, (Fig.33). It seemed possible that the increased size of the cementite particles was responsible for the enhanced La and Lc values, and prenucleation experiments were carried out in an attempt to verify this hypothesis. Specimens were heated at temperatures below 1000°C in order to produce a given distribution of Fe_3C particles, followed by a graphitisation treatment above 1000°C.

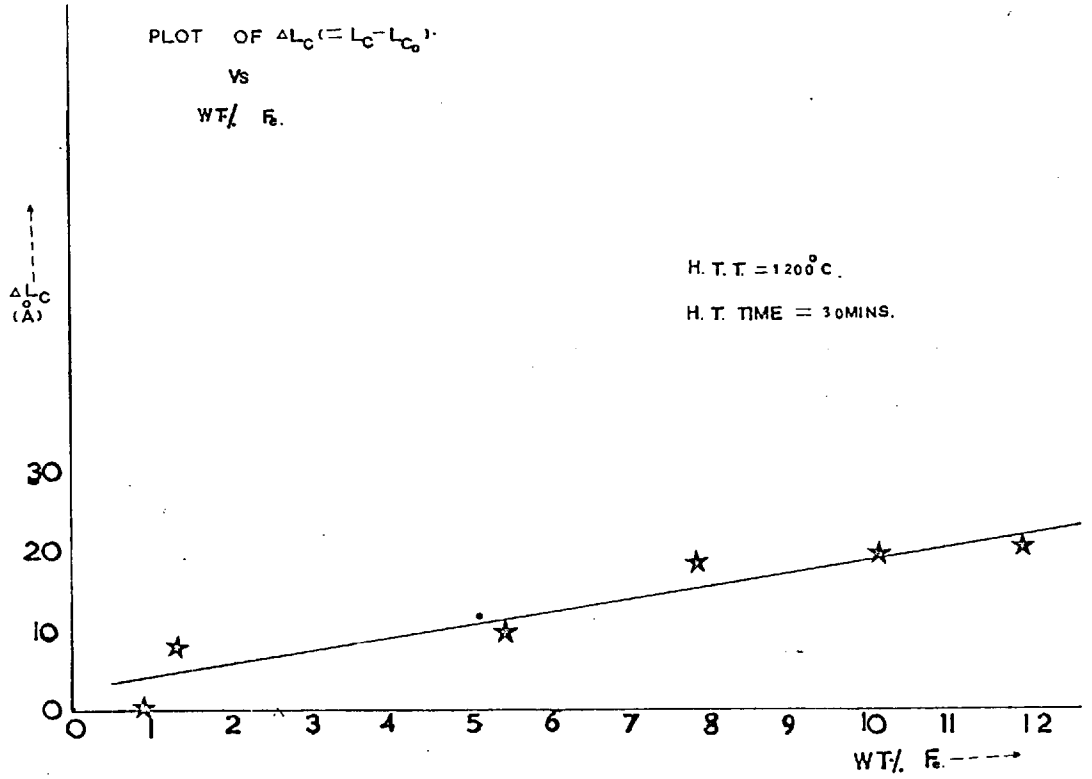

PLOT OF $\Delta L_c (= L_c - L_{c_0})$
VS
WT/. Fe.
H. T. T. = 1200°C.
H. T. TIME = 30MINS.
ΔL_c (Å)
30
20
10
0
0 1 2 3 4 5 6 7 8 9 10 11 12
WT/. Fe.

FIG.70

10.8.1. Constant prenucleation temperature and time but varying iron concentration.

Specimens with varying iron concentrations were prenucleated at 600°C for 2 hours and then each one given a graphitisation treatment at 1200°C for 30 minutes. La and Lc values were then measured and the results plotted in Fig.71, together with comparable results without prenucleation (these have already been shown in Fig.69). The prenucleated results are denoted by $L'a$. In the present case the value of $L'a_o$ was determined from a pure carbon film after heat treatment under the same conditions of temperature and time and was found to be about 20 Å.

We denote the improvement in La as a result of prenucleation by,

$$\Delta L'a = L'a - L'a_o,$$

and the improvement in La as a result of the addition of iron by,

$$\Delta La = La - La_o \text{ as before.}$$

Then,

$\Delta L'a - \Delta La$ = improvement as a result of prenucleation only. Fig.72 shows a plot of $\Delta L'a - \Delta La$ against iron concentration. It can be seen that the advantage of prenucleation does not increase indefinitely with increase in iron content.

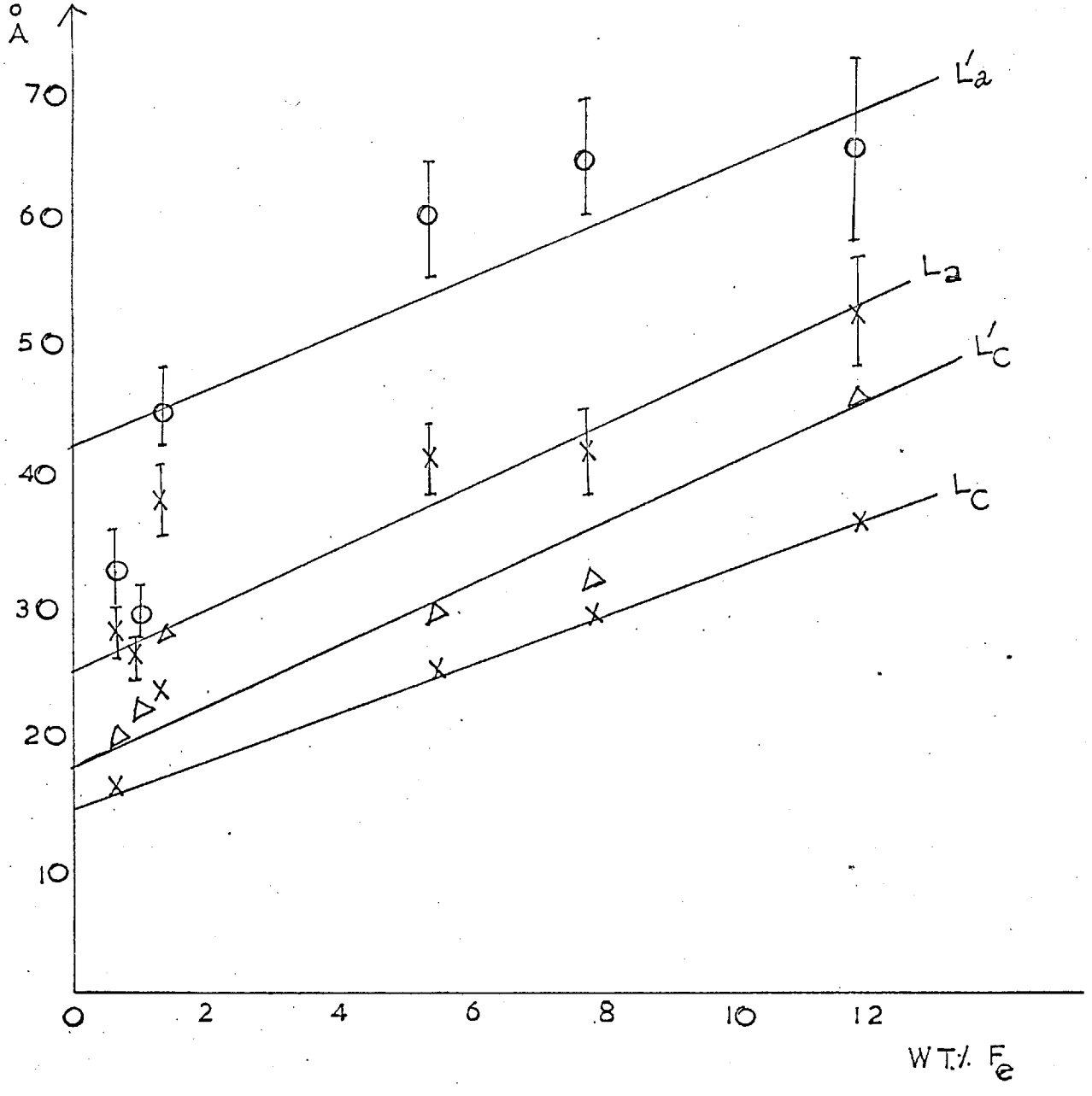


FIG. 71

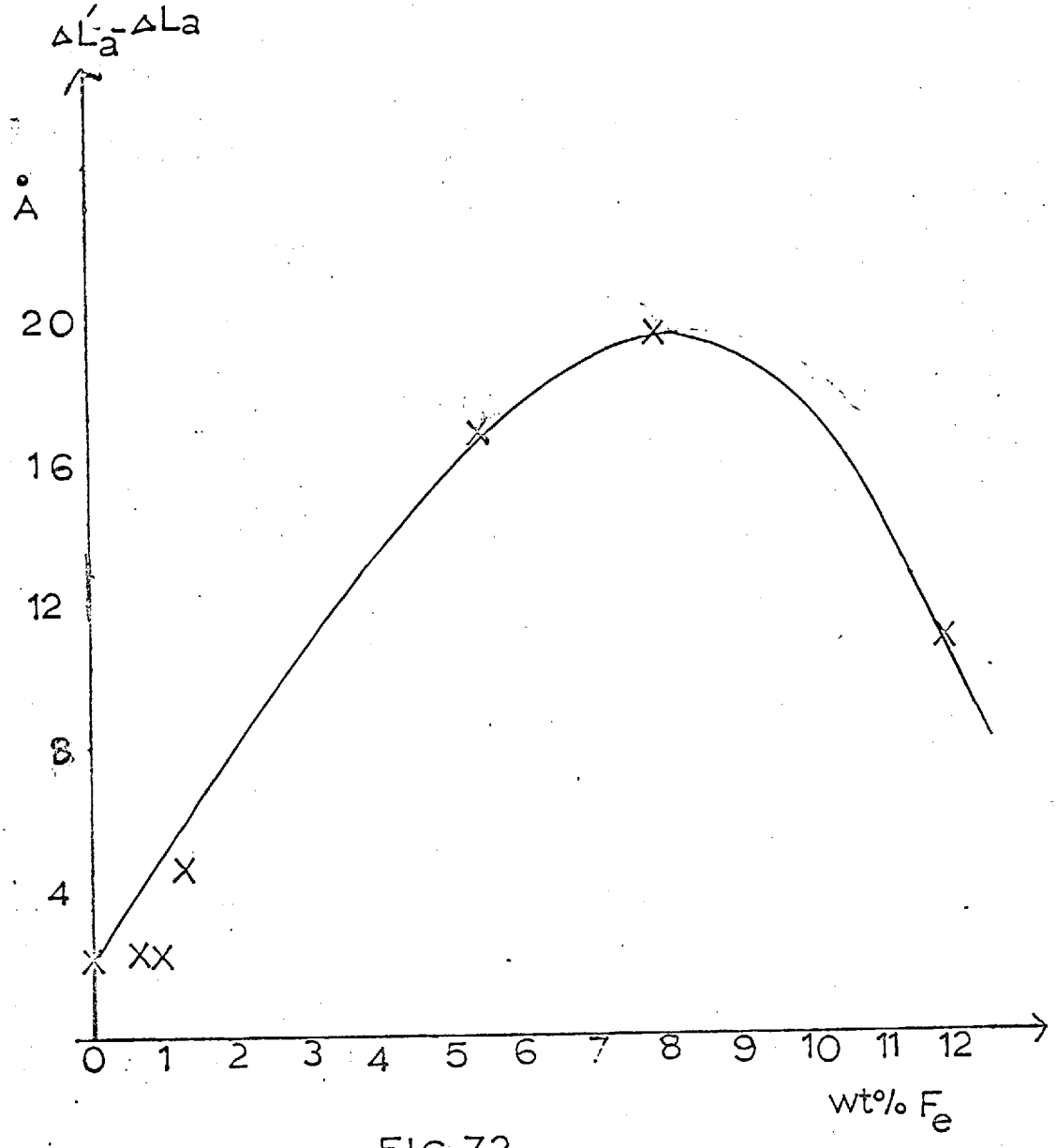


FIG. 72

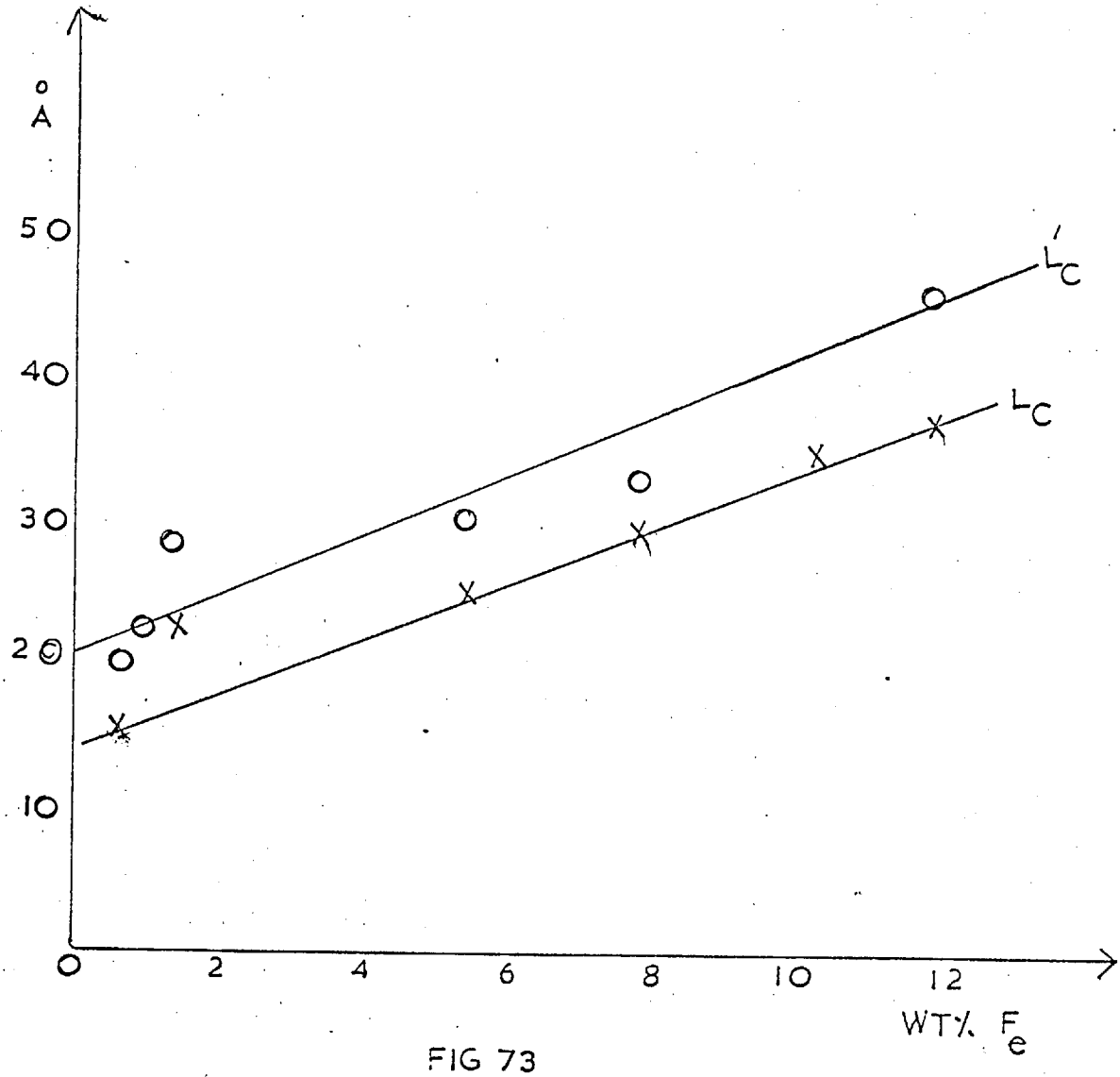


FIG 73

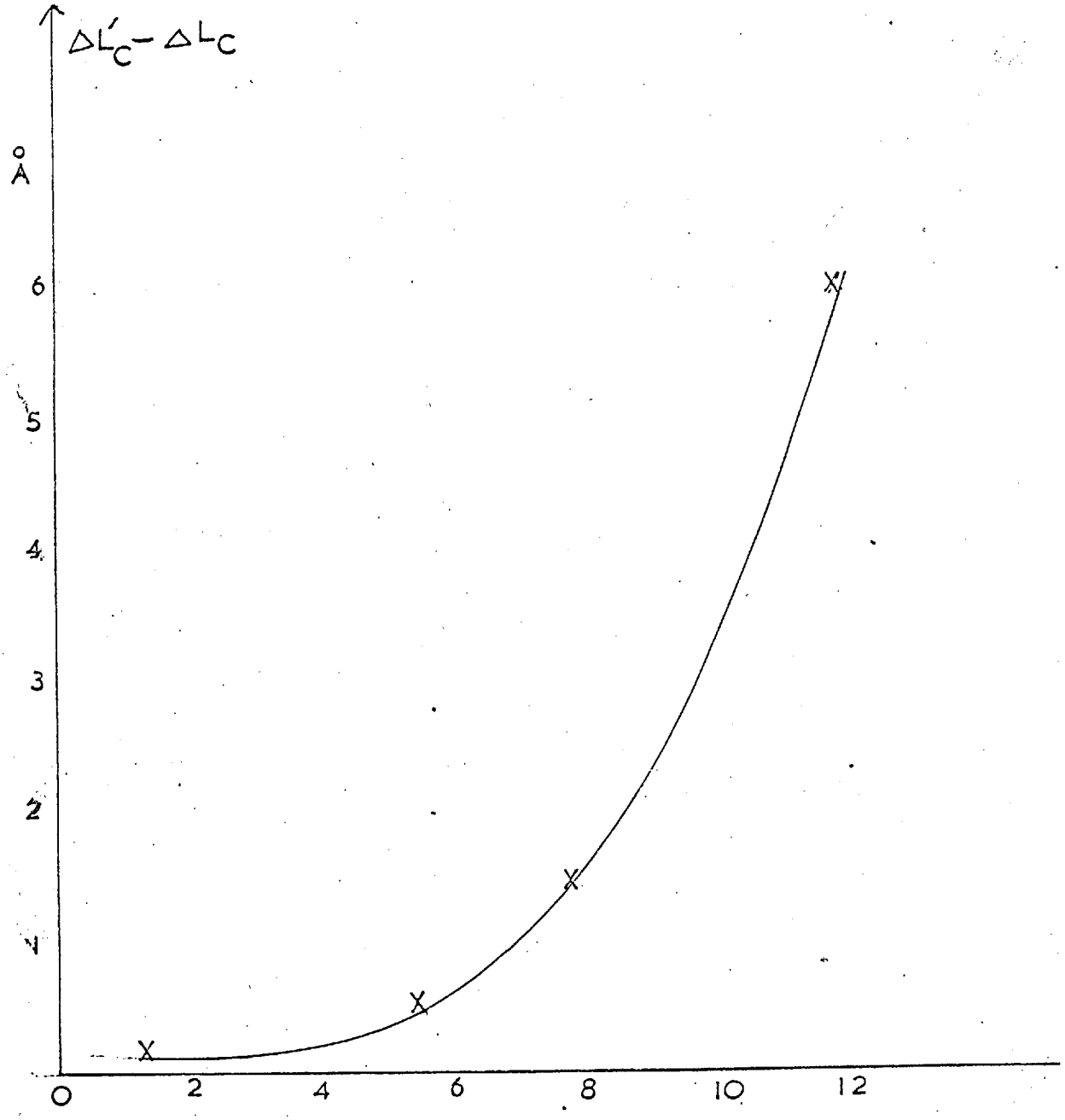


FIG. 74

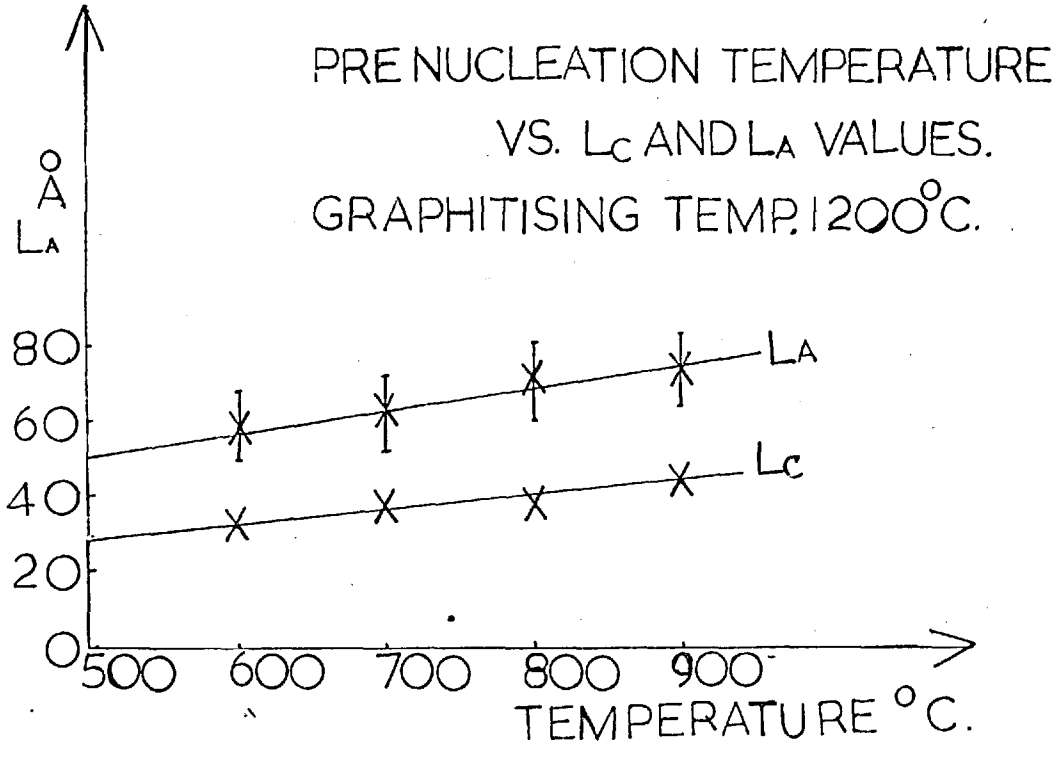

PRE NUCLEATION TEMPERATURE
VS. Lc AND LA VALUES.
GRAPHITISING TEMP. 1200°C.
Å
LA
80
60
40
20
0
500
600
700
800
900
TEMPERATURE °C.
LA
Lc

FIG. 75

Figs 73 and 74 show equivalent plots of Lc, $L'c$ and $\triangle Lc' - \triangle Lc$ as functions of iron content. As before the values of Lc_o and Lc'_o are taken to be those derived from a carbon film containing .6 wt.% of iron.

10.8.2. Effect of Prenucleation temperature and time.

La and Lc values obtained from specimens (5.9%Fe) first prenucleated at different temperatures followed by heat treatment at 1200°C for 30 minutes are shown in figure 75. A similar plot obtained from specimens (.9 wt%Fe) first prenucleated for different times at 800°C and then graphitised at 1200°C for half an hour is presented in figure 76. Both these plots reveal that prenucleation temperature and time play an important role in the growth of La. The last points of the La and Lc curves of figure 76 however, show small values; these are probably in error, due to the fact that they were derived from diffraction patterns which were overexposed.

10.9. Effect of heat treatment atmosphere.

The argon furnace was used to heat treat specimens at temperatures up to 2000°C. Heat treatments above this temperature were not possible because of rapid evaporation from the carbon electrodes of the furnace. On heat treatment in argon the production of cementite was observed, this was stable up to a very high temperature compared to heat treatment in vacuo. Carbide particles with very well

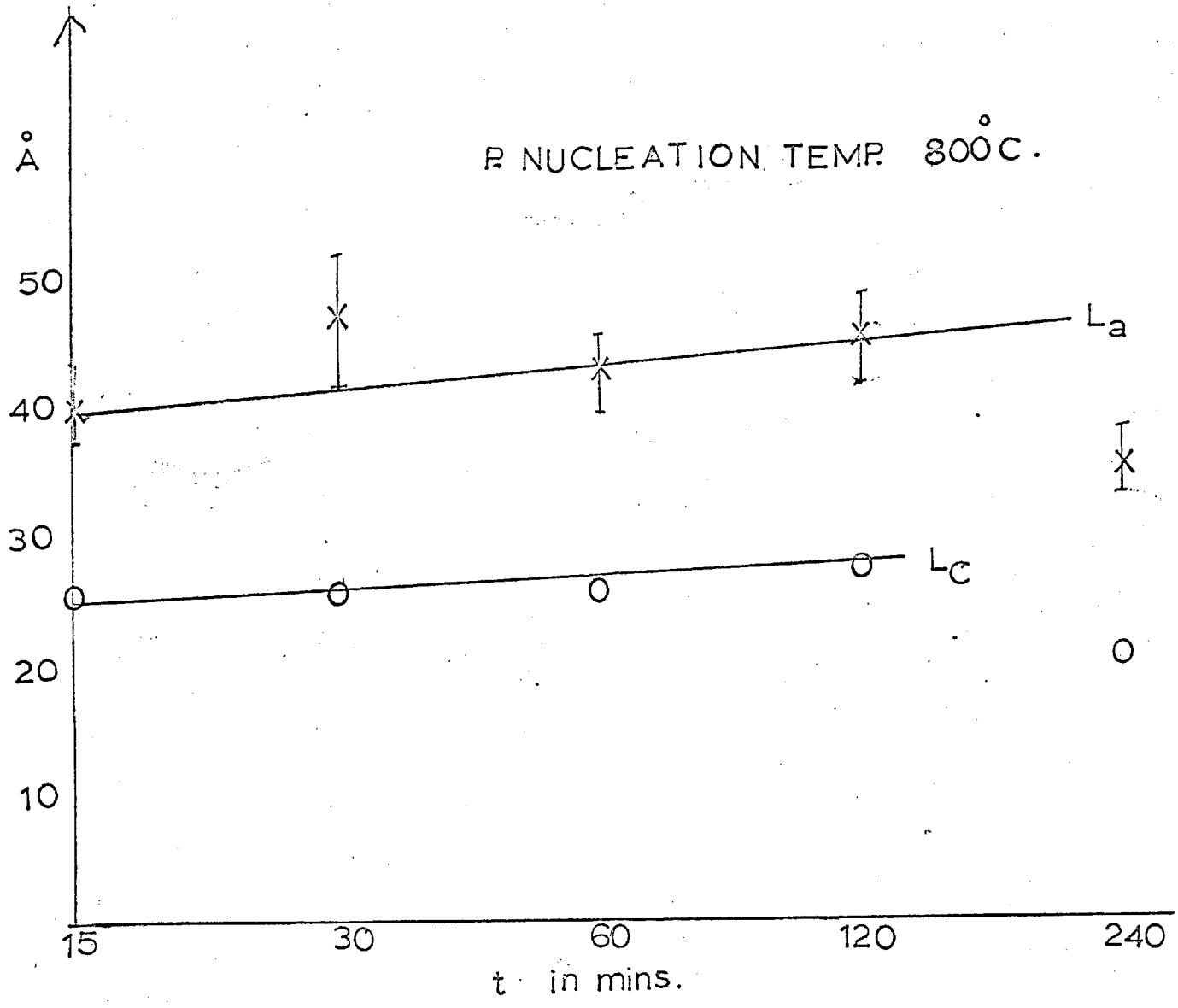

Å
R NUCLEATION TEMP. 800°C.
50
40
30
20
10
L_a
L_c
15
30
60
120
240
t in mins.

FIG.76

developed facets were observed, as shown in Fig.77 obtained from a specimen containing 5.4 wt°/o Fe and heated at 1200°C for 7 minutes. La and Lc values were measured from specimens with the above concentration at different temperatures and the results are given in fig.78; these show that argon has no apparent effect on their growth. This result is not particularly significant, however, due to the variation in residence time; this was necessary because at higher temperatures prolonged heating caused considerable evaporation of amorphous carbon, as mentioned earlier, thus making the film too thick for electron microscopy.

10.10. Effect of chlorine atmosphere.

Some specimens were first heat treated to produce cementite and then reacted with chlorine in an attempt to remove iron. The purpose of this experiment was to measure La and Lc in films which had not been heated above the decomposition temperature of cementite. The electron diffraction pattern shown in fig.79 is taken from a specimen heated at 1200°C in argon followed by heat treatment in chlorine at 100°C and shows very broad peaks indicating very small values for La, Lc (~ 20Å for La). The micrograph corresponding to this specimen shows how the chlorine is attacking and changing the appearance of the particles.

10.11. Anisotropic layer growth.

Presland and White reported large variations in the

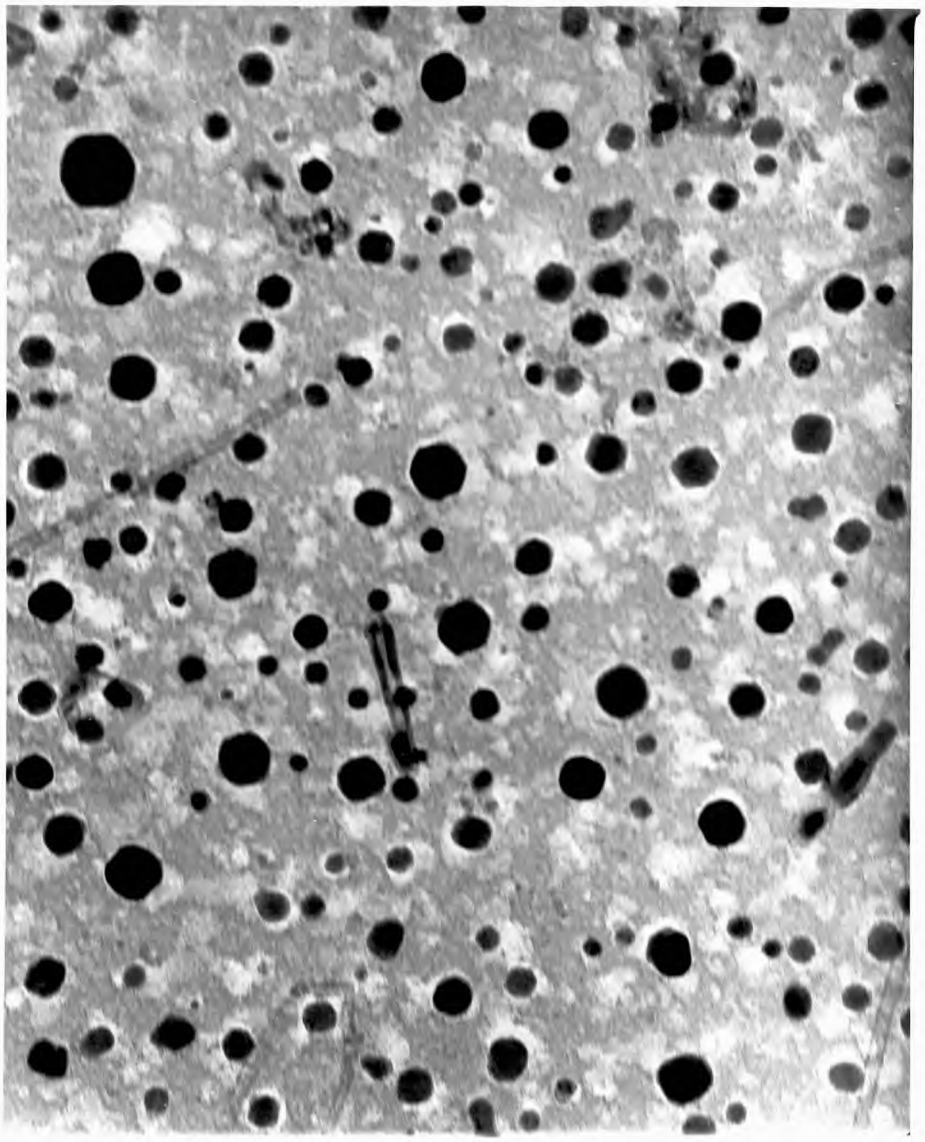


FIG 77 X 80,000

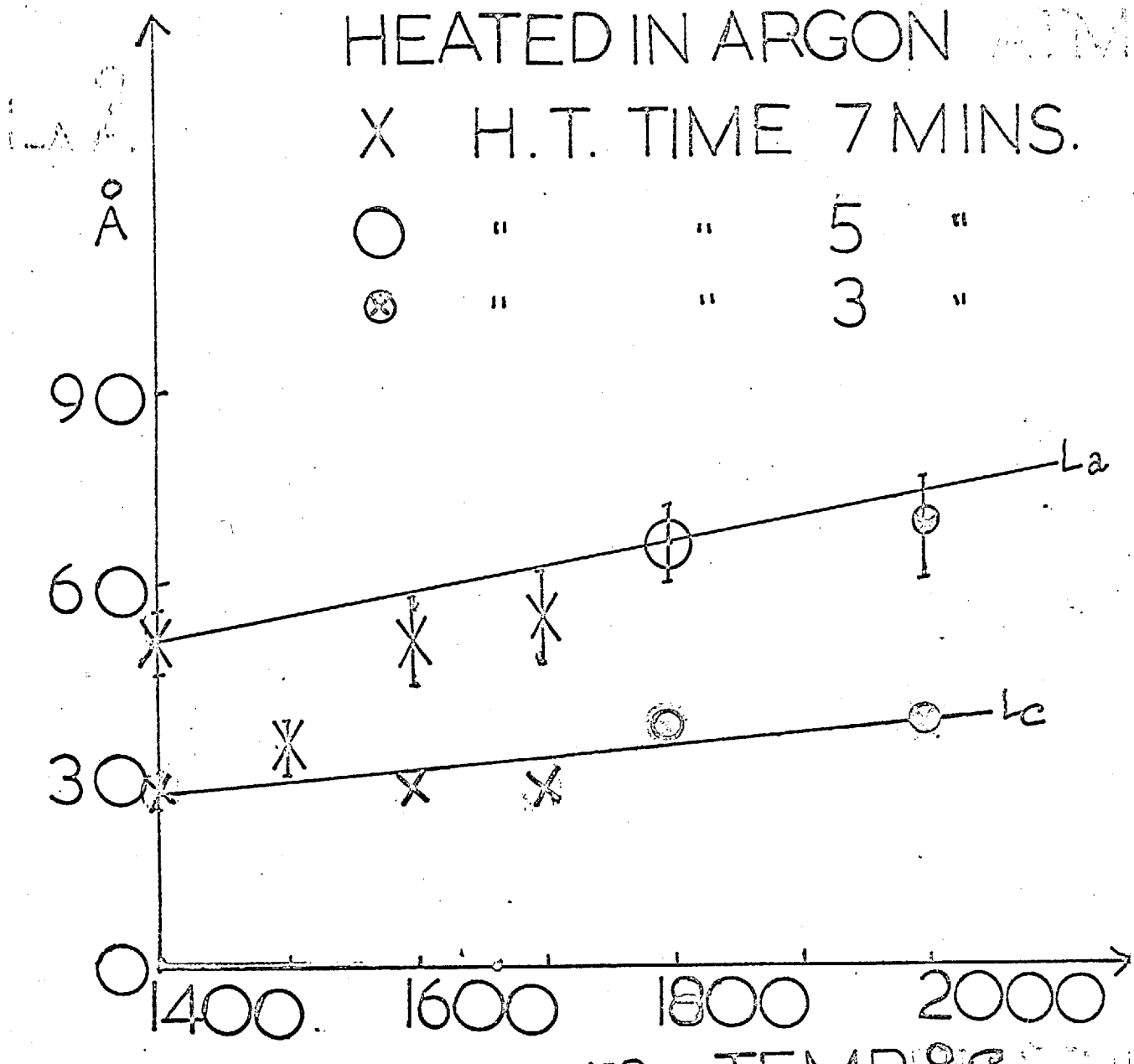
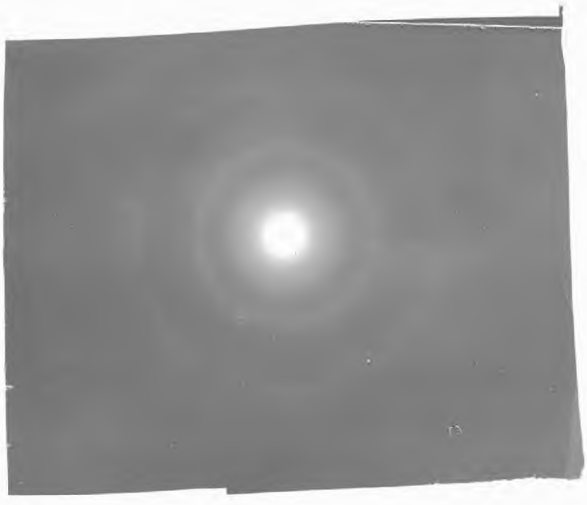

HEATED IN ARGON
X H.T. TIME 7 MINS.
" " 5 "
" " 3 "
Å
90
60
30
0
La
Lc
1400
1600
1800
2000
TEMP. °C

FIG. 78



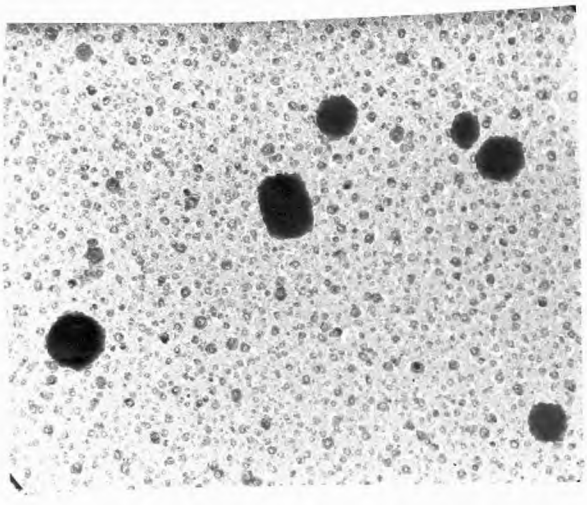


FIG 79 X 40,000

values of La in pure heat treated carbon film measured from the same ring using the same plate but along different diameters.[67] They investigated the effect further by measuring line breadths as a function of azimuth angle around a diffraction ring, and showed that the value of La measured in this way varied periodically with azimuths, the period being π . They concluded that crystallites in the film were growing anisotropically parallel to the basal plane and this conclusion was subsequently confirmed by electron microscopy of similar films heated at much higher temperatures (2400°C) which showed lathe shaped crystallites.

This effect was sought in present study using a specimen containing a small amount of iron. Line breadths from (10) and (11) relfections and also from the (002) reflections were measured at different azimuthal angles, at intervals of 20°. No systematic variation was observed and the values of La and Lc appeared to be constant to within the limits of accuracy obtainable.

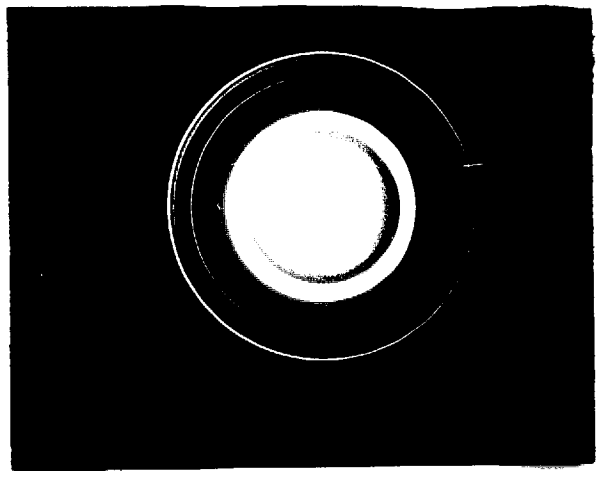
CHAPTER XI

11. Effect of other metals.

Composite films of carbon and other metals like platinum, nickel, vanadium and copper were produced by co-evaporation in the same manner as carbon/iron films. These were then heated in vacuo at different temperatures followed by characterisation by electron diffraction and microscopy.

11.1. Platinum/carbon system.

The composition of the film was determined and was found to be 20.0 wt. percent (1.5 at %) platinum. Electron diffraction patterns from the films heat treated at 700-1000°C gave rings belonging to platinum only; a specimen heat treated at 1100°C for 15 minutes, however, showed extra rings in addition to those attributable to f.c.c. platinum. The electron diffraction pattern and a corresponding micrograph are shown in fig. 80. The lattice spacings corresponding to these additional rings are shown in table 7. Some of them are clearly due to presence of carbon, but at least three, with spacings 2.79, 1.73 and 1.59 angstroms cannot be attributed to either platinum or carbon. They do however coincide with the forbidden reflections of platinum, i.e. those which should have a structure factor of zero. These additional lines can therefore be described



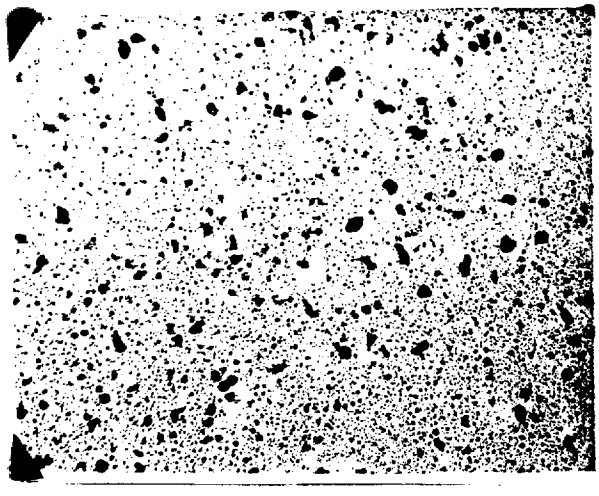


FIG 80 X40,000

TABLE 7

EXPERIMENTAL VALUES.			PLATINUM A.S.T.M.				GRAPHITE		P.CUBIC CELL.	
Ring No.	Dia.Cm.	Int.	dÅ	dÅ	Int.	hkl	dÅ	hkil	dÅ	hkl
1.	1.10	V.W.	4.32							
2.	1.4	S	3.39				3.35	0002		
3.	1.7	W	2.79						2.77	110
4.	2.1	S	2.26	2.26	100	111				
5.	2.25	M	2.10				2.12	$10\bar{1}0$		
6.	2.45	S	1.94	1.96	53	200				
7.	2.75	W	1.73						1.75	210
8.	3.0	W	1.59						1.60	211
9.	3.45	S	1.37	1.38	31	220				
10.	3.85	M	1.23				1.23	$11\bar{2}0$	1.24	310
11.	4.0	S	1.19	1.18	33	311				
12.	4.2	W	1.13	1.13	12	222				
13.	4.5	W	1.05				1.06	$20\bar{2}0$	1.05	321
14.	4.85	W	.980	.980	6	400	.969	$11\bar{2}4$		
15.	5.3	M	.897	.900	22	331				
16.	5.4	M	.880	.877	20	420				
17.	5.95	M	.799	.800	29	422				
18.	6.3	W	.754							

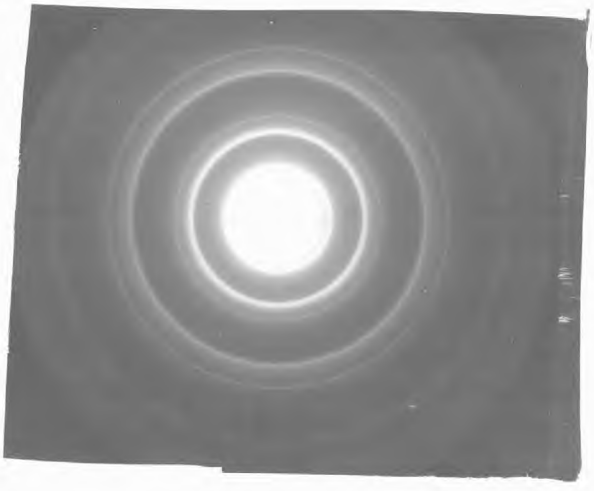
as superlattice reflections and can be interpreted by assuming that carbon atoms replace a number of platinum atoms in the platinum unit cell.

This result appears to confirm the findings of Konig[179] who made an electron diffraction study of a specimen produced by alternate deposition of carbon and platinum on a thin collodion film followed by heating in vacuo at 1100°C for several hours. The appearance of the primitive cubic superlattice lines was believed to be due to the production of a platinum carbide.

At 1200°C the diffraction pattern consisted of platinum and graphite lines only and the extra lines were found to disappear. The specimen was then heated at temperatures higher than this and at 1400°C it was found that the metal was vaporised leaving behind graphitic carbon only. From the diffraction pattern obtained from such a film the La and Lc values were determined using half peak breadths and were found to be 67Å and 34Å respectively.

11.2. Nickel/carbon system.

A nickel carbon film containing 17 wt. percent nickel was produced by co-evaporation. The specimens prepared from this evaporation were heated at 300-900°C in vacuo and the electron diffraction patterns obtained in each case showed the production of a carbide. The lattice parameters calculated from a diffraction pattern of a specimen heat treated at 600°C for 2 hours is given in



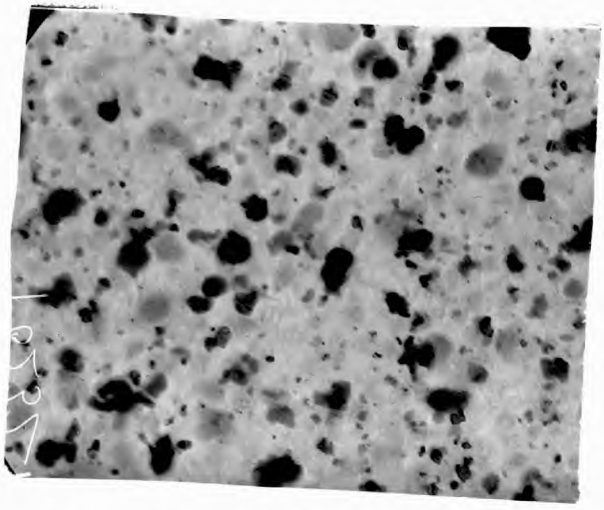


FIG. 81 X 40,000

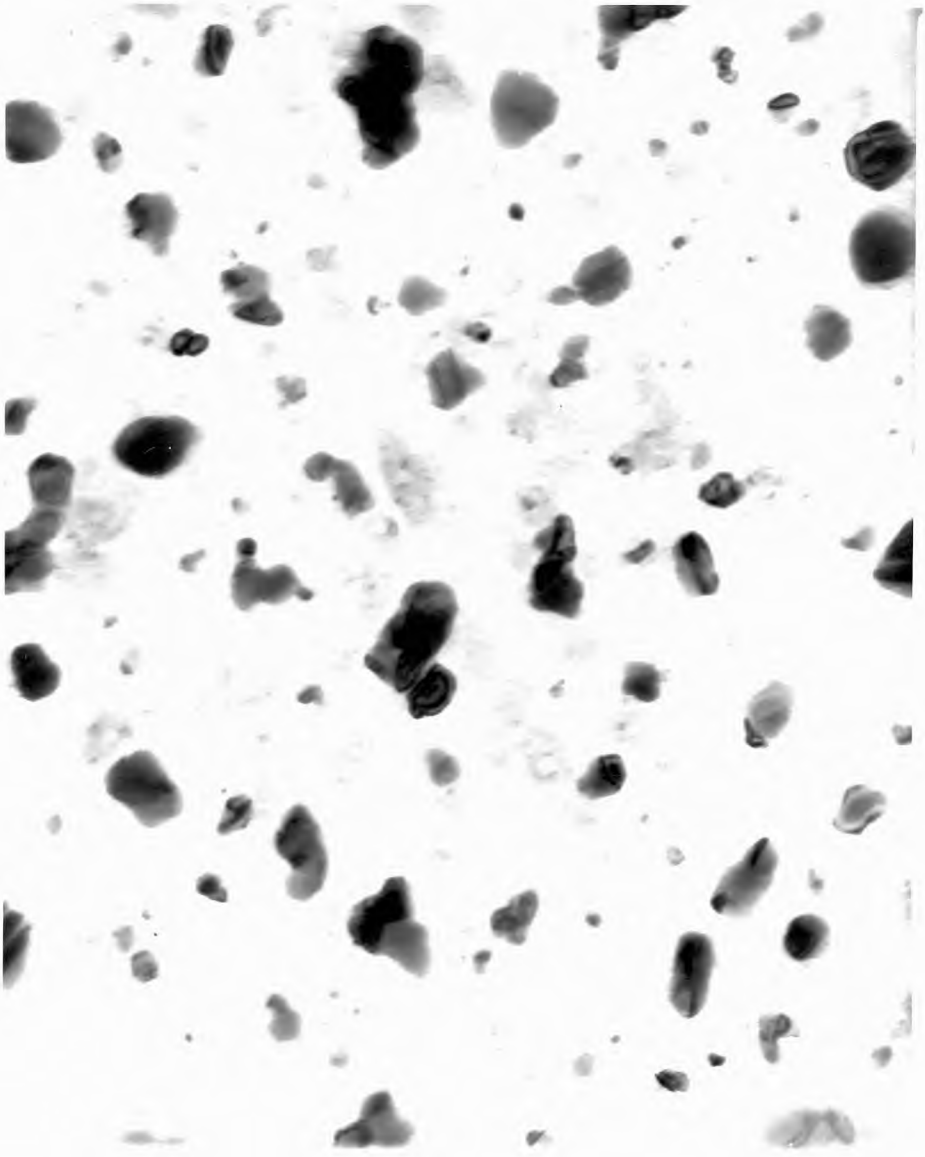


FIG 81B

x 80,000

Table 8. The last columns of the table represent the d-spacings for graphite and Ni_xc (x>4) taken from the A.S.T.M. index file. Fig. 81 shows the electron diffraction patterns and the microstructures of the carbide.

Table 8

Experimental values				Ni_xC, A.S.T.M.			Graphite	
Ring No.	Dia. Cm.	Int.	dÅ	dÅ	Int.	hkl	dÅ	hkil
1.	1.40	S	3.39				3.35	0002
2	2.25	M	2.11				2.12	$10\bar{1}0$
3	2.35	S	2.02	2.03	100	111		
4	2.70	S	1.76	1.76	80	200		
5	3.80	S	1.25	1.25	60	022		
6	3.90	M	1.21				1.23	$11\bar{2}0$
7	4.45	S	1.06	1.06	60	311		
8	4.70	V.W.	1.01	1.02	40	222		
9	5.40	V.W.	.88	.88	20	400		
10	5.85	M	.81	.81	60	133		
11	6.00	M	.79					
12	6.55	M	.72					

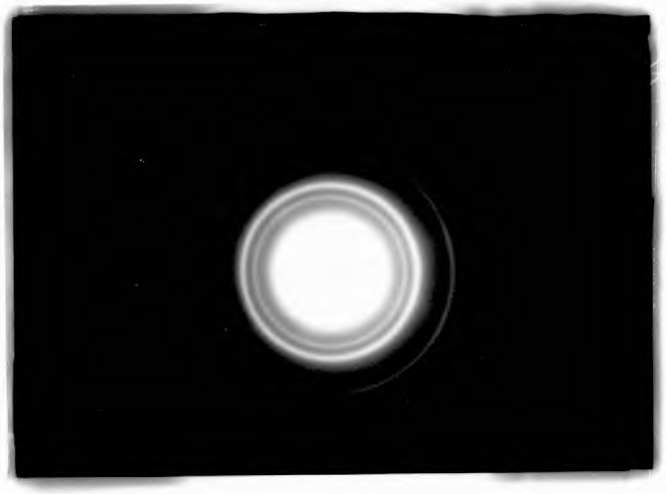
These results are clearly consistent with the nickel carbon compound Ni_xC (x>4) which has a lattice parameter of 3.536Å. The occurrence of this compound Ni_xC was also observed by Pugh[180] et.al. during their x-ray analysis of diamond. One of the specimens heat treated at 300°C was

reheated at 1200°C for half an hour to vaporise the nickel; the diffraction pattern of this specimen showed the presence of graphitic carbon only. La and Lc values were measured as before using half peak breadths and were equal to 64Å and 37Å respectively.

11.3. Vanadium/carbon system

A film was prepared by co-evaporation which was found to contain 7.4% wt. of vanadium. Specimens made from this film were heated in vacuum at 600-1000°C. The diffraction diagrams from specimens heated between 600-800°C produced a carbide whose chemical composition was VC as compared with the A.S.T.M. data; while specimens heat treated above 800°C produced some extra diffraction lines, some of them belonging to graphite and some to vanadium. The data for the lattice parameters obtained from the diffraction diagram corresponding to a specimen heat treated at 600°C for 2 hours have been tabulated below. The electron diffraction photograph corresponding to the data in table [illegible] is given in fig.82. This carbide was found to be stable up to 1200°C but at 1400°C the metal completely vaporised leaving behind graphitic carbon. The La and Lc values were measured for a specimen heated to this temperature and gave values of 51Å and 28Å respectively.

Recently Venables et.al.[182] reported that when a sample of the vanadium carbide with composition V_6C_5 is



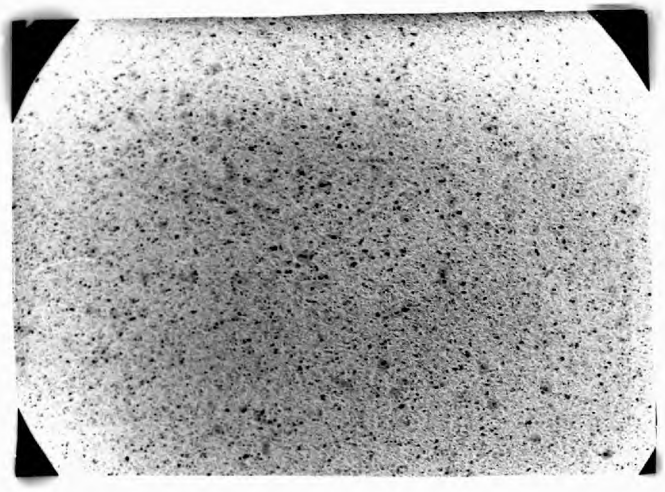


FIG. 82. X40,000

examined in a 100 kv electron microscope for an extended period the superlattice diffraction spots diminished in intensity and disappeared entirely after approximately half an hour. The conclusion that a refractory material like vanadium carbide can be damaged by an electron beam is somewhat surprising. In the present study this effect was investigated by exposing a specimen of vanadium carbide (VC) produced at 600°C to the 100kv electron beam for about an hour. No change at all in the intensity of the diffraction rings was observed.

Table 9

Experimental				A.S.T.M. data for Vc		
Ring No.	Diam.cm.	Int.	dÅ	dÅ	Int	hkl
1	1.95	S	2.43	2.40	100	111
2	2.30	S	2.06	2.07	100	200
3	3.25	S	1.46	1.47	50	220
4	3.80	M	1.25	1.25	25	311
5	3.95	M	1.20	1.20	10	222
6	4.55	V.W.	1.04	1.04	5	400
7	5.00	V.W.	.95	.95	5	331
8	5.10	M	.93	.93	10	420
9	5.66	M	.84	.85	5	422
10	5.95	V.W.	.79	.80	3	511,333

11.4 Carbon/copper system.

Several evaporations to produce a copper/carbon film were carried out but in no case could a film with more than .4 wt. percent of copper be produced. The difficulty of obtaining a higher copper concentration in the film was presumably due to the wide difference in vapour pressures of the two evaporants. The heat treated films with .4 wt% copper did not produce any carbide; this was not unexpected, since the phase diagram shows that this percentage of copper would remain in solution at all temperatures. The diffraction patterns gave broad diffraction rings even at temperatures up to 1000^{o}C suggesting that the copper present had no catalytic effect on graphitisation.

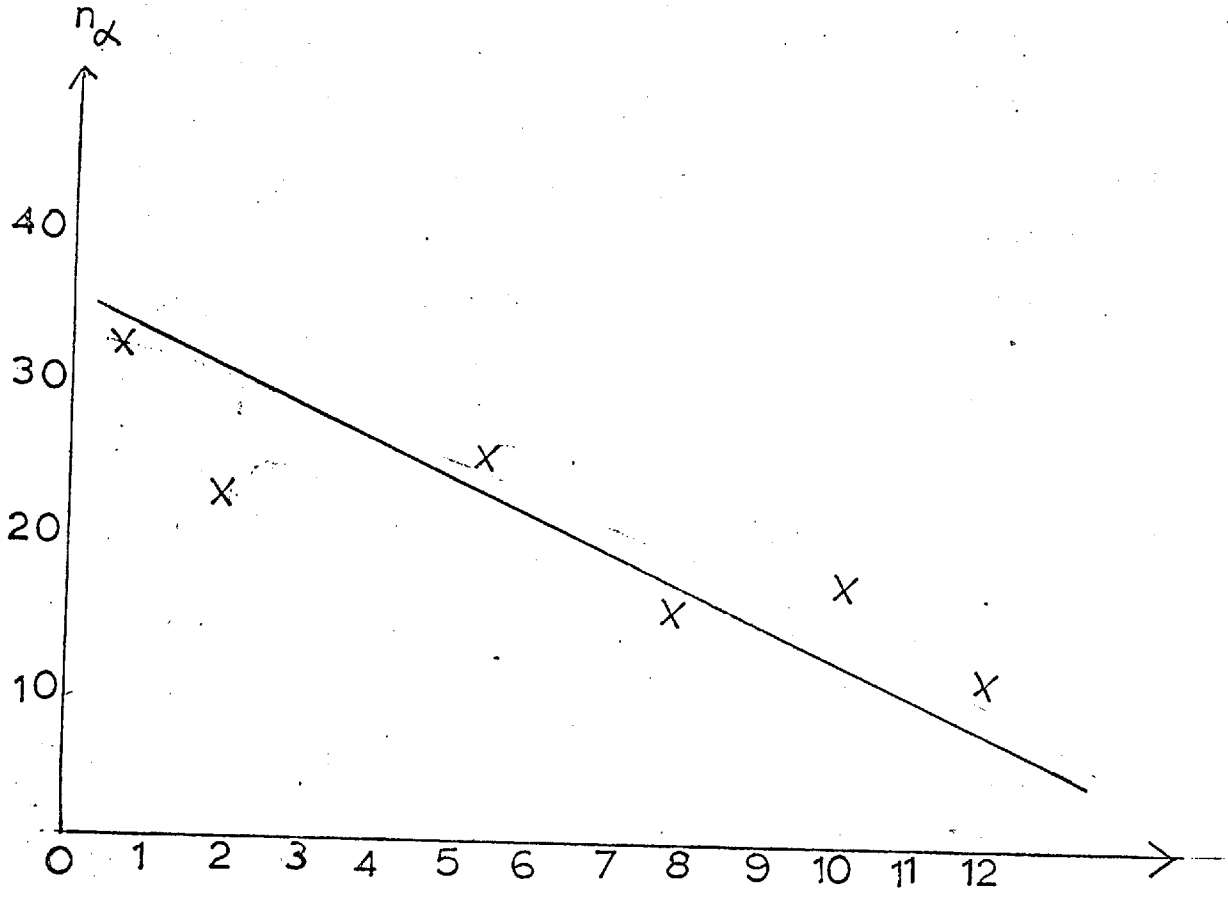


FIG.83

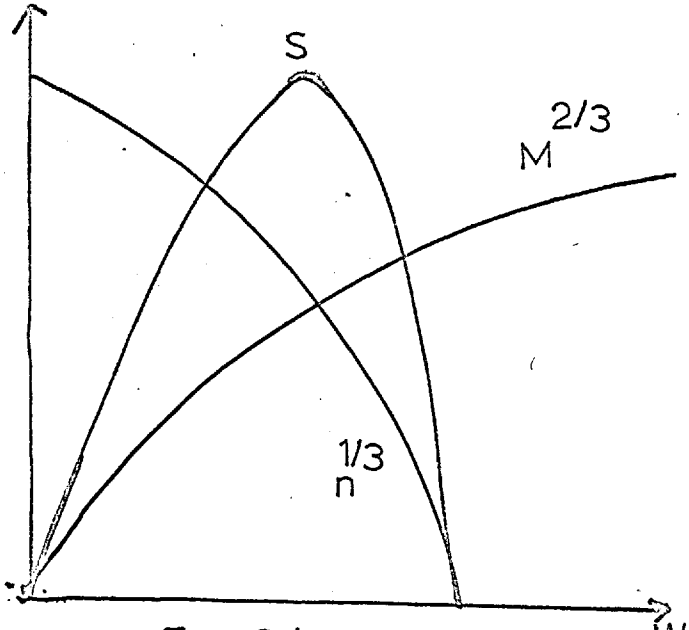


FIG. 84.

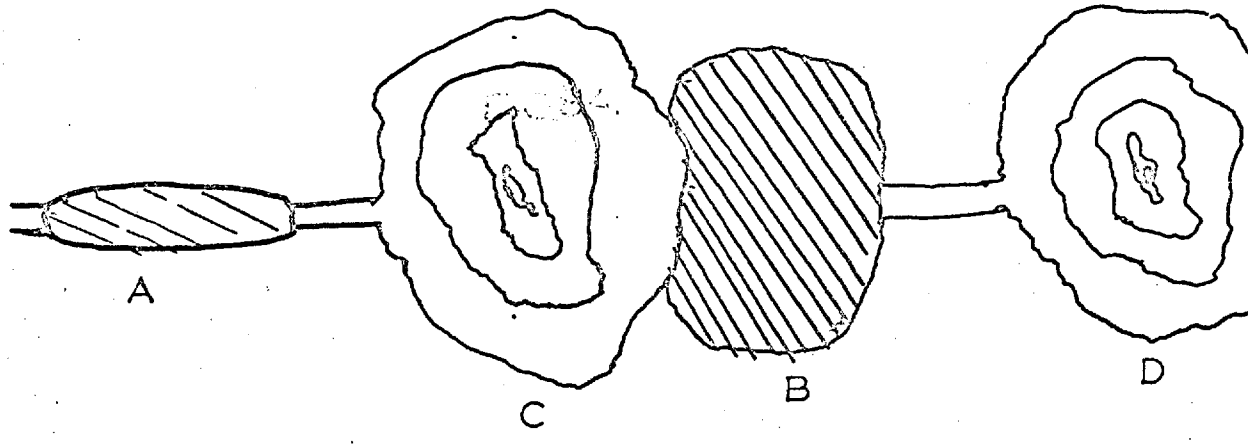


FIG. 84 A

CHAPTER XII

12. Discussion.

12.1. Preparation of thin metal/carbon films by coevaporation.

It has now been established that metal/carbon cermet films can be successfully prepared by co-evaporation of the two components using simple equipment. This is probably because the arc method for evaporating carbon produces a very rapid temperature rise, equivalent to flash evaporation, which is a standard technique for alloy evaporation. A serious limitation however, is that it is not possible to predetermine the composition of the condensed film and the method relies on the use of electron proble microanalysis. The latter is the only analytical technique of sufficient sensitivity and resolution to permit the accurate characterisation of the film in terms of composition and homogenity.

In every case examined the as-deposited film was found to be amorphous. By a simple extension of Mader's[132] equation, this situation could have been predicted since in all cases

$$T_s < .3\frac{(T_c + T_M)}{2} \quad \ldots\ldots\ldots\ldots \quad (91)$$

where, T_s = the substrate temperature,

T_M = M.P. of metal

T_c = M.P. of carbon.

It is not clear what value of T_c to take, but a lower limit to this is provided by T_M; Thus for example the R.H.S. of equation (91) would give 267°C in the case of iron so that a substrate at room temperature would be expected to lead to an amorphous deposit.

Mader was able to show that the co-evaporation technique can produce homogeneous alloys of a composition corresponding to a miscibility gap in the bulk phase diagram. For the metal/carbon systems studied in this thesis, bulk phase diagrams do not exist, at least over the ranges of composition investigated. The films produced however, behaved very similarly to Mader's, i.e. beginning with a homogeneous amorphous structure they gave rise to a metastable phase at a temperature approximately given by equation (90A). The only exception to this was the platinum/carbon system from which platinum was in general precipitated; even here however, an unusual phase appeared over a narrow temperature range (See chapter XI).

12.2 Phase transformation in metal/carbon films:

When carbon films containing iron, nickel and vanadium were heated a carbide was precipitated in each case. For iron this was cementite, Fe_3C, although the overall composition of the film was always very different from that which would correspond to Fe_3C ! the higher carbides which might

have been expected were not in fact observed. Similarly for nickel and vanadium a single carbide was precipitated in each case, regardless of the composition used. In the case of platinum the metal was usually formed, but even here some evidence was obtained for the production of a platinum-carbon compound which has been described in the literature as a carbide.(179)

In view of the small thickness of the films used it is interesting to speculate about the probable nature of the nucleation sites of the carbide particles. Thus it would not have been unreasonable to expect nucleation to occur at the film surfaces. That this was not so is borne out by Figs. 54, 55A, which show that even when the particle size was comparable with the film thickness there was no evidence that these precipitates had grown on the surface.

A serious limitation in the use of transmission electron microscopy for the study of precipitation in these films is lack of information provided concerning both position and size measured in a direction normal to the specimen plane. Thus not only are we unsure of the position of the precipitate particle within the film but we also lack knowledge concerning their thickness, and without this the relatively accurate measurement of precipitate diameter is limited in value. Thus the initial assumption that the cementite particles were spheroidal was easily demonstrated to be incorrect since it gave rise to a calculation of

cementite volume many times greater than the iron content of the film would permit. It was therefore assumed that the particles were discs lying within and parallel to the film and their volume was calculated by approximating them to oblate ellipsoid of revolution of constant eccentricity. This eccentricity was then calculated by equating the volume of the ellipsoid to the total possible volume of cementite, when the ellipsoids were at their largest.

The assumption of constant eccentricity throughout the growth of the precipitate particles is justified, according to Ham.[101]

The semi-minor axis b of the largest ellipsoids can be calculated from the estimated eccentricity e by using the relationship,

$$\frac{b}{a} = (1 - e^2)^{\frac{1}{2}}$$

Even for the largest particles b is only 12 Å and hence the particle thickness 2b is 24 Å. Hence 2b is much less than the film thickness.

The axial ratio $\frac{a}{b}$ is 10. This value should be compared with that found by Pitsch[183] who studied the precipitation of cementite in thin films of iron andalso found disc shaped particles of axial ratio 25 to 60. By plotting a function of the volume fraction of the precipitate against a function of the time according to the method of Zener and Wert a series of straight lines were obtained. This confirmed that

the precipitation was diffusion controlled. Also the exponent n (see equation 65) derived from the slopes of these lines was found to have 1.1. This is close to the value n = 1 predicted by Ham for the case in which disc shaped precipitate particles grow by a diffusion limited process, and again confirms the correctness of the assumption made as to the shape of the particles. It should also be noted that the value of n agrees well with the value of 1.15 found by Pitsch, the only other worker to have studied cementite growth in thin films (in his case, Fe.)

It is significant that the cementite particles are not only disc shaped but have their plane parallel to the film plane. This result is analogous to that found by Presland and White in their study of graphitisation in thin evaporated carbon films. They concluded from both diffraction and microscopic evidence that graphite crystallites grew in their films with their basal planes predominantly parallel to the film plane.

This type of preferred orientation may be due to two different types of mechanisms. First it may be assumed that the precipitate nuclei are planar, that they are oriented in all possible directions, that all grew with equal speed but only those parallel to the film plane succeed in growing large. This would imply however, that some precipitate particle should, in transmission, appear edge on, and these were never seen in the present work.

The second type of mechanism involves the assumption that the nucleus may be of any shape, but that the growth conditions are anisotropic, growth being favoured in the film plane as compared with the direction normal to the film plane. The results of Presland and White may possibly account for such an anisotropy of growth in the present instance. Thus it is being established that the rate of growth of the cementite particles is limited by diffusion of iron. As deposited amorphous carbon is isotropic but at the heat treatment temperature used in the present work some modification of the carbon structure will have begun. Any such changes will tend towards the formation of preferred orientation, as already shown by Presland and White, and this effect may well be enhanced by the presence of iron. This anisotropy of structure in the carbon matrix will give rise to an equivalent anisotropy in the diffusion coefficient of iron, the expected values being higher parallel to the film plane than normal to it. Thus the conditions for anisotropic growth of the cementite would be established.

Since thin solid films are usually produced with considerable residual stress, either tensile or compressive, it is of course possible for this stress to be responsible for the anisotropic growth of the precipitate. It is not immediately clear however, in the present state of knowledge of thin film stresses how this mechanism might work in detail.

12.3 Coarsening of precipitates:

During heat treatment the number of particles was found to decrease whilst the average particle size increased (See Fig.44). As a result of this so-called "coarsening" process the larger particles grew at the expense of the smaller ones. The driving force for the change is the tendency to reduce the total free energy of the system by reducing the total area of the precipitate/matrix interface. This involves the diffusion of solute atoms from regions close to the small particles to regions around the large particles, due to the fact that the concentration of solute atoms in the solution in equilibrium with a precipitate is larger in the case of small particles than for large particles.

12.4 Diffusion of metals in carbon:

Thin films prepared by co-evaporation of carbon and a metal have shown themselves to be extremely useful for the measurement of diffusion coefficients. Thus, since the growth of the cementite in the iron/carbon system has been shown to be diffusion controlled it follows that the growth of the precipitate can be used as a measure of the diffusion rate.

In view of what has been said earlier about the anisotropy of diffusion in thin films the two dimensional approach based on the use of Einstein's equation (Chapter IX) provides a relatively simple method of measuring the diffusion coefficient, at least to within an order of magnitude, and can also be used to give an estimate of the activation energy

for diffusion. In fact the latter value (19.5 k.cal) is not too far from the value of 16.1 k.cal obtained by using the Zener-Wert method.

It has not been possible to find a value for the diffusion coefficient of iron in carbon in the literature. Wolfe [184] et al. have used a radio tracer method to measure the diffusion coefficients of Ag, Ni, U, Th and Ra in 3 different graphites; for Ni they reported activation energies of 47.2 ± 2.2 k.cal for diffusion in the a-direction and 53.3 ± 4.8 k.cal for diffusion in the c-direction, using pyrolytic graphite. Truitt et al [185] reported the activation energy of thorium in pyrolytic carbon (c-direction) as 60 k.cal/mole.

These values are considerably higher than those measured for iron in carbon using the techniques described in this thesis. A possible reason for this is that the structure of evaporated carbon is quite different from that of pyrolytic graphite. In particular, it is almost certainly porous, and the low values 16-20 k.cals for the activation energy may correspond to diffusion of iron over the internal pore surfaces.

Thus, it is interesting to note that the activation energies found are similar to that reported by Wert for the precipitation of cementite from super saturated ferrite in the temperature range 25-315°C, namely 18.4 k.cal/mole. When one campares the relative atomic sizes of iron and carbon, this result seems surprising, since the iron atom is

larger than the carbon atom. It should be borne in mind, however, that in practice a carbon body is likely to consist either of graphite, with its very large c-spacing of about 3.4 Å, or of a less well defined carbon with considerable porosity, so that the diffusion of iron may be relatively easy, at least as far as the activation energy is concerned.

On the other hand, the values for D_o of 3.7×10^{-12} $cm^2/sec.$ using Einstein's equation and 4.9×10^{-12} $cm^2/sec.$ using the Zener/Wert method also seem extraordinarily low. For example Wolfe found $D_o = 2.2$ $cm^2/sec.$ for the diffusion of Ni along the c-axis of pyrographite while the results of Truitt et al for the diffusion of Thorium along the c-direction of Pyrolytic carbon suggest a value of $D_o \approx 3 \times 10^{-6}$ $cm^2/sec.$

It is difficult to suggest an explanation for these very low diffusion coefficients; they do, however, seem to indicate that if metallic atoms can be trapped within a carbon having a structure similar to that of evaporated carbon, they would aggregate only with difficulty. This could be of considerable importance with regard to the in-service behaviour of catalysts embodying finely divided metals distributed within the so-called molecular sieve carbons. Clearly more work is required to evaluate the diffusion coefficients of catalyst metal under these conditions, and the techniques described here might prove extremely valuable for this

purpose. In particular it should be noted that, while the accuracy of the method may not be high, it is extremely sensitive. Qualitatively the results obtained using Ni and Pt seem to show that the diffusion rates for these metals were certainly not higher than those found for iron.

12.5 Decomposition of carbides.

In films formed by co-evaporation of carbon with iron, nickel and vanadium, carbides were formed, and these decomposed on heating to temperatures above about 1000°C. In each case the films after decomposition showed the presence of carbon only, all traces of metal having disappeared. Presumably this was because the metals formed as a result of the decomposition reaction were lost. Consider the case of iron. Its vapour pressure is approximately 10^{-5} torr at 1094°C, and it seems possible therefore that the decomposition reaction was accompanied by loss of iron through evaporation, since heat treatments were normally carried out at a pressure of $\sim 10^{-5}$ torr.

Heat treatments carried out in atmospheric argon, however, also resulted in carbide decomposition and loss of iron at temperatures above 1800°C, although the temperature at which the vapour pressure of iron becomes equal to 760 torr is 2735°C. There are two possibilites here. Iron must have been lost to the film either by surface diffusion to the graphite mount or by vapour phase transport to the cooler

part of the furnace (the argon furnace uses a flow system).

Attempts were made to characterise the morphology of the iron carbide particles during decomposition; and to relate them to the structure of the carbon film formed after decomposition. Thus fig.54, which is a transmission micrograph of a film which has undergone partial decomposition, contains three different types of feature. The large partially transparent particles (A) are cementite, probably little thicker than the film itself. The spherical particles (B) were only observed during the decomposition, and probably consist of pure iron, perhaps in a molten state, undergoing evaporation. They were frequently observed adjacent to the "shell" structures (C) which correspond to fully decomposed carbide particles and are in evidence in all films heat treated above 1000°C. (Cf. FIG. 84A)

These shell features can be seen also in fig.66 which is a scanning micrograph of a fully decomposed film.

From this evidence it may be concluded that the carbide particles, even at their largest are either flat or are raised very little above the surface, but that bubble shaped features are produced when they decompose. A possible explanation for this may be as follows: when the carbide particle decomposes it does so from the outside in, producing a shell of carbon around itself. If this shell were relatively impervious to iron vapour, the pressure within

the shell would increase as decomposition proceeded, and might become sufficient to inflate the shell. This vapour would then find its way out of the shell, either continuously by diffusion or instantaneously through a break in the shell wall. Fig. 81B which shows a partially decomposed nickel/carbon film seems to prove that loss of metal has taken place intermittently and incidentally confirms that the mechanism suggested above for the decomposition of cementite also applies to the nickel case.

Unfortunately, this explanation does not account for the presence of solid or molten iron in spherical globules close to the decomposed cementite particles, and this observation seems to suggest that the iron formed during decomposition goes through a transition state in which it is liquid, prior to evaporation.

12.6 Graphitisation catalysis.

The "inflation" mechanism suggested above would require, first, that the iron and nickel carbide particles decomposed at the surface initially, and second, that the carbon so formed was relatively impervious to iron and nickel vapour. These requirements would be met if the carbide formed a graphitic carbon on decomposition, and if the c-axes of the crystallites so formed were parallel to one another and perpendicular to the carbide surface at every point. The structure of this carbon would thus be similar to that of

a pyrolytic deposit, the permeability would be low parallel to the c-axis and the orientation of the graphitic carbon would be governed by the orientation of the carbide surface.

It is suggested that the major effect on graphitisation of adding iron and nickel was the result of this process.

Thus, Acheson's theory that the catalytic action is based on the formation and decomposition of carbides is verified. The present investigation does not support Yamada's conclusion that iron can catalyse the graphitisation of carbon without formation of a carbide; there is no evidence that iron acts by dissolving the carbon and segregating it as graphite.

Let us consider first an alternative proposition, viz. that iron atoms can enhance graphitisation simply by diffusing through the carbon. Fig.71 demonstrates that this is not true. In both cases the same amount of iron has diffused through the film and been lost to the external environment, yet those films which were pre-treated so as to allow cementite to form proved to be much more graphitic. Furthermore, all the results of the prenucleation experiments show that the values of both La and Lc in the final carbon film increase with increasing cementite particle size in the prenucleation stage. Thus, increasing the prenucleation time and temperature, and increasing the iron concentration, all lead to increased cementite particle diameters as shown by figs. (33, 35, 40); figs. (71, 75, 76) show that these same treatments also increase L_a and L_c .

The lateral extent of the carbon crystallites (i.e. the local value of L_a) formed by the surface decomposition of cementite would be affected by the radius of curvature of the cementite surface at that point. Thus the larger the cementite particle, and the flatter its surface, the more graphitic (in terms of increased L_a) would be the carbon formed.

There is another factor, however. Fig. 72 shows that the improvement in L_a as a result of prenucleation of cementite is not monotonic with increasing iron concentration, but falls after reaching a maximum. It may be that this effect is due to the importance of the cementite surface. Thus it can easily be shown that the surface area 'S' of the cementite within the film is proportional to the product of $n^{1/3}$ and $W^{2/3}$, where n is the number of particles per unit volume, and W is the weight percentage of iron. Fig.83 shows that n falls with increasing W, so that the effect of W on S can be shown schematically in fig. 84. It can be seen that S has a maximum and is similar in shape to fig. 84. It seems possible therefore that the cementite surface plays an important role possibly through the fact that the most graphitic carbon is formed at the outer carbide/carbon interface, and as this interface moves inwards the local value of L_a decreases.

It is suggested therefore that the effect of iron on graphitisation is via the formation of cementite particles.

This leads to the conclusion that a two phase carbon structure should be produced after cementite decomposition, since the most graphitic carbon will be localised at the sites of the cementite particles, while the matrix carbon from which, and through which, the iron diffused to form the cementite, will still be relatively amorphous. This prediction is at least partially confirmed by evidence such as fig.60. This dark field micrograph was obtained by using the (002) reflection and demonstrates that the most graphitic parts of the film are localised. It has not yet however, proved possible by this method to show unambiguously that this graphitic carbon corresponds in position to the original cementite particles. This is because only a few basal planes can be selected at any one time by the dark field technique. Examination of fig. 81B however, which is a bright field micrograph showed dark concentric rings which are the traces of successive decomposition shells. Since no metal is present the enhanced scattering which gives rise to the dark rings is probably due to the presence of carbon crystallites oriented with their basal planes parallel to the electron beam. These would lead to strong scattering outside the objective aperture.

The crystallite diameters are crystallite heights and in heat treated carbon films can be estimated from the moiré patterns produced by the overlapping crystallites with their basal planes roughly parallel to the beam.

From these moiré bands, which correspond to crystallite boundaries, the L_a and L_c values can be estimated. From fig. 60 the highest La and Lc values estimated are 500 Å and 167 Å respectively. These are roughly seven times larger than those calculated from the diffraction analysis for the same specimen. The diffraction results give an average value only however, and the discrepancy serves to reinforce the conclusion that the local values of La and Lc at positions corresponding to the original carbide/carbon interface are much larger than the average for the film.

The major difference between diffraction patterns obtained from carbon films after cementite decomposition, and pure carbon films of the type studied by Presland and White, is that the former contain (002) rings while the latter do not. This difference appears now to arise from the fact that in the former case graphitic carbon was produced with basal planes tangential to the local cementite/carbon interface, coupled with the fact that this interface is roughly spheroidal. Thus all orientations of the carbon c-axis arise.

12.7 Other metals.

12.7.1. Nickel.

The results for nickel were very similar to those obtained using iron, and much of what has been said about the mechanism for catalysis of graphitisation applies equally

well to nickel. This is curious however, in that the nickel analogue of cementite viz. Ni_3C is reported to be unstable above about 500°C. The carbide observed in this work was not however, Ni_3C but an indeterminate compound previously reported by Pugh[180] et al with the formula Ni_xC where $x > 4$

12.7.2. Vanadium:

Vanadium/carbon films behaved similarly to the iron/carbon and nickel/carbon systems, in that a carbide, VC was precipitated, and the decomposition of this carbide resulted in enhancement of graphitisation. The details of the decomposition process were not studied, since only one composition (7.4wt.% V) was investigated, and the largest VC particles formed were smaller than the film thickness.

12.7.3. Platinum.

The main difference between the platinum/carbon system and those described above was that the metal alone was precipitated on heating, except for the anomalous effect observed at 1100°C. The presence of superlattice reflections at this temperature may indicate that the carbon which is undoubtedly dissolved in platinum at this temperature takes up regular positions in the platinum lattice.

It is of interest to note, first. that platinum could be removed from the film by heating to 1400°C in vacuo, second, that the resulting carbon films were more graphitic than

uncatalysed carbon film at this temperature and third, that these carbon films gave (002) reflections. The last point seems to show that graphitisation was enhanced in that carbon which was adjacent to the platinum-carbon interface.

12.7.4. Copper.

As stated in Chapter XI the copper concentration attained was insufficient to produce any observable results from this system. It may be important in this context that copper had the lowest melting point of all the metals studied and it may be that the difference in vapour pressure between copper and carbon was too great to permit the formation of films of higher copper concentration.

12.8 Future developments.

This preliminary study used a rather crude method for the formation of metastable cermet films by co-evaporation. To make further use of such films, a more sophisticated preparation technique is needed. Two possibilities present themselves. The first is to use two separate electron beam sources, each with its own shutter and deposition rate monitor; this would have the advantage that both composition and film thickness could be predetermined. An alternative approach would be to prepare an intimate mixture of the two constituent elements in powder form to pelletise this under pressure and to use it as the target in a shuttering system, since sputtering has the advantage that the composition of

the deposit is the same as that of the target.

An interesting variant on the approach used in the present work would be to co-deposit the components onto substrates held at varying temperatures below the decomposition temperature of the appropriate carbide. A large effect on the nucleation and growth of the carbide would be expected which in turn would influence the structure of the resulting carbon films formed after decomposition.

A number of improvements could be suggested which would lead to better characterisation. If thick enough deposits could be produced (at least .1 mm) then x-ray techniques would become available. Unfortunately neither vacuum evaporation nor sputtering lend themselves to the formation of other than thin films. Better results can be achieved with electron diffraction however, especially if a combination of scanning diffraction and energy analysis is used. The reason for this is that much of the inaccuracy which arises during profile studies is due to the presence of a large background component of inelastically scattered electrons. These have suffered an energy loss and Grigson [186, 188] has shown that by using filtering techniques much improved electron diffraction profiles can be obtained.

This, in turn leads to the possibility of making measurements of carbide volume by estimating the area under a specific diffraction peak, and it would be instructive to

compare this with the results obtained by direct imaging. The latter, too, could be refined by making more use of the image analysing computer, especially in the more advanced form now available. Thus, if a full prticle size distribution were obtained for each specimen, the analytical methods of Woodhead[187] could be used to study the nucleation and growth of the carbides.

One of the difficulties encountered in the present investigation was that when the cementite particles were conveniantly large enough for detailed study, they exceeded the film thickness. The use of high voltage electron microscopy would make it possible to examine films upto ten microns in thickness (assuming these could be made). They could also be heat treated in situ so that the detailed behaviour of the cementite particles during formation and decomposition could be followed.

Reflection electron diffraction would also provide useful crystallographic information on the decomposition of cementite if the latter could be obtained in film form, perhaps by the hot substrate method referred to above.

Finally, more detailed studies on the relationship between the graphite parameters La and Lc and the surface area of the carbide precipitate particles should be carried out.

REFERENCES

1. W.H.Bragg and W.L.Bragg, Proc. Roy. Soc. (London A 89, 277, 1913.
2. J.D.Bernal, Proc. Roy. Soc. A 100, 749, 1924.
3. A.W.Hull, Phy. Rev. 20, 113, 1922.
4. H.Lipson, A.R.Stokes, Nature, 146, 130, 1942.
5. E.J.Freise, A. Kelly, Phil. Mag. 8, 1519, 1963.
6. Chemistry and Physics of carbon Vol. I, P.1. P.L. Walker edited.
7. S.Amelinekx, P.Delavignette, J. Appl. Phy. 31, 2126, 1960.
8. P.Delavignette, S.Amelincks, J. Appl. Phy. 31, 1961, 1960.
9. F.E.Fuzita, K.Izui, J.Phy. Soc. Japan 16, 214, 1961.
10. H.Hashimoto, R.Uyeda, Acta. Cryst. 10, 143, 1957.
11. I.M.Dawson, E.A.C.Follett, Proc. Roy. Soc. A 253, 390 1959.
12. J.M.Thomas, Chemistry and Physics of Carbon. Vol. I, P. 121, P.L.Walker edited.
13. C. Roscoe, J.M.Thomas, Carbon, 4, 383, 1966.
14. G.Hughes, J.M.Thomas, H.Marsh, R.Reed, Carbon I, 339, 1964.
15. J.M.Thomas, C.Roscoe, K.M.Jones, G.D.Ranshaw, Phil. Mag. 10, 325, 1964.
16. K.Wirtz Int. conference on peaceful uses of Atomic energy, United Nations New York, 8, 496, 1956.
17. P.L.Walker, G.Imperial, Nature 180, 1184, 1957.

18. T.Tsuzuku, Proc. 3rd Carbon Conference 433, 1959.

19. L.C.F.Blackman, A.R.Ubbelohde, Proc. Roy. Soc. A 266, 20, 1962.

20. L.M.Foster, G.Lang, H.C.Stumpf, American Min. 43, 285, 1958.

21. S.B.Austerman, S.M.Myron, J.W.Wagner, Carbon, 5, 549, 1967 Pergamon Press.

22. A.E.B.Presland, P.L.Walker, Carbon, 7, 1, 1969 Pergamon Press.

23. A.R.Brown, G.R.Hall, W.Watt, Nature, 172, 1145, 1953.

24. L.C.F.Blackman, G.A.Saunders, A.R.Ubbelohde, Proc. Roy. Soc. A 264, 19, 1961.

25. A.W.Moore, A.R.Ubbelohde, D.A.Young, Proc. Roy. Soc. A 280, 153, 1964.

26. R.J.Diefendorf, J. Chem. Phy. 57, 815, 1960.

27. J.H.Oxley, A.C.Serest, N.P.Veigil, J.M.Blocher, Am. Inst. of Chem. Eng. J. 7, 489, 1961.

28. T.J.Hirt, H.B.Palmer, Carbon 1, 65, 1963, Pergamon Press.

29. J.C.Bokros, Carbon 3, 17, 1965, Pergamon Press.

30. R.J.Price, J.C.Bokros, K.Koyama, J.Chiu., Carbon 4, 263, 1966, Pergamon Press.

31. J.R.Bokros, Carbon, 3, 201, 1965, Pergamon Press.

32. R.Bacon, J. Appl. Phy. 31, 283, 1960.

33. L. Meyer, Proc. 3rd carbon conf. 451, 1959.

34. B.E.Warren, Phy. Rev. 59, 693, 1941.

35. B.E.Warren, P.Bodenstein, Acta Cryst. 18, 282, 1965.

36. D.E.Bradley, Brit. J. Appl. Phy.5,65, 1953.

37. A.Cosslett, V.E.Cosslett, Brit. J. Appl. Phy. 8, 374, 1957.

38. J.Kakinoki, K.Katada, T.Hanawa, Acta Cryst. 13, 448,1960.

39. J.A.Turnbull, G.M.Jenkins, G.K.Williamson, J.Nuc. Mats. 7, 215, 1962.

40. A.E.B.Presland, J.R.White, Carbon 7, 77, 1969 Pergamon Press.

41. J.J.Becker, Ph. D. Thesis, Univ. of London 1966.

42. U.Hoffman, Ber, 13, 65, 1821, 1932.

43. H.E.Blayden, H.L.Riley, A.Taylor, J. Chem. Soc. 67, 1939.

44. H.E.Blayden, H.L.Riley, A.Taylor, J. Chem.Soc. 62, 180, 1940.

45. J.J.Kipling, R.B.Wilson, Trans Faraday Soc., 56, 557, 1960.

46. J.J.Kipling, B. McEnancy, Fuel, 43, 367, 1964.

47. J.J.Kipling, J.N.Sherwood, P.V.Shooter, N.R.Thomson Carbon 1, 315, 321, 1964.

48. R.E.Franklin, Proc. Roy. Soc. A 209, 196, 1951.

49. C.R.Kinney, Proc. of the 1st and 2nd Carbon Conf. P.83, 1956.

50. C.R.Kinney, R.C.Nunn, P.L.Walker, Jr. Ind. Eng. Chem. 49, 880, 1957.

51. J.M.Thomas, J.O.Williams, H.Marsh, B.Rand, Carbon, 4, 143, 1966.

52. R.E.Franklin, Acta Cryst. 4, 253, 1951.

53. G.E.Bacon, Acta Cryst. 4, 558, 1951.

54. C.R.Houska, B.E.Warren, J.Appl. Phy. 25, 1503, 1954.

55. J. Maire, J.Mêring, Proc. 3rd Carbon Conf. 337, 1957.

56. J.Maire, J.Mêring, Industrial Carbon and Graphite P.204. Soc. of Chem. Ind. London 1958.

57. H.Takahashi, H.Kuroda, H.Akamato, Carbon, 2, 432, 1965, Pergamon Press.

58. J.Méring, J.Maire, J.Chim. Phys. 57, 803, 1960.

59. W.Ruland, Acta Cryst. 18, 992, 1965.

60. S.Mizushima, Proc. 4th Carbon Conf. 417, 1959, Pergamon Press.

61. J.A.Turnbull, G.K.Williamson, Trans. Brit. Ceramic Soc. 62, 807, 1963.

62. F.V.Fair, F.M.Collins, Proc. 5th Carbon Conf. Vol. I, 503, 1961, Pergamon Press.

63. S.Mizushima, Proc. 5th Carbon Conf. Vol. 2, 439, 1961, Pergamon Press.

64. D.B.Fischbach, Appl. Phys. Letters, 3, 168, 1963.

65. D.B.Fischbach, Nature, 200, 1281, 1963.

66. J.R.White, Ph.D. Thesis, Univ. of London, 1968.

67. A.E.B.Presland, J.R.White, In the Press.

68. E.G.Acheson, U.S.Patent Nos. 40756, 573523, 695405, and 732202.

69. H.Akamatu, K.Sato, J. Phy. Soc. Japan, 22, 127, 1949.

70. I Yamada, Symposium on Carbon, Session III - 21, Tokyo, 1964.

71. T.Ishikawa, S.Magari, Y Mizutani, S.Yoshizawa, Tech. Repts. Eng. Res. Inst. Kyoto Univ. No. 121, 1965.

72. T.Ishikawa, S.Magari, Y. Mizutani, S.Yoshizawa, Tech. Repts. Eng. Res. Inst. Kyoto Univ. No. 125, 1966.

73. J. Gillot, B.Lux, P.Cornuault, F.Duchaffant, J. Appl. Chem. 17, 298, 1967.

74. S.M.Irving, P.L.Walker, Jr. Carbon 5, 399, 1967, Pergamon Press.

75. A.E. Karu, M.Beer, J.Appl. Phy. 37, 2179, 1966.

76. S.D.Robertson, Nature, 221, 1044, 1969.

77. T.Noda, Y. Sumiyoshi, N. Ito, Carbon, 6, 813, 1968, Pergamon Press.

78. A.S.Schwartz, J.C.Bokros. Carbon 5, 325, 1967, Pergamon Press.

79. C. Yokokawa, K. Hosokawa, Y.Takegami, Carbon 5, 475, 1967, Pergamon Press.

80. T. Noda, M. Inagaki, Carbon, 2, 127, 1964, Pergamon Press.

81. T.Noda, M. Inagaki, T.Sekiya, Carbon, 3, 175, 1965, Pergamon Press.

82. J. D.Watt, R.E.Franklin, Ind. Carbon and Graphite P.321, London, 1958.

83. M.L.Pearce, E.A.Heintz, J. of Phy. Chem. 70, 1935, 1966.

84. R.H.Bragg, D.D.Crooks, R.W.Fenn, M.L. Hammond, Carbon 1,171, 1964, Pergamon Press.

85. T.Noda, H.Kato, Carbon, 3,289, 1965, Pergamon Press.

86. P.G.Shewmon, Diffusion in solids, McGraw-Hill Book Company Inc. 1963.

87. R.K.Hardy, T.J.Heal. Progress in Metal Physics, Vol. 5. P.143, Pergamon Press, 1954.

88. D.Turnbull, Solid State Physics, Vol. 3. P.225, Academic Press, 1956.

89. J.W.Christian, The Theory of transformations in Metals and alloys. Pergamon Press, 1965.

90. C.Zener, J. Appl. Phy. 20, 950, 1949.

91. C.Wert and C.Zener, J. Appl. Phy. 21, 5, 1950.

92. C.Wert, J. Appl. Phy. 20, 943, 1949.

93. D. Turnbull. Defects in crystalline solids, Phy. Soc. London. P.203, 1954.

94. W.A.Johnson, R.F.Mehl. Trans. Am. Inst. Min. Met. Eng. 135, 416, 1939.

95. R.H.Doremus Trans. Met. Soc. Am. Inst. Min Eng. 218, 590, 1960.

96. R.H.Doremus, E.F.Koch, Trans. Met. Soc. Am. Inst. Min. Eng. 218, 591, 1960.

97. C.Wert. Phy. Rev. 79, 601, 1950.

98. R.H.Doremus, Acta Met. 7, 399, 1959.

99. C.Zener, J. Appl. Phy. 20, 962, 1949.

100. F.S.Ham. J. Appl. Phy. 30, 1518, 1959.

101. F.S.Ham. J. Phy. Chem. of Solids. 6, 335, 1958.

102. W.J.McG.Tegart. The electrolytic and chemical Polishing of Metals.

103. D.H.Kay. Techniques for electron Microscopy. Chapter X by R.Phillips.

104. P.B.Hirsch, A.Howie, R.B.Nicholson, D.W.Pashley, M.J. Whelan Electron Microscopy of thin crystals. Butterworths 1965.

105. G.W.Groves, J.Washburn, A.Kelly, G.K.Williamson, Phil. Mag. 5, 991, 1960.

106. G.R.Booker, R.Stickler, Brit. J. Appl. Phy. 13, 446, 1962.

107. R.Castaing. Rev. Met. 52, 669, 1955.

108. L.Holland, Vacuum deposition of thin films. Chapman and Hall, 1958.

109. L.Harries, B.M.Siegel, J.Appl. Phy. 19, 739, 1948.

110. W.Pitsch, J. Inst. of Metals. 87, 444, 1958, 1959.

111. N. Nagakusa J.Phy. Soc. Japan 12 482 1957.

112. N.Nagakusa, J. Phy. Soc. Japan, 14, 186, 1959.

113. S. Ogawa, J. Mizuno, D.Watanbe, F.E.Fujia, J. Phy. Soc. Japan, 12, 999, 1957.

114. R.Weil, H.J.Read, J. Appl. Phy. 21, 1068, 1950.

115. E.C.Potter, Electro-chemistry, Clever-Hume, London, 1956.

116. R.W.Wood, Phil. Mag. 30, 300, 1915.

117. R.W.Wood. Phil. Mag. 32, 364, 1916.

118. I. Langmuir, Proc. Nat. Acad. Sci. 3, 141, 1917.

119. J.Frenkel, Z. Physik, 27, 117, 1924.

120. P.Benjamin, C.Weaver, Proc. Roy. Soc. 252, 418, 1952.

121. H.J.Levenstein, J.Appl. Phy. 20, 306, 1949.

122. H.Meyer, Physik dunner schichten vol.2, 1955.

123. D.S.Campbell, Proc. Amer. vac. soc. P.29, 1962, Pergamon Press.

124. J.D.Cockcroft, Proc. Roy. Soc. A 119, 243, 1928.

125. J.Eastermann, Z.Physik, 33, 370, 1925.

126. D.W.Pashley, Phil. Mag. 10, 127, 1964.

127. R.C.Newman, D.W.Pashley, Phil.Mag. 46, 927, 1955.

128. G.A.Bassett, Proc. conf. on electron Microscopy, Delft. Vol. I, 270, 1961.

129. D.W.Pashley, Advances in Physics. Vol. 14. 327, 1965.

130. G.A.Bassett, Phil. Mag. 3, 1042, 1958.

131. D.W.Pashley, Advances in Physics, vol.5, 173, 1956.

132. J.P.Hirth, G.M.Pound, Condensation and Evaporation, Nucleation and growth kinetics, Pergamon Press, 1963.

133. D.W.Pashley, M.J.Stowell, J. Vac. Sci. and Tech., 3, 156, 1966.

134. E.Kneller, J.Appl. Phy. 32, 1355, 1962.

135. E.Kneller, J.Appl. Phy. 35, 2210, 1964.

136. S.Mader, The use of thin films in Physical investigations J.C.Anderson edited, Academic Press, P.433, 1966.

137. S.Mader, The J. of Vacuum Sc. and Tech. 2, 35, 1965.

138. S.Mader, "Amorphous alloy films and their thermal stability". Paper presented in the thin film conf. in the Univ. of Southampton, April, 1968.

139. V.K.Zworykin, G.A.Morton, E.G.Ramberg, J.Hillier, A.W. Vance, Electron optics and electron Microscope, New York, Wiley, 1948.

140. V.E.Cosslett, Introduction to electron optics, Oxford, Clarendon Press, 1950.

141. O. Klemperer, Electron Optics, Cambridge University Press, 1953.

142. C.E.Hall, Introduction to Electron Microscopy, New York, McGraw-Hill, 1953.

143. P.R.Thornton, Scanning electron Microscopy. Chapman and Hall, 1968.

144. W.Bollman, J.Appl. Phy. 32, 869, 1961.

145. H.Hashimoto, M.Mannami, T.Naiki, Phil.Trans.Roy.Soc. A 253, 459, 1961.

146. G.P.Thomson, W.Cochrane, Theory and Practice of Electron Diffraction, London, McMillan 1939.

147. Z.A.Pinsker, Electron diffraction, London, Butterworth, 1953.

148. C.Davisson, L.H.Germer, Nature, 119, 558, 1927.

149. J.Biscoe, B.E.Warren, J.Appl. Phy. 13, 364, 1942.

150. R.E.Franklin, Acta Cryst. 3, 107, 1950.

151. A.J.C.Wilson, Acta Cryst. 2, 245, 1949.

152. G.W.Brindley, J.Mering. Acta Cryst. 4, 441, 1951.

153. B.E.Warren, P.Bodenstein, Acta Cryst. 20, 602, 1966.

154. R.Diamond. Acta Cryst. 10, 359, 1957.

155. R.Diamond, Acta Cryst. 11, 129, 1958.

156. O.J.Guentert, S.Cvilevich, Carbon, 1, 309, 1964.

157. J.Kakinoki, K.Katada, T.Hanawa, T.Ino, Acta Cryst. 13, 171, 1960.

158. S.Bohler. Electron Microscopical specimen Preparation Techniques. Booklet with Balzers BA 350 ...Unit.

159. L.Holland, Vacuum deposition of thin films, Chapman and Hall, 1958.

160. G.Hass, R.E.Thun. Physics of thin films, Vol. 3, 1966.

161. S.Tolansky, Multiple beam Interferometry.

162. L.S.Birks, Electron probe microanalysis.

163. K.F.Heinrich, Electron Probe x-ray analysis.

164. A.E.B.Presland, J.R.White, J.Sci.Inst.Series 2, Vol.2. 67, 1969.

165. J.H.L.Watson, J.Appl. Phy. 18, 153, 1947.

166. J.Hillier, J.Appl. Phy. 19, 226, 1948.

167. R.L.Stewart, Phy. Review, 45, 488, 1934.

168. C.Fisher. Particle size analysis conference, Paper 9, 1966.

169. M.Cole, The microscope and crystal Front Vol. 15, No.4. P.148, 1966.

170. S.J.Gregg, K.S.W.Sing, Adsorption, Surface area and Porosity, P.25, Academic Press, 1967.

171. G.Herdan, Small Particle Statistics, Elsvier Publishing Company, 1953.

172. A.Westgren, G.Phragmen, J. of Iron and Steel Inst. No. 1. 241, 1922.

173. H.B.Hendricks, Zeit. für Kristallographie, 74, 534, 1930.

174. H.Lipson, N.J.Petch, J.Iron and Steel Inst. No.II, P.95, 1940.

175. W.Hume-Rothary, G.V.Raynor, A.T.Little, J.Iron and Steel. Inst. 1, 143, 1942.

176. N.J.Petch, J.Iron and Steel Inst. 1, 143, 1944.

177. W.A. Hill, B.W.Davey, Physics Rev. 17, 549, 1921.

178. P.G.Shewmon, Diffusion in Solids. McGraw-Hill, Series in Materials Science and Engineering, 1963.

179. H.Konig, Nature wissenschaften, 38, 154, 1951.

180. H.L.D.Pugh, J.Lees, J.A.Bland, Nature, 191, 865, 1961.

181. R.Bernier, Ann. Chim, 6, 104, 1951.

182. J.D.Venables, R.G.Lye Rias, Technical Report 68-15C. October 1968.

183. W. Pitsch, Acta Met.3, 542, 1955.

184. J.R. Wolfe, D.R. McKenzie, R.J. Borg, Paper presented in the Second Industrial carbon and graphite conference, 1965.

185. J. Truitt, G.D. Alton, C.M. Blood, Applied Phy. letters, 3, 150, 1963.

186. P.N. Denbigh, C.W.B. Grigson, J.Sci. Inst. 42, 305, 1965.

187. J.H. Woodhead, Metallography, 1, 35, 1968.

188. M.H.Tompsett, C.W.B. Grigson, Nature, 206, 923, 1965.

ACKNOWLEDGEMENTS

I should like to express my deep gratitude to my supervisor Dr. A.E.B. Presland for his continued interest, advice and encouragement at all stages of the work.

I am also indebted to Mr. K.C. Sarmah and Mr. G.K. Barooah for their help and encouragement before and after coming to this country. I also thank my brother and sister for their sacrifice during this period of three years.

I am also grateful to all my fellow students, Mr. P. Marlow and other well wishers whose help and encouragement have been invaluable to me.

I am also indebted to the Imperial College of Science and Technology for partial financial assistance towards the completion of the project.

Finally, I express my thanks to the Government of Assam, India for an educational loan and the Nowgong College authority for granting me a study leave of three years.